Simulation of time-dependent crack propagation in a quasi-brittle material under relative humidity variations based on cohesive zone approach : application to wood

Ngoc Anh Phan

THÈSE PRÉSENTÉE

POUR OBTENIR LE GRADE DE

DOCTEUR DE

L'UNIVERSITÉ DE BORDEAUX

ÉCOLE DOCTORALE DES SCIENCES PHYSIQUES ET DE L'INGENIEUR

SPÉCIALITÉ : MECANIQUE

Par : Ngoc Anh PHAN

Simulation of time-dependent crack propagation in a quasi-brittle material under relative humidity variations based on cohesive zone approach: application to wood

Sous la direction de : Stéphane MOREL

Soutenue le 20 Janvier 2016

Membres du jury :

M. GRIL Joseph,	Directeur de recherche CNRS, Université Montpellier, France	Président du jury
M. NAVI Parviz,	Professeur, Ecole Polytechnique Fédéral de Lausanne, Suisse	Rapporteur
M. DUBOIS Frédéric,	Professeur, Université de Limoges, France	Rapporteur
M. MARTIN Eric,	Professeur, Université de Bordeaux, France	Examinateur
M. DOURADO Nuno,	Professeur auxiliaire, Université de Minho, Portugal	Examinateur
Mme. CHAPLAIN Myriam,	Maître de Conférences, Université de Bordeaux, France	Encadrante
M. MOREL Stéphane,	Professeur, Université de Bordeaux, France	Directeur de thèse
M. FERET Thomas,	Ingénieur, Fédération de L'Industrie Bois Construction, France	Invité
M. COUREAU Jean-Luc	Maître de Conférences, Université de Bordeaux, France	Invité, Encadrant

Abstract:

This thesis is dedicated to the simulation of the fracture behavior of wood under long-term loading and variable relative humidity conditions. Indeed, wood is well-known to be a highly hygroscopic material in so far as its mechanical and fracture properties are very dependent on moisture. Moreover, the stability of an existent crack in a structural element can be strongly affected by the sudden variations of relative humidity (RH) and can lead to unexpected failure of the element.

The thermodynamic approach proposed in this thesis includes the mechano-sorptive effect in the analytical expression of the deformation, by operating a decoupling of the strain in a mechanical part and a mechano-sorptive part in material. Moreover, the quasi-brittle fracture of wood is here simulated from a cohesive zone model whose cohesive parameters are functions of the moisture in order to mimic the moisture-dependent character of the fracture properties. On this basis, an increment formulation allows the integration of the effect of sudden RH variations on the fracture process zone (cohesive zone) by introducing an additional stress field along this zone. As a function of the RH variation, this additional stress field depends on not only the stress state and the crack opening along the cohesive zone but also the material moisture ahead of the zone (undamaged material). In the finite element analysis, an algorithmic tangent operator is used to solve the non-linear problem combining mechano-sorptive model and cohesive zone model including the effect of sudden RH variations.

The simulation of a notched structural element submitted to a constant load and cyclic RH variations exhibits a strong coupling between the mechano-sorptive behavior and the effect of the RH variations on the fracture process zone (FPZ). This coupling results in an increase of the crack propagation kinetic and leads to a precocious failure compared to those obtained from the mechano-sorptive model or from the effect of sudden RH variations on the FPZ. Moreover, the coupling between the mechano-sorptive model and the effect of sudden RH variations on the FPZ which cannot be predicted by a simple superposition of both effects, showing the interest of such a numerical approach in order to describe the complex behavior of wood structural elements submitted to variable climatic conditions.

Keywords: quasi-brittle, relative humidity variations, wood, cohesive zone, fracture process zone, time-dependent crack growth, mechano-sorption, coupling.

Titre : Simulation de la propagation de fissures dans un matériau quasi-fragile soumis à des variations d'humidité relative selon une approche de zone cohésive: application au bois

Résumé :

Cette thèse est consacrée à la simulation du comportement à la rupture de bois sous des chargements à long terme et sous des conditions d'Humidité Relatives (HR) de l'air variables. Il est connu que le bois est un matériau fortement hygroscopique, ses propriétés mécaniques et de rupture sont en effet très dépendantes de sa teneur en eau. En outre, la stabilité d'une fissure existante dans un élément structural peut être fortement influencée par les variations, en particulier brusques, d'humidité relative qui peut conduire à la rupture inattendue de l'élément.

L'approche thermodynamique proposée intègre l'effet de mécanosorption dans l'expression analytique de la déformation, en découplant les déformations mécaniques et celles dues au comportement mécanosorptif du matériau. En outre, la rupture quasi-fragile du matériau bois est traduite par un modèle de zone cohésive dont les paramètres de cohésion sont fonctions de la teneur en eau afin de simuler l'effet de l'humidité sur les propriétés de rupture. Sur cette base, une formulation incrémentale permet l'intégration de l'effet des variations soudaines d'humidité relative (autrement dit, le choc hydrique) sur la zone d'élaboration (zone cohésive) en introduisant un champ de contraintes supplémentaires le long de cette zone. Fonction de la variation de HR, ce champ de contraintes supplémentaires dépend de l'état de contrainte et de l'ouverture de la fissure le long de la zone cohésive, mais également de l'humidité en pointe de fissure (matériau non endommagé). Dans l'analyse par éléments finis, un opérateur tangent algorithmique est utilisé pour résoudre le problème non linéaire en combinant le modèle de mécanosorption et le modèle de zone cohésive et en intégrant l'effet du choc hydrique.

La simulation du comportement d'une éprouvette entaillée soumise à un chargement constant et à des variations cycliques de HR montre un fort couplage entre le comportement mécanosorptif et l'effet du choc hydrique HR sur la zone d'élaboration. Ce couplage entraîne une augmentation de la propagation des fissures et conduit à une fissuration plus précoce par rapport à celle obtenue à partir du modèle de mécanosorption seul ou à partir du modèle de zone cohésive en intégrant l'effet des variations soudaines de HR. En outre, le couplage entre le modèle mécanosorptif et le modèle de zone cohésive en intégrant l'effet du choc hydrique montre l'intérêt d'une telle approche numérique pour décrire le comportement complexe des éléments de charpente en bois soumis à des conditions climatiques variables, comportement qui ne peut être prédit par une simple superposition des deux modélisations.

Mots clés : quasi-fragile, variations d'humidité relative, bois, zone cohésive, fracture process zone, propagation de fissure, mécanosorption, couplage.

Unité de recherche
L'Institut de Mécanique et d'Ingénierie au département Génie Civil et Environnemental à l'Université de Bordeaux

Résumé étendu de la thèse

Le bois est considéré comme un matériau hydromécanique orthotrope dont le comportement mécanique dépend fortement de la teneur en eau et de la température. Sous des conditions environnementales constantes (humidité relative (HR) et de la température), le bois présente un comportement viscoélastique linéaire. Cependant, si l'on tient compte de la variation de l'humidité et de la température, le comportement mécanique devient plus complexe en raison de l'effet du couplage entre la sollicitation mécanique et l'état hydrique (comportement thermo-hydro-mécanique (THM)). Le comportement viscoélastique du bois sous humidité variable, appelé comportement de mécano-sorption, induit des réponses différentes en phase de séchage et en phase d'humidification.

De nos jours, la construction de structures en bois est en progression en raison du contexte écologique et environnemental. Dans ce contexte, le matériau bois présente un intérêt particulier pour relancer le secteur de la construction. Cependant, de par le changement climatique, les structures en bois peuvent être impactées. En raison du comportement THM du bois, le changement climatique (tels que les variations importantes de HR et/ou de la température) peut conduire à l'apparition et au développement de fissures dans les composants porteurs de la construction bois (poutre, poteau ...) ; ceci réduira la résistance et la durée de vie de la structure. En outre, en raison du coût économique, la conception des ouvrages nécessite de ne pas surdimensionner les éléments tout en respectant les limites réglementaires.

En Europe, le code de conception pour les structures en bois est actuellement l'Eurocode 5 (EC5) ; la résistance du matériau est déterminée à partir d'essais à court terme (environ cinq minutes). Dans ce code, l'effet de l'humidité est introduit par un coefficient de réduction k_{mod} appliqué à la résistance du matériau dont la valeur dépend de l'une des trois classes de service réglementaires (classes d'humidité), ces classes dépendent de la température et l'humidité relative moyennes de l'air environnement. Même si le coefficient k_{mod} a l'avantage de fournir des réponses simples lors de la conception, il peut être la cause d'un surdimensionnement sécuritaire ou d'un sous-dimensionnement dangereux de la structure par manque de connaissances.

Parallèlement à l'EC5, depuis quelques décennies, plusieurs travaux ont été consacrés au comportement hydromécanique du matériau de bois en prenant en compte le com-

portement viscoélastique couplé avec des variations d'humidité. Lorsque la structure est simultanément soumise à un chargement mécanique et à des variations de l'humidité, la déformation augmente, ce qui pourrait provoquer une défaillance prématurée de la structure. Les effets des variations de l'humidité sur la propagation des fissures ne sont pas encore clairement identifiés. Par conséquent, la question de l'influence de l'environnement variable sur les propriétés mécaniques ainsi que sur le processus de la propagation des fissures dans le bois commence à gagner en attention.

Au cours des trois dernières décennies, de nombreux modèles de mécanosorption ont été proposés et mis au point dans le but d'expliquer clairement le phénomène mécanosorptif, ainsi que le phénomène de transfert, de couplage entre la température et l'humidité, dans le matériau bois. Cependant, la plupart des modèles ne considèrent pas la propagation des fissures dans l'élément afin de simplifier le problème lié aux conditions limites pour le transfert thermo-hydrique dans le bois; et ils ne permettent pas de décrire clairement chaque mécanisme de déformation dans le matériau. A côté de l'établissement de modèles de mécano-sorption, le comportement à la rupture du bois est aussi d'avantage étudié afin de mieux comprendre le processus de propagation de la fissure. Le comportement à la rupture du bois est généralement considéré comme un comportement quasi-fragile dans lequel une zone d'élaboration appelée Fracture Process Zone (FPZ) existe à la pointe de la fissure. Le matériau dans la FPZ (zone de fibres endommagées) est sensible aux variations brusques de HR. Sous un environnement extérieur variable, les structures en bois sont plus sensibles à la fissuration que sous des conditions constantes en raison de l'effet des variations d'humidité sur la propagation de la fissure. Cependant, l'effet des variations d'humidité sur la cinétique de propagation de la fissure a encore été peu abordé, il n'y a pas d'étude intégrant l'effet des variations d'humidité sur le comportement mécanosorptif du substrat bois et sur la zone d'élaboration de la fissure.

L'objectif de cette thèse est d'établir une méthode plus robuste pour définir la cinématique de fissuration dans le bois sous des variations d'humidité. Le principal problème est l'étude du couplage entre l'état d'hydrique et la propagation des fissures, ainsi que l'étude de l'effet sur la propagation de la fissure d'un choc hydrique sur la FPZ. Pour atteindre notre but, une méthode est proposée en intégrant l'effet de l'humidité dans le FPZ. Cette méthode nous permet de visualiser le phénomène de couplage entre le comportement THM du bois et le processus de propagation de la fissure. Une modélisation en 3D est réalisée en prenant en compte : (i) la diffusion de l'humidité dans le bois, (ii) le comportement de mécano-sorption viscoélastique dans le substrat de bois et (iii) la zone d'élaboration de la fissure (FPZ).

Cette thèse porte sur une compréhension approfondie du bois en tant que matériau complexe, hygroscopique dont les propriétés de fissuration sont fortement dépendantes de l'humidité et de ses variations. Deux types d'essais de fissuration ont été réalisés sur des

éprouvettes de caractérisation en mode I (mTDCB : modified Tapered Double Cantilever Beam) en pin Maritime (en configuration TL : Tangentiel et Longitudinal) sous une large gamme de teneurs en eau MC : (i) essais monotones (quasi-statique) sous différents MCs permettant de déterminer la courbe de résistance à la propagation des fissures (critère de la propagation des fissures) et les paramètres du modèle de la loi cohésion (ii) essais de fluage sous variations d'humidité permettant d'étudier la propagation des fissures.

A partir des essais monotones, les propriétés de rupture du bois ont été déterminées et des courbes de résistance ont été obtenues pour dix différentes teneurs en eau allant de 5% à 30%. Sur cette base, les lois cohésives (bilinéaires adoucissantes) correspondantes à ces 10 humidités ont été déterminées. Le processus de fissuration pour toutes les humidités peut être obtenu pour les autres teneurs en eau par interpolation linéaire à partir des paramètres de cohésion connus. Il n'est pas possible d'effectuer un suivi de la fissure lors de l'essai de propagation : la longueur réelle de la fissure est en effet très difficilement observable dans le matériau bois. La longueur de la fissure est obtenue grâce à l'approche de la Mécanique Linéaire Elastique de la Rupture équivalente (calcul par la méthode des éléments finis) à partir des enregistrements de la force et du déplacement des points d'application de la charge. Les résultats montrent que le comportement à la rupture du bois dépend fortement de la teneur en eau. Pour les teneurs en eau inférieures à 22-25%, la résistance au plateau, l'ouverture critique, la longueur caractéristique correspondant à la zone de microfissures, ainsi que la longueur caractéristique de la FPZ augmentent avec la teneur en eau. En outre, la résistance à la traction et le ratio d'énergie cohésive diminuent avec la teneur en eau. Cependant, pour les teneurs en eau égales ou supérieures à 22- 25%, l'influence de l'humidité sur le comportement à la rupture semble négligeable.

Dans la simulation de la propagation de la fissure sous HR variable, les propriétés viscoélastiques en fonction de l'humidité sont introduites par un modèle 3D de mécanosorption viscoélastique sur la base du principe de la thermodynamique. Le modèle 3D mécanosorptif est basé sur la formulation incrémentale 1D proposée et validée par Husson et Dubois (2012). L'approche thermodynamique traduit l'effet de mécanosorption dans l'expression analytique de la déformation en opérant un découplage de la partie mécanique et de la partie mécanosorptive de la déformation dans le bois. En outre, une formulation incrémentale permet d'intégrer l'effet du choc hydrique sur la FPZ en introduisant une charge climatique incrémentale supplémentaire dans cette zone. Pour représenter la FPZ, un modèle de zone cohésive (CZM) est appliqué. Le chargement climatique supplémentaire dû aux variations rapides d'humidité sur la FPZ ne dépend pas seulement de la contrainte et de l'ouverture des fissures, mais aussi de l'humidité dans la zone cohésive. Le calcul est réalisé sous le code éléments finis CAST3M, des modèles ont été intégré sous le code source Esope afin de résoudre le problème non linéaire intégrant le comportement mécanosorptif viscoélastique et l'effet du choc hydrique sur la zone d'élaboration de la fissure.

Dans ce travail, le processus de diffusion de l'humidité a été analysé à température constante et HR variables, sous charge constante. En outre, le coefficient de diffusion a été supposé être indépendant de la contrainte. Dans le modèle 3D de mécano-sorption viscoélastique, le modèle de Kelvin Voigt généralisé à deux branches a été utilisé. Sous l'hypothèse selon laquelle les facteurs orthotropes sont indépendants de l'humidité, les fonctions fluage suivant les directions tangentielle et radiale ont été considérées proportionnelles à la fonction de complaisance de fluage suivant la direction longitudinale.

Des simulations, avec ou sans intégration du comportement mécanosorptif, avec ou sans prise en compte du choc hydrique sur la FPZ (surcharge climatique), nous permettent de mieux comprendre les mécanismes qui influent sur la propagation des fissures causées par le séchage et l'humidification. En outre, en raison des variations de l'environnement extérieur, divers phénomènes liés au processus de propagation des fissures peuvent être éventuellement isolés dans les simulations numériques mais difficiles expliqués à travers des études expérimentales.

Les résultats du modèle numérique ont montré que, en plus de l'effet de la viscoélastique sur la propagation de la fissure (en raison de l'augmentation de l'énergie élastique stockée dans la structure), la variation d'humidité peut également être à l'origine d'une augmentation de la propagation de la fissure. L'effet du comportement mécanosorptif viscoélastique sur la propagation de la fissure apparaît plus important que l'effet du choc hydrique sur la FPZ au cours de la première phase d'humidification ; inversement au cours de la première phase de séchage. Par contre, le couplage de ces deux effets a plus d'influence que l'effet individuel de chacun sur la propagation de la fissure. Pendant la phase de séchage, la fissure a tendance à se propager. La vitesse de propagation dépend du choc hydrique : la propagation avance lentement ou pas pendant la phase d'humidification, et accélère pendant la phase de séchage. Ces résultats sont similaires à ceux observés expérimentales dans l'étuve climatique sur les éprouvettes de pin Maritime. Malgré la grande dispersion des résultats expérimentaux, les simulations numériques enveloppent les réponses expérimentales et en particulier traduisent assez bien la propagation soudaine de la fissure conduisant à des défaillances précoces. La comparaison des résultats expérimentaux avec les résultats numériques obtenus en intégrant le phénomène d'hygro-verrou seul souligne la nécessité de tenir compte du choc hydrique sur la zone cohésive. Le couplage semble être la clé de la description pertinente des réponses expérimentales, mais un tel couplage est complexe et ne peut être décrit que par une approche numérique comme proposée dans cette thèse.

Même si le modèle actuel nécessite d'autres validations par des résultats expérimentaux afin de vérifier la pertinence de la simulation dans le cas des variations de HR complexes, le modèle permet d'estimer le temps à rupture pour diverses structures fissurées soumises ou non à des conditions environnementales variables (dans la mesure où le chemin de

la fissure potentiel est connu : emplacement de l'interface cohésive), ce qui est l'un des avantages de cette méthode car elle est capable de donner une référence pour définir un état ultime des structures.

Implanté dans un code éléments finis 3D (dans le code source), cette méthode peut être appliquée pour les structures complexes où l'état mécanique de la structure dépend fortement d'une ou plusieurs interactions (par exemple, l'interaction entre les composants des structures telles que les assemblages, goujon collé, etc. ...).

Une application pratique de la méthode proposée aux constructions était un des objectifs de cette thèse. Cependant, cette tâche est assez compliquée en raison du long temps de calcul numérique ainsi que de la nécessité de valider une formulation simplifiée adéquate. Néanmoins, il nous permet de mieux comprendre le comportement du matériau ainsi que de prédire la durée de vie des structures et encourage une étude plus approfondie sur ce sujet.

To my wife Huyen, my children Dat, Uyen

To my parents

Acknowledgement

I wish to thanks Alexandre GANGNANT for being my spokesperson, my translator, my dictionary when I first came to the laboratory and for all the discussions we have.

I would like to extend my heartfelt to my parents, my sisters for giving me unlimited encouragement, understanding and love.

Finally, for my wife, Huyen TRAN, there are really no words or no ways for me to express my appreciation for her being always where my eye can see, for her endless love, her non-stop support and without which none of this would have been materialized.

Contents

List of Figures

x

xi

List of Tables

Abbreviations

CZM Cohesive Zone Model

DCB Double Cantilever Beam

EC5 Eurocode 5

EMC Equilibrium Moisture Content

eq.LEFM equivalent Linear Elastic Fracture Mechanics

FEA Finite Element Analysis

FPZ Fracture Process Zone

LEFM Linear Elastic Fracture Mechanics

MC Moisture Content

mTDCB modified Tapered Double Cantilever Beam

R-curve Crack growth resistance curve

RH Relative Humidity

SL Stress Level

TDCB Tapered Double Cantilever Beam

THM Thermo-Hydro-Mechanical

TSL Traction-separation law

Nomenclature

$\mathbb{A}$ perturbation stress coefficient of the cohesive zone

a (equivalent) crack length

a_{sf} stress-free crack length (the main crack length)

$\mathbb{B}$ strain-displacement transformation matrix of wood substrate

$\bar{t}$ specific time when the compliance in the history is equal to the current one (i.e. $C(\bar{t}) \equiv C_{n+1}$) during the softening case ($\Delta\, MC_n > 0$)

$\mathbb{B}_{joint}$ strain-displacement transformation matrix of joint

$\mathbb{C}^e$ elastic compliance tensor

$\mathbb{C}^{e\_ms}$ elastic mechano-sorptive compliance tensor

$\mathbb{C}^{tan}$ total tangent operator of the whole model

$\mathbb{C}^{ve\_ms}$ viscoelastic mechano-sorptive compliance tensor

d damage state of the joint element

$\mathbb{D}$ second-order diffusion tensor

d_j damage state at the jth joint element

δ displacement of the loading point

Δa_c characteristic equivalent crack length in R-curve

Δa_u crack length corresponding to the peak load

$\Delta\sigma_{FPZ,n}$ perturbation stress due to the rapid varying moisture on the cohesive zone

$\Delta\sigma_{j,n}^*$ stress perturbation at the jth joint element due to the rapid varying moisture during Δt_n

$\Delta\underline{\varepsilon}^e$ instantaneous elastic strain increment

$\Delta\underline{\varepsilon}^{e\_ms}$ recoverable elastic mechano-sorptive strain increment

$\Delta\underline{\varepsilon}^{MC}$ shrinkage-swelling strain increment

$\Delta\underline{\varepsilon}^{ve\_ms}$ recoverable viscoelastic mechano-sorptive strain increment

$\widetilde{\underline{\varepsilon}}_n^{e\_ms}$ elastic mechano-sorptive strain (at the first spring) which summarizes history effects of the humidity and the external mechanical loadings

$\widetilde{\underline{\varepsilon}}_{i,n}^{ve\_ms}$ viscoelastic mechano-sorptive strain (at the ith Kelvin Voigt branch) which summarizes history effects of the humidity and the external mechanical loadings

E_L^{exp} corrected experimental longitudinal modulus

$\underline{\varepsilon}^{e\_ms}(\bar{t})$ elastic mechano-sorptive strain (at the first spring) corresponding to the specific time $\bar{t}$

$\underline{\varepsilon}_i^{ve\_ms}(\bar{t})$ viscoelastic mechano-sorptive strain (at the ith Kelvin Voigt branch) corresponding to the specific time $\bar{t}$

$\mathbf{F}_{n+1}^{MC\_FPZ}$ total external climatic loading until the time t_{n+1}

$\mathbf{F}_{n+1}^{ext}$ external loading at the time t_{n+1}

$\mathbf{F}_{n+1}^{int}$ internal loading at the time t_{n+1}

f_t tensile strength (in the cohesive law)

$G(a)$ strain energy release rate

G_f critical cohesive fracture energy

G_{fb} cohesive energy related to the crack bridging cohesive behaviors

$G_{f\mu}$ cohesive energy related to the micro-cracking behaviors

$G_{f\mu}/G_f$ cohesive energy distribution ratio

$G_R(a)$ resistance to the crack growth (R-curve)

G_u energy release rate corresponding to the peak load

k_{mod} reduction coefficient in the material strength in EC5

l_{coh} length of the cohesive zone (FPZ)

l_{coh}^c characteristic length of the fracture process zone (FPZ fully developed)

l_μ characteristic length of the micro-cracking zone

$\lambda(a)$ numerical compliance function

$\lambda_{exp}(a)$ experimental compliance function

$\lambda_{virt}(a)$ virtual compliance function

$MC_{j,n}$ moisture at the jth joint element at the time t_n

$MC_{j,n+1}$ moisture at the jth joint element at the time t_{n+1}

$MC_{joint,n}$ moisture distribution on the fracture process zone

$MC_{average}$ average moisture in the specimen

MC_{eq} equilibrium moisture of wood corresponding to the environment RH obtained from the sorption isotherm curve

MC_{FPZ} average moisture at the FPZ tip

MC_{surf} moisture content at the wood surface

P_{max} peak-load in the monotonic test

ψ multiplicative correction factor

$\mathbf{R}(\mathbf{u}_{n+1}^j)$ residual force corresponding to the jth iteration at the time t_{n+1}

$\sigma_{joint}(MC_n)$ stress field on the cohesive zone corresponding to MC_n

$\underline{\sigma}(\bar{t})$ stress (at the first spring) corresponding to the specific time $\bar{t}$

$\underline{\sigma}_i^{k,ve\_ms}(\bar{t})$ stress (at the spring of the the ith Kelvin Voigt branch) corresponding to the specific time $\bar{t}$

T temperature

$\theta_\psi(a)$ error generated function of the multiplicative correction factor ψ versus crack length

$\mathbf{u}_{n+1}^j$ displacement corresponding to the jth iteration at the time t_{n+1}

ε^e instantaneous elastic strain

ε^{e_ms} recoverable elastic mechano-sorptive strain

ε^{MC} shrinkage-swelling strain

ε^{ve_ms} recoverable viscoelastic mechano-sorptive strain

w crack opening displacement

w_c critical crack opening displacement

w_j crack opening displacement at the jth joint element

Introduction

Wood is considered as an orthotropic hygromechanical material. The mechanical behavior strongly depends on Moisture Content (MC) and on temperature in the material. Under constant environmental conditions (Relative Humidity (RH) and temperature), the wood exhibits a linear viscoelastic behavior. However, when taking into account the variation of the moisture and the temperature, the mechanical behavior becomes more complex due to the coupling effect between the mechanical solicitation and the environment condition (the well-known coupling is named as the Thermo-Hydro-Mechanical (THM) processing). The viscoelastic behavior of wood under varying moisture is called the mechano-sorptive behavior which induces different responses in drying phase and in humidification phase.

Nowadays, the construction of timber structures is increasing due to the environmental and the ecological context. In this context, wood material has a special interest to revive construction sector. However, owing to the climate change, timber structures are affected. Due to the THM processing, the climate change (such as variations of RH and/or of temperature) induces appearance and development of cracks in components of timber elements (i.e., beam, column...) which reduces the strength and the lifetime of the structure. Moreover, due to the economic cost, the structure design is required not for oversized dimension but to respect the limit range of the security.

In Europe, the design code for timber structures is currently the Eurocode 5 (EC5) using material strength which is determined on the basis of short-term tests (about five minutes). In the code, the varying humidity effect is introduced by a reduction coefficient k_{mod} applied to the material strength. Structures are assigned to one of three service classes (moisture classes), characterized by average temperature and RH of the surrounding air. The average Equilibrium Moisture Content (EMC) in most softwood not exceeds 12% in service class 1 and 18-20% in service class 2. In service class 3, the EMC may be higher. There are five load duration classes: permanent, long-term (up to 10 years), medium-term (less than 6 months), short-term (less than one week), and instantaneous. For solid wood, the coefficient k_{mod} are given for class 1 and 2 as followed: 0.6, 0.7, 0.8, 0.9 and 1.1 corresponding to the order of the five load duration classes, respectively. For the service class 3, the coefficient k_{mod} varies as followed: 0.5, 0.55, 0.65, 0.7, 0.9.

If the coefficient k_{mod} has the advantage to provide simple answers to implement in the design procedure, but it can be the cause of a safe over-dimension or a danger under-dimension of the structure by a lack of knowledge. Alongside the standard code EC5 for several decades, fundamental works have been devoted to the subject of hygromechanical behavior of the wood material by taking into account the viscoelastic behavior coupled with climatic variations. When the structure is simultaneously subjected to the applied stress and variations of the moisture, the deformation is increased, which could cause the premature failure of the structure. In addition, although the maximal or average amplitude of consecutive moisture cycle acting in the real structure is smaller than the moisture corresponding to one of the service classes in the EC5, the structure is more or less dangerous because of a significant influence of moisture variations on the strength and on the crack growth. However, the effects of varying moisture on the crack growth have not yet been clearly identified. Therefore, the impact issue of the varying environment condition on the mechanical properties as well as on the crack growth process in wood began to gain more attention.

During three last decades, many mechano-sorptive models have been proposed and developed in order to clearly explain most of the mechano-sorptive phenomena as well as the coupling phenomenon between the temperature and the moisture transfer in the wood material. However, most of models do not consider the crack growth in the structure in order to simplify the problem of the limit condition, of the boundary condition for the thermo-hydric transfer in wood; and possibly to clearly observe each deformation mechanism in the material. Beside the development of the mechano-sorptive models for wood, fracture behavior of wood is also more investigated to better understand the crack process in the structure. The fracture behavior of wood is commonly accepted as a quasi-brittle behavior in which a softening zone called Fracture Process Zone (FPZ) exists ahead of the crack tip. The material in the FPZ (i.e., damaged fibres) is sensibly influenced due to the sudden RH variations. Under variations of the external environmental condition, the cracked timber structures are more affected than under constant conditions due to the coupling between the varying moisture effect and the crack growth. However, there is a very little work on the topic of the moisture effect on the crack growth kinetics: the coupled effect of the varying moisture (on the mechano-sorptive behavior of the wood substrate and on the process zone) on the crack growth kinetics.

The aim of the thesis is to establish a more robust method to analyze the cracked timber elements under humidity variations. The main problem is the coupling between the hydride and mechanical states during the crack propagation, as well as the coupled effect (which are the mechano-sorptive behavior and the rapid varying moisture on the FPZ) on the crack growth. To achieve our purpose, a method will be proposed in which

the moisture effect is integrated into the FPZ. This method allows us to visualize the coupled phenomenon between the THM processing of wood and the crack growth process. In this method, three principal problems will be investigated thanks to 3D modeling such as:

- the moisture diffusion in wood,
- the viscoelastic mechano-sorptive behavior in wood substrate,
- the fracture process zone.

This thesis focuses on the development of a deeper understanding of wood as a complex, highly hygroscopic material whose mechanical and fracture properties are dependent on moisture. The thermodynamic approach includes the mechano-sorptive effect in the analytical expression of the deformation, by operating a decoupling of the strain in a mechanical part and a mechano-sorptive part in wood material. Moreover, an increment formulation allows to integrate the rapid varying moisture effect on the FPZ by introducing an additional increment climatic loading into this zone. To represent the FPZ in the structure, a Cohesive Zone Model (CZM) is applied. Based on this, the additional climatic loading due to rapid varying moisture on the FPZ depends not only on the stress and the crack opening state but also on the moisture in the cohesive joint. In order to combine two or more models in the Finite Element Analysis (FEA), an algorithmic tangent operator is used to solve the non-linear problem combining mechano-sorptive model and moisture-dependent cohesive zone model including the effect of sudden RH variations. The obtained results are promising. The main stages of the present thesis are presented in the following paragraphs.

In the first chapter, a brief review of the literature is given on the hygroscopic and the mechanical behavior of wood. A brief review of wood mechano-sorptive models is also presented, which allows us to choose the most adequate models for our study.

The second chapter discusses fracture mechanics in general and quasi-brittle fracture in particular. Owing to the development of a non-negligible non-linear domain in the quasi-brittle behavior, an equivalent Linear Elastic Fracture Mechanics approach (eq.LEFM) is applied to describe this behavior. Fracture behavior of wood is also presented while investigating the influencing factors. Moreover, crack growth process of wood in viscoelastic media is also discussed.

The third chapter presents a detail description of the studied material, the experimental methodology as well as the analytical, numerical study of the fracture behavior depending on the moisture. This chapter presents two fracture tests in mode I at a wide range of MCs on Maritime pine samples : (i) monotonic (quasi-static) tests under different MCs allow to determine crack growth resistance curve (crack growth criterion) and cohesive

model parameters of the material and (ii) creep tests under humidity variations allow to study the crack growth of the structure.

The fourth chapter is destined to describe results obtained from the previous chapter, the resistance curves and the cohesive parameters are studied in relation with the moisture content. Moreover, the characteristic length of the FPZ and of the macro fibring zone depending on the moisture is described. The correlation between the R-curve, the cohesive parameters and the length of the FPZ at whatever moisture is also investigated.

The fifth chapter presents the main work of the thesis. In the 3D numerical analysis, two models are used in which the viscoelastic mechano-sorptive model is applied to the wood substrate and the moisture-dependent cohesive zone model is applied to the FPZ. An algorithmic tangent operator is used to solve the non-linear problem. Based on the thermodynamic approach, this chapter presents the establishment of a total tangent operator for the 3D mechano-sorptive behavior. Moreover, an additional increment climatic loading along the cohesive zone is proposed in order to integrate the rapid varying moisture effect on the FPZ.

The final chapter undertakes a number of simulations of our method on different scenarios of loading and humidity. The experimental results are obtained from creep tests under humidity variations which are detailed in the third chapter. This chapter presents comparisons of the effect of the viscoelastic behavior, of the mechano-sorptive behavior as well as of the rapid varying moisture integrated in the FPZ on the crack growth of the structure in order to better visualize each effect and coupling effect on the crack growth kinetics.

Chapter 1

Hygromechanical behavior of wood

This chapter presents the literature view on hygroscopic and mechanical behavior of wood. The mechanical behavior strongly depends on the moisture and the temperature. Under a constant environmental condition (RH and temperature), wood material exhibits linear viscoelastic behavior. However, when taking into account the varying moisture and/or temperature, the mechanical behavior in wood becomes more complex. The viscoelastic behavior of wood under varying moisture is called mechano-sorptive behavior which induces different behaviors in the drying phase and the humidification phase. To better explain these phenomena, mechano-sorptive models are proposed and divided into two categories:

- model with independent activation (where the relation between the creep deformation and the mechano-sorptive deformation is not strongly coupled),
- model with combined activation (where the coupling between two mechanisms is assumed).

Before performing a brief review of mechano-sorptive models, the description of the wood material and the hygroscopic behavior of wood will be presented in the next paragraphs.

1.1 Wood composition

Wood is considered as an orthotropic viscoelastic material, the orthotropic axes are: the longitudinal direction (L), the radial direction (R) and the tangential direction (T) as illustrated in Figure 1.1a. As shown in Figure 1.1b, a tree trunk is generally composed of millions individual wood cells which differ in size and shape, depending upon their physiological role in the tree. Each species possesses a distinguish arrangement patterns from the others. The longitudinally long cells create the bulk of the wood and provide "grain" to the material.

source: http://www.britannica.com/media/full/603935/55253
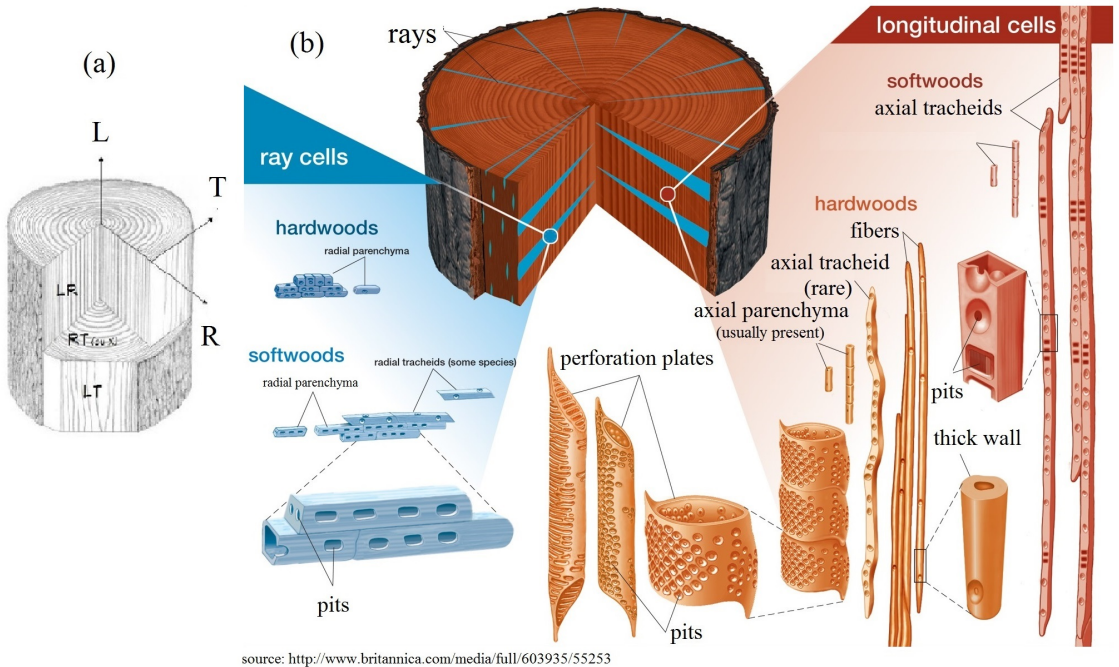
Figure 1.1: Wood composition

As shown in Figure 1.1b, according to Kollmann and Cote [92], softwoods mainly consist of tracheids (long cells with 3 - 5 mm) which are about 20 - 80x10^{-6} m in diameter while hardwoods mainly consist of wood fibers cells. Similar to tracheids, wood fibers are elongated cells but smaller, only less than 20^{-6} m in diameter and from 0.7 to 3 mm long. In the living tree, wood fibers do not serve for the fluid transport. The role of the tracheids or the wood fibers is to provide mechanical support for the wood. Figure 1.2 presents a scanning electron micrograph of a hardwood specimen in which wood fibers (F), vessels (V), rays (R) are illustrated [92].
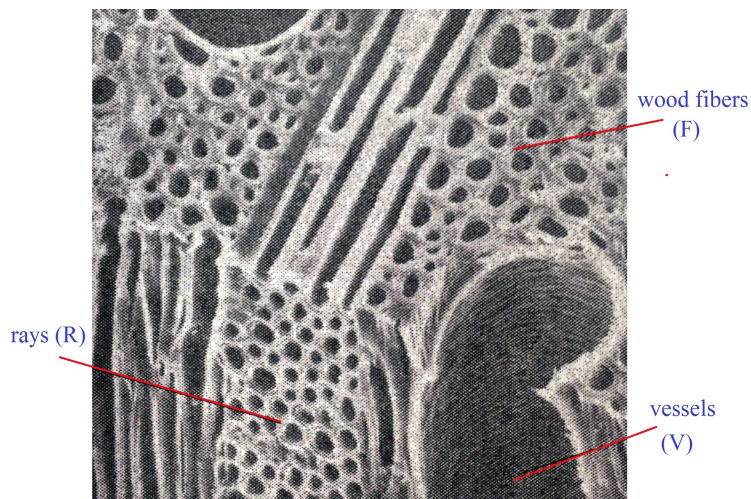
Figure 1.2: Representation of micrograph of a hardwood specimen. Adapted from [121]

1.2 Hygroscopic behavior

1.2.1 Water in wood

According to Kollmann and Cote [92], water in wood, as illustrated in Figure 1.3, is found in two principal forms: bound water and free water.

source: http://www.britannica.com/media/full/603935/
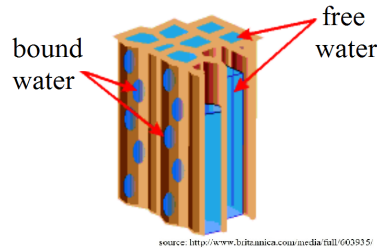
Figure 1.3: Schematic representation of water in wood

- **Bound water:** is held within the cell walls by adsorption force. In the amorphous regions, the molecules of the bound water are adsorbed by the hydroxyl groups that are situated on the hemicellulose macromolecules, amorphous cellulose and lignin. Therefore, the bound water permeates the cell walls. This has important implications for the volume changes associated with moisture changes.

- **Free water:** is not held by any forces and is situated in the micro-pores in wood cell cavities. Free water is subjected to the capillary pressure.

1.2.2 Moisture content

Considering as a hygroscopic material, wood material absorbs the water vapor from the atmosphere. The moisture content in wood is defined as a percentage of oven-dry weight. The moisture content MC is the weight of water contained in the wood, expressed as:

$$MC = \frac{m - m_0}{m_0}.100\% \tag{1.1}$$

where m represents the weight of the wood at the moisture content MC (total weight) and m_0 is the weight of the oven-dry wood.

1.2.3 Saturation point of fibers

Fiber saturation point of wood is defined as the moisture content at which the cell walls are saturated with the bound water and without the free water. The fiber saturation point varies from species to species, but its averages are about $23 - 30\%$ for most wood species [68, 92]. For Maritime pine, the fiber saturation point is commonly accepted around 30%. Below the fiber saturation point of wood, an addition or a removal of the bound water has a pronounced effect on all wood properties [68, 92].

1.2.4 Equilibrium moisture content

The adsorption of bound water molecules with the hydroxyl groups is an exothermic reaction generating heat [92, 121, 151]. The energy required to evaporate a free water molecule is smaller than to remove a bound water molecule, i.e., existing free water evaporates before the bound water does. Through the form of water vapor, wood can take in or give off more moisture. Water contained in wood exerts vapor pressure, which is determined by the maximum size of the capillaries filled with the water at any time. If water vapor pressure in the ambient space is lower than vapor pressure, desorption takes place. Largest-sized capillaries, which are full of water at the time, will be empty first. Vapor pressure within the wood falls as water is successively contained in smaller capillaries.

An equilibrium stage in the material is eventually reached when the vapor pressure within the wood equals to the vapor pressure in the ambient space around the wood. The amount of moisture that remains in the wood at this stage is termed the equilibrium moisture content (EMC) [151]. Because of its hygroscopic, wood tends to reach a moisture that is in equilibrium with the RH and the temperature of the surrounding air. The EMC of wood depends on the ambient RH (a function of the temperature) significantly. Siau [151] reported that the EMC also varies very slightly with species, mechanical stress, drying history of wood, density, extractive content and the direction of sorption in which the moisture change takes place (i.e., adsorption or desorption).

1.2.5 Sorption hysteresis

For a given temperature, equilibrium moisture content is different when RH is achieved by an upward or a downward change. However, under the conditions, RH does not vary from one extreme to the other. Hence, the EMC in wood surface is an intermediate value between the global adsorption and desorption curves. This phenomenon is called sorption (i.e., adsorption and desorption). A hygroscopic isotherm curve for the Maritime pine is plotted in Figure 1.4.

Several chemical and physical processes have been influencing on the sorption phenomenon inside the wood body, not to forget the supplementary contributory of the affinity of the cellulose in wood for water and the size of the internal surface (e.g. for cellulose about 6.10^6 cm^2/cm^3) [92]. The ratio of the adsorbed to the desorbed moisture content over the relative vapor pressure varying between 0.10 and 0.95 is quite constant [92]. Zsigmondy (1911) explained that the hysteresis phenomenon was primarily different in the desorption and the adsorption phase due to contact angles of the water against the capillary walls [92].
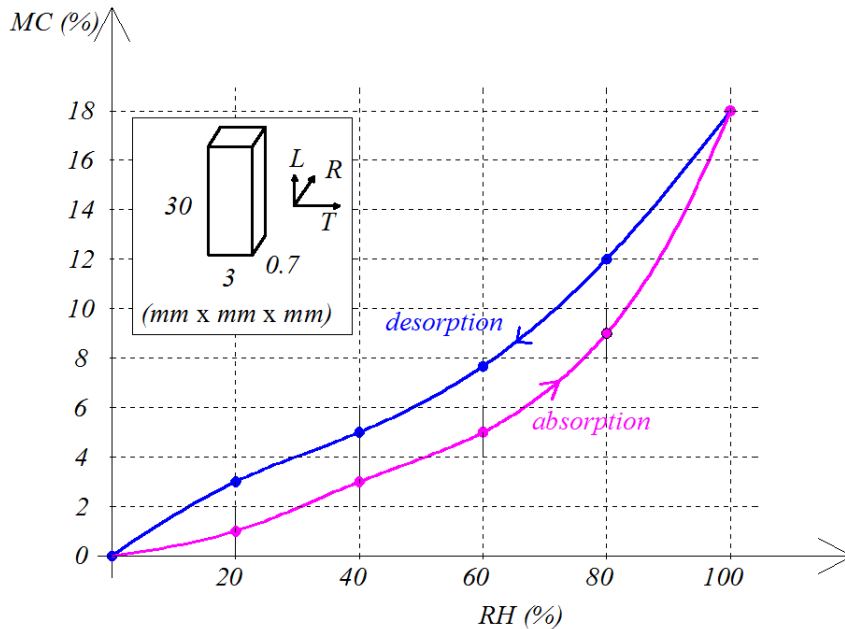
Figure 1.4: Hygroscopic isotherms curve of the Maritime pine [131]

However this theory may be not applicable at low relative vapor pressures because of the impossibility of the capillary condensation. Nevertheless, it is generally accepted an explanation that the hysteresis is related to the hydroxyl groups of cellulose and lignin in wood.

1.2.6 Coupled thermal-hydric behavior

The application of high temperatures on wood may induce chemical degradation of its compositions which causes a molecular relaxation and a variation of its mechanical properties [92, 121]. Because the wood has a multi-transition behavior where each transition may be related to a chemical component of wood [58, 86]. For example, the adsorption phase in wood is accompanied by the evolution of the heat energy in the material.

Many studies [107–109, 121, 160] indicated that a strongly coupled thermal-hydric behavior takes place in wood material. The moisture diffusion in wood is related to the temperature state; and inversely, the heat conduction is also linked to its moisture status. To study the coupled thermal-hydric behavior, Merakeb et al. [107–109] proposed a model by integrating the laws of Fourier and of Fick through two coupled coefficients.

Fourier's law allows to obtain the heat transfer by thermal conduction in the material, which is defined as a function of the temperature variation versus time. Similarly, Fick's law allows to obtain the moisture distribution in the material, which is defined as a function of the water variation versus time. The Fourier's and Fick's equation are expressed in eqs.(1.2) and (1.3), respectively.

$$\frac{\partial T}{\partial t} = \nabla(\mathbb{D}_T \nabla T) \tag{1.2}$$

9

$$\frac{\partial MC}{\partial t} = \nabla(\mathbb{D}_{MC}\nabla MC) \tag{1.3}$$

where $\mathbb{D}_T$ and $\mathbb{D}_{MC}$ are, respectively, the tensor of the thermal conduction and the moisture diffusion coefficients.

By introducing coefficients α_{MC} and β_T in which α_{MC} is the Dufour coefficient, and β_T is the Soret coefficient, the coupling between the thermal and the moisture effects can be written as eqs.(1.4) and (1.5), respectively.

$$\frac{\partial T}{\partial t} = \nabla(\mathbb{D}_T\nabla T) + \alpha_{MC}\frac{\partial MC}{\partial t} \tag{1.4}$$

$$\frac{\partial MC}{\partial t} = \nabla(\mathbb{D}_{MC}\nabla MC) + \beta_T\frac{\partial T}{\partial t} \tag{1.5}$$

1.2.7 Shrinkage and swelling

The addition or the removal of the bound water in wood leads to the phenomenon of shrinkage or swelling deformation. Below the fiber saturation point, when the moisture decreases the shrinkage occurs; reversely, the swelling takes place when the moisture increases. The shrinking and the swelling are proportional to the decreasing or the increasing of the varying MC [157].

Due to the anisotropic nature of wood, the volume change under the shrinkage and the swelling effect is not equal in all directions [92]. The greatest dimensional change occurs in the tangential direction. Shrinkage from the pith outwards, or radially, is usually considerably less than the tangential shrinkage, while the longitudinal (along the grain) shrinkage is so small than it is usually neglected. The longitudinal shrinkage is 0.1% to 0.3%, in contrast to the transverse shrinkage, which is 2% to 10%. The tangential shrinkage is often about twice as great as in the radial direction, although in some species it is much than five times. The axial shrinkage is so small that it is negligible in terms of the dimensional change. However, for some species, the radial and tangential recesses are almost identical, these species are less sensitive to drying slots. The greater shrinkage in the tangential direction causes distortion in lumber with the different orientations.

According to Kollmann and Cote [92], the differential transverse shrinkage of wood is related to:

- The alternation of late wood and early wood increments within the annual ring,
- The influence of wood rays on the radial direction,
- The features of cell wall structures such as microfiber angle modifications and pits,
- The chemical composition of the middle lamella.

In order to describe the hygromechanical behavior of wood, a brief description of the viscoelastic behavior is presented in the next paragraph, which allows us to clarify the mechano-sorptive behavior of wood.

1.3 Viscoelastic behavior

Without variation of the hygroscopic condition, it is well-known that the wood material has a linear viscoelastic behavior [92, 121], which can be characterized by creep-recovery tests or stress relaxation-recovery tests. We would like to give a very brief description of this behavior.

1.3.1 Creep and recovery test

Figure 1.5 shows an ideal representation of a creep-recovery test in which the evolution of stress and strain versus time can be devised in three parts:

- at $t = t_o$, the application of an instantaneous σ_o produces an instantaneous strain ε_0
- during $t > t_o$, the maintenance of a constant stress σ_o leads to a strain $\varepsilon(t)$ which evolves versus time $(\varepsilon(t) > \varepsilon_o)$
- at $t = t_1$, a decreasing of the stress σ_o leads to an instantaneous recovery. Depending on wood type and on stress level, the strain recovery $\varepsilon_r(t-t_1)$ can be total or partial.
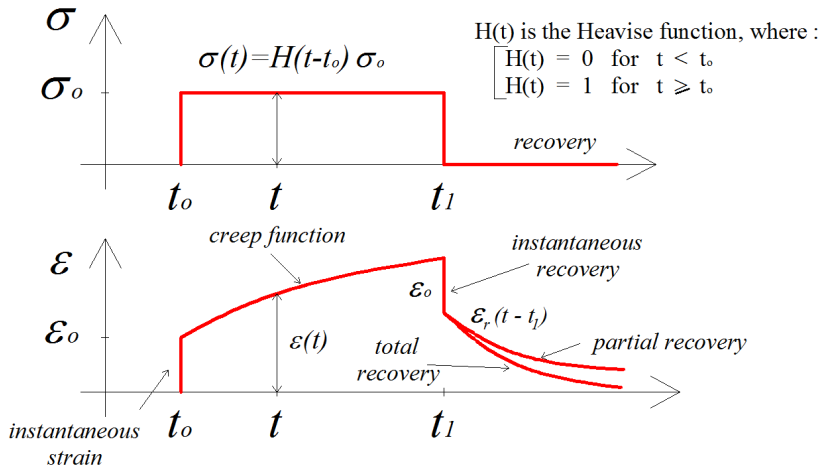
Figure 1.5: Schematic representation of a creep-recovery test of a viscoelastic wood material

Under constant stress σ_o, the strain $\varepsilon(t)$ is a function of time and of σ_o such as:

$$\varepsilon(t) = \tilde{\varepsilon}(t, \sigma_o) = J(t)\sigma_o \tag{1.6}$$

where $J(t)$ is the creep function or the creep compliance. For a non-aging viscoelastic material like wood, the creep function is defined by:

$$J(t - t_o) = \frac{\varepsilon(t - t_o)}{\sigma_o} \tag{1.7}$$

where t_o is the time of application of the stress σ_o.

In general case, at the time t, the response of a viscoelastic material depends on the history of the mechanical loading. If the viscoelastic is linear, based on Boltzmann's superposition principle, the strain response due to the stresses $\Delta\sigma_o$, $\Delta\sigma_1$, $\Delta\sigma_2$... $\Delta\sigma_n$, which are, respectively, applied at the time t_o, t_1, t_2... t_n, is expressed by the relationship:

$$\varepsilon(t) = \sum_{i=0}^{n} \Delta\sigma_i J(t - t_i) \ , \ t > t_n \tag{1.8}$$

Eq.(1.8) can be generalized as:

$$\varepsilon(t) = \int_{t_0}^{t} J(t - \tau)\frac{d\sigma(\tau)}{d\tau} d\tau \tag{1.9}$$

where τ is a time variable ranging from t_o to t, and the derivative induces the finite steps and $\varepsilon_o = J_o.\sigma_o$. J_o is the instantaneous elastic compliance of the material. Note that, eq.(1.9) represents the Boltzmann superposition integral of the uni-dimensional iso-hygro-thermal stress-strain equation for a linear viscoelastic material.

1.3.2 Stress relaxation-recovery test

Figure 1.6 shows an ideal representation of a stress relaxation-recovery test.
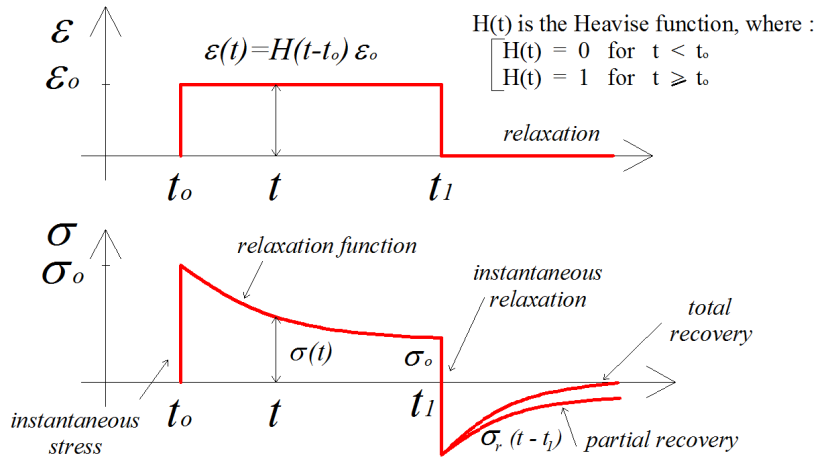
Figure 1.6: Schematic representation of a stress-relaxation test of a viscoelastic wood material

In the stress relaxation-recovery test, the relation of stress and strain consists in three parts:

- at t_o, the application of a constant strain ε_o produces an instantaneous stress σ_o
- between t_o and t_1, the maintenance of a constant strain ε_o leads to a stress $\sigma(t)$ which evolves versus time $(\sigma(t) < \sigma_o)$
- at $t = t_1$, a rapid decreasing of the deformation ε_o leads to an instantaneous relaxation.

The stress recovery $\sigma_r(t - t_1)$ can be partial or total. If the stress recovery is total, the behavior is purely viscoelastic. If the stress recovery in only partial, leading to a permanent stress σ_p after a long period of time, the behavior is elasto-visco-plastic.

Like the creep function, the relaxation function is given:

$$R(t - t_o) = \frac{\sigma(t - t_o)}{\varepsilon_o} \tag{1.10}$$

where t_o is the time of application of the strain ε_o.

In practice, it is easier to maintain a constant stress than a constant strain. Hence, the creep recovery test is usually preferred to the stress recovery test.

Note that, if the stress level is high, wood may exhibit a non-linear viscoelastic behavior (Fig. 1.7): the creep function depends on the stress; and the stress relaxation function depends on the strain. Consequently, the Boltzmann superposition principle is not applicable for the non-linear viscoelastic behavior. In this case, the relations between the time-depend strain and stress may be expressed by the Green-Rivlin formulation (eq.(1.11)), which is summarized in [117].
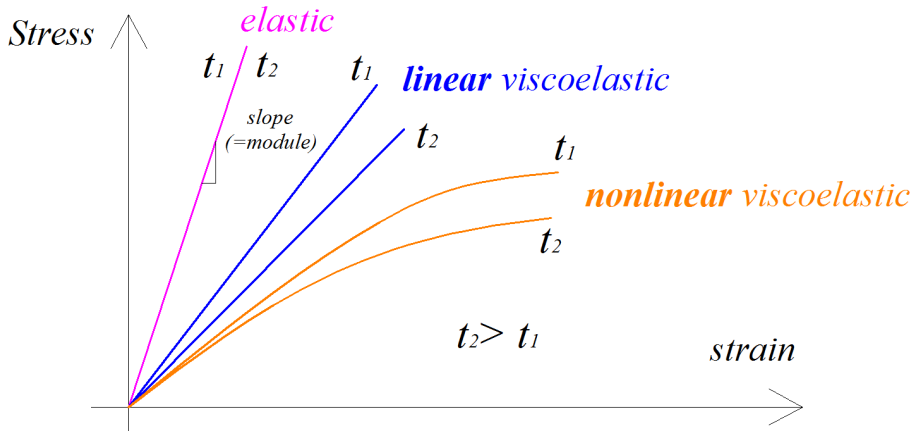
Figure 1.7: Stress-strain behavior of elastic and viscoelastic materials at two values of elapsed time

$$
\begin{aligned}
\varepsilon(t) \quad = \quad & \int_{0-}^{t} J_1(t - \tau_1) \frac{\partial \sigma(\tau_1)}{\partial \tau_1} d\tau_1 \\
+ \quad & \iint_{0-}^{t} J_2(t - \tau_1, t - \tau_2) \frac{\partial \sigma(\tau_1)}{\partial \tau_1} \frac{\partial \sigma(\tau_2)}{\partial \tau_2} d\tau_1 d\tau_2 \\
+ \quad & \iiint_{0-}^{t} J_3(t - \tau_1, t - \tau_2, t - \tau_3) \frac{\partial \sigma(\tau_1)}{\partial \tau_1} \frac{\partial \sigma(\tau_2)}{\partial \tau_2} \frac{\partial \sigma(\tau_3)}{\partial \tau_3} d\tau_1 d\tau_2 d\tau_3 \\
+ \quad & ...
\end{aligned} \tag{1.11}
$$

The eq.(1.11) can be reduced in a nonlinear polynomial function of stress. For example, its third-order function can be rewritten as eq.(1.12). However, the Green-Rivlin formulation is difficult to calibrate in experiments even for the third-order equation given in eq. (1.12). Other simplified alternative expressions have been proposed for nonlinear formulation [53, 120].

$$\varepsilon(t) = \sigma S_1(t) + \sigma^2 S_2(t) + \sigma^3 S_3(t)... \tag{1.12}$$

1.3.3 Rheological models

Rheological models facilitate the modeling of the material viscoelastic behavior. To study the linear viscoelastic behavior of wood, two rheological models are commonly proposed:

- generalized Kelvin Voigt model used for the creep recovery test
- generalized Maxwell model used for the stress relaxation test

1.3.3.1 Generalized Kelvin Voigt model

As shown in Figure 1.8, a generalized Kelvin Voigt model consists of Kelvin Voigt's cells associated in series with a spring K_0. The ith Kelvin Voigt cell is composed by a purely viscous damper η_i and purely elastic spring K_i connected in parallel. The elastic spring K_0 represents the instantaneous elastic response. To accurately better modeling of the behavior, numerous Kelvin Voigt cells associated in series are commonly used.
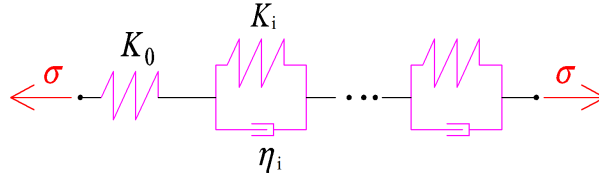
Figure 1.8: Generalized Kelvin Voigt model

Based on the generalized Kelvin Voigt model (N branches), the strain $\varepsilon(t)$ and the creep function $J(t)$ for the non-aging material can be expressed in eqs.(1.13) and (1.14), respectively.

$$\varepsilon(t) = \int_0^t J(t,\tau).\frac{\partial \sigma}{\partial \tau} d\tau \tag{1.13}$$

$$J(t) = \frac{1}{K_0} + \sum_{i=1}^{N} \left[\frac{1}{K_i}.\left(1 - exp^{-\frac{t}{\tau_i}} \right) \right] \tag{1.14}$$

with τ_i is the retardation time expressed as $\tau_i = \frac{\eta_i}{K_i}$.

1.3.3.2 Generalized Maxwell model

As shown in Figure 1.9, a generalized Maxwell model consists of Maxwell's cells associated in parallel with a spring K_0. The ith Maxwell cell is composed by a purely viscous damper η_i and purely elastic spring K_i connected in series. The Maxwell cell is used to translate the viscous behavior while the spring stiffness translates the apparent rigidity of the long term. The elastic spring K_0 represents the instantaneous rigidity. To accurately better modeling of the behavior, numerous Maxwell cells associated in parallel are commonly used.
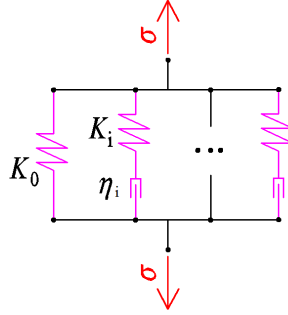
Figure 1.9: Generalized Maxwell model

Based on the generalized Maxwell model (N branches), the stress $\sigma(t)$ and the relaxation function $R(t)$ for the non-aging material can be expressed in eqs.(1.15) and (1.16), respectively.

$$\sigma(t) = \int_0^t R(t,\tau).\frac{\partial \varepsilon}{\partial \tau} d\tau \tag{1.15}$$

$$R(t) = K_0 + \sum_{i=1}^N \left[K_i.exp^{-\frac{t}{\tau_i}} \right] \tag{1.16}$$

with τ_i being the relaxation time expressed as $\tau_i = \dfrac{\eta_i}{K_i}$.

As presented in the section 1.2 and the previous section, the wood material simultaneously exhibits hygroscopic and viscoelastic behaviors. It is acceptable to consider that wood is a viscoelastic material with mechanical properties changing with the temperature and the humidity. Under varying temperature and humidity, wood behavior is not the same that under constant condition (coupling effect).

1.4   Mechano-sorptive behavior

1.4.1   State-of-the-art

Today, a common topic is the influence of climatic changes on wood behavior. The timber structures usually placed in outdoor conditions are simultaneously influenced by environmental condition variations. The structure is not only influenced by the variation of the humidity and the thermal environment, but is also subjected to stress variation due to the interaction of mechanical loads and the environmental condition variations.

Under constant environmental condition, its behavior can be regarded as a linear viscoelastic material but this assumption is valid only for small deformations and at low stress state, which is also the case in the real life. However, when taking into account the climate influence, the behavior becomes more complicated. The behavior of wood under drying phase is different from the one observed under humidification phase.

Generally, load creeps with time (at a constant humidity) and the amount of creep is higher under more wet conditions due to mechanical properties of wood material. However, as shown in Figure 1.10, the creep acceleration is resulted from interactions between the mechanical state and the humidity variations. In the context of the durability of the structure, the moisture effect plays an important role in the structural design [3, 5, 6, 73, 149, 150].
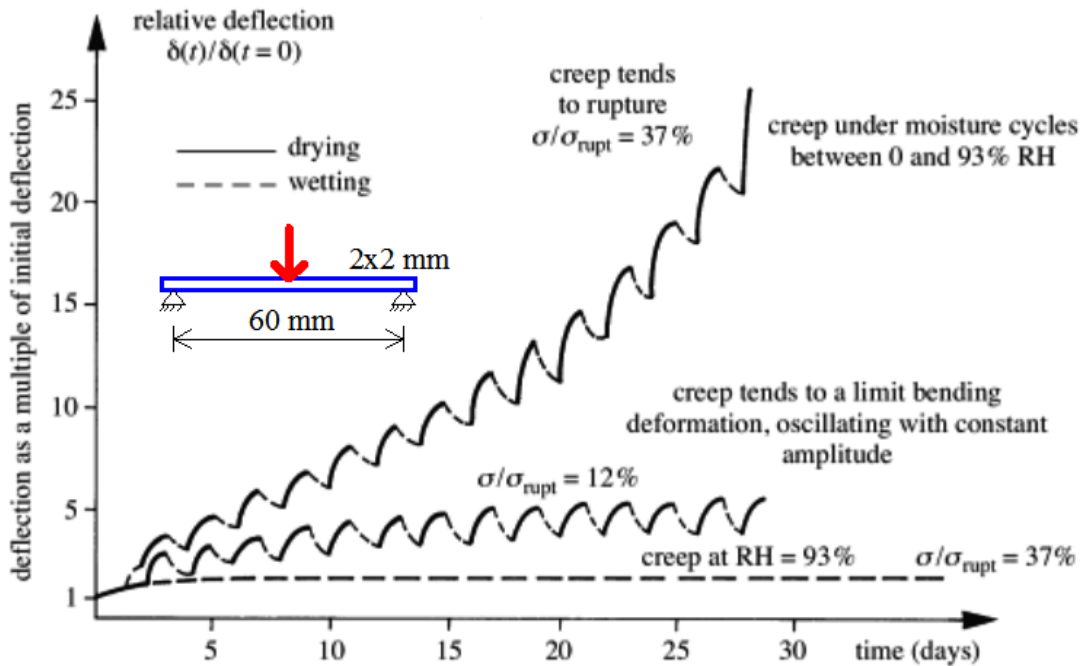
Figure 1.10: Wooden beam (beech) under cyclic relative humidity variations. Extracted from [73]

16

Many works have been devoted to the comprehension of the structure under moisture variation since the early 1960s [5]. Following Armstrong and Kingston (1960) [5], the adsorption-desorption process, associated with local variations of the moisture may advance creep considerably. This particular feature of wood material, a coupling between the mechanical response of wood and adsorption-desorption processes [3, 5, 6] was named mechano-sorptive effect by Grossman (1976) [66]. Various physical interpretations have been proposed [9, 32, 33, 54, 71, 72, 76, 103, 105, 119, 119, 136, 144, 160, 164] although until now, no clear consensus was reached; the real mechanism has not yet been well achieved.

1.4.1.1 Main specificity of the mechano-sorptive effect

An up-dated and extended version of the detailed review on the main feature of the mechano-sorptive effects given by Grossman (1976) and other authors [32, 66, 80, 131, 135] is therefore presented. These main features are presented in Figs. 1.11 and 1.12 which shows a typical mechano-sorptive creep curve.
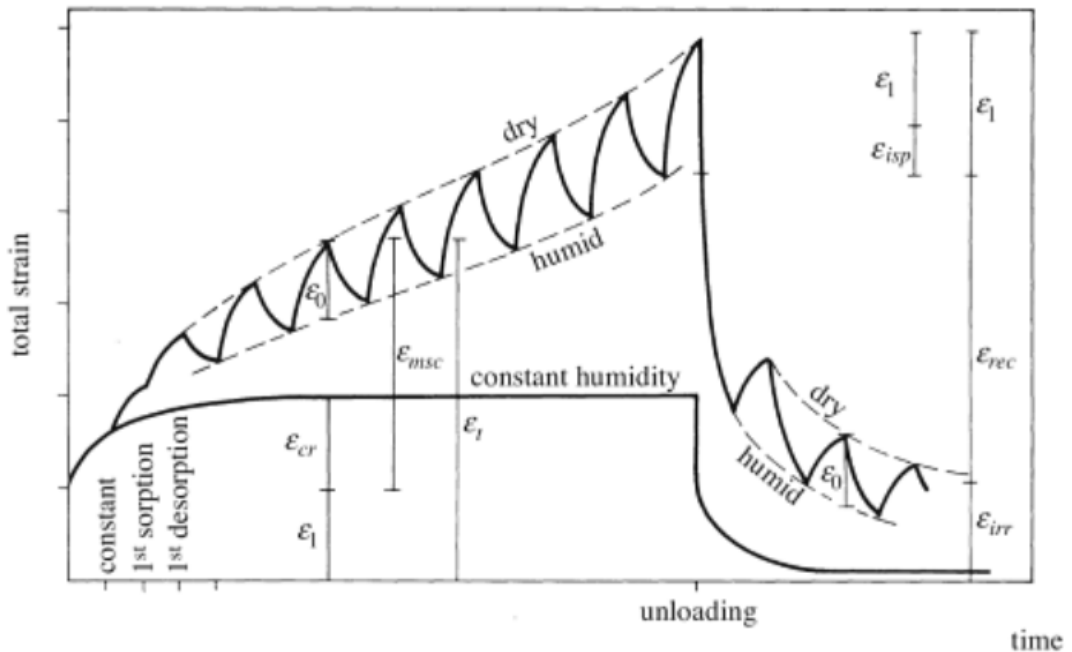
Figure 1.11: Schematic representation of a typical mechano-sorptive creep curve [66]. In this figure, ε_l is the instantaneous strain, ε_{cr} is the creep strain, ε_{msc} is the mechano-sorptive creep strain, ε_0 is the amplitude of mechano-sorptive creep strain for one humidification/drying cycle, ε_{rec} is the reversible creep strain, ε_{irr} is the irreversible creep strain
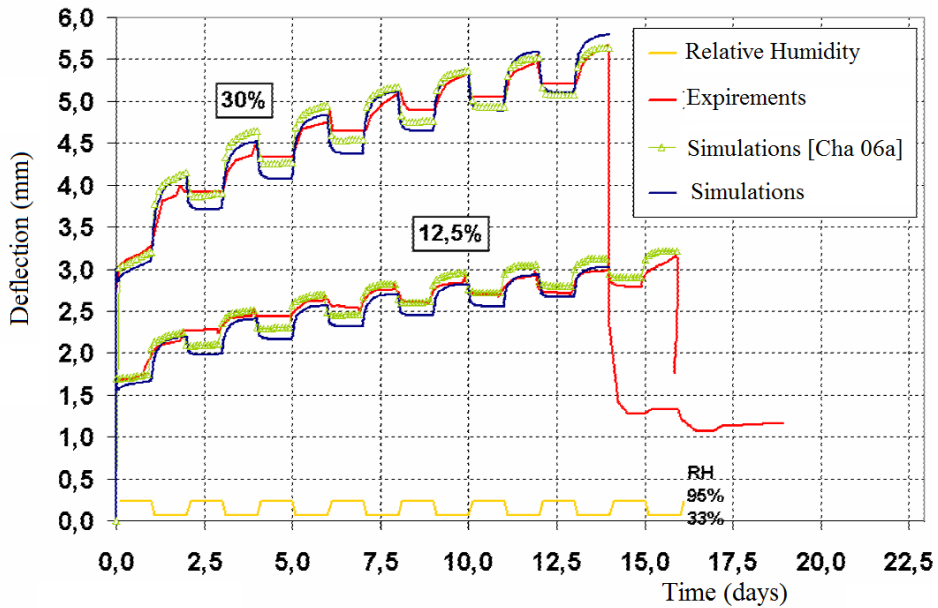
Figure 1.12: Deflection under cyclic relative humidity variations at different stress levels (12.5% and 30%). Extracted from [32]

As shown in Figures 1.10, 1.11 and 1.12, some main features of mechano-sorption can be listed as below:

- Deformation increases when the moisture decreases (drying phase), deformation decreases when the moisture increases (humidification phase) [5, 6, 73, 149].

- The first sorption phase (humidification or drying phase) generally causes a deformation increasing due to the viscoelastic strain of wood [5, 6, 73, 149].

- Below the fiber saturation point, the mechano-sorptive deformation is only influenced by the magnitude of the moisture change [6, 98].

- The deformation in saturated wood is much greater than in dry wood [6].

- Constant moisture in wood does not result in any mechano-sorptive effect [4]

- The failure time of timber structure with the mechano-sorption effect is smaller than those without the mechano-sorption effect [73, 149, 150].

- Due to the mechano-sorption effect, the rigidity of the structure is progressively reduced [73, 149, 150].

- At a low stress (in bending test), the oscillation amplitudes of the deflection curve tends to increase and then becomes constant after a number of moisture cycles. At a higher stress, the increasing in amplitude never stop leading to the failure of the structure [73]. At low stress levels (in tension test) the oscillation amplitudes decreases [79].

18

- After unloading, the instantaneous elastic recovery strain is equal to or greater than the initial elastic strain due to the reduction of the rigidity of the structure [60].

- The recovery phase is accelerated by the moisture cycling as shown in Figure 1.11. The recovery deformation during the drying phase is smaller than during the humidification phase [3, 136].

- The mechano-sorptive effect on the deformation is generally much greater than the effect of the time (without the varying moisture).

- The mechano-sorptive phenomenon occurs in most of wood species [77, 136].

According to Navi et al. [121], the kinetics of the developments of the mechano-sorptive effect is significantly influenced by the structure size due to the time needed to reach the moisture equilibrium in the structure. For example, for two specimen sizes: 1x1x60 mm^3 and 20x20x900 mm^3, it is considered that the mechano-sorption effect is similar, but the time necessary to reach the EMC is different for two specimens (i.e., about 2 - 3 $hours$ in the thin specimen and about 50 $hours$ in the thick specimen).

As presented above, most previous studies have only investigated the mechano-sorptive effect at a constant temperature. Besides that, Fridley et al. [56] have tested lumber in bending in cyclic temperature conditions, the moisture was kept constant. They reported that a trend to shorter times-to-failure was observed at higher temperature for most stress level.

1.4.1.2 Modeling of the mechano-sorptive effect

Modeling of viscoelastic behavior of wood under varying moisture began in the seventies. Different thermodynamic approaches have been proposed to model these phenomena. These models are based either on purely phenomenological (macroscopic) considerations or on the physical interpretation of the deformation at the wood molecular level. Most of them are rheological models based on Maxwell or Kelvin Voigt model and on the assumption of the linear viscoelastic and the non-aging of the wood material.

As mentioned in the previous paragraph, the time-dependence creep and the mechano-sorptive effect are not the same. If they are not strongly coupled together, the total deformation is considered as the sum of various deformations: instantaneous deformation, viscoelastic deformation, deformation due to mechano-sorption, deformation due to shrinkage-swelling effect. In addition, these deformations are assumable to be independently measured. Models based on this assumption are called model with independent activation.

On the other hand, if the wood behavior has a strong interaction between the deformation due to the effect of time (viscoelastic creep) and those due to the moisture variation

19

(mechano-sorptive creep), models based on this assumption are called model with combined activation. Figure 1.13 shows schematic representation of the total deformation for two models: independent and combined activation.
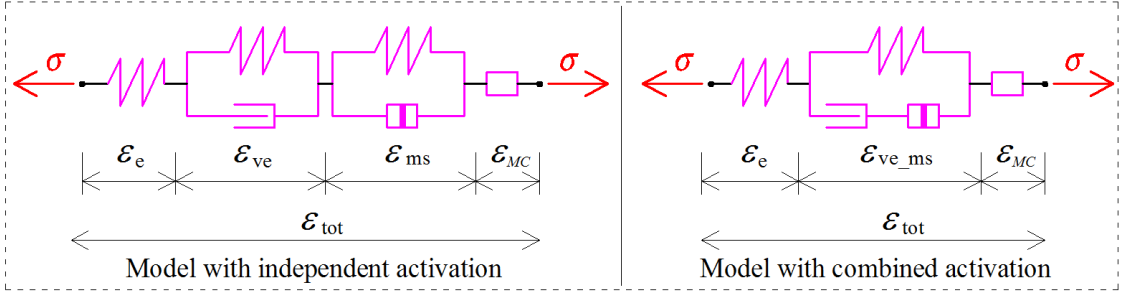
Figure 1.13: Mechano-sorptive models: independent and combined activations

- In the model with independent activation, the total deformation is expressed as:

$$\varepsilon_{tot} = \varepsilon_e + \varepsilon_{ve} + \varepsilon_{ms} + \varepsilon_{MC} \tag{1.17}$$

- In the model with combined activation, the total deformation is expressed as:

$$\varepsilon_{tot} = \varepsilon_e + \varepsilon_{ve\_ms} + \varepsilon_{MC} \tag{1.18}$$

In eqs.(1.17) and (1.18), ε_{tot} is the total strain, ε_e is the instantaneous elastic strain, ε_{ve} represents the viscoelastic deformations, ε_{ms} represents the mechano-sorptive deformations (decoupled); ε_{ve_ms} represents the coupled deformation between the viscoelastic and the mechano-sorptive deformations. The shrinkage and swelling effect ε_{MC} ($= \varepsilon_{MCo} + \varepsilon_{MC\sigma}$) is defined as the sum of two parts: the free shrinkage-swelling ε_{MCo} and the shrinkage-swelling under loading $\varepsilon_{MC\sigma}$. Moreover, the shrinkage and the swelling effect ε_{MC} can be considered as the coupled deformation $\varepsilon_{MCo\sigma}$.

1.4.2 Mechano-sorptive models

1.4.2.1 Independent activation models

1.4.2.1.a Leicester model

Leicester model (1971) [98] is considered as the first mechano-sorptive model. The model consisted in two elements in series with an elastic and a mechano-sorptive element. The total deformation is given as:

$$\varepsilon_{tot} = \varepsilon_e + \varepsilon_{ms} \implies \dot{\varepsilon}_{tot}(t) = \dot{\varepsilon}_e(t) + \dot{\varepsilon}_{ms}(t) \tag{1.19}$$

where the elastic strain ε_e and the mechano-sorptive deformation ε_{ms} are given in eqs.(1.20) and (1.21), respectively.

$$\varepsilon_e = \frac{\sigma}{k} \tag{1.20}$$

$$\dot{\varepsilon}_{ms} = -\frac{\sigma}{k}m.\dot{M}C \quad (1.21)$$

where k is an elastic module (the author did not precise if this module depends on the moisture content MC). The coefficient m allows to model the shrinking and the swelling effect. In the humidification phase, $m = 0$.

1.4.2.1.b Ranta-Maunus model

Ranta-Maunus (1975) [136] has proposed a description of the wood behavior under varying moisture by developing a theory of hydro-visco-elasticity. The total deformation is given in eq.(1.17) where the first derivative of the elastic strain ε_e, the free shrinkage-swelling deformation ε_{MC}, the viscoelastic deformation ε_{ve} and the mechano-sorptive deformation ε_{ms} are given in eqs.(1.22), (1.23), (1.24) and (1.25), respectively.

$$\dot{\varepsilon}_e = \frac{\dot{\sigma}(t)}{k(MC,T)} \quad (1.22)$$

$$\dot{\varepsilon}_{MC} = \alpha\dot{M}C \quad (1.23)$$

$$\dot{\varepsilon}_{ve} = \sigma J(t) \quad (1.24)$$

$$\dot{\varepsilon}_{ms} = m\sigma\dot{M}C \quad (1.25)$$

In Ranta-Maunus's model, the elastic module $k(MC,T)$ depends on the moisture MC and on the temperature T. The coefficient m is the hydro-viscoelastic constant for describing the humidification phase (m^+) and the drying phase (m^-). Thanks to the coefficient m, the model allows to distinguish the first humidification phase by the value m^{++}. As written in eq.(1.25), the deformation due to the mechano-sorptive effect is linearly related to moisture content. In this model, the recovery is ignored.

1.4.2.1.c Martensson model

Martensson (1988, 1994) [104, 105] has proposed a model in which the deformation due to the mechano-sorptive effect depends on the rate of the moisture change $\dot{M}C$ and on the current moisture MC based on an assumption that there is no interaction between the moisture response and the mechanical response. The total deformation is given in eq.(1.17) where the elastic deformation ε_e, the free shrinkage-swelling deformation ε_{MC}, the viscoelastic deformation ε_{ve} and the mechano-sorptive deformation ε_{ms} are given in eqs.(1.26), (1.27), (1.28) and (1.29), respectively.

$$\dot{\varepsilon}_e = \frac{\dot{\sigma}}{k(MC)} \quad (1.26)$$

$$\dot{\varepsilon}_{MC} = \alpha\dot{M}C \quad (1.27)$$

$$\dot{\varepsilon}_{ve} = \sigma J(t) \quad (1.28)$$

$$\dot{\varepsilon}_{ms} = \chi\frac{\sigma}{\sigma_u}\dot{\varepsilon}_{MC} \quad (1.29)$$

where σ_u is the ultimate stress in the uni-axial tension and χ is a material parameter describing the mechano-sorptive behavior.

The viscoelastic strain under a constant stress and moisture conditions is expressed in eq.(1.28) through the creep compliance function $J(t)$ based on a rheological model with N Kelvin Voigt branches. Note that if the moisture content is higher, the creep develops faster; the varying moisture effect on the viscoelastic strain.

$$\dot{\varepsilon}_{ve} = \int_0^t J[\xi(t) - \xi(\tau)] d\sigma J(\tau) \tag{1.30}$$

where $\xi(t)$ is a material time, defined by $d\xi = dt/a(MC)$. At a reference moisture state MC_r, the material time is equal to the real time, i.e. $a(MC_r) = 1$.

1.4.2.1.d Hunt and co-workers model

Hunt et al. (1986, 1988, 1989) [77–79] have proposed the same total deformation as eq.(1.17). Different from the Ranta-Maunus's model, the shrinkage-swelling strain in Hunt's model is considered as the strain depending on the deformation state of the material. The shrinkage-swelling strain is given as:

$$\dot{\varepsilon}_{MC}(t) = \dot{\varepsilon}_{MCo}(t) + \dot{\varepsilon}_{MC\sigma}(t) \tag{1.31}$$

where the free shrinkage-swelling strain ε_{MCo} and the shrinkage-swelling strain due to the mechanical loading $\varepsilon_{MC\sigma}$ are given, respectively, in eqs.(1.32) and (1.33).

$$\dot{\varepsilon}_{MCo}(t) = \alpha.\dot{M}C(t) \tag{1.32}$$

$$\dot{\varepsilon}_{MC\sigma}(t) = m.\varepsilon(t).\dot{M}C(t) \tag{1.33}$$

where m is a constant material coefficient independent of the varying moisture. Note that, the shrinkage-swelling strain due to the mechanical loading $\varepsilon_{MC\sigma}$ in eq.(1.33) has the same form as the mechano-sorptive strain ε_{ms} in the Ranta-Maunus's model by replacing the stress σ by ε.

In the Hunt's model, the mechano-sorptive strain ε_{ms} is given as:

$$\varepsilon_{ms}(t) = \sigma_0. \left[J_1. \left(1 + exp^{-a_1. \sum \delta_{MC}} \right) + J_2. \left(1 + exp^{-a_2. \sum \delta_{MC}} \right) \right] \tag{1.34}$$

where δ_{MC} is the absolute value of any moisture variation in wood. J_1, J_2 are the creep mechano-sorptive compliance functions. a_1 and a_2 are suitable coefficients.

1.4.2.1.e Toratti model

Toratti (1992) [110, 164] has proposed a generalized Kelvin Voigt model integrating the moisture effect where an accelerated creep depends on the moisture content. The total deformation is given as eq.(1.17) where the elastic strain ε_e, the viscoelastic strain ε_{ve} the

free shrinkage-swelling deformation ε_{MC} and the mechano-sorptive deformation ε_{ms} are given in eqs.(1.35), (1.37), (1.36) and (1.38), respectively.

$$\dot{\varepsilon}_e = \frac{\dot{\sigma}}{k(MC)} \tag{1.35}$$

$$\dot{\varepsilon}_{MC} = \alpha \dot{M}C \tag{1.36}$$

$$\dot{\varepsilon}_{ve} = \sigma J(t) \tag{1.37}$$

$$\dot{\varepsilon}_{ms} = \frac{J^{\infty}\sigma - \varepsilon_{ms}}{\tau_{ms}} \left| \dot{M}C \right| \tag{1.38}$$

In eq.(1.38), J^{∞} is the limit creep mechano-sorptive compliance function, τ_{ms} is the relaxation time for the mechano-sorptive creep. This model allows to obtain the recovery deformation during varying moisture. But the viscoelastic strain ε_{ve} in eq.(1.37) is interpolated by the reference creep compliance $J(t)$ at a given constant moisture. The elastic module $k(MC)$ depends on the moisture MC.

1.4.2.1.f   Destrebecq, Nguyen, Saifouni, Moutou Pitti model

Based on a hygro-lock approach, the authors (2014) [122] have proposed a model in which the viscoelastic behavior is represented by a Kelvin Voigt cell in parallel with a Maxwell cell as illustrated in Figure 1.14.
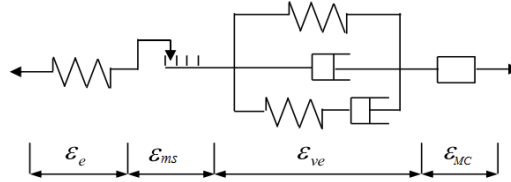
Figure 1.14: Analogue model for the coupled hygro-mechanical effects

The model allows describing the effects of the creep as well as the relaxation. The total deformation is given in eq.(1.17) where the elastic strain ε_e, the free shrinkage-swelling deformation ε_{MC}, the viscoelastic strain ε_{ve} and the mechano-sorptive deformation ε_{ms} are given in eqs.(1.39), (1.40), (1.41) and (1.42), respectively.

$$\dot{\varepsilon}_e = \frac{\dot{\sigma}}{k(MC)} + \dot{\varepsilon}_e^{MC} \tag{1.39}$$

$$\dot{\varepsilon}_{MC} = \alpha . \dot{M}C \tag{1.40}$$

$$\dot{\varepsilon}_{ve} = \sigma . J(t) \tag{1.41}$$

$$\dot{\varepsilon}_{ms} = -\dot{\varepsilon}_e^{MC} = \frac{k'(MC)}{k^2} . \dot{M}C . \tilde{\sigma} \tag{1.42}$$

where:

$$\tilde{\sigma} = \frac{k(MC).k(\bar{M}C)}{k(MC) - k(\bar{M}C)} . \varepsilon_{ms} \tag{1.43}$$

23

According to the authors, the mechano-sorptive strain ε_{ms} is considered as hydro-lock strain during a drying phase, which is independent of stress variations at a constant humidity. During a humidification phase, ε_{ms} gradually decreases until the mechano-sorptive effect disappears when the moisture content returns to the value $\bar{MC}$ at the beginning of the drying phase corresponding to the current mechanical loading. $\bar{MC}$ is the reference value of MC for which the mechano-sorptive effect has disappears.

1.4.2.2 Combined activation models

1.4.2.2.a Bazant model

Bazant (1985) [9] has proposed a model based on the diffusion process between a micro and a macro-distribution in wood. Based on a generalized Maxwell model of N branches and taking into account a term relating to the fluid and the thermal expansion, the total deformation is given in eq.(1.44).

$$\varepsilon_{tot} = \frac{\dot{\sigma}^i}{k^i} + \frac{\sigma^i}{\eta^i} + \alpha \dot{H} + \beta \dot{T} \tag{1.44}$$

$$\sigma = \sum_i^N \sigma^i \tag{1.45}$$

where α and β are the coefficients of the hydric expansion and the thermal expansion, respectively. i denotes the ith element in the generalized Maxwell model. k is the constant elastic module. The viscous η, depending on the hydric expansion $\dot{H}$ and the thermal expansion $\dot{T}$, is given as:

$$\frac{1}{\eta^i} = \frac{\varphi^i(MC)}{k^i \tau^i} e^{(\frac{Q_c}{RT_{ref}} - \frac{Q_c}{RT})} f^i(\dot{H}) \tag{1.46}$$

$$\dot{H} = \dot{h} + c\dot{T} \tag{1.47}$$

where h is the relative humidity (relative vapor pressure) in the macropores (capillary pores, or cell lumen).

In the Bazant model, the author uses equation (1.44) to characterize the macro and micro-circulation, which are mainly related to the work for the concrete, by using the Pickett effect. However, the parameters identification remains difficult to be practically verified and assessed these considerations in the mechano-sorptive effect for wood material.

1.4.2.2.b Mukudai and Yata model

Mukudai and Yata (1987) [119] has proposed a rheological model based on two behaviors in parallel for wet (I) and dry (II) states as shown in Figure 1.15. The mechanical response of two states is controlled by a lever effect which depends on the varying moisture phase. Based on this, the stress distribution in the two branches depends on the given moisture level.
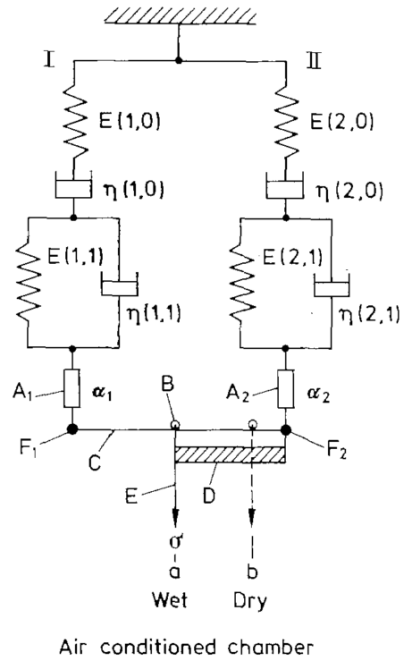
Figure 1.15: Mukudai's model: viscoelastic elementary model for wood under moisture change [119]. Under humidification phase: Model I. Under drying phase: Model II

In Figure 1.15, A_1, $A2$ are hygroscopic parameters having swelling and shrinkage coefficients α_1, α_2, respectively. B is a running block. D is a hygroscopic coefficient representing the stress bias by the swelling and the shrinkage effect. F_1 and F_2 are pine connections. The operation of the bar D is involved by following moisture variations. This does not allow to have a rheological model to the pure sense (i.e., a single behavior law). Furthermore, parameter values taken by the authors for the calculations are not properly justified.

1.4.2.2.c   Gril model

Gril (1988) [65] has proposed a hygro-lock model based on a consideration of the characteristics of the micro-structure. In the Gril's model, it is assumed that a hydric activation for creep depends on the history of the moisture in wood. The hygro-lock effect represents the capacity of the material to mobilize its free energy for a temporary strain blocking during drying phases under stress (called a mechano-sorptive stress) and to release this deformation under wet conditions. The mechano-sorptive effect is hence considered as inducing a temporary drop of potential barriers, due to a temporary decreasing in the binding energy. Based on this assumption, the deformation is blocked in drying phase, but can be recovered at an humidification phase.

1.4.2.2.d   Van Der Put model

Van Der Put (1989) [167] proposed a model based on thermodynamic concepts allowing to take into account the activation energy between molecules. The material is considered as elastic except for the mechano-sorptive deformation due to the control of the molecules. Hence, the moisture and the heat transfer in wood can dictate the creep response. The coupled viscoelastic mechano-sorptive and elastic deformations in a generalized Maxwell model is given as:

$$\dot{\varepsilon}^i = \frac{\dot{\sigma}^i}{K^i} + (A^i + B^i \varepsilon^i).sinh(\sigma^i \rho^i (1 - C^i \varepsilon^i)) \tag{1.48}$$

where i denotes the ith element of the generalized Maxwell model. ρ is the activation energy. A, B and C are parameters for the configuration variation. In the model, the mechano-sorptive effect is less important for the great size of structures due to the diffusion time.

1.4.2.2.e   Hanhijrvi model

Hanhijrvi et al. (2000, 2001, 2003) [70–72] proposed a 3D constitutive equation based on a generalized Maxwell model based on the same concept of the Van Der Put's model.
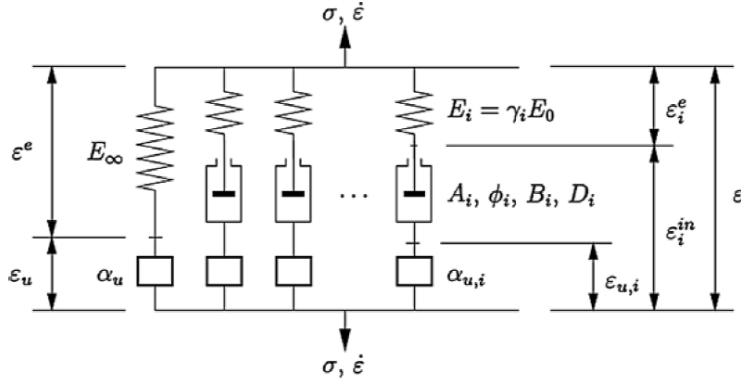
Figure 1.16: First Hanhijrvi model [70]

Their first model was written for civil applications and was essentially based on a 1D formulation by adding a hygro-expansion element (Figure 1.16). The strain rate and stress of the model are expressed in eqs.(1.49) and (1.50), respectively.

$$\dot{\varepsilon}_i = \frac{\dot{\sigma}_i}{K_i} + (A_i.sinh(\phi_i \sigma_i + Btanh(D\dot{h})) + \alpha_i^h \dot{h} \tag{1.49}$$

$$\sigma = \sum_i^N \sigma^i \tag{1.50}$$

where i denotes the ith element of the generalized Maxwell model. A_i, B_i and D_i are material parameters governing the ith element; α_i^h is the parameter of the hygro-expansion element. $\dot{h}$ is the rate of relative vapor pressure change (interchangeable with moisture content rate).

1.4.2.2.f Husson and Dubois model

Husson and Dubois (2009, 2012) [49, 80–82] proposed a mechano-sorptive model with two different types of behavior for modeling the wetting and drying phases (based on the hygro-lock approach which was conducted by Gril [65]) by employing Hook's law for the softening behavior (humidification phase) and Bazant's law for the hardening behavior (drying phase) [9].

Before their work, Randriambololona [135] reported some difficulties involved in the synchronization of these two constitutive laws (Hook's and Bazant's law).

In the Husson and Dubois's model, the hygro-lock model is applied for all springs in a generalized Kelvin Voigt model (N branches) as shown in Figure 1.17. Based on this, the elastic stiffness k of the spring exclusively depends on the moisture content (i.e., $k = k(MC)$) and not on its variations.
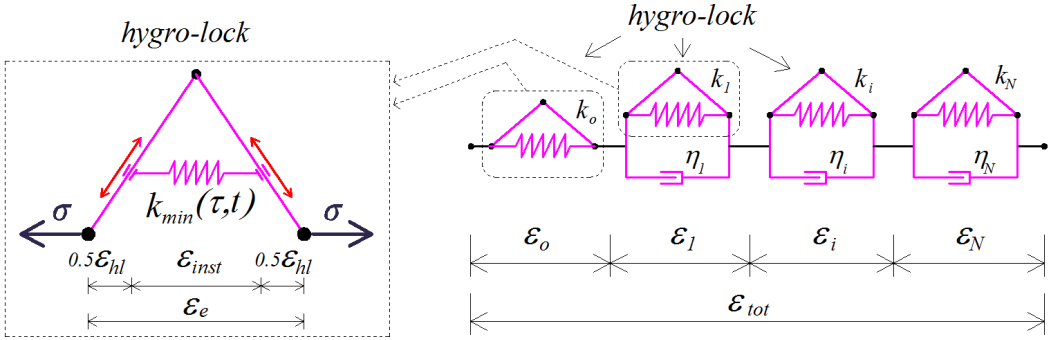
Figure 1.17: The generalized viscoelastic mechano-sorptive Kelvin Voigt model (based on the hygro-lock approach)

Based on the hygro-lock approach, the total elastic strain ε_e in a spring, as shown in Figure 1.17, is considered as the sum of an instantaneous recoverable strain ε_{inst} and a residual strain ε_{hl}: $\varepsilon_e = \varepsilon_{inst} + \varepsilon_{hl}$. Moreover, the total elastic strain ε_e can be written in the general form as:

$$\varepsilon_e(t) = \int_0^t \frac{1}{k_{min}(\tau, t)} \cdot \frac{\partial \sigma}{\partial \tau} d\tau \tag{1.51}$$

where k_{min} represents the minimum stiffness value between times t and τ, induced by moisture content variations as illustrated in Figure 1.18. In this figure, the time t' is an intermediary variable which allows synchronizing the mechanical field and moisture content histories. The minimum stiffness can be rewritten as:

$$k_{min}(\tau, t) = \min k(t') \quad \text{with} \quad t' \in [\tau, t] \tag{1.52}$$

Using the concept of the maximum compliance $C_{max}(\tau, t) = 1/k_{min}(\tau, t)$, the total elastic strain ε_e in eq.(1.51) can be expressed as:

$$\varepsilon_e(t) = \int_0^t C_{max}(\tau, t) \frac{\partial \sigma}{\partial \tau} d\tau \tag{1.53}$$

27
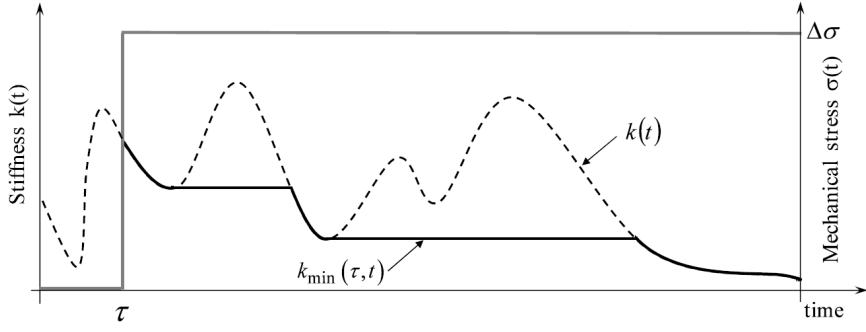
Figure 1.18: Definition of minimum stiffness. Extracted from [49]

From the total elastic behavior in a spring (eq.(1.51)), the linear viscoelastic mechano-sorptive behavior for one Kelvin Voigt cell is given for any mechanical stress as:

$$\varepsilon_e(t) = \int_0^t \left[\int_\tau^t \frac{1}{\eta(\vartheta)} exp^{-\int_\tau^\vartheta \frac{k_{min}(\alpha,t)}{\eta(\alpha)} d\alpha} d\vartheta \right] . \frac{\partial \sigma}{\partial \tau} d\tau \tag{1.54}$$

According to authors, the complex form as written in eq.(1.54) exhibits two phenomena:

- the strain evolution is controlled by the hygro-lock effect,

- the strain expression indicates a generalization of the reduced time principle, as presented by Schapery (1997), including the hygro-lock effect and the moisture memory.

By introducing a pseudo creep function $J(t,\tau)$ in accordance with the Boltzmann formulation, the eq.(1.54) is given as:

$$\varepsilon(t) = \int_0^t J(t,\tau) . \frac{\partial \sigma}{\partial \tau} d\tau \tag{1.55}$$

where:

$$J(t,\tau) = \int_\tau^t \frac{1}{\eta(\vartheta)} exp^{-\int_\tau^\vartheta \frac{k_{min}(\alpha,t)}{\eta(\alpha)} d\alpha} d\vartheta \tag{1.56}$$

For a generalized Kelvin Voigt model, the total strain is obtained as:

$$\varepsilon(t) = \varepsilon_0(t) + \sum_{i=1}^N \varepsilon_i(t) \tag{1.57}$$

By summing the mechano-sorptive behavior and adapting to the strain separation for each element in the generalized Kelvin Voigt model, the eq.(1.57) presents the constitutive viscoelastic mechano-sorptive behavior as:

$$\varepsilon(t) = \int_0^t \frac{1}{k_{min}^0(\tau,t)} . \frac{\partial \sigma}{\partial \tau} d\tau + \sum_{i=1}^N \int_0^t \left[\int_\tau^t \frac{1}{\eta^i(\vartheta)} exp^{-\int_\tau^\vartheta \frac{k_{min}^i(\alpha,t)}{\eta^i(\alpha)} d\alpha} d\vartheta \right] . \frac{\partial \sigma}{\partial \tau} d\tau \tag{1.58}$$

According to the Boltzmann formulation, the pseudo creep function $J(t,\tau)$ in eq.(1.58) may be rewritten as:

$$J(t,\tau) = \frac{1}{k_{min}^0(\tau,t)} + \sum_{i=1}^{N} \int_\tau^t \frac{1}{\eta^i(\vartheta)} exp^{-\int_\tau^\vartheta \frac{k_i^{min}(\alpha,t)}{\eta^i(\alpha)} d\alpha} d\vartheta \tag{1.59}$$

where i denotes the ith Kelvin Voigt branch; k^0 is the stiffness of the first branch (i.e., the spring), as shown in Figure 1.17.

1.4.2.3 Comparison of mechano-sorptive models

For the model with independent activation, the ones which are based on Maxwell or/and Kelvin Voigt model indicate that the creep deformation is accumulated due to the varying moisture. However, these two model types give different recovery responses. For example, in the model type of Maxwell (Ranta-Maunus, Leicester), the mechano-sorptive deformation is partially irreversible under the unloading phase; while in the model type of Kelvin Voigt (Toratti, Hunt, Martensson), this deformation can be totally recovered during the moisture variation after the unloading phase. In addition, the one based-on Kelvin Voigt model allows a slow increment of the creep deformation until the limit of the creep deformation after some moisture cycles; while in the one based on Maxwell model there is not a limit value.

In the principle of the model independence activation, the evaluation of the characterization of mechano-sorptive parameters appears to be difficult to carry out under creep tests and this effect may depend on the size and the geometry of the structure under varying moisture.

For the model with the combined activation, the one based-on Maxwell or/and Kelvin Voigt model indicates that the viscoelastic deformation and the mechano-sorptive deformation are controlled by the viscosity of the material. It physically explains better the phenomenon of the moisture effect on the mechanical response at the molecular and microstructure level of wood. The viscoelastic mechano-sorptive deformation results from the coupling between the viscoelastic properties and the mechanism of the moisture effect. Moreover, this deformation depends on the variation of the moisture as well as on the history of the moisture in wood.

As mentioned in this chapter, the coupled effects between the applied loading and the moisture in the wood induces rising of the creep responses. Whatever hypothesis considered, there are still several outstanding issues, which do not convince researchers. Using a generalized Kelvin Voigt model, it makes easier the physical interpretation of the different rheological elements: hydric, thermal, elastic and inelastic strain components. Even if Hunt has reported that the mechanical and the mechano-sorptive creep may not

be uncoupled, it seems difficult to model the global behavior of wood only with one element (for viscoelastic and mechano-sorptive deformation). On other hand, the use of a large number of elements for each mechanism of deformation renders the application of laws difficult be performed. It is the reason why choosing a law associating a small number of nonlinear elements (one or two) in association with a purely elastic behavior seems to be a good compromise.

1.5   Conclusion

This chapter gives a brief review on the wood material and on the hygromechanical behavior of wood. Wood is considered as an orthotropic viscoelastic material. The mechanical behavior depends on the moisture and the temperature in wood. The creep deformation under the variation of the moisture is more important than that under wood moisture constant. Furthermore, different response of wood in drying phase or humidification phase due to the hysteresis phenomenon of wood is observed. Many models are proposed to better explain these phenomena and they are divided into two approaches:

- the model with independent activation such as Ranta-Maunus, Leicester, Toratti, Hunt, Martensson models,
- the model with combined activation such as Bazant, Gril, Hanhijrvi, Husson and Dubois models.

However, all models were developed based on the assumption that the material and the structure are not damaged which simplifies the problem (e.g., limit condition, separated deformations...).

A timber structure under the external condition is influenced by both the loading solicitation and the climate change. Due to the manufacturer of the construction, damage sometimes exists leading to a stress concentration which possibly makes crack propagate further. Owing to crack growth, the analysis of the timber structure under varying moisture is more complex in which the theory of the elastic, viscoelastic, mechano-sorptive behavior and the fracture are simultaneous applied.

The main objective of this thesis is to develop a method for modeling the crack growth of the structure under varying moisture. Therefore, the mechano-sorptive model based on the work of Husson and Dubois has been selected to describe the behavior of wood substrates, which will be presented and developed in chapter 5. The analysis of the cracked structure is also based on the theory of the fracture mechanic. Consequently, fracture mechanics in general and fracture behavior of wood in particular will be presented in the next chapter.

Chapter 2

Fracture mechanics

This chapter deals with fracture mechanics in general and quasi-brittle fracture in particular. Linear Elastic Fracture Mechanics approach (LEFM) is commonly accepted as the theoretical basis in fracture mechanic for brittle materials. However, LEFM is not applicable for quasi-brittle materials due to the development of a non-negligible non-linear domain, called Fracture Process Zone (FPZ). Taking into account FPZ, an equivalent Linear Elastic Fracture Mechanics approach (eq.LEFM) is used for the quasi-brittle materials. In the equivalent LEFM, an equivalent elastic crack length is determined from the compliance function. In addition, crack growth resistance curve (R-curve) considered as a crack propagation criterion, is defined as energy release rate in function of the equivalent crack length. As a very useful and potential way, the concept of cohesive crack are successfully implemented in Finite Element Analysis (FEA) in order to mimic the development of FPZ.

Moreover, fracture properties of wood are also summarized under impact factors such as: density, moisture, temperature, geometry, size effect, etc... At the end of this chapter, crack growth kinetics of wood in viscoelastic media within the framework of LEFM is also presented.

2.1 Fracture mechanics and quasi-brittle fracture

2.1.1 A general review of fracture mechanics

First of all, Inglis (1913) [83] found a phenomenon at the vertex of a degenerated elliptical cavity in which stress tended to infinity. Based on his outlines, Griffith (1920) [64] proposed a concept of elastic strain energy G, namely fracture energy. Based on the energy balance principle, a crack can propagate enough to fracture a material (i.e., $G = 2\gamma$). This means that the gain in surface energy is equal to the loss of strain energy (γ is defined as surface energy of the material). This equation is considered as the crack propagation criterion and as the base for first theory of the fracture.

However, Griffith's theory was only successfully applied to the elastic brittle fracture.

To extend this theory for engineering materials having a limited plasticity zone, Irwin (1957) [84] proposed some modifications of the theory. A plastic strain energy G_p is added in order to take into account the fracture energy needed to propagate (i.e., $G = 2\gamma + G_p$). Based on his suggestion, Linear Elastic Fracture Mechanic (LEFM) was officially established. Moreover, Irwin [84] introduced a concept of stress intensity factor K_I, namely fracture toughness. Hence, a critical stress intensity factor K_{Ic} is also considered as crack propagation criterion. K_{Ic} is one of the most fundamental and useful parameter in fracture mechanics. In addition, for an isotropic material, Irwin also proposed a relation between stress intensity factor K_I (local approach) and energy release rate G (global approach) in Mode I as expressed by:

$$G_I = \begin{cases} K_I^2 \dfrac{1-\nu^2}{E_I} & \text{for plane strain} \\ K_I^2 \dfrac{1}{E_I} & \text{for plane stress} \end{cases} \tag{2.1}$$

where E_I and ν are Youngs modulus and Poissons ratio, respectively.

Many authors have begun to pay interest in fracture mechanics field of ductile materials. Dugdale [51] proposed a simple model in which stress values at the crack tip were limited by the yield strength of the material. That yielding was confined to a narrow band along the crack line. Barenblatt [8] also suggested a model represented by a cohesive zone at a molecular level instead of the macroscopic plasticity. In the Barenblatt's model, a softening zone existed on account of the assumed plasticity, which was the main different point compared to the Dugdale's model.

Another eminent contribution on elasto-plastic fracture mechanics was the introduction of a path-independent J-integral by Rice [142] in order to calculate strain energy release rate. Considering an arbitrary counterclockwise path around the crack tip, the J-integral for a non-loading crack lips (Fig. 2.1) is given as eq.(2.2). Furthermore, Rice [142] proved that the energy release rate G is equivalent to the J-integral.
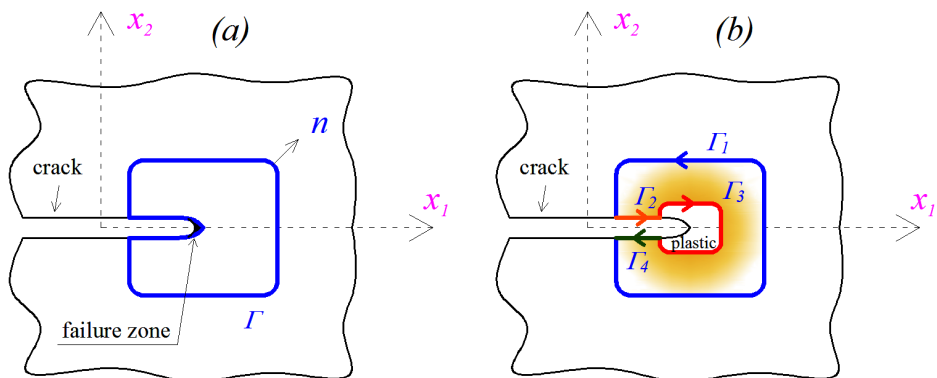
Figure 2.1: (a) J-integral curve and (b) Paths for J-integral calculation around a notch in a 2D elastic-plastic material

$$J = \int_{\Gamma} (W_e.n_j - \sigma_i.\frac{\partial u_i}{\partial x_j})d\Gamma \qquad (2.2)$$

where W_e designates the elastic strain energy density ($= \int_0^{\varepsilon_{ij}} \sigma_{ij}d\varepsilon_{ij}$) with σ_{ij} standing for the elastic strain tensor component. Γ is an arbitrary curve which is oriented by the normal vector characterized by its components n (See Fig. 2.1). σ_i is the component of the traction vector ($= \sigma_{ij}.n_j$), with n_j being the components of the unit vector normal to Γ; u_i is the displacement vector component; $d\Gamma$ is the length increment along the contour Γ ($\Gamma = \Gamma_1 \cup \Gamma_2 \cup \Gamma_3 \cup \Gamma_4$).

Compared to the first theory on brittle fracture, elasto-plastic fracture mechanic has been well developed into a general theory for fracture (LEFM approach). However, many authors recommended that LEFM approach may be not successfully applied for a material exhibiting a non-negligible non-linear domain ahead of the crack tip. This is explained by the presence of the non-linear domain leading to difficult calculating of the elastic strain energy density using the LEFM. Consequently, by taking into account this non-linear domain, a new material type is described as a quasi-brittle material.

2.1.2 Fracture behavior of a quasi-brittle material

In quasi-brittle materials, the presence of a nonlinear zone is considerably higher than in materials characterized by a very brittle behavior. The nonlinear zone at the crack tip consists in a softening zone and a hardening zone. Figure 2.2 shows a sketch describing the comparison of the softening zone and the nonlinear hardening zone for three commonly material types: brittle, ductile and quasi-brittle.
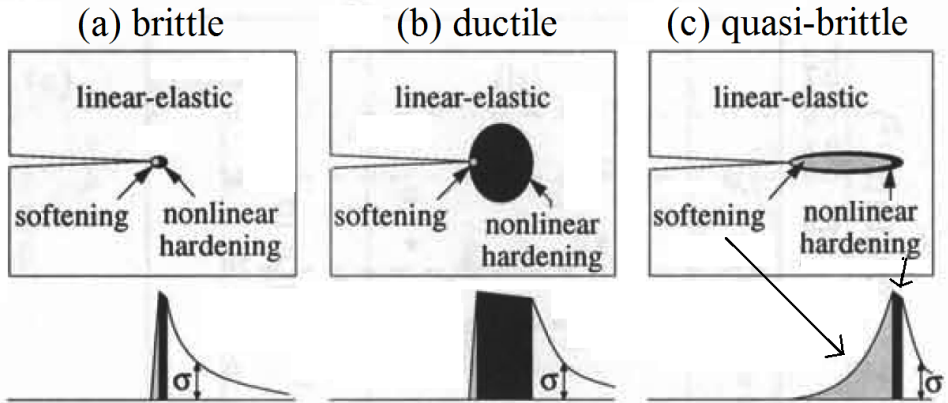
Figure 2.2: Relative sizes of Fracture Process Zone (FPZ) [12]

As shown in Figure 2.2c, the nonlinear hardening zone in quasi-brittle materials is negligible in volume compared to the softening zone. According to Bazant et al. [12], the nonlinear hardening zone exhibits barely the transition between the elastic response and the damaged material. The softening zone, called Fracture Process Zone (FPZ), is where

the material undergoes progressive damage due to many argumentation such as: micro-cracking, crack-bridging, void coalescence, frictional slips, and other analogous phenomena [11, 12, 113, 115]. In this region, after the tensile strength is overtaken, the tensile stresses decrease progressively with the increasing of strains. Materials exhibiting a quasi-brittle behavior at failure are commonly cited as concrete, rock, cement mortars, tough fiber composites, ceramics, wood, etc [12].

Moreover, in Figure 2.2a, the ratio defined by the size of FPZ and the non-linear hardening zone, in brittle material is low. This is the reason why it is practically neglected; while the materials exhibiting a ductile behavior (Fig. 2.2b), this ratio is sufficiently small so that the LEFM may be fully applied (mostly treated by the elasto-plastic fracture mechanics). For quasi-brittle materials, the size of the FPZ is large enough to take into account in the strain energy. Because the FPZ leads to the non-negligible macroscopic stress redistribution with a non-negligible amount of dissipated energy from the structure [11, 12, 113, 115]. Consequently, a modification of LEFM approach is required to investigate the quasi-brittle behavior in the fracture analysis.

An adaptation of the LEFM approach called 'equivalent LEFM', is usually applied on the quasi-brittle material. [11, 12, 113, 115]. Figure 2.3 shows a schematic representation for the equivalent LEFM approach. In this approach, the non linearity of the load-displacement response (due to the development of the FPZ or the main crack propagation with its FPZ) is explained by an increase of the elastic compliance of the specimen [12, 113, 115]. According to Morel et al. [113, 115], an equivalent LEFM crack length a_{eq} is defined as the crack length of a structure considered purely linear elastic giving the same compliance as the one of the cracked structure with its FPZ (Fig. 2.3). The eq.LEFM approach provides useful approximation of crack growth process by means of a resistance curve (R-curve) for the quasi-brittle material [12, 39, 115, 177].
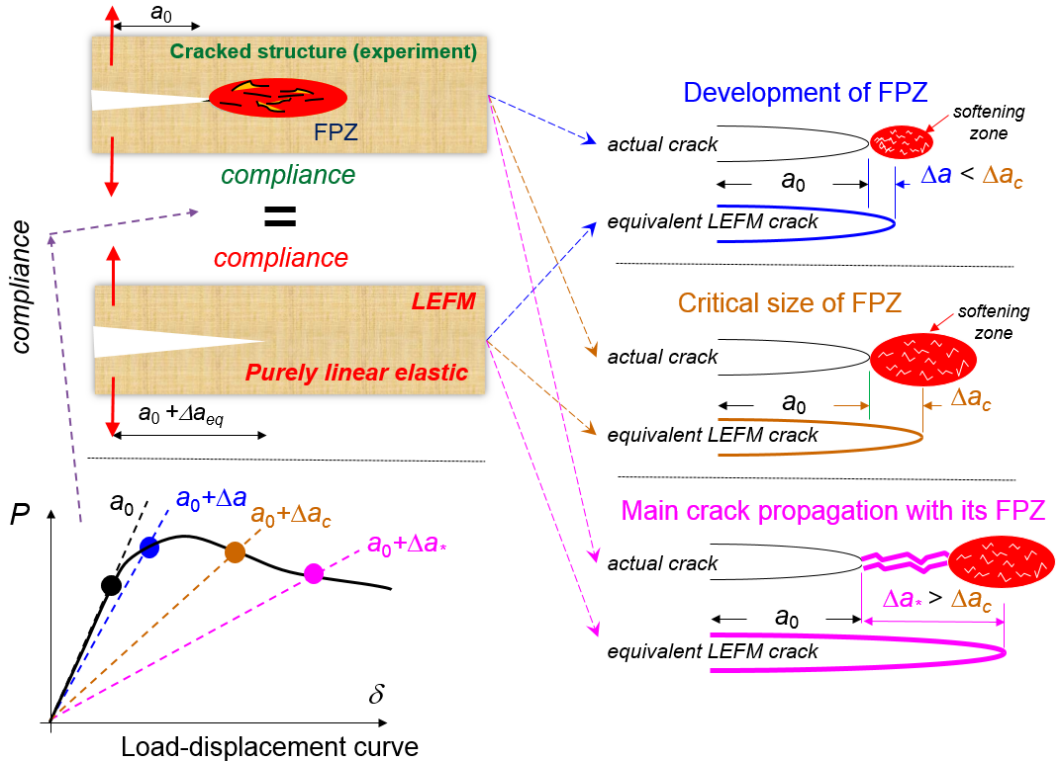
Figure 2.3: Schematic representation for the equivalent Linear Elastic Fracture Mechanics (eq.LEFM). Note that red color represents FPZ in the actual crack configuration

2.1.3 Crack growth resistance curve (R-curve)

Crack growth resistance curve (R-curve) is defined as the relation of the energy release rate versus the equivalent crack length a in the framework of the equivalent LEFM [11, 12, 113, 115]. An R-curve is established by concerning the progressive increase of the compliance obtained during experiments. Fig. 2.4 shows a brief relation of the load-displacement curve and the corresponding R-curve.

As shown in Figure 2.4, for a given point of the load-displacement curve (P, δ), the equivalent elastic crack length a corresponding to the compliance value $\lambda = \delta/P$ is extracted from compliance function $\lambda(a)$ (dichotomous procedure). When the crack length a is obtained, the crack growth resistance curve $G_R(a)$ can be then determined from the following equation of LEFM:

$$G_R(a) = G(a) = \frac{P^2}{2b} \frac{\partial \lambda(a)}{\partial a} \qquad (2.3)$$

where P is the applied load, b is the specimen thickness and $\lambda(a)$ is the compliance function.
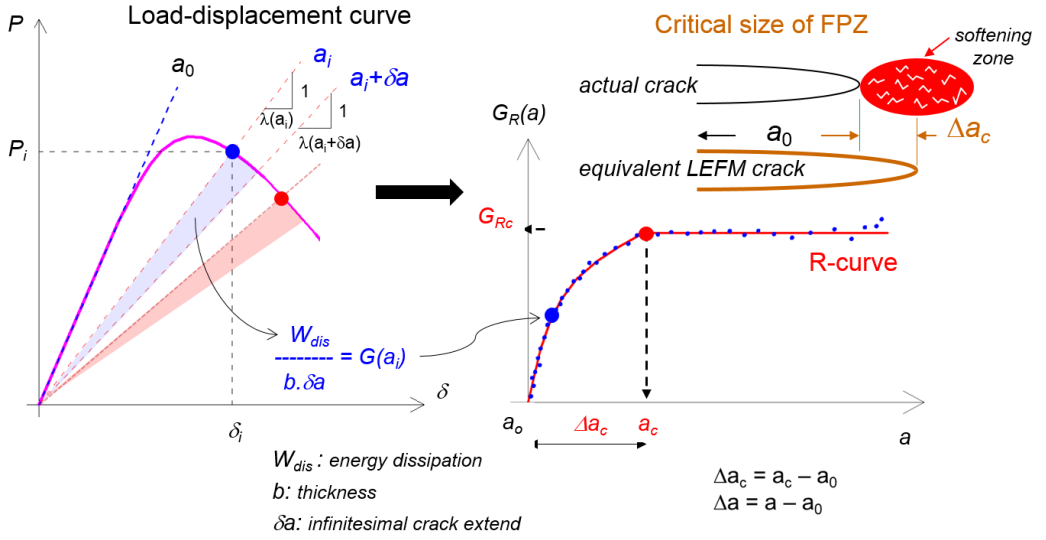
Figure 2.4: Sketch of the evaluation of crack growth resistance curve (R-curve)

According to Bazant et al. [12], Morel et al. [37, 113, 115], two zones of R-curve (Fig. 2.4) can be distinguished:

- a first rising zone corresponding to the development of the FPZ in which toughening mechanisms take place such as the micro-cracking and the crack bridging;
- a plateau zone of the resistance associated to the self-similar propagation of the main crack with its critical FPZ.

Moreover, in Figure 2.4, the plateau value of the R-curve is noted as G_{Rc} and the characteristic crack length noted as a_c. The characteristic crack length a_c allows to estimate the characteristic equivalent LEFM length of the FPZ, $\Delta a_c = a_c - a_0$ [113] which is also called as the *internal length* in quasi-brittle materials. [12, 115]. On the other hand, the R-curve $G_R(a)$ as shown in Figure 2.4 can be easily fitted by an analytical function defined as:

$$
G_R(\Delta a) = \begin{cases} \dfrac{G_{Rc}}{\Delta a_c{}^\beta} \Delta a^\beta & \text{if } \Delta a < \Delta a_c \\ G_{Rc} & \text{if } \Delta a \geq \Delta a_c \end{cases} \tag{2.4}
$$

where $\Delta a = a - a_0$ corresponding to the equivalent crack length increment; and β is the power law exponent characterizing the curvature of the rising zone of the R-curve (associated to the FPZ development regime).

In the relation between the R-curve and the load-displacement curve, Carpinteri et al. [24], Bazant et al. [12] (studied on concrete), Morel et al. [115] (studied on wood) showed that the peak load of a specimen (most of geometry) generally occurs in the rising zone of R-curve. In other terms, the peak load is obtained corresponding to the energy release rate smaller than the plateau resistance associated to the self-similar propagation of the

main crack (Fig. 2.5). This observation is significantly important in the structure (i.e. concrete structure, timber structure...) because the peak load is commonly referenced in the structure design.

(a) $G - a$ curve   (b) $P - \delta$ curve
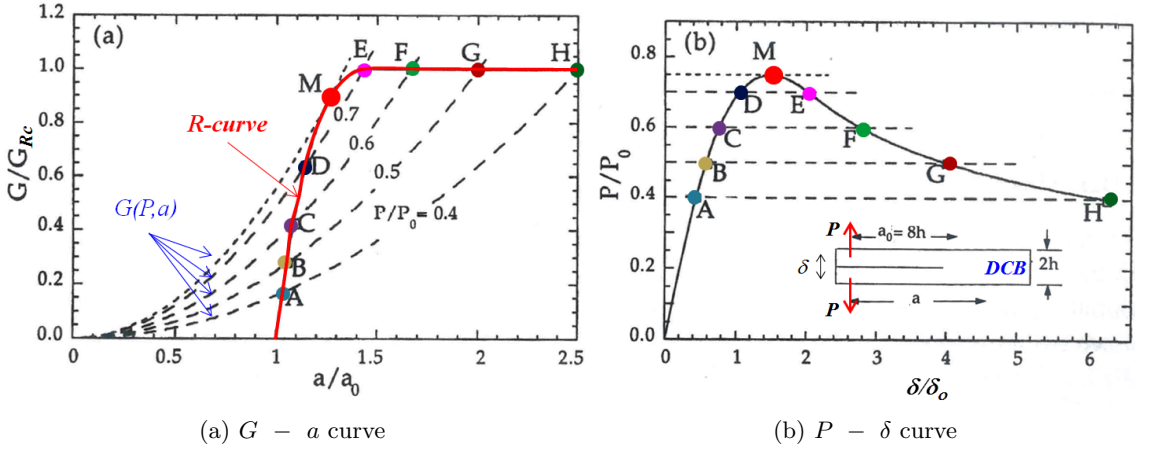
Figure 2.5: Representation of fracture processes in DCB specimen. Adapted from [12]

According to LEFM, the energy release rate corresponding to a load P is given:

$$G(P, \alpha) = \frac{P^2 g(\alpha)}{E b^2 D} \tag{2.5}$$

where $\alpha = a/D$, b is the thickness, D is the ligament of the specimen; $g(\alpha)$ is a dimensionless energy release rate function. Generally, $g(\alpha)$ and therefore $G(P, \alpha)$ are increasing functions of the crack length for most structures (called positive geometry).

As illustrated in Figure 2.5a, $G(P, a)$ corresponding to a succession of increasing values of P are shown by dashed curves. Note that, according to the principle, each dash curve cuts the R-curve in two points (Fig. 2.5a): once before reaching the peak load (along the arc A-B-C-D-M, the load is increasing (Fig. 2.5b)) and after that (along M-E-F-G-H, the load is decreasing (Fig. 2.5b)).

To find the peak load, it is necessary to solve the condition that assures that the R-curve is tangent to a peak load (point M in the $G - a$ curve in Figure 2.5a). This condition is very easy to impose graphically, but it may be difficult to solve analytically or numerically. Analytically, according to Bazant et al. [12], Morel et al. [115], the relative crack length corresponding to the peak load is the solution of the equation:

$$\frac{G'_R(\alpha)}{G_R(\alpha)} = \frac{g'(\alpha)}{g(\alpha)} \tag{2.6}$$

where $G'_R(\alpha) = \dfrac{\partial G_R(\alpha)}{\partial \alpha}$ and $g'(\alpha) = \dfrac{\partial g(\alpha)}{\partial \alpha}$.

Owing to the fact that most of the materials used for building structures are quasi-brittle (i.e. concrete, wood, rock, cement mortars...), in numerical point of view, cohesive crack theory and model are developed in order to deal with the presence of FPZ in the fracture analysis.

2.1.4 Cohesive crack model

In the literature, a brief overview of cohesive crack models such as its numerical aspects, advantages, limitations and challenges can be easily found [12, 38, 52, 132]

For quasi-brittle materials, Hillerborg and co-workers [75] firstly suggested a new non-linear fracture model, based on the cohesive crack theory in the work of Dugdale and Barenblatt [8, 51], to analyze the physical behavior of concrete in fracture. Unlike previous models which can be only applied to initial cracked structures, the cohesive crack model can describe the behavior of a structure from crack initiation to failure. This approach is one of the most widely used nonlinear fracture models.

2.1.4.1 Assumption of the cohesive crack theory

Accoring to Hillerborg et al. [75], Petersson et al. [125], Carpinteri et al. [24, 25], various simplified assumptions are considered as:

- The material is locally considered under damage within the FPZ, the surrounding material remains undamaged (Fig. 2.6). As a result, the whole material, excluding the FPZ, is linear-elastic.
- The material starts to damage when the maximum principal stress reaches its tensile strength f_t (Fig. 2.6).
- The damage process of the material is partially activated. The damaged material is still able to transfer stresses on the surfaces of the cohesive zone: the stress is followed by a cohesive law (Fig. 2.6). This law describe the evolution of stress in function of crack opening displacement w (i.e., $\sigma = f(w)$). When the function $f(w)$ decreases monotonically, it corresponds to softening behavior.
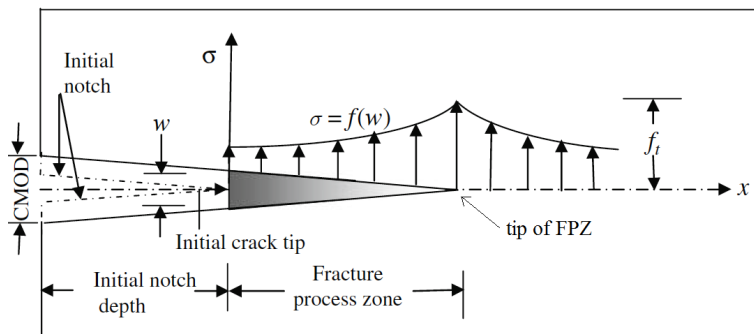
Figure 2.6: Stress distribution and cohesive crack growth in mode I for concrete. Adapted from [95]

2.1.4.2 The softening function of cohesive law

As illustrated in Figure 2.7 for a quasi-brittle material, based on the softening function, the distribution of the normal stress (tensile stress) varies non uniformly along the length

of the FPZ. In the softening function, the stress σ decreases with the increase of the relative displacement discontinuity w. At the tip of FPZ: $\sigma = f_t$ and $w = 0$. As recommended by Hillerborg [75], the position of the FPZ tip is not the real crack tip (Fig. 2.6). In this case, the equivalent crack length in the quasi-brittle material can be obtained from the equivalent LEFM approach (as mentioned in the previous section) [12, 115].
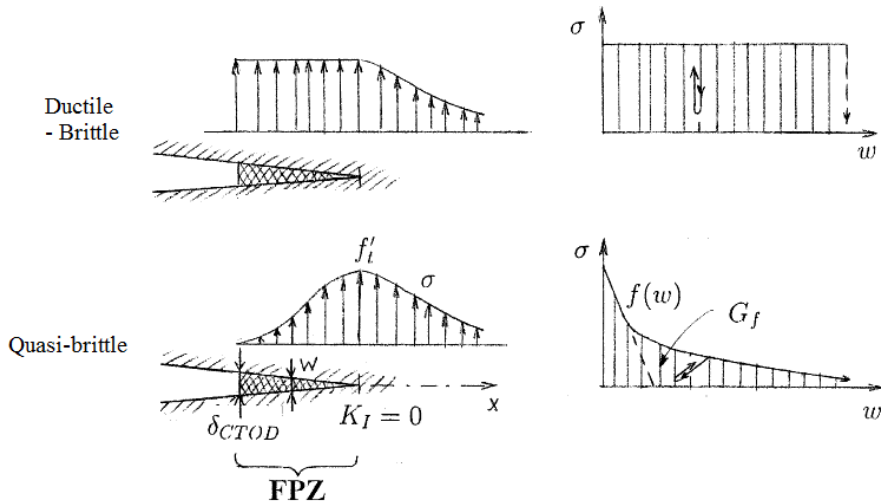
Figure 2.7: Softening curve of the material. Adapted from [12]

Based on the cohesive law, the critical cohesive energy G_f is mathematically evaluated as the area under the softening diagram as illustrated in Figure 2.7, and can be written as:

$$G_f = \int_0^{w_c} f(w)\mathrm{d}w \tag{2.7}$$

where w_c is the critical crack opening corresponding to the critical cohesive energy G_f. Consequently, the critical cohesive energy G_f is considered a significant fracture property of this type of material.

2.1.4.3 Advantage and limitation of cohesive crack model

The cohesive zone model has a convenient mathematical idealization for describing the material damage zone in the quasi-brittle material. One of the most important advantages is that the model can be easily implemented in numerical analysis tools such as finite element method or boundary element method [52].

Nevertheless, cohesive crack models have some limitations: it is sometimes difficult to experimentally identify the material parameters governing the model. The characterization of the softening law is not easy and remains a crucial task. The intrinsic limitations are essentially linked to the simplifying assumptions in the model such as: a localized discontinuity, closed crack condition, non-dissipative condition of the bulk material [52].

2.1.4.4 Cohesive zone model in numerical calculations

A description of the cohesive finite element formulation for modeling fracture and delamination solids is presented on detail in [2, 16, 35, 55]. Many authors used the CZM to study the fracture in elasto-plastic and brittle solids [22, 165, 166] as well as for the quasi-brittle such as concrete [52, 67, 69, 132, 143, 145, 171], and wood [37, 41, 113, 128, 173, 176, 178]. The numerical simulation consists in a bulk material modeled as a continuum domain and a cohesive zone which represents the FPZ (Fig. 2.8). In cohesive zone, cohesive joint elements are used. Based on this, the principle of the virtual work for the bulk material and the cohesive zone is written as:

$$\int_{\Omega} \sigma : \delta\varepsilon \mathrm{d}\Omega + \int_{\Gamma_c} \sigma_{joint}\delta w \frac{1}{J}\mathrm{d}\Gamma_c = \int_{\Gamma_f} F\delta u \mathrm{d}\Gamma_f + \int_{\Omega} f\delta u \mathrm{d}\Omega \qquad (2.8)$$

where all parameters in eq.(2.8) are illustrated in Figure 2.8. δu is the virtual displacement field. F and f are, respectively, the external loading in surface Γ_f and in volume Ω. Ω is the current volume of the bulk material ($\Omega = \Omega_1 \cup \Omega_2$). Γ_f is the current external surface area over which the external loading in surface is applied; σ is the Cauchy stress tensor. ε is the virtual rate of the deformation tensor. σ_{joint} is the cohesive stress; w is the displacement jumps across the cohesive surfaces. Γ_c is the current internal surface area over which the cohesive forces are acting. J is the Jacobian of the transformation between the current deformed and original undeformed areas of the cohesive surfaces.
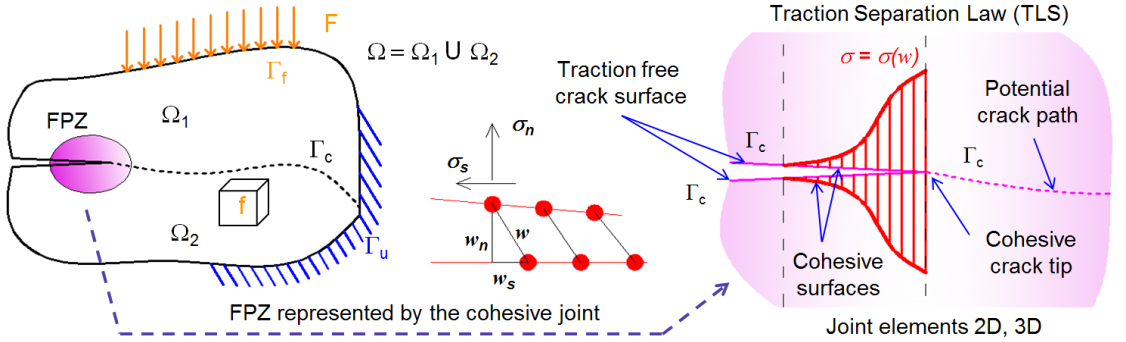
Figure 2.8: Sketch of the concept of cohesive zone model

Based on eq.(2.8), the virtual work δW_c of the cohesive forces in 2D or 3D can be rewritten as:

$$\delta W_c = \int_{\Gamma_c} \sigma_{joint}\delta w \frac{1}{J}\mathrm{d}\Gamma_c = \int_{\Gamma_c} (\sigma_n\delta w_n + \sigma_s\delta w_s)\frac{1}{J}\mathrm{d}\Gamma_c \qquad (2.9)$$

where σ_n and σ_s are, respectively, the normal and tangential stresses of the joint; δw_n and δw_s are, respectively, the normal and tangential displacement jump rates across the surface of the cohesive zone.

According to Beer [13], the virtual displacement jump rates can be written in terms of the joint element *nodal* shape functions N and the *nodal* virtual displacement jump rate

in FEA (i.e., w_s and w_n in Figure 2.8). Based on this, the *discretized* virtual work δW_c in the current configuration is given as:

$$\delta W_c = \int_{\Gamma_c} (\delta w_n^T N^T \sigma_n + \delta w_s^T N^T \sigma_s) \frac{1}{J} d\Gamma_c \tag{2.10}$$

where T indicates a transpose operation in matrix or in vector.

From eq.(2.10), the virtual work dW_c of the cohesive zone can be integrated, based on an updated Lagrangian formulation, and used with bulk finite elements. The first variation of the virtual work δW_c is obtained as:

$$d\delta W_c = \int_{\Gamma_c} (\delta w_n^T N^T d\sigma_n + \delta w_s^T N^T d\sigma_s) \frac{1}{J} d\Gamma_c + \int_{\Gamma_c} (\delta w_n^T N^T \sigma_n + \delta w_s^T N^T \sigma_s) d(\frac{1}{J}) d\Gamma_c \tag{2.11}$$

where $d\sigma_n$ and $d\sigma_s$ are, respectively, the incremental normal and tangential stresses located at the surface of the cohesive zone.

By considering an infinitesimal deformation of the cohesive element, the second term in eq.(2.11) can be negligible. Hence, the eq.(2.11) can be approximated as:

$$d\delta W_c = \int_{\Gamma_c} (\delta w_n^T N^T d\sigma_n + \delta w_s^T N^T d\sigma_s) \frac{1}{J} d\Gamma_c \tag{2.12}$$

The relation of the incremental stress and the incremental displacement jump in the cohesive joint is expressed as:

$$\left\{ \begin{array}{c} d\sigma_n \\ d\sigma_s \end{array} \right\} = \mathbb{C} \left\{ \begin{array}{c} dw_n \\ dw_s \end{array} \right\} \tag{2.13}$$

where $\mathbb{C}$ is given as:

$$\mathbb{C} = \left[\begin{array}{cc} \dfrac{\partial \sigma_n}{\partial w_n} & \dfrac{\partial \sigma_n}{\partial w_s} \\ \dfrac{\partial \sigma_s}{\partial w_n} & \dfrac{\partial \sigma_s}{\partial w_s} \end{array} \right] \tag{2.14}$$

Substituting the incremental stress in terms of the incremental displacement jump from eq.(2.13) into eq.(2.12), and writing the incremental displacement jump in terms of the incremental displacement cohesive element nodal, the tangent stiffness matrix of cohesive joints is given as:

$$\mathbb{K}_T = \int_{\Gamma_c} B^T \mathbb{C} B \frac{1}{J} d\Gamma_c \tag{2.15}$$

where B is the derivative of the shape functions (matrix) that relates the nodal rate to the velocities of the displacement jumps within the cohesive element.

The tangent stiffness matrix $\mathbb{K}_T$ for cohesive joints implemented in eq.(2.15) gives an approximate tangent for Newton-Raphson iterations and then equilibrium is ensured upon convergence.

2.2 Fracture behavior of wood

Wood is considered an orthotropic material (see Section 1.1) which can develop several crack orientations in the fracture test. Therefore, for mode I, there are six principal systems (Fig. 2.9): TL, RL, LR, TR, RT and LT, in which the first and second letter indicates, respectively, the direction of the loading and the direction of crack propagation [150]. In the literature, the fracture test in the LR or the LT system is rarely studied [7]. However, other RL or TL system are frequently studied for the design practice.
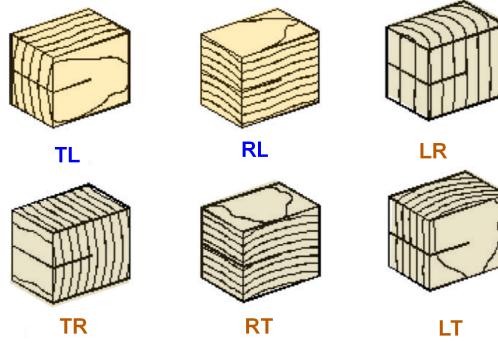
Figure 2.9: Six principal crack propagation systems for wood

A comprehensive overview of the application of the Linear (LEFM), Non-Linear Elastic Fracture Mechanics (NLFM) methods as well as a discussion of the experimental test corresponding to LEFM, NLFM methods is given by [15]. Some studies [17, 36, 87, 94, 126, 133, 138, 139, 161, 169, 170] are performed by using LEFM, idealizing wood as brittle material, the wood seems to be in the brittle behavior, so fracture toughness K_{Ic} or specific fracture energy G_F were considered adequate to characterize the fracture process (Fig. 2.10). G_F quantifies the whole energy required for separating wood fibers.
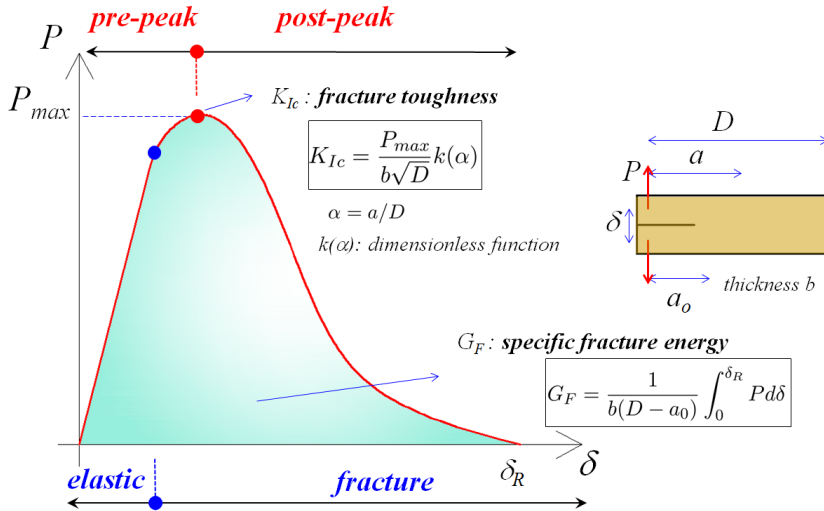
Figure 2.10: Determination of K_{Ic} and G_F in the LEFM

However, when a crack propagates parallel to the grain, the presence of a tensile softening zone is observed [40, 44, 115, 128, 161, 173, 176]. A fiber bridging zone in wood, represents the tensile softening zone, is typically shown in Figure 2.11 [159]. The fracture process zone of wood is associated with the processes of the micro-cracking and the fiber bridging [100, 113, 158, 161, 163]). As a result, the fracture behavior in wood is commonly treated as a quasi-brittle material in the NLFM [12]. Consequently, it is commonly accepted that fracture property (i.e., G_F or G_{Rc} in the global approach) is the basic parameter for fracture behavior of wood.
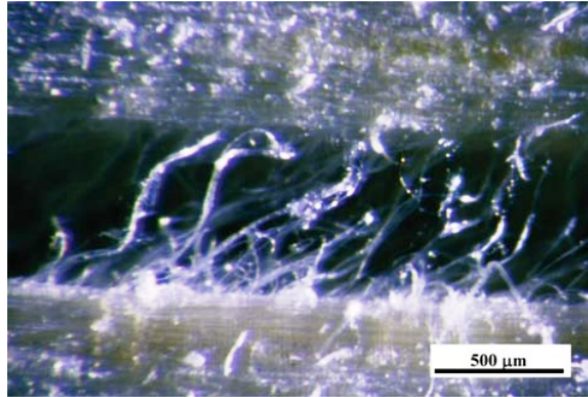
Figure 2.11: Fiber bridging in spruce during the tensile loading in RL fracture system causing the energy dissipation and thus retarding the crack propagation [159]

It is well-known that fracture behavior of wood depends on many factors such as density, moisture, temperature, geometry, size effect... [17, 36, 40, 43–45, 87, 94, 100, 111, 113, 115, 126, 128, 130, 133, 138, 139, 161, 169, 170, 173, 176]. A brief overview of the factor effects on the fracture properties of wood is given in the following paragraphs.

2.2.1 Influence of the density on the fracture property of wood

First of all, similar to elastic proprieties, fracture toughness of wood is strongly dependent on the density: the fracture toughness increases with the increase of the density [7, 61, 93, 99, 126] (See Fig. 2.12).

The relation of the density and fracture toughness K_{Ic}, proposed by Gibson and Ashby [61], is a power law dependence as $K_{Ic} = (k\rho/\rho_s)^{3/2}$, where k is a constant material parameter. This relation is given based on the observation at the cellular level: the crack have to across a greater amount of cellulose, this leads to a high fracture toughness to propagate [61]. However, as shown in Figure 2.12, in the range of densities from 400 to 600 kg/m^3, the relation between of K_{Ic} and density is not clear.
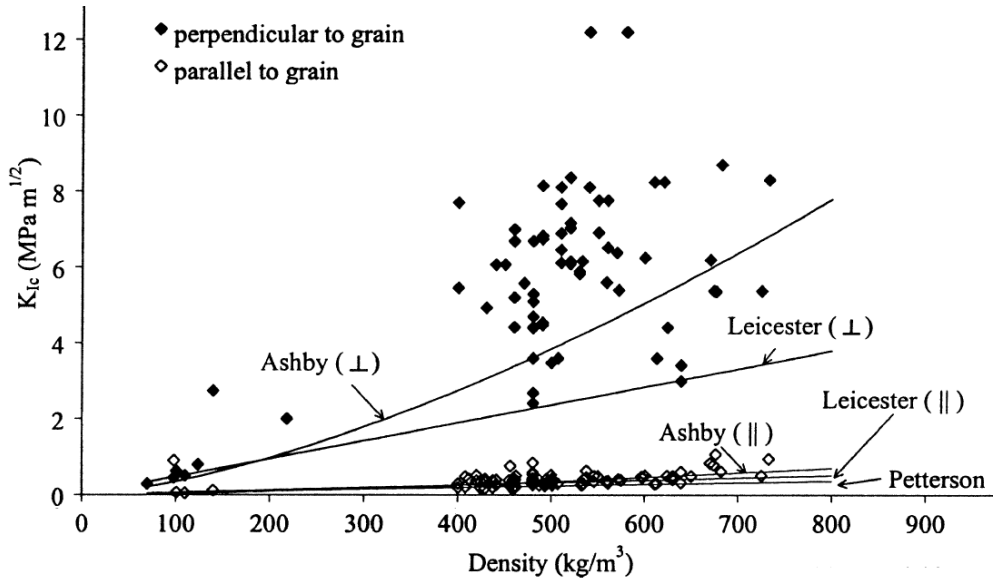
Figure 2.12: Density effect on fracture toughness (mode I). Extracted from [36]

2.2.2 Influence of the moisture content on the fracture property of wood

According to Petterson et al. [126], an increasing of the MC induces the decreasing of the fracture toughness in TL system. Kretschmann et al. [94] have tested southern pine at different MC to study the stress intensity factors in mode I (K_I) and mode II (K_{II}). They indicated that these factors increase with the decreasing of the moisture from the saturated state to a peak between 7% and 13%. From tests on Single Edge Notched (SEN) specimens of oak and pine at three moisture contents (6%, 9% and 12%), Prokopski et al. [133] have observed a decreasing of K_{Ic} for pine and an increasing of K_{Ic} for oak when MC increases. Reiterer et al. [138] have used Wedge Splitting Test (WST) specimens on the Maritime pine at four MC (7%, 12%, 18% and 55%) to study fracture behavior in mode I. They have found that G_F increases when the moisture increases.

According to Vasic and Stanzl-Tschegg [170], an increasing moisture from 7% to 30% led to a decreasing of the fracture toughness of pine and beech and to a strong decreasing between 7% and 12% MC in oak and beech in RL system. The increasing of G_F with increasing MC was obviously related to the moisture which induces higher 'ductility' (extensibility) of wood and thus demonstrates the underlying deformation mechanism better than the fracture toughness [170]. Using in-situ real-time material Scanning Electron Microscopy (ESEM), Vasic et al. [170] reported that water droplets from cell lumen move away from the process zone during the loading prior to the crack extension. Their observation was based on an assumption that stress gradients at the crack tip might have a significant effect on the local moisture distribution by the free water flow and the vapor diffusion at the vicinity of the crack.

Recently, Xavier et al. [173] have studied the moisture effect on the fracture behavior

44

of the Pinnus Pinaster in the RL system (mode I) of DCB specimens with MC ranging from 0% to about 13%. By using R-curve and cohesive zone model, they showed that the increasing of moisture leads to the increasing of the energy release rate either at the maximum load (P_{max}) or at the plateau regime.

Most of all results obtained in previous studies [17, 87, 94, 126, 133, 138, 139, 161, 169, 170, 173] show that fracture energy increases with the increasing of the moisture. This is mainly explained by an increased fiber bridging effect and an increase of the ductility in wood.

2.2.3   Influence of the temperature on the fracture property of wood

Reiterer et al. [137] studied the WST specimen in RL system at four temperatures (20^oC, 40^oC, 60^oC and 80^oC). Before heating and testing, the conditioned moisture for all specimens is 12%. Due to the heating procedure, the moisture was reduced by 1% for 40^oC, by 2% for 60^oC and 4% for 80^oC. They indicated that K_{Ic} decreases with increasing temperature for both spruce and beech. This is explained by the fact that bonding between the different layers of the wood cell wall might be weakened and a softening of the macromolecular matrix substances hemicellulose and lignin appeared from 60^oC to 80^oC.

Using scanning electron microscope images of the fracture surfaces, they showed that fracture surface of spruce with a temperature of 20^oC seems to be rougher; and more cell wall fragments torn out of the cell walls are visible, while fracture surface of a sample with 80^oC is depicted (Fig. 2.13). They reported that the energy is more dissipated at lower temperatures. However, the effect of the variation moisture in wood or the coupling effect of the temperature and the moisture on fracture behavior of wood is not clearly mentioned in their study.
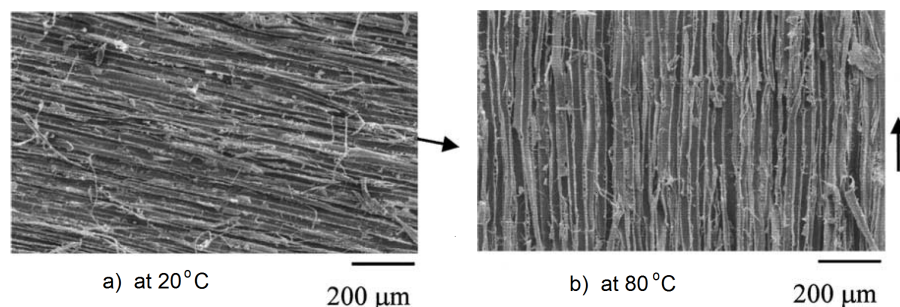
Figure 2.13: Typical fracture surfaces of spruce samples. The arrows indicate the macroscopic fiber direction. Extracted from [137]

2.2.4 Influence of the geometry on the fracture property of wood

The influence of the geometry on the fracture property of wood is also an other interesting topic due to a different compliance of specimens. Practically, by considering the same height or length of the specimen, the fracture energy depends on the shape of the wood specimen (i.e, the evolution of the compliance with the crack extend).

Using Double Cantilever Beam (DCB) and Tapered Double Cantilever Beam (TDCB30, TDCB60) specimens of Spruce as shown in 2.14, Morel et al. [116] indicated that G_{Rc} and Δa_c in R-curve increase with the average compliance of specimens. Due to the geometry, the TDCB60 specimen compliance is higher than those of DCB specimen. Consequently, the G_{Rc} obtained in TDCB60 specimen is the highest, while the G_{Rc} of DCB specimen is the smallest.

	DCB	TDCB30	TDCB60
a_o	240	240	240
b	0	30	60
c	510	510	510
d	990	990	990
e	400	400	400
h	300	300	300
L	100	100	100
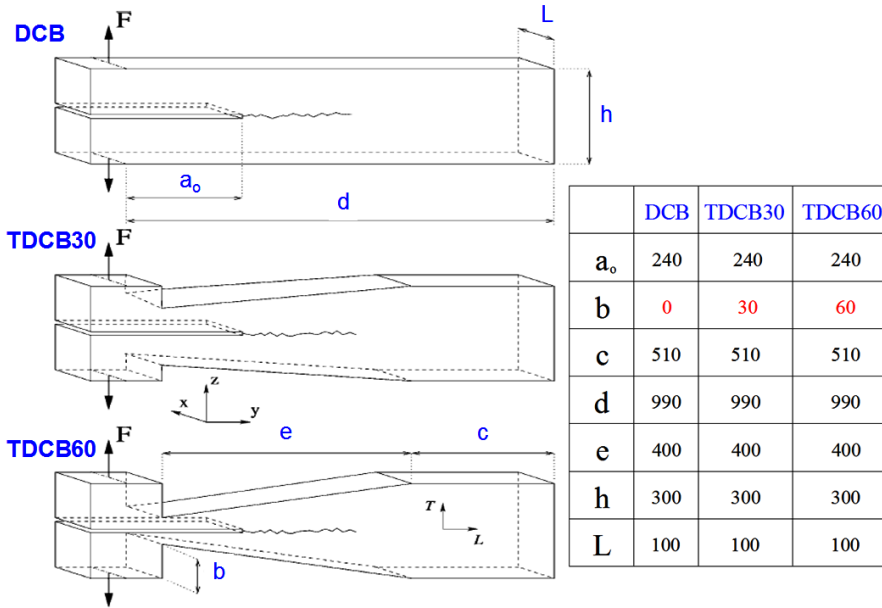
Figure 2.14: Three different shapes: DCB, TDCB30 and TDCB60

2.2.5 Influence of the specimen size on the fracture property of wood

One of the most significant current discussions in the fracture behavior for material in general and for wood in particular is the size effect on the fracture property of the material due to a context of the small size sample in the laboratory and the large size structure in the reality. Most of studies are based on the study of Bazant et al. [12], the size effect law. This size effect law allows to describe the size effect on the nominal strength of geometrically similar notched structures of different characteristic sizes D.

According to Morel [111], for $D > D_{max}$, R-curve becomes independent of the structure size; for $D < D_{max}$, R-curve depend on the structure size. A representation is given in Figure 2.15.
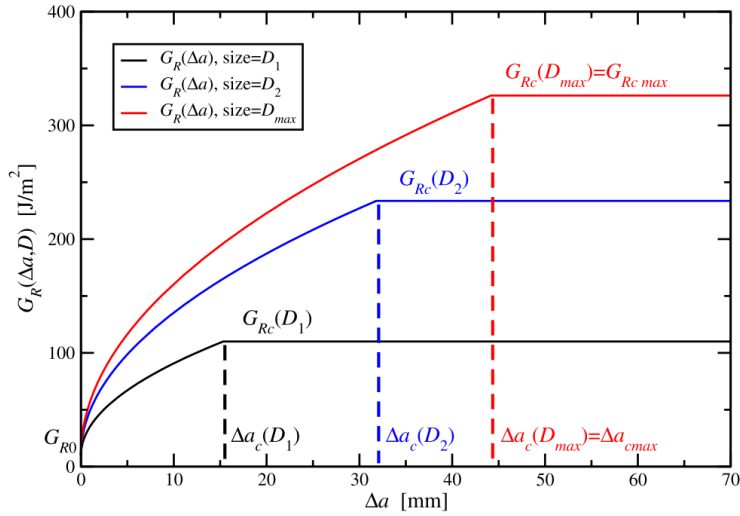
Figure 2.15: R-curves obtained for different characteristic sizes D ($D_1 \ll D_2 \ll D_{max}$). Adapted from [111]

Moreover, testing with a Single-Edge-Notched Beam (SENB) specimen loaded in three-point-bending on the Maritime pine, Dourado et al. [43], Morel and Dourado [114] reported that with the exception of the smallest structure (corresponding to structure sizes $D < D_4 = 280\ mm$ in Figure 2.16), R-curves appear superimposed leading to a single R-curve, i.e., a R-curve independent of the structure size.

Series	D (mm)
D_0	17.5
D_1	35
D_2	70
D_3	140
D_4	280
D_5	560
D_6	1120
D_7	2240
D_8	4480
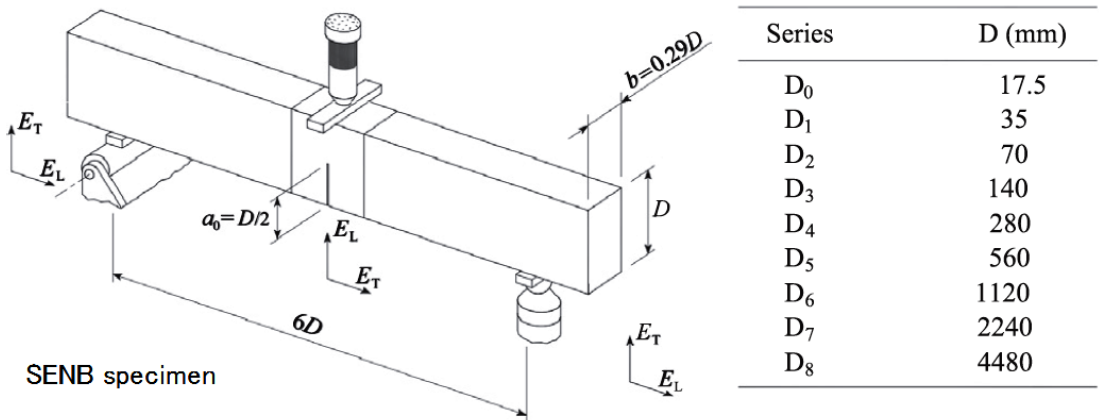
Figure 2.16: SENB wood specimen characterized by its characteristic dimension D corresponding to the specimen height. The initial notch length is $a_0 = D/2$ [114]

2.2.6 Influence of the loading orientation on fracture property of wood

Studies of the influence of the loading orientation (crack plane system in wood) on K_{Ic} and on G_F were performed on different wood species (e.g., spruce, pine, beech, oak). Using the WST specimen at 65%RH, Vasic et al. [169, 170] reported that in Spruce and Beech wood, G_F in TR system is higher than those in RL system; conversely for the Oak

wood. Their results are summarized in Figure 2.17.
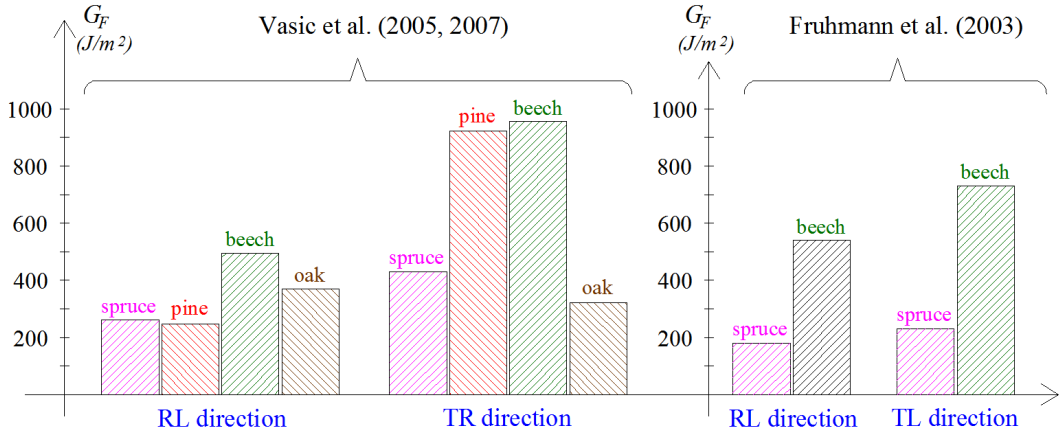
Figure 2.17: Specific fracture energy (Mode I) of different wood species

Details of micro-structural influences such as the role of rays have been studied by Fruhmann et al. [57]. In beech wood, with more numerous and stronger rays in the FPZ, a stronger 'bridging effect' occurs in TL system leading to consuming more energy than in the RL system where the early wood is dominant (Fig. 2.17). Moreover, the reinforcement effect of wood rays in RL system was obviously not large enough to overcome the lack of late wood. In spruce, wood rays also occur but contribute only 5-10% to the volume of the material and are bundled to significantly smaller cross sections which leads to that: the reinforcing effect is less pronounced and the specific fracture energy for the RL system is smaller than for the TL system.

2.2.7 Influence of the mixed mode loading on fracture property of wood

Due to the loading direction compared to the potential crack plane (Fig. 2.18), the fracture of wood has a complex mode of rupture: opening mode (mode I) and sliding modes (mode II: in-plane shear and mode III: anti-plane shear). Generally, the DCB and the End-Notched Flexure (ENF) specimens are used for fracture test in mode I and mode II, respectively. In mixed-mode, the tensile and shearing stress components are functions of the opening and shear displacements at the process zone, respectively. The combined fracture energy (for each component) is inferior to the specific fracture energy in pure modes (mode I, mode II).

Most of studies [40, 57, 176] reported that K_{IIc} and G_F obtained in mode II is higher than that obtained in mode I (about 2.5-3.5 times). By correlating fractographic with load-displacement curves of beech and spruce, Fruhmann et al. [57] showed that mode I results in a rather ductile behavior and a comparably small damage zone, whereas for mode II and mode III the damaged volume is essentially greater and the FPZ is more complex.
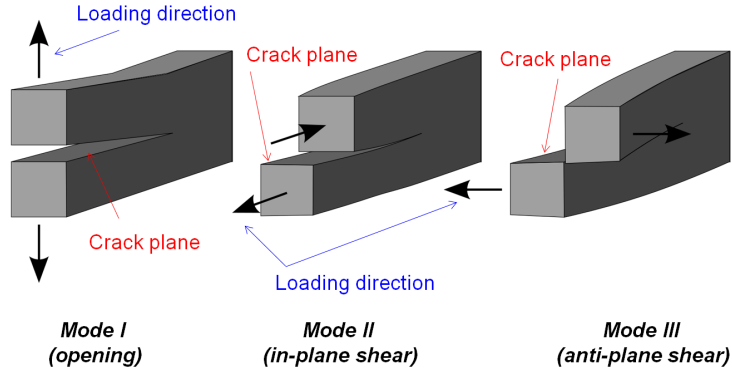
Figure 2.18: Sketches of three pure modes

To study fracture criteria under mixed-mode condition, MMB test is frequently used thanks to the easily mode-ratio variation [40, 130, 176]. As shown in Figure 2.19, the MMB test is considered as a combination of the DCB and the ENF tests; the mode ratio (G_I/G_{II}) can be altered by changing the loading lever c. To describe the self-similar propagation of the main crack in mixed-mode, fracture criteria are applied [40, 176]:

$$\left[\frac{G_I}{G_{Ip}}\right]^m + \left[\frac{G_{II}}{G_{IIp}}\right]^n = 1 \tag{2.16}$$

where G_{Ip} and G_{IIp} correspond to the specific fracture energy relative to pure mode I (DCB test) and to pure mode II (ENF test), respectively. G_I and G_{II} are, respectively, the specific fracture energy relative to mode I and mode II components in mixed mode.
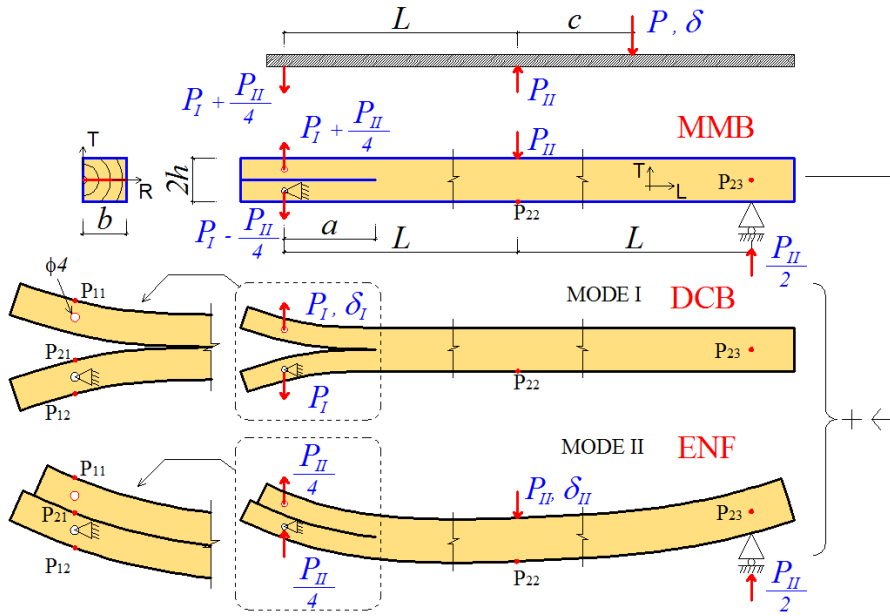
Figure 2.19: Schematic representation of MMB test [130]

The form of the mixed mode fracture criterion defined in eq. (2.16) is now widely accepted, values of exponents m and n remain however a questionable point. In a sake of

simplicity of eq. (2.16), these coefficients are recommended to be selected as integer and reasonable values. Three different fracture criteria, named as linear ($m = 1; n = 1$), semi-quadratic (elliptic) ($m = 1; n = 2$) and quadratic ($m = 2; n = 2$), are usually considered in order to describe the fracture envelop of mixed mode resistances to crack growth of wood [40, 96, 176].

2.2.8 Influence of the strain rate on fracture property of wood

Moreover, the fracture property of wood is also influenced by the strain rate. According to Conrad et al. 2003 [36], a sub-critical crack growth can take place at low strain rates, whereas at higher strain rates due to the shorter times, the higher fracture toughness values result is obtained.

Using Compact Tension (CT) specimen of dry Norway spruce with four loading rates (0.05, 1, 50 and 200 mm/min), Vasic et al. [168] reported that the fracture toughness decreased at both slow static (e.g. 1 mm/min) and high loading rate.

Based on these studies of many factors on fracture behavior of wood such as: geometry, size effect..., it can be generally concluded that fracture toughness (K_{Ic}) or fracture energy (G_F or G_{Rc}) are not an intrinsic material property.

2.3 The crack growth in viscoelastic media

2.3.1 Time-dependent crack growth

Owing to the context of the increasing timber structure in the world, the crack growth in wood are attracting widespread interest. However, the main problem is related to the viscoelastic theory applied to the fracture analysis. It is generally accepted that the viscoelastic deformation in wood may cause an additional energy concentration in the crack tip vicinity leading to crack propagation [20, 34, 46, 48, 50, 146, 147]. On the other term, the energy release rate involve with the time (i.e., the time-dependence crack growth).

2.3.2 Application of LEFM in viscoelastic media

Depending on the assumption of the process zone at the crack tip and the mechanical properties of material, various studies have been performed to analyze the viscoelastic fracture [19, 20, 34, 46–48, 50, 62, 90, 91, 106, 146, 147]. In LEFM, the concept of the stress intensity factor (local approach), the crack opening displacement approach [21, 154] or the correspondence principle [62, 146, 147] can be used when the creep strains in the process zone are considered negligible. By introducing of a fictive time, Schapery [146, 147] suggested that a viscoelastic creep crack growth could be described using the theory of equilibrium cracks in brittle fracture [8]. In addition, for the concept of the energy release rate (global approach), based on the path-independent J-integral, the steady state creep

analogue is proposed [148]. However, for high moisture conditions, these methods do not deal with the viscous dissipation in local energy balance equations.

2.3.3 The path-independent viscoelastic integral method

To determine the energy release rate in an orthotropic linear viscoelastic material, Dubois et al. [34, 46–48, 50] proposed a new invariant surface integral $G\theta_v$ method. In their study, two new concepts were proposed: *strain* intensity factor represented to the viscoelastic *strain* field and *crack opening* intensity factor represented to viscoelastic *displacement* field. Due to the viscoelastic properties, the *strain* intensity factor and the *crack opening* intensity factor evolve versus time. Based on the relation between these new factors from the progress of the crack tip, the energy release rate depending on the time is evaluated. The equation in the $G\theta_v$ method will be presented in the next paragraphs.

Besides the $G\theta_v$ method, another development of the viscoelastic integral J_{ve} method is proposed and can be directly defined in function of each deformation mechanisms in the total viscoelastic deformation [106]. In addition, the viscoelastic integral J_{ve} method can be applied to the case with the presence of initial strain or residual stress (but not both) in finite element modeling.

On the basis, the invariant integral $G\theta_v$ and J_{ve} methods are principally similar and based on the energy concept (global approach): the energy balance principle is applied for all equilibrium states in the structure. Compared to the global approach, the stress intensity factor or the crack opening displacement at the crack tip in the local approach do not evolve versus time. That can be considered as a limitation of the local approach. In the following paragraphs, the path-independent viscoelastic integral method (both $G\theta_v$ and J_{ve} methods) is presented.
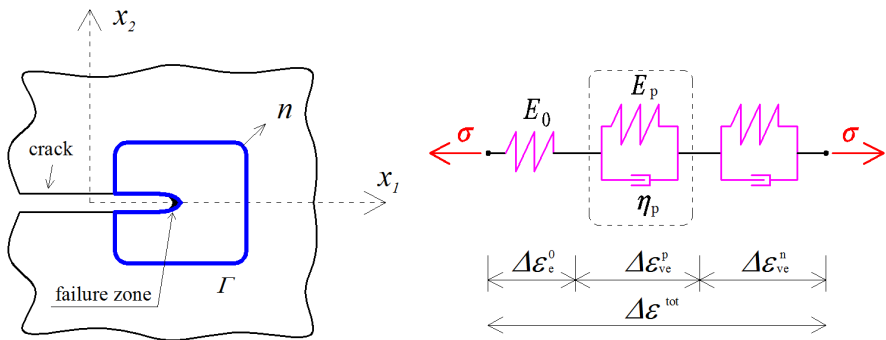
Figure 2.20: The path-independent viscoelastic integral and Kelvin Voigt branches

Based on the J-integral (eq.2.2 in Section 2.1.1), the energy release rate G_v^p corresponding to p^{th} branch of the Kelvin-Voigt model, as shown in Figure 2.20) for both methods is given as:

$$G_v^p = J_v^p = \int_{\Gamma}(W^p.n_j - \sigma_{ij}^p.n_j.\frac{\partial u_i^p}{\partial x_j})d\Gamma \tag{2.17}$$

where p indicates the pth branch as shown in Figure 2.20. W^p is the elastic strain energy density. σ_{ij}^p is the elastic stress (from traction) tensor component. Γ represents a generic path around the crack tip, n is the component of the outward normal to Γ along the crack direction. $\frac{\partial u_i^p}{\partial x_j}$ is the derivative of the displacement field corresponding to the direction of crack growth x_i. The elastic strain energy density W^p corresponding to p^{th} branch can be written as:

$$W^p = \sigma_{ij}^p.\varepsilon_{ij}^p \tag{2.18}$$

Based on the superposition of each deformation mechanism (Fig. 2.20), the total deformation ε and the total energy release rate $G(a,t)$ due to viscoelastic deformation are given as eqs.(2.19) and (2.20), respectively.

$$\varepsilon = \varepsilon^0 + \sum_{p=1}^{N} \varepsilon^p \tag{2.19}$$

$$G(a,t) = G_{ve}J_{ve} = J_e^0 + \sum_{p=1}^{N} J_v^p \tag{2.20}$$

2.3.4 Crack growth process in viscoelastic media

The crack propagation criterion in a viscoelastic medium is generally developed from the one in elastic materials [14, 34, 46–48, 50, 88–90, 123]. Hence, the crack propagation in wood under a constant loading is assumed to start when the total energy release rate reaches the critical value obtained under the monotonic test (quasi-static test) for mode I.

$$G_I(a,t) = G_F \tag{2.21}$$

where G_F is the critical fracture energy of material, obtained from the LEFM approach.

In eq.(2.21), the energy release rate $G_I(a,t)$ is obtained corresponding to a failure zone at the crack tip. According to Dugdale [51], the size of this established failure zone is the crack extension in LEFM (Fig. 2.21). With an assumption of a constant failure stress σ_y, the size α of this failure zone is given as:

$$\alpha = \frac{1}{\pi} \left(\frac{K_I^{\sigma_y}}{\sigma_y} \right)^2 \tag{2.22}$$

where $K_I^{\sigma_y}$ is the stress intensity factor, σ_y is the yield stress of the material (critical strength for wood).

From eq.(2.22), the stress increasing gives a localized plastic behavior in the process zone at the crack tip, but it can not be physically defined the actual mechanical state in this zone (see Fig. 2.21). Schapery [146, 147] proposed a model, which is more realistic, to determine the size α_{ve} of the process zone in a viscoelastic medium. By assuming that a localized damaged zone at the crack tip takes place in a thin strip zone with a length
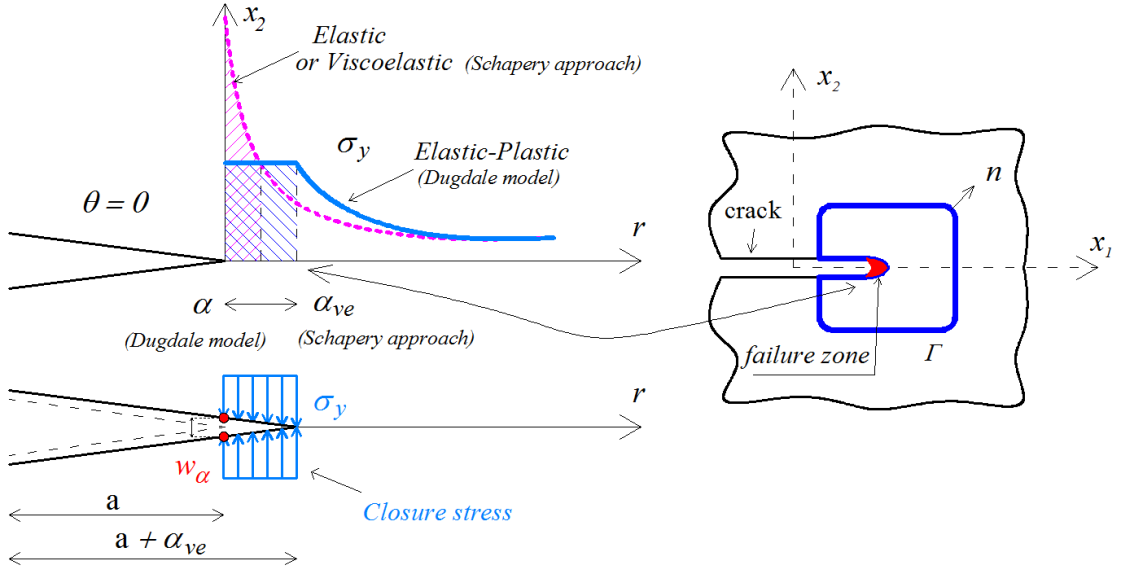
Figure 2.21: Schematic representation of the progressive crack-lip decohesion with a crack tip plastic zone ($\alpha = \alpha_{ve}$)

α_{ve} (Fig. 2.21): the mechanical behavior may be nonlinear and rate-dependent. The size α_{ve} is, using a form Dugdale assimilation α, given as:

$$\alpha_{ve} = \frac{\pi}{2} \left(\frac{K_I^{\sigma_y}}{\sigma_y} \right)^2 \tag{2.23}$$

According to Schapery [146, 147], the material is damaged in the process zone which is not considered as viscoelastic; outside this zone, the material is considered as linear viscoelastic. Beside Schapery's work, Knauss [89, 90] or Nielsen [123] solved the Griffith problem [64] for a finite thickness process zone assuming a linear viscoelastic behavior.

Schapery [146, 147] and Nielsen [123] proved that the displacement at the boundary of the process zone in viscoelastic media may be determined by using the elastic solution, but by replacing the elastic compliance with a viscoelastic creep compliance. The viscoelastic compliance may be selected by a simple power law and an amplified scale time. However, the simple power-law relationship may be practically not valid with experiment when the time scale is large [123, 146, 147]. To overcome this difficulty, it is necessary to take into account a complex viscoelastic model (e.g., rheological models presented in Section 1.3.3), however this task is impossible with the analytical analysis.

Schapery [146, 147], Nielsen [123], Dubois et al. [46–48, 50] reported that crack growth process in viscoelastic media can be described by a progressive decohesion of crack lips in the process zone. Based on this, the crack propagates with a crack extension δa with the same size α of the failure zone (i.e., $\delta a = \alpha$). The energy release rate associated with the crack extension is related to the work (energy) required to close the crack in this zone. Note that, within the framework of LEFM, for wood, the plastic zone α at the crack tip is sufficiently small (confined within the singularity dominated zone).

Using an assumption of constant stress σ_m in the size α of the process zone (Dugdale model), Schapery [146, 147] proposed that the dissipated energy $G_I(a, t)$ can be simplified as:

$$G_I(a, t) = \sigma_m w_\alpha \tag{2.24}$$

where w_α is the crack opening displacement.

Moreover, the critical fracture energy can be written as:

$$G_F = \sigma_m w_c \tag{2.25}$$

where w_c is the critical crack opening displacement

Based on eqs.(2.24) and (2.25), the crack propagation criterion can be simply reduced as:

$$w_\alpha = w_c \tag{2.26}$$

From eq. (2.26), if the critical crack tip opening displacement w_c is constant over a wide range of crack growth rates, the crack speed can be evaluated by solving the following problem in function of the time given as:

$$w_\alpha(a + \alpha, \Delta t) = w_c \tag{2.27}$$
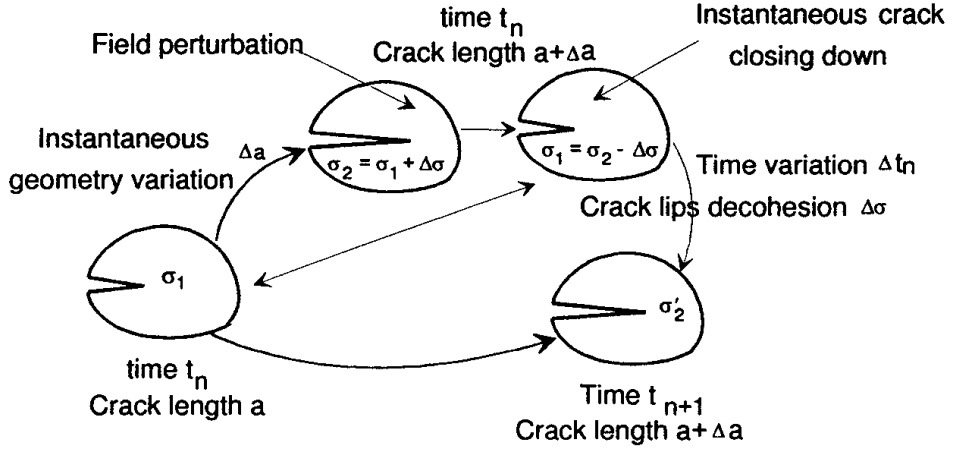
Figure 2.22: Viscoelastic crack growth algorithm. Extracted from [48]

Based on eqs.(2.26) and (2.27), the crack growth in a viscoelastic medium has been studied through the analytic solution [14, 88, 91, 123, 123, 146, 147] and the finite element method [34, 46–48, 50]. For FEA, a viscoelastic crack growth algorithm, as shown in Figure 2.22, is proposed by Dubois et al. [34, 46–48, 50] by considering the process zone followed the Dugdale model or the Schapery model. In Figure 2.22, when the crack propagates during viscoelastic calculation process, it is required a projection of the mechanical field (stress and strain) from the configuration (with the crack length a) to the

new configuration (with the new crack length $a + \Delta a$) in order to conserve the mechanical history and to use it later.

2.3.5 Coupling thermo-hygro mechanical and viscoelastic behavior

The coupling mechanical and thermal loads in wood is also analyzed. To take into account the effects of mechanical and thermal loadings, Moutou Pitti et al. [118, 140, 141] proposed an T-integral based on conservative law: a combination of real, virtual displacement fields, and real, virtual thermal fields. Moreover, in the same time, the analytical formulation is a bi-linear form of free energy density. According to the generalization of Noethers method, the application of Gauss Ostrogradskis theorem combined with curvilinear cracked contour, the T-integral is given as:

$$
\begin{aligned}
A &= \int_\Gamma \tfrac{1}{2} [\sigma_{ij,k}^v u_i - \sigma_{ij}^u v_{i,k}] n_j d\Gamma \\
&+ \int_\Gamma \tfrac{1}{2} [\gamma \Delta T_{,j}(v_k - \psi_k) - \gamma \Delta T(v_{k,j} - \psi_{k,j})] n_j d\Gamma \\
&+ \int_L \tfrac{1}{2} [p v_{1,1} - q v_{2,1}] dx
\end{aligned}
\tag{2.28}
$$

In eq.(2.28), the first integral is the classical term of the T-integral which represents the effect of mechanical loads applied far from the crack. σ_{ij}^u and σ_{ij}^v are stress tensor components deduced from the real and virtual displacement field, respectively. The second integral represents the effect of thermal loading induced by temperature variation ΔT and a virtual displacement field ψ. γ is a real coefficient function of elastic material properties. The third integral represents the effect of pressures p and q applied perpendicularly to the crack edges (along the axis x_1 and x_2, respectively, in Figure 2.20).

2.4 Conclusion

This chapter presents an overview about fracture mechanics: LEFM approach is generally applied for brittle materials when considering the sharp crack tip; for the quasi-brittle material, due to the development of FPZ ahead of the crack tip, equivalent LEFM is successful to apply by means of R-curve. Cohesive crack model is developed and frequently used in order to mimic the damaged material in FPZ.

This chapter has also presented fracture properties of wood under various effects such as: the density, the moisture, the temperature, the size effect, the geometry, the mixed-mode, the loading direction, the deformation rate... The time-dependent crack growth phenomenon in viscoelastic media (such as wood) is presented. Based on the energy concept, the path-independent viscoelastic integral methods have been developed. The temperature effect integrated in the viscoelastic integral has been presented.

Owing to the context of climatic change, the changes of moisture in wood have to be considered on the fracture analysis. On the other hand, the main problem is given as the coupling hygro-mechanical state in the material as well as the variation of the structure configuration due to the crack propagation.

Wood is gradually accepted as a quasi-brittle material due to the development of the FPZ (i.e., micro-cracking and fiber bridging zone). Moreover, the material in FPZ is more or less rapidly damaged due to the sensibility of the varying moisture. Consequently, it is necessary to study the quasi-brittle fracture behavior of wood (such as R-curve and cohesive law) in function of the moisture and the crack growth under the variation of humidity.

In the next chapter, a detail description of the studied material, the experimental methodology is presented. Fracture test in mode I are performed on Maritime Pine at a wide range of moisture contents in order to characterize the fracture response of the material under humidity variation.

Chapter 3

Experiments and Methods

In this chapter, detailed descriptions of the studied specimen, the experimental methodology as well as the study of the fracture behavior are presented. As this thesis focuses on the fracture behavior taking into account the moisture influence, two different tests in mode I (on TL system) at a wide range of MC are performed on Maritime pine specimens:

- monotonic (quasi-static) tests under different moisture contents
- creep tests: crack propagation under RH variation

The term "fracture test" used later in this thesis will be then understood either as monotonic test or as creep test. The method and the objectives of each test are different. The monotonic tests allow obtaining fracture properties of wood at different MC (from dry to saturated moisture), which next allow to determine the R-curve and cohesive zone model parameters of the material. Using obtained fracture properties from these first tests, the creep tests are carried out to characterize the fracture response of the material under moisture content variation. Moreover, Weibull distribution function for each CZM parameter at all moisture is also determined.

3.1 Material and specimen

3.1.1 Maritime pine (Pinnus Pinaster)

Elastic properties of the Maritime pine used in this thesis are given in Table 3.1.

Table 3.1: Elastic properties of Maritime pine at 12% MC [68]

$E_L^{12\%}$ (MPa)	$E_T^{12\%}$ (MPa)	$E_R^{12\%}$ (MPa)	$G_{LT}^{12\%}$ (MPa)	$G_{LR}^{12\%}$ MPa)	$G_{TR}^{12\%}$ (MPa)	ν_{TL}	ν_{RL}	ν_{TR}
13 500	1054	1657	1 094	1 032	84	0.425	0.385	0.315

Thanks to elastic properties given in Table 3.1, the variation of the elastic properties of the Maritime pine versus moisture is used in FEA introducing the following Guitard's

relations [68]:

$$
\begin{cases}
E_L(MC) & = & E_L^{12\%} & [1 - 0.015(MC - 12)] \\
E_T(MC) & = & E_T^{12\%} & [1 - 0.030(MC - 12)] \\
E_R(MC) & = & E_R^{12\%} & [1 - 0.030(MC - 12)] \\
G_{LT}(MC) & = & G_{LT}^{12\%} & [1 - 0.030(MC - 12)] \\
G_{LR}(MC) & = & G_{LR}^{12\%} & [1 - 0.030(MC - 12)] \\
G_{TR}(MC) & = & G_{TR}^{12\%} & [1 - 0.030(MC - 12)]
\end{cases}
\tag{3.1}
$$

The unit of MC in eq.(3.1) is %.

According to Guitard's results [68], moisture seems to have a negligible effect on Poisson's ratios. Hence, the Poisson's ratios is consequently considered to be moisture independent in this thesis.

3.1.2   mTDCB specimen

The chosen specimen must enable a sufficient crack length to observe the influence of the humidity on the fracture behavior of wood. Thus, from the monotonic fracture tests, we can obtain a stable crack process, a constant energy release rate as well as a stable force in the post-peak regime. The constant energy release rate is determined versus the crack length; this rate is needed to separate the effect of the mechanical loading and of the humidity environment on the wood specimen. The stable force in the post-peak regime also gives stable crack growth during the creep tests under the humidity variation.

Fracture tests in mode I have been frequently carrying out on different specimen types: Double Cantilever Beam (DCB) and modified Tapered Double Cantilever Beam (mTDCB) [18, 39, 128, 175, 177]. Several authors [42, 172, 175] have used the DCB to determine the fracture energy. From both theoretical and experimental point of view, they found that the energy release rate increases in function of the crack length. The crack propagation on the DCB specimen occurs irregularly; moreover, the crack growth can be 'sudden' after the post-pic which can be explained by the significant evolution of the energy release rate versus the crack length. Undoubtedly, this evolution depends on the specimen geometry: this is why a inclined profile of the DCB specimen - called Tapered Double Cantilever Beam (TDCB) - is interesting and suitable in the mentioned context.

In this thesis, the TDCB geometry has been modified, the obtained specimen is called modified Tapered Double Cantilever Beam (mTDCB). The dimensions of the mTDCB are presented in Figure 3.1a. The volume of the mTDCB specimen is about 98.6 cm^3. This geometry assures best compromise between the stable crack growth in the inclined zone 1 of the specimen as well as sufficient resistance. Moreover, the specimen dimensions assure quasi-constant force in the post-pic regime during the monotonic test. In addition, thanks to these stability, creep tests under humidity variation can be performed. The

crack evolution will only depend on MC variations and on viscosity. If the sizes of a specimen are greater than these dimensions (e.g., 1.5 times), the creep tests can not be carried out due to the limit of the experimental equipment such as the oven, the volume of the climatic room, the imposed load level...

Figure 3.1: (a) Dimension of mTDCB specimen, (b) cutting position of mTDCB specimens for the 2 fracture tests

Fracture tests in mode I are performed on TL system on Maritime pine specimens with a density of $515 \pm 40\ kg/m^3$ at 12% MC. Furthermore, specimens used in the two different fracture tests are twin extracted from the same piece of wood (Fig. 3.1b) to assure more similar properties between them. The strength of the specimen (b) is supposed to be the same as the one of specimen (a). Hence, the strength of the specimen (a) is used to determine the stress level applied on the specimens (b) during the creep test.

The initial crack length ($a_0 = 40\ mm$) is machined with a band saw (thickness 1 mm) and prolonged a few millimeters with a sharp blade which is sliced along the notch tip to initiate the crack. The crack front alignment is verified by measuring the initial crack length on both sides of the specimen. The ligament length (d) of the specimen is 225 mm. The ratio $\alpha_0 = a_0/d$ is 0.18 in order to obtain the fully development of the FPZ in the zone 1.

3.1.3 Preparation and conditioning of specimens

In this thesis, the specimen preparation is the subject to rigorous and precise process such as an accurate alignment of the specimen in the tangential and longitudinal directions of wood as well as a selection of wood pieces which are hold only very large radius of growth rings, homogeneity of the growth rings, thickness, etc...

Three hundred specimens were prepared for the monotonic tests and one hundred

for the creep tests. Specimens were stored into climatic boxes at ten different Relative Humidities. Specimens can reach desired moisture such: 5%, 8%, 10%, 12%, 15%, 18%, 20%, 22%, 25% and 30% in about 2 weeks to 10 weeks. Each climatic box was conditioned under a constant temperature (20^0C). The equilibrium moisture content of the specimen was obtained when its weight between 2 days did not change, with a reasonable tolerance (0.05 g). The balance used in this thesis is limited to 200 g with a measurement error tolerance of 0.01 g. The mean weight of mTDCB specimens at 12% MC is about 51 g.

Before and after the fracture test, the weight and dimensions of each specimen were measured. The moisture loss during the test was small and its effects are negligible.

3.2 Fracture tests in mode I

In this section, two different tests in mode I at a wide range of moisture contents are presented:

- monotonic (quasi-static) tests under different MCs in order to determine the strength (maximal load), the R-curve and cohesive zone model parameters.
- creep tests under RH variation in order to investigate the fracture response of the material under the humidity variation.

3.2.1 Monotonic (quasi-static) tests under different moisture contents

A mechanical tension-compress machine (with total capacity of 50 kN) is used to perform the fracture test. A load cell with the capacity of 500 N has been installed and the cross head displacement rate was controlled. The loading points displacements were obtained with an optical sensor (for the moisture 8%, 12%, 30%) and with a camera (for the moisture 5%, 10%, 15%, 18%, 20%, 22%, 25%). The use of two different displacement measurements has no special reason except that a technical problem has occurred: the optical sensor has been in-operate after 3 moisture contents tests.

In order to minimize the viscoelastic effects and to avoid the change of the moisture content during the fracture tests, the complete quasi-static fracture of the specimen for each moisture was obtained in 3 ± 1 min. Therefore, the velocity of the imposed displacement was 1 mm/min for MC lower than 22% and 2 mm/min for higher MC. During experimental tests, load/displacement data was recorded to calculate the fracture energy (acquisition frequency of 10 Hz). The obtained experimental data necessary to determine the resistance curve and to identify the parameters of the cohesive zone model, which will be presented in the section 3.3.1 and 3.3.2, respectively.

3.2.1.1 Tests with an optical sensor

Figure 3.2 presents the monotonic test device using an optical sensor. In this system, the displacement at the loading points is evaluated from the difference between locations of two targets placed on the loading axis which are on the upper and on the lower fibers of the specimen (Fig. 3.2). During the fracture test, the upper target is followed by the optical sensor. The applied load and the displacements are stored and calculated by a computer connected directly to the tension-compressive machine.
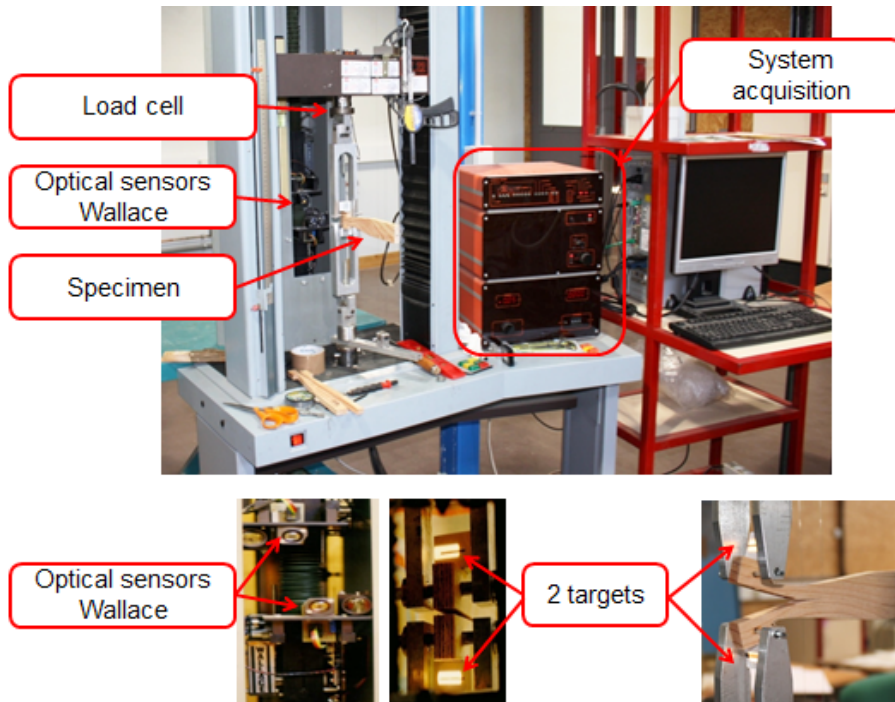
Figure 3.2: Experimental setup for monotonic tests using an optical sensor

3.2.1.2 Tests with a camera

The monotonic test device using a camera is described in Figure 3.3. The aim of the system is to follow the displacements of two loading points P_1, P_2 and of two other points O_1, O_2. Displacements P_1 and P_2 allow determining the displacement to be used in the load-displacement curve; the displacements O_1 and O_2 give the evolution of the crack opening displacement. A integrated software allows to determine the movement of all point by analyzing the images captured by the camera. To support the analysis process, the distance P_0P_1 is 10 mm and constant.
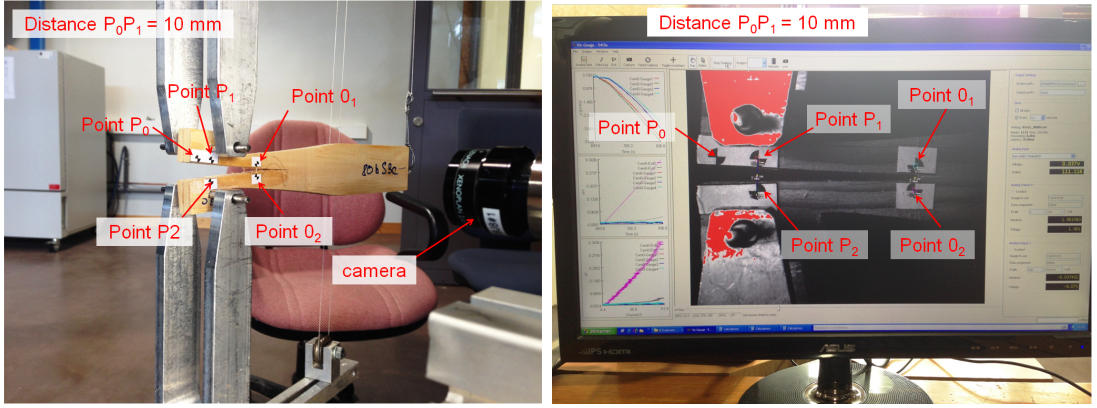
Figure 3.3: Experimental setup for monotonic test using a camera

3.2.2 Creep tests: crack propagation under RH variations

A new test equipment was designed for the creep tests to study separately the effect of RH and temperature (Fig. 3.4). To begin, only tests with humidity variation and a quite stable temperature have been performed.
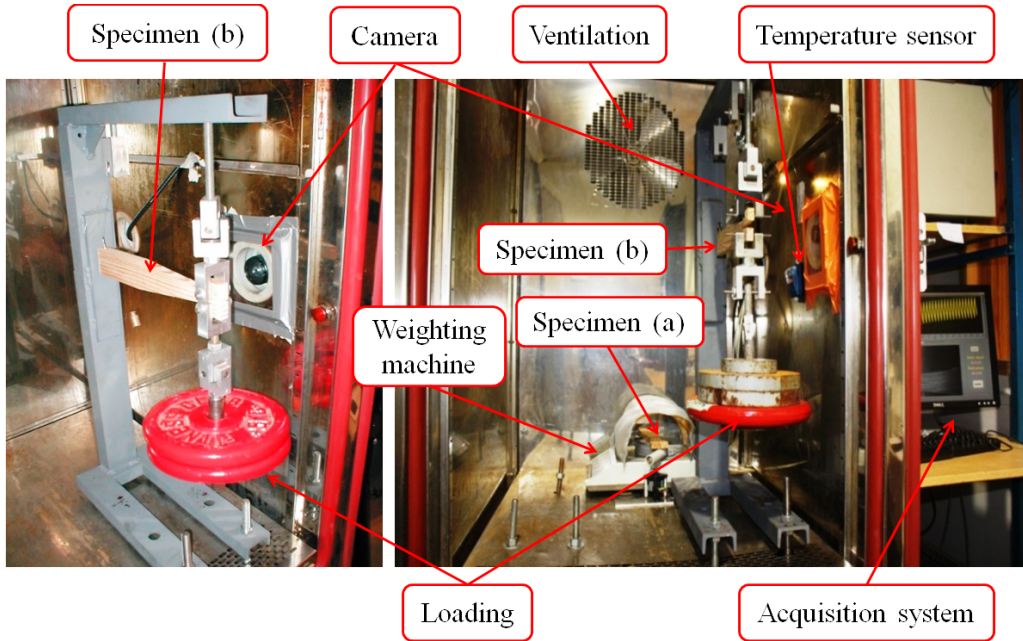
Figure 3.4: Experimental setup for creep test inside the climatic box using a camera

Creep tests were carried out inside a controlled climatic environment where the temperature was kept constant at $T = 20^oC$ while the RH has varied from 40% to 90% every 12 hours (Fig. 3.5). Note that the testing specimen (b) was conditioned at the same moisture content as the specimen (a) under monotonic test (Fig. 3.1b). During the test, the specimen (a) is put on a balance in the climatic box to obtain the average weight evolution (Fig. 3.4). The stress level SL for the creep test will vary from 0.55 to 0.90 of the strength of the specimen (a) (i.e., P_{max}) (Fig. 3.5).
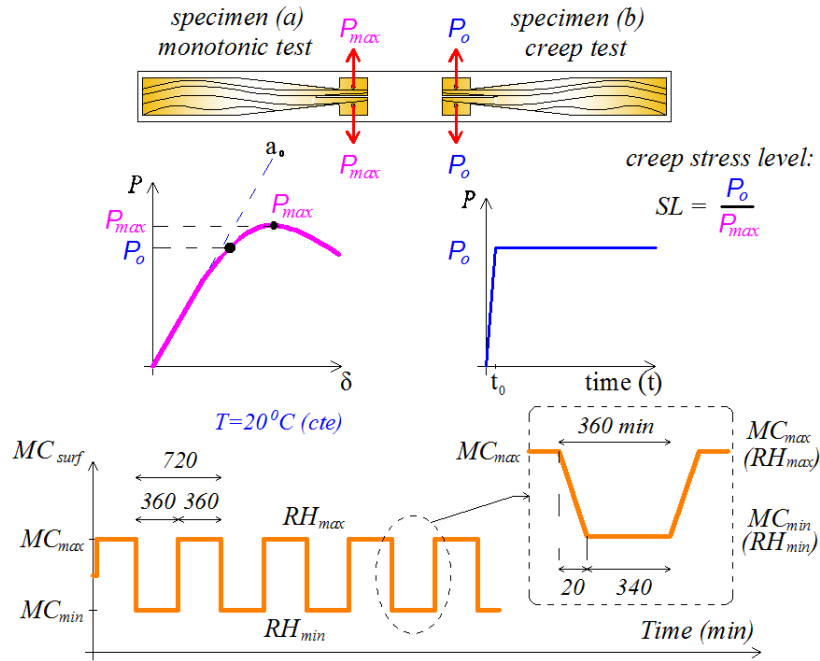
Figure 3.5: Experimental setup for creep tests in the climatic box

A digital camera is also employed to follow the evolutions of the loading point displacement and of the crack opening displacement of specimen during the creep test (1 image every 10 min) (Figs. 3.4 and 3.6).
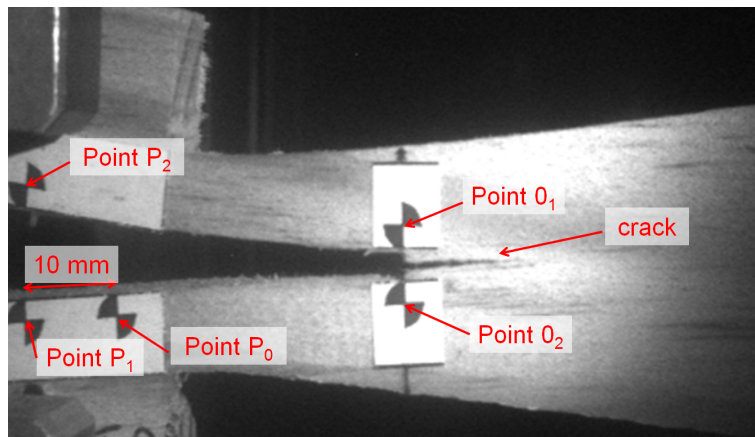
Figure 3.6: Setup to obtain the loading points displacement and the crack opening displacement from an image processing analysis during the creep test

The experimental data obtained from the creep test under humidity variations will be analyzed and used to compare numerical analysis results which will be presented in Chapter 6.

3.3 Fracture behavior characterization

Based on the experimental results obtained from the monotonic tests under 10 moisture contents, the resistance curve was evaluated and cohesive parameters were identified.

3.3.1 Resistance curve

As mentioned in Section 2.2, due to the presence of a non-negligible FPZ ahead of the crack tip in a quasi-brittle material such as wood, the visibility of the crack tip from the image is not clear during fracture tests. Hence, LEFM cannot be directly applied to estimate the fracture energy in wood material [12, 40, 41, 115, 176]. In this section, based on the equivalent LEFM approach, the crack growth criterion (Resistance curve) was estimated from the experimental data obtained from the monotonic tests (see Section 3.2.1).

3.3.1.1 Equivalent LEFM approach

In the equivalent LEFM (eq.LEFM) approach, the eq.LEFM crack length a_{eq} is defined as the crack length of a specimen considered as linear elastic everywhere which gives the same compliance as the one of the experimental cracked specimen with its FPZ [12, 111, 113, 115] (see Section 2.1.2).

In order to verify if the equivalent LEFM can be applied to describe the fracture behavior of wood at several MC, loading-unloading cycles were performed. Typical cycles at 12% MC (Fig. 3.7) and at 30% MC (Fig. 3.8) show that the initial linear elastic behavior for a given cycle (i.e., cycle 4) corresponding to the secant compliance which can be determined from the unloading point of the previous cycle (i.e., cycle 3). As a result, the eq.LEFM can be applied at all moisture contents. For high moisture (e.g., 30% MC), an inelastic displacement (due to a viscous deformation) occurs and lead specimen more damaged. In this case, the eq.LEFM can become inapplicable after some cycles (after cycle 4, Fig. 3.8) due to the inelastic displacement because the time for one fracture test excess the recommended time for the fracture test (i.e, $3 \pm 1 \ min$).

During the monotonic tests, the experimental load P and the loading point displacement δ were measured, but the evolution of the real crack length of the specimen (Figs. 3.3 and 3.4) can not be directly obtained due to the development of the FPZ. As a result, the eq.LEFM approach is used to determine the equivalent crack length. This approach also requires the knowledge of the compliance evolution versus the equivalent crack length a_{eq}. Not experimentally obtained for all a_{eq} values, the compliance must be determined through analytic or finite element methods. In this thesis, to obtain compliance function, the numerical method is used and detailed in the next section. To simplify, the equivalent crack length a_{eq} is noted a in following sections.
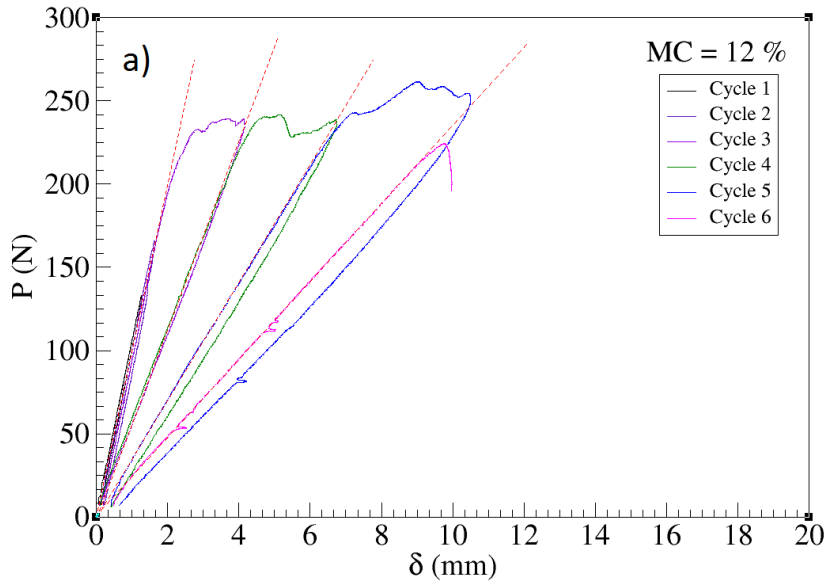
Figure 3.7: Typical load-unloading cycles test at 12% MC. The straight lines correspond to the initial stiffness of each cycles
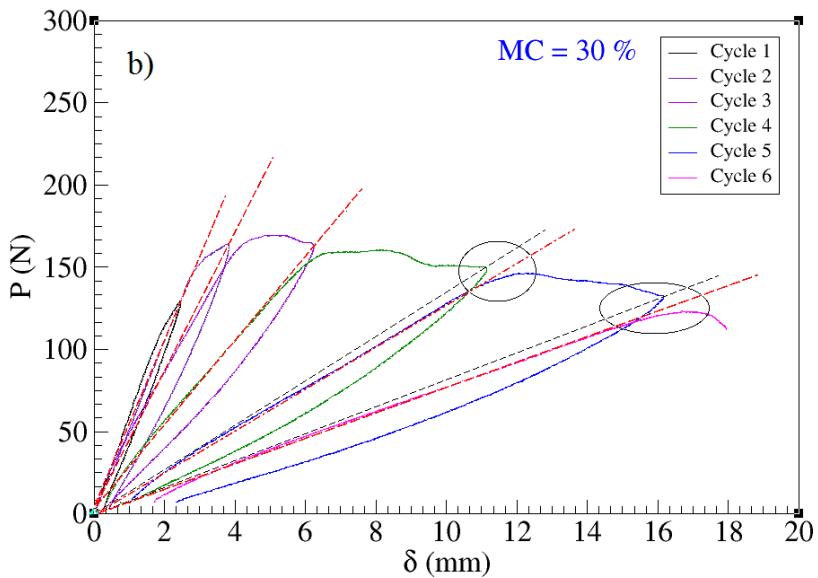
Figure 3.8: Typical load-unloading cycles test at 30% MC. The straight lines correspond to the initial stiffness of each cycles

3.3.1.2 Numerical compliance function versus the crack length

In this study, the compliance is determined by the finite element method. $Cast3M$ is used as the finite element code. In the FEA, the mesh of the specimen is modeled with the full geometry (Fig. 3.9), so the compliance function takes into account effects due to the crack tip rotation and due to the deflection caused by shearing at the crack tips. In addition, the compliance resulted from displacements at loading points obtained in 2D analysis is more accurately determined than the 1D modeling (beam theory) due

to the complex geometry of the mTDCB specimen (i.e., the inclined profile). The effect of the mesh size is also studied (Fig. 3.9). The theoretically crack path of the specimen is supposed to be along the ligament and rectilinear (parallel to the longitudinal direction of the specimen).
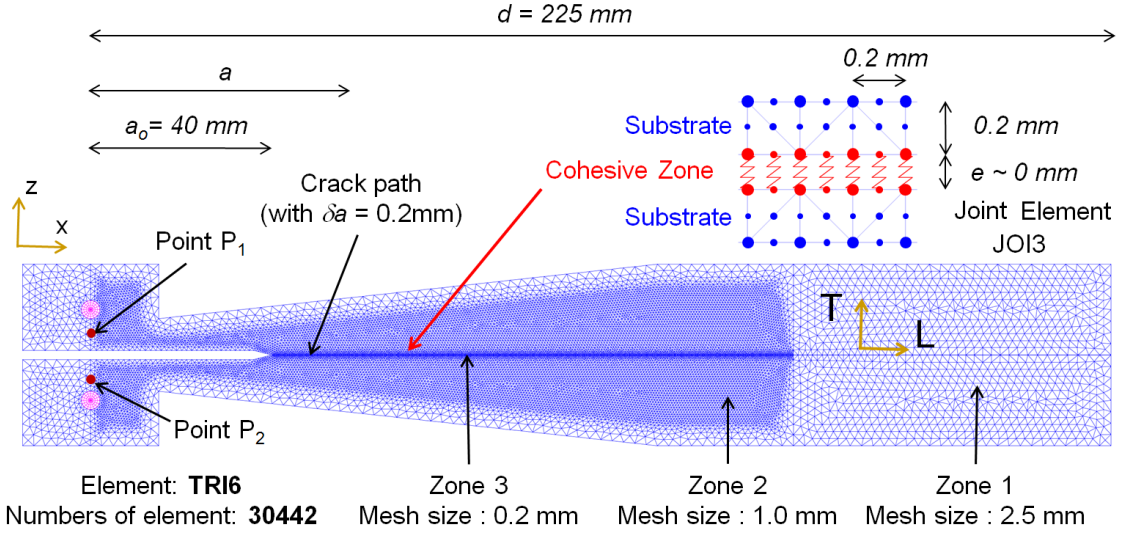
Figure 3.9: Specimen mesh. Note that joint element (for the cohesive zone) is not used when determining the compliance function

For each moisture, based on the elastic properties of the wood material in Table 3.1 and eq.(3.1), the evolution of the specimen compliance is computed as:

$$\lambda(a) = \delta/P \tag{3.2}$$

where δ is the difference between the two loading points P_1 and P_2 displacements (Fig. 3.9). The numerical compliance functions obtained for all MCs are summarized in Table 3.2.

Table 3.2: Polynomial coefficients of the numerical compliance function $\lambda(\alpha, MC)$ obtained by FEA using elastic properties given in Table 3.1. $\lambda(\alpha, MC)$ in mm/N, ($\alpha = a/d$).

$$\lambda(\alpha, MC) = C_7\alpha^7 + C_6\alpha^6 + C_5\alpha^5 + C_4\alpha^4 + C_3\alpha^3 + C_2\alpha^2 + C_1\alpha + C_0$$

MC	C_7	C_6	C_5	C_4	C_3	C_2	C_1	C_0
5%	187.5	-380.2	301.5	-113.4	20.47	-1.361	0.868	0.1033
8%	198.5	-401.3	317.4	-119.1	21.46	-1.428	0.910	0.1087
10%	206.7	-416.9	329.1	-123.3	22.19	-1.478	0.941	0.1127
12%	215.6	-433.8	341.8	-127.8	22.97	-1.531	0.974	0.1170
15%	230.7	-462.2	363.0	-135.4	24.28	-1.620	1.029	0.1241
18%	248.3	-495.2	387.4	-144.1	25.78	-1.723	1.091	0.1323
20%	261.9	-520.5	406.0	-150.6	26.91	-1.802	1.137	0.1385
22%	277.2	-548.9	426.9	-158.0	28.18	-1.891	1.188	0.1454
25%	304.7	-599.4	463.8	-171.0	30.41	-2.050	1.276	0.1574
30%	369.3	-717.0	549.1	-200.8	35.55	-2.429	1.464	0.1839

Moreover, the numerical evolution of the crack opening displacement versus the crack length is obtained and presented in Table 3.3. The chosen of 7 degree of polynomial function $\lambda(\alpha, MC)$ or $w(\alpha, MC)$ is need for a good determination of the R-curve and the cohsive parameters. Because the estimation of the equivalent crack length is sensitive to the compliance value.

Table 3.3: Polynomial coefficients of the crack opening displacement function $w(\alpha, MC)$ obtained by FEA using elastic properties given in Table 3.1. $w(\alpha, MC)$ in mm, $(\alpha = a/d)$.

$$w(\alpha, MC) = W_7\alpha^7 + W_6\alpha^6 + W_5\alpha^5 + W_4\alpha^4 + W_3\alpha^3 + W_2\alpha^2 + W_1\alpha + W_0$$

MC	W_7	W_6	W_5	W_4	W_3	W_2	W_1	W_0
5%	174.0	-362.8	299.5	-120.3	23.80	-1.480	0.3967	0.00152
8%	184.8	-384.4	316.9	-127.1	25.17	-1.585	0.4205	0.00162
10%	192.8	-400.5	329.7	-132.2	26.19	-1.664	0.4381	0.00169
12%	201.7	-418.0	343.7	-137.7	27.30	-1.752	0.4575	0.00178
15%	216.7	-447.7	367.3	-147.0	29.17	-1.903	0.4902	0.00191
18%	234.3	-482.4	394.8	-157.8	31.36	-2.085	0.5285	0.00208
20%	247.9	-509.1	415.9	-166.1	33.05	-2.227	0.5579	0.00221
22%	263.4	-539.4	439.8	-175.5	34.96	-2.393	0.5913	0.00235
25%	291.2	-593.6	482.4	-192.3	38.38	-2.697	0.6508	0.00261
30%	357.0	-720.7	581.9	-231.3	46.42	-3.447	0.7891	0.00321

3.3.1.3 Correction of the numerical compliance function

The experimental compliance function $\lambda_{exp}(a)$ and the numerical one $\lambda(a)$ obtained from the FEA are different one from each other. This difference is usually due (i) to approximations of the elastic properties used in FEA compared to experimental ones; (ii) to slight geometrical imperfections of the experimental specimen compared to the theoretical (numerical) one. These differences can also be linked to an experimental crack path which is not perfectly straight and aligned in the expected direction as was assumed numerically.

In order to establish the correspondence between the numerical compliance function $\lambda(a)$ and the experimental one $\lambda_{exp}(a)$, a multiplicative correction factor ψ has been proposed by Morel et al. [115]. The multiplicative factor ψ is given in eq.(3.3).

$$\lambda_{exp}(a) = \psi\, \lambda(a) \tag{3.3}$$

The multiplicative correction factor ψ is applied at all the crack length $(a \geq a_0)$. Note that, the multiplicative correction factor ψ can be estimated only for the initial crack length a_0 (as written in eq.(3.4)) associated to the perfect elastic material without damage state. Because at this state, the FPZ does not exist, the eq.LEFM length of the

initial crack corresponds exactly to its actual length.

$$\psi = \frac{\lambda_{exp}(a_0)}{\lambda(a_0)} \tag{3.4}$$

In this study, the preparation of the specimen to be used in fracture tests is subjected to a rigorous and precise process (see Section 3.1.3) and hence the contribution of the geometric imperfections to the correction factor ψ is assumed to be negligible. As a result, it seems reasonable to attribute this scatter to the difference between the actual elastic properties and those used in the FEA (i.e., the natural modulus scattering: E_L, E_T and G_{LT}).

In this way, a study of the influence of scatter in elastic properties on the compliance function $\lambda(a)$ as well as on the multiplicative correction factor ψ is proposed and detailed in next section.

3.3.1.4 Influence of scatter in elastic properties on $\lambda(a)$ and ψ

Firstly, the influence of the elastic properties scattering on $\lambda(a)$ is studied. We define orthotropic factors as $f_a = E_T/E_L$; $f_b = G_{LT}/E_L$. The variation of the elastic properties is studied as a function of:

- the modulus E_L ($f_a = $ cte, $f_b = $ cte),
- the modulus E_T through the orthotropic factor $f_a = E_T/E_L$ ($E_L = $ cte, $f_b = $ cte),
- the modulus G_{LT} through the orthotropic factor $f_b = G_{LT}/E_L$ ($E_L = $ cte, $f_a = $ cte)

According to Sih [152] for orthotropic materials, the effective elastic modulus E_I^* and the strain energy release rate $G(a)$ corresponding to mode I are written in eqs. (3.5) and (3.6), respectively.

$$
\begin{aligned}
E_I^* &= \left[\sqrt{\frac{S_{22}}{S_{11}}} + \frac{2S_{12} + S_{33}}{2S_{11}} \right]^{-\frac{1}{2}} \left[\frac{S_{11}S_{22}}{2} \right]^{-\frac{1}{2}} \\
&= \left[\sqrt{\frac{E_L}{E_T}} - \nu_{LT} + \frac{1}{2}\frac{E_L}{G_{LT}} \right]^{-\frac{1}{2}} \left[\frac{1}{2E_L E_T} \right]^{-\frac{1}{2}} \\
&= E_L \left[\sqrt{\frac{1}{fa}} - \nu_{LT} + \frac{1}{2}\frac{1}{fb} \right]^{-\frac{1}{2}} \left[\frac{1}{2fa} \right]^{-\frac{1}{2}} \tag{3.5}
\end{aligned}
$$

$$
\begin{aligned}
G(a) &= \frac{K_I^2(a)}{E_I^*} \\
&= \frac{1}{\sqrt{2}E_L} \left[\sqrt{\frac{1}{fa}} - \nu_{LT} + \frac{1}{2}\frac{1}{fb} \right]^{\frac{1}{2}} \left[\frac{1}{\sqrt{fa}} \right] K_I^2(a) \tag{3.6}
\end{aligned}
$$

where: $S_{11} = 1/E_L$, $S_{22} = 1/E_T$, $S_{12} = -\nu_{LT}/E_L$ and $S_{33} = 1/G_{LT}$.

Based on eq.(3.6), we obtain the compliance function $\lambda(a)$ from the energy release rate $G(a)$ as:

$$\lambda(a) = \int_{a_0}^{a} \frac{2b}{P^2} G(x) dx$$

$$= \frac{1}{\sqrt{2}E_L} \left[\sqrt{\frac{1}{f_a}} - \nu_{LT} + \frac{1}{2} \frac{1}{f_b} \right]^{\frac{1}{2}} \left[\frac{1}{\sqrt{f_a}} \right] \int_{a_0}^{a} \frac{2b}{P^2} K_I^2(x) dx \qquad (3.7)$$

A "virtual" compliance $\lambda_{virt}(a)$ is estimated from the FEA by varying elastic properties of wood around the reference value given in Table 3.1 (at 12%MC) such as:

$$\begin{cases} 12000 \ MPa \le E_L \le 15000 \ MPa & \text{with } E_L = 13500 \text{ MPa at } 12\% \text{ MC} \\ 0.070 \le f_a \le 0.085 & \text{with } f_a = 0.0775 \text{ at } 12\% \text{ MC} \\ 0.072 \le f_b \le 0.090 & \text{with } f_b = 0.0810 \text{ at } 12\% \text{ MC} \end{cases} \qquad (3.8)$$

By changing the elastic properties values in eq.(3.8), we consider the virtual $\lambda_{virt}(a)$ as the experimental compliance $\lambda_{exp}(a)$ presented in eq.(3.3). The compliance $\lambda(a)$ is estimated from the FEA by the reference value given in Table 3.1 (at 12% MC). The function $\lambda(a)$ is considered as the numerical compliance function, presented in eq.(3.3).

Based on eq.(3.3), the theoretical multiplicative correction factor ψ between the numerical compliance $\lambda(a)$ and the virtual compliance $\lambda_{virt}(a)$ is given as:

$$\psi^*(a) = \frac{\lambda_{virt}(a)}{\lambda(a)} \qquad (3.9)$$

At the initial crack length a_0, the multiplicative correction factor ψ is defined as:

$$\psi = \frac{\lambda_{virt}(a_0)}{\lambda(a_0)} \qquad (3.10)$$

Figure 3.10 shows the relation of the elastic properties values (E_L, E_T and G_{LT}) with the virtual compliance function $\lambda_{virt}(a)$ and with the multiplicative correction factor ψ.

As shown in Figure 3.10 and eq.(3.7), the compliance function $\lambda_{virt}(a)$ as well as the multiplicative correction factor ψ is mainly dependent on the modulus E_L than others (E_T and G_{LT}). Approximately, the correction factor ψ is linearly proportional to the longitudinal modulus E_L used to obtained the virtual compliance (Fig. 3.10b). Note that the obtained relation of the compliance function and the elastic properties in FEA is in agreement with those obtained in previous studies [39, 40, 176, 177] which are based on the analysis performed from the beam theory (for different geometries).
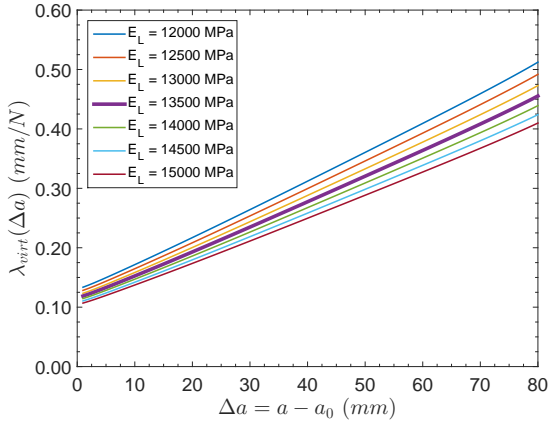
(a) Influence of E_L on $\lambda_{virt}(a)$
(with $f_a = 0.0775$, $f_b = 0.0810$)
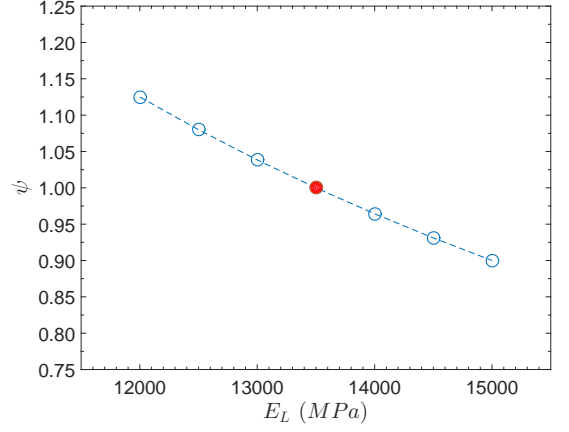
(b) Relative between ψ and E_L
(with $f_a = 0.0775$, $f_b = 0.0810$)
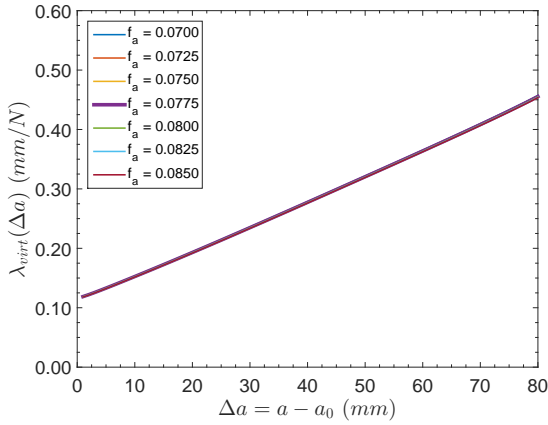
(c) Influence of E_T on $\lambda_{virt}(a)$
(with $E_L = 13500$MPa, $f_b = 0.0810$)
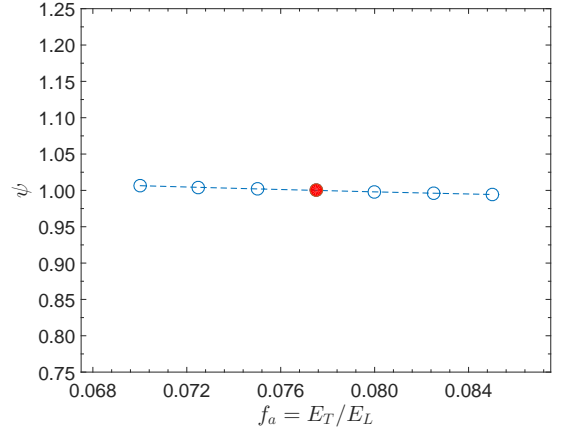
(d) Relative between ψ and E_T
(with $E_L = 13500$MPa, $f_b = 0.0810$)
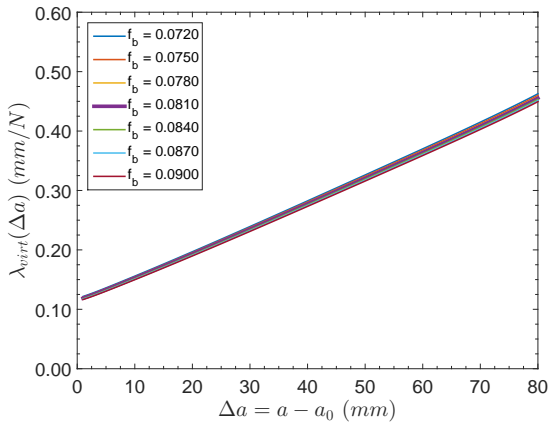
(e) Influence of G_{LT} on $\lambda_{virt}(a)$
(with $E_L = 13500$MPa, $f_a = 0.0775$)
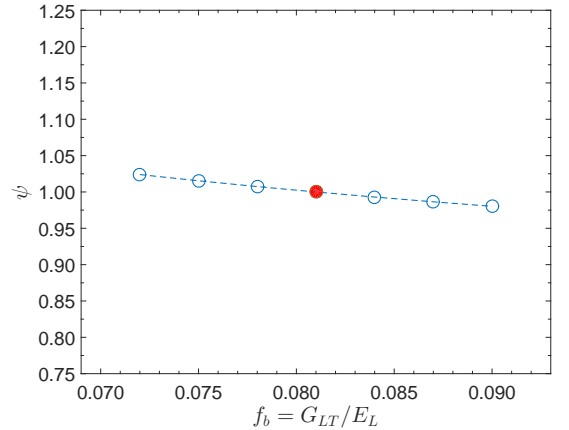
(f) Relative between ψ and G_{LT}
(with $E_L = 13500$MPa, $f_a = 0.0775$)

Figure 3.10: Influence of the elastic properties on the virtual compliance $\lambda_{virt}(a)$ and on the multiplicative correction factor ψ ($= \lambda_{virt}(a_0)/\lambda(a_0)$). At 12% MC (red points), the reference values are $E_L = 13500$ MPa, $f_a = E_T/E_L = 0.0775$ and $f_b = G_{LT}/E_L = 0.0810$

Secondly, in order to study the influence of the varying elastic properties of wood on the multiplicative correction factor ψ at all crack lengths $(a \geq a_0)$, a function $\theta_\psi(a)$, which is an error generated function (of the multiplicative correction factor) versus the crack length a, is given in eq.(3.11).

$$\theta_\psi(a) = \frac{\psi^*(a)}{\psi} \tag{3.11}$$

Figure 3.11 shows the error generated function $\theta_\psi(a)$ obtained from the variations of E_L, f_a and f_b in ranges previously defined. As shown in Figure 3.11, values of the error generated function $\theta_\psi(a)$ induced by the variation of E_L is smaller than those with E_T (i.e., f_a) and G_{LT} (i.e., f_b) variations. As expected intuitively, the difference of $\theta_\psi(a)$ in case of variation of f_a and f_b remain lower than 0.7%. While $\theta_\psi(a)$ in case of variation of E_L is close to zeros (i.e., the difference of the error generated function is approximately zero). As a consequence, a multiplicative correction factor ψ (as the proposed in eqs.(3.3) and (3.4), i.e., $\psi = \psi(a_0)$) is relevant to correct the effect of the elastic properties scattering.

Based on the results presented in Figure 3.10 and Figure 3.11, the multiplicative correction factor ψ (eq.(3.3)) can be successfully applied so far as $\theta_\psi(a)$ at 12% MC remains lower than 0.7%. The $\theta_\psi(a)$ obtained at other MC is similar to the one obtained at 12% MC. If E_T (i.e., f_a) and G_{LT} (i.e., f_b) both change, $\theta_\psi(a)$ obtained for each moisture is still lower. Consequently, with these error values (lower than 0.7%), the application of the multiplicative correction factor $\psi = \psi(a_0)$ (i.e., $\psi(a) \approx \psi$) seems acceptable for the compliance function in the FEA (no crack length dependence and no orthotropic factors influence on ψ). The value of ψ obtained for all tested specimens at 10 moisture are summarized in Table 4.1 (Section 4.2).
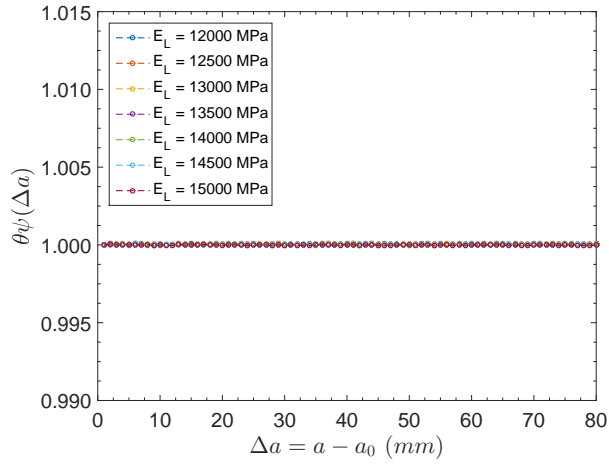
(a) Relation between $\theta_\psi(a)$ and E_L
(with $f_a = 0.0775$, $f_b = 0.0810$)
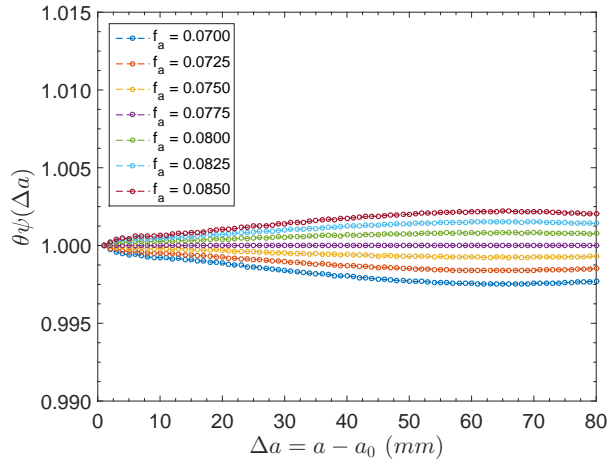
(b) Relation between $\theta_\psi(a)$ and E_T
(with $E_L = 13500$ MPa, $f_b = 0.0810$)
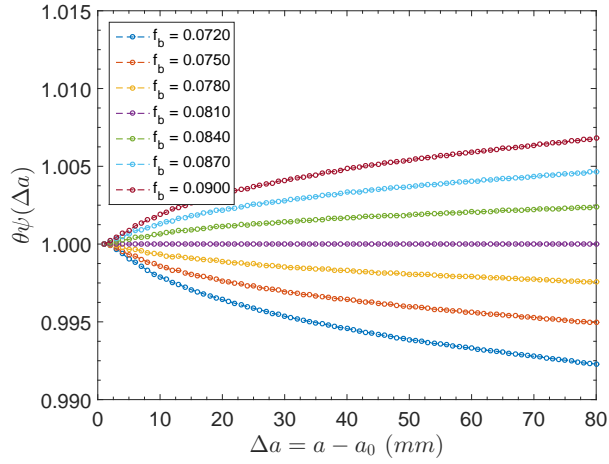
(c) Relation between $\theta_\psi(a)$ and G_{LT}
(with $E_L = 13500$ MPa, $f_a = 0.0775$)

Figure 3.11: Influence of the elastic properties on the error generated function $\theta_\psi(a)$. Note that, at 12%MC, the reference values are $E_L = 13500$ MPa, $f_a = E_T/E_L = 0.0775$ and $f_b = G_{LT}/E_L = 0.0810$

3.3.1.5 Determination of the R-curve parameters

From the monotonic fracture tests, the resistance to the crack growth $G_R(a)$ is usually estimated from the energy release rate $G(a)$. In practice, for a given point of the load-displacement curve (P, δ), the first step of the computation procedure of $G_R(a)$ consists in estimating the crack length a from the experimental compliance $\lambda = \delta/P$ on the basis of the compliance function $\lambda(a)$.

When the crack length a is obtained from the compliance function $\lambda(a)$, the resistance to the crack growth $G_R(a)$ must coincide with the energy release rate $G(a)$. $G(a)$ is determined from the expression:

$$G_R(a) = G(a) = \frac{P^2}{2b} \frac{\partial \lambda(a)}{\partial a} \tag{3.12}$$

where P is the applied load, b is the specimen thickness and $\lambda(a)$ is the compliance function.
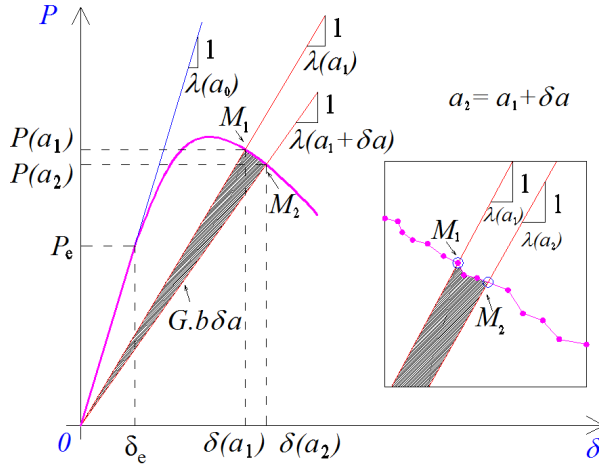
Figure 3.12: Sketch of the elastic strain energy release rate

In this thesis, the strain energy release rate is directly estimated from experimental results (load-displacement curve). Let us consider two consecutive points M_1 $(\delta(a_1), P(a_1))$ and M_2 $(\delta(a_2), P(a_2))$ of the load-displacement curve (Fig. 3.12). The elastic strain energy δE (dashed zone), released during a crack growth extension $\delta a = a_2 - a_1$, can be expressed as:

$$\delta E = \delta W - \delta U \tag{3.13}$$

where δW represents the external work of the applied load and δU corresponds to the complementary energy due to the applied load P as given in eqs.(3.14) and (3.15), respectively.

$$\delta W = W_2 - W_1 = \frac{P(a_1) + P(a_2)}{2} [\delta(a_2) - \delta(a_1)] \tag{3.14}$$

$$\delta U = U_2 - U_1 = \frac{1}{2} P(a_2)\delta(a_2) - \frac{1}{2} P(a_1)\delta(a_1) \tag{3.15}$$

73

The eq.(3.13) can be rewritten as:

$$\delta E = \delta W - \delta U = \frac{1}{2}P(a_1)\delta(a_2) - \frac{1}{2}P(a_2)\delta(a_1) \tag{3.16}$$

The energy released during an infinitesimal crack extension δa (shaded area in Figure 3.12) is obtained by dividing terms δE by the infinitesimal crack surface $\delta A = b\delta a$ such as:

$$G(a) = \frac{\delta E}{\delta A} = \frac{1}{b\delta a}\left[\frac{1}{2}P(a_1)\delta(a_2) - \frac{1}{2}P(a_2)\delta(a_1)\right] \tag{3.17}$$

As suggested in [112, 115], based on the eq.LEFM approach, the small equivalent crack extension δa is often approximately equal to 1% of the the initial notch length, (i.e. $\delta a = 0.4 \ mm$ for mTDCB specimen in this thesis).

As mentioned in the section 2.1.3, in the quasi-brittle material, the characteristic equivalent crack length Δa_c (in R-curve) is proportional to the characteristic length of the fracture process zone (i.e., l_{coh}^c). Therefore, in the following, the influence of the moisture on the FPZ is also studied. To incorporate these complex phenomena acting on the FPZ, cohesive zone models are frequently used in numerical analysis, which is impossible to perform with the analytical analysis.

3.3.2 Cohesive zone model

3.3.2.1 Bi-linear approximation of the softening function

In the cohesive zone model (CZM), several traction-separation laws have been employed to model fracture in wood [10, 39, 45, 113, 162, 173]. According to Morel et al [113], a bi-linear approximation function better exhibits the fracture behavior of the quasi-brittle material (i.e., concave function). Moreover, this bi-linear function exhibits the coupling phenomenon of the micro-cracking energy dissipation and of the crack-bridging energy dissipation (Fig. 3.13). This function is characterized by four parameters:

- the critical cohesive energy G_f (J/m^2),
- the critical crack opening displacement w_c (mm),
- the tensile strength f_t (MPa),
- the energy distribution (characterized by the ratio $G_{f\mu}/G_f$).

The critical cohesive energy G_f corresponds to the sum of the energies $G_{f\mu}$ and G_{fb} which are usually interpreted as the energies related to the micro-cracking and the crack bridging cohesive behaviors, respectively [113, 162]. Based on the stress distribution in the cohesive interface (Fig. 3.13), the characteristic length of the FPZ l_{coh}^c is defined as the distance between two positions of two integration points A and C in which: at the point A, the stress is equal to the tensile strength f_t and at the point C, the crack opening reaches the w_c (stress-free). Moreover, the length of the cohesive zone associated to the
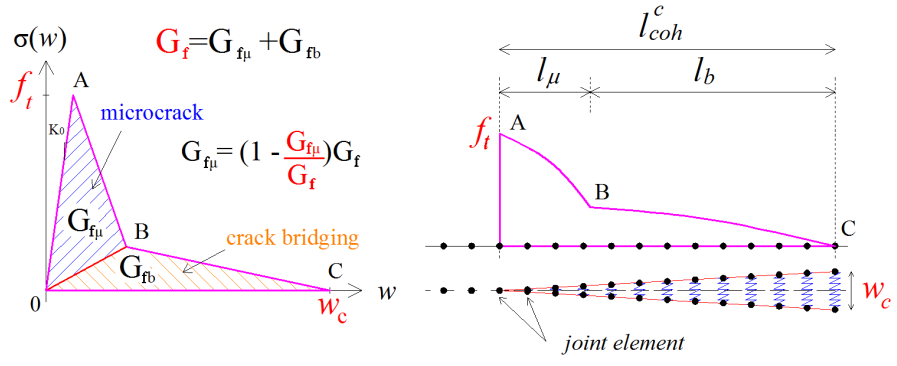
Figure 3.13: Bi-linear softening function in cohesive zone model

micro cracking zone l_μ is the distance between two positions of two points A and B. At the point B, the stress corresponds to the intersection of the micro crack and the crack bridging in the cohesive law (Fig. 3.13).

Consequently, the bi-linear softening softening (Fig. 3.13) is used in this study in order to analyze the fracture behavior of wood under moisture effect. Before the identification of cohesive law parameters and the characteristic length of the FPZ versus moisture, the effect of the mesh size and the cohesive joint stiffness on the FEA is preliminary studied.

3.3.2.2   Effect of mesh size and initial stiffness of the cohesive joint

A simplified 2D modeling of the mTDCB specimen (at 12% MC) is performed. The dimensions and the mesh size were illustrated in Fig. 3.1 and Fig. 3.9, respectively. The mechanical properties of wood substrates were presented in Table 3.1. The parameters of the bi-linear law of the cohesive joint are: $G_f = 598$ (J/m^2), $w_c = 0.6$ (mm), $f_t = 3.85$ (MPa), $G_{f\mu}/G_f = 0.58$ [128].

3.3.2.2.a   Mesh size effect

Five cases were studied and presented in Table 3.4. Figure 3.14 shows the mesh size effect of the cohesive zone on the load-displacement curve (a), on the energy release rate curve (b) and on the stress distribution (c) for these 5 cases.

Table 3.4: Mesh size (in mm) chosen for the 5 studied cases. $l^e_{joint}(mm)$ is the size of the joint elements in the cohesive zone; $l_{sub}(mm)$ is the size of the elements in the wood substrate (Fig. 3.9)

case	l^e_{joint}	l_{sub}
1	0.1	2.0
2	0.2	2.5
3	0.5	3.5
4	2.0	6.0
5	3.0	8.0

(a) on the load-displacement curve

(b) on the energy release rate curve

(c) on the stress distribution (x_r denotes
the abscissa along the cohesive interface
considered from the initial notched a_0)
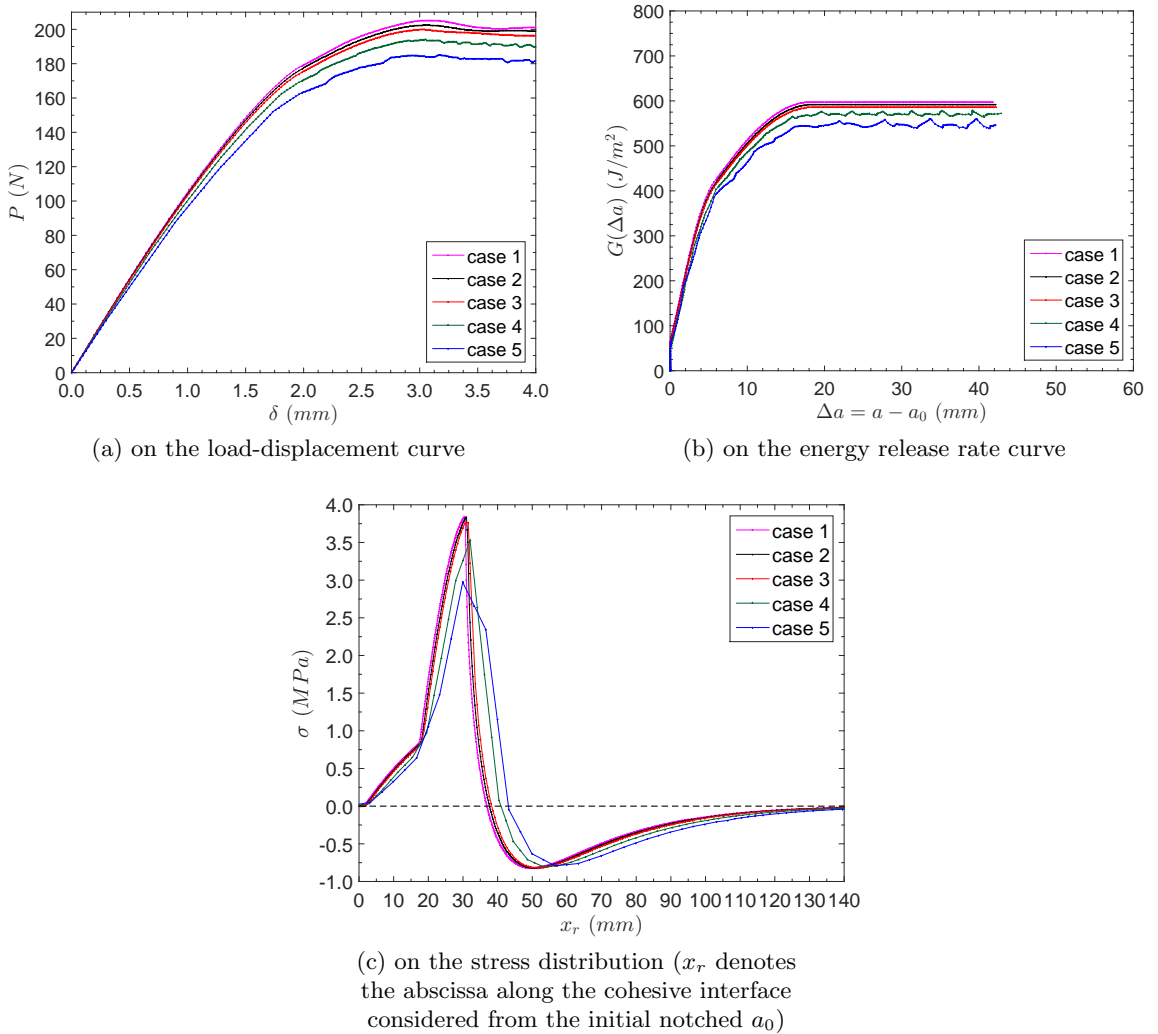
Figure 3.14: Influence of the mesh size for 5 cases (Table 3.4)

In Figure 3.14, we observe a good convergence of curves obtained with mesh size cases 1 to 3, which well corresponds to the recommendation of a mesh refinement with CZM. From the results obtained with mesh sizes cases 4 and 5, one observes that perturbations appearing in the load-displacement curve as well as in the energy release rate curve. These two last cases do not describe well the fracture behavior and the macroscopic response. In this thesis, fully aware of the mesh size effect, the specimen will be modeled with the mesh size of 0.2 mm in the cohesive zone and of 2.5 mm in the wood substrate (case 2).

3.3.2.2.b Effect of the initial stiffness of the cohesive joint

In nonlinear fracture mechanics, the initial stiffness K_o of the cohesive joint (as illustrated in Fig. 3.13) plays a important role on the elastic response of the structure. In LEFM the elastic response (characterized by a macroscopic initial stiffness R_o) allows to distinguish two phenomena:

- non damage (with the actual macroscopic stiffness equal to R_o);
- damaged (with the actual macroscopic stiffness smaller than R_o).

The initial specimen stiffness R_o is defined as $R_o = P_e/\delta_e$, with the load P_e and the displacement δ_e corresponding to the end phase of the macroscopic elastic response of the specimen (where the crack begins to propagate, in the framework of the LEFM approach). The initial stiffness K_o influences the crack initiation phase of structure through the initial specimen stiffness R_o.

In order to study the effect of the initial cohesive stiffness K_o on the initial specimen stiffness R_o, five cases were analyzed in Table 3.5. Figure 3.15 shows the effects of K_o on the load-displacement curve and on initial specimen stiffness R_o.

Table 3.5: Initial cohesive stiffness K_o chosen for the 5 studied cases

case	K_o (MPa/mm)
1	$K_o = 1.E6$
2	$K_o = 1.E5$
3	$K_o = 1.E4$
4	$K_o = 2.E3$
5	$K_o = 1.E3$

(a) on the load-displacement curve

(b) on the normalized initial specimen stiffness
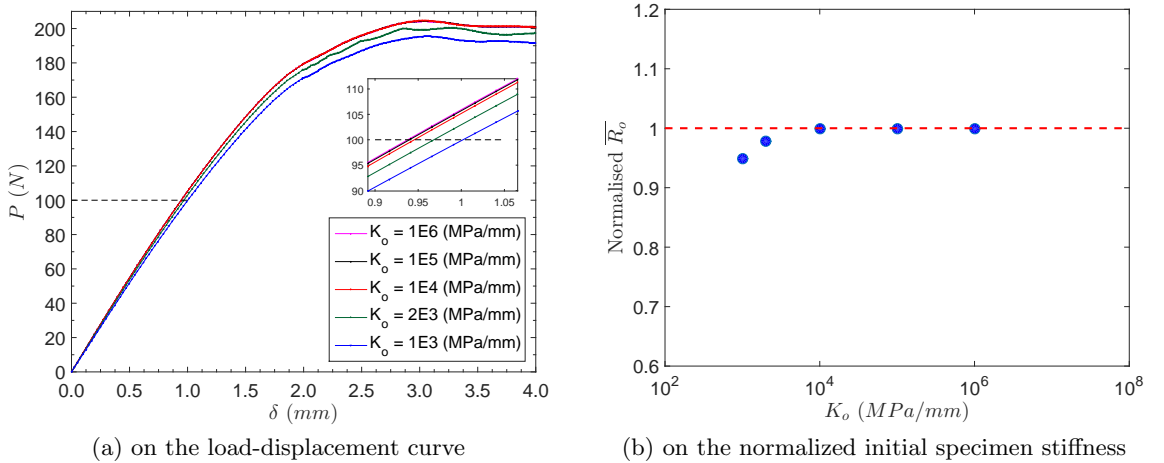
Figure 3.15: Influence of the initial cohesive stiffness for 5 cases

In Figure 3.15b, the normalized stiffness $\overline{R_o}$ is defined by the ratio of the initial specimen stiffness (corresponding to K_o obtained from NLFM) and the initial specimen stiffness R_o obtained from LEFM approach (in which specimen is modeled with elastic properties everywhere and without the joint element). In this study, the load value of 100 N was considered to be obtained at the end of elastic response of the specimen.

In Figure 3.15b, the results obtained with K_o equal or higher than $1.E4$ MPa/mm are close to 1 (i.e., corresponds to the analyzed case based on LEFM approach). Consequently,

in this thesis, the initial stiffness with $K_o = 1.E4$ MPa/mm (case 3) will be used in the cohesive zone model.

3.3.2.3 An identification procedure of cohesive parameters

As presented in the previous section, experimental R-curves were obtained from the load-displacement curve $(P-\delta)$. By fitting the experimental R-curve with an the analytical function $(G_R(\Delta a) = \dfrac{G_{Rc}}{\Delta a_c{}^\beta} \Delta a^\beta$, see eq.(2.4)), the R-curve parameters such as G_{Rc}, Δa_c and β are determined.
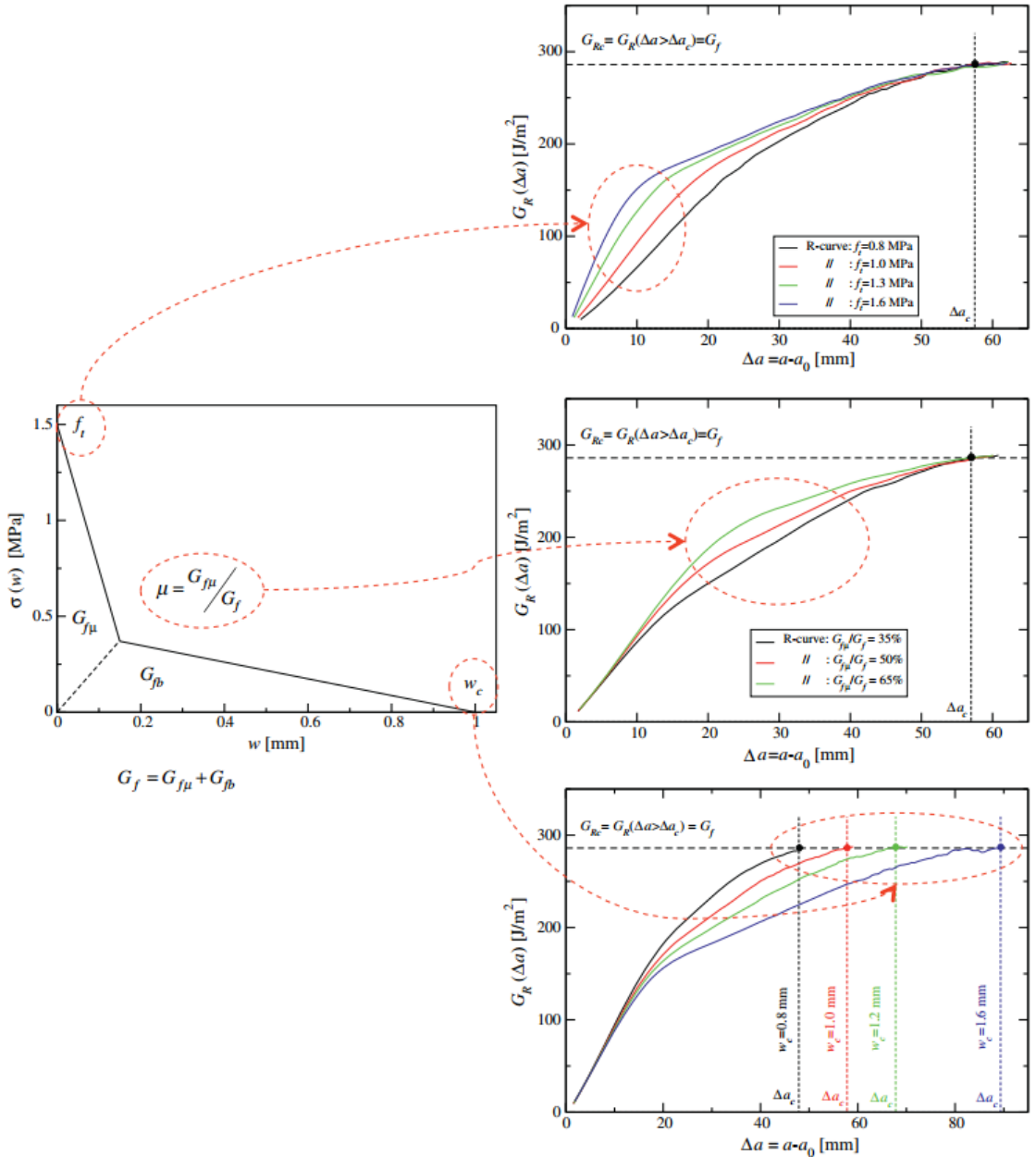
Figure 3.16: Sketch of the connections between the bi-linear function and the corresponding R-Curve [37]

Morel et al. [37, 113] showed a strong relation between the R-curve parameters and the bi-linear parameters in the CZM, which is applied for wood material (Fig. 3.16). Based on this relation, in order to save computation time and avoid the presence of the local minimum problem, an identification procedure of the cohesive law parameters within a reasonable accuracy, inspired by the one proposed by Morel et al. [113], is given:

- Step 1: the critical cohesive energy G_f is equal to the plateau resistance G_{Rc}: $G_f = G_{Rc}$.

- Step 2: an iterative process is carried out by changing the value of the critical crack opening displacement w_c until the numerical result $\Delta a_{c_{num}}$ matches the experimental result (i.e., $\Delta a_{c_{num}} = \Delta a_c$) within a reasonable accuracy. To reduce the computation time for w_c, the crack opening displacement w obtained from the experimental test (i.e., displacements of two points O_1 and O_2 as shown in Figure 3.3) is used as an initial value of w_c for the iteration procedure.

- step 3: an iterative process is carried out by changing the value of the tensile strength f_t until the numerical result $G_{R_{num}}$ matches the experimental result (i.e., $G_{R_{num}} = 0,25 G_f$) within a reasonable accuracy.

- Step 4: once the cohesive law parameters: G_f, w_c (characterizing the plateau of the R-curve) and f_t (corresponding to the initial part of the R-curve) have been determined, the cohesive energy ratio $G_{f\mu}/G_f$ is able to be determined. In this case, the parameter $G_{f\mu}/G_f$ mainly influences the central part of the R-curve.

By using the above procedure, the cohesive law parameters for 10 moisture contents were determined. The influence of moisture on each cohesive law parameter is analyzed and presented in the following chapter.

3.4   Conclusion

The influence of the moisture content on the fracture behavior (mode I) of Maritime pine has been investigated on mTDCB specimen. Monotonic tests have been carried out under a widely range of the moisture content in order to determine the R-curve and cohesive zone model parameters versus moisture. The creep tests were performed inside a climate room in order to characterize the fracture response of the material under RH variations.

A correction method to obtain the compliance function was proposed and developed without the necessity to determine the elastic modulus for each specimen. It is also not necessary to perform a monitoring during the propagation fracture test to measure the crack length which is very difficult to measure accurately in wood. The crack length is obtained based on the eq.LEFM approach (finite element calculation).

The results of R-curve and cohesive parameters versus moisture are presented in the next chapter. Moisture effect on each parameters in cohesive law and on the length of the FPZ are also analyzed in chapter 4.

Chapter 4

R-curve and cohesive parameters versus moisture content

Further to the chapter 3, in this chapter Resistance curves and cohesive zone parameters are studied in relation with moisture content. The critical energy release rate and the characteristic crack length are two important parameters to describe the resistance curve. The characterizations results of R-curve in function of the moisture are presented and analyzed. The relative energy release and the crack length at the peak load versus moisture are compared to those at the steady-state (at the plateau regime).

The moisture effect on each cohesive parameters is presented. Moreover, the characteristic lengths of the FPZ and of the micro-cracking zone are depending on moisture. Correlation of the cohesive parameters with moisture are also investigated.

From the performed large experimental campaign, a statistic approach is proposed to extract the main results of the study.

4.1   Crack growth under low and high moisture contents

In order to better understand the crack growth phenomenon at several moisture, this section aims to studying fracture mechanisms (i.e., micro-cracking and fiber bridging) in wood, based on experimental results obtained at 10 moisture contents.

At the begin of the loading, some short cracks appear around the crack tip due to a singular stress; when this stress reaches the tensile strength, fibers presenting short cracks are damaged and deformed but not broken (as shown in Figure 4.1). Through the damaged but not yet broken fibers around the crack tip, the stress can be transferred from the upper to the lower parts of the specimen but the transfer decreases when the deformation of the fibers increases. The stress transfer establishes an initial softening zone (FPZ) in the vicinity of the crack tip. On the other hand, the description of the last phenomenon corresponds to the same concept of the cohesive theory. We consider that the short cracks exist in the micro-cracking zone (Fig. 4.1).

When the load increases, the short crack will be more developed and fibers are more damaged. The fibers deformation level depends on the mechanical properties of wood. At this state, two different damaged zones exist: the micro-cracking and the fiber bridging zone (or macro-cracking zone) (Fig. 4.1).

In reality, even with recent adapted methods such as the digital image correlation technical (DIC), the topographic technical or with the criterion based on the width of short crack, we still do not have a feasible and robust method to clearly distinguish these two zones in experimental test. Nevertheless, we can overcome this difficulty thanks to the bi-linear function in CZM where the separation of two zones is described by the cohesive energy ratio $G_{f\mu}/G_f$ (see Section 3.3.2.1).
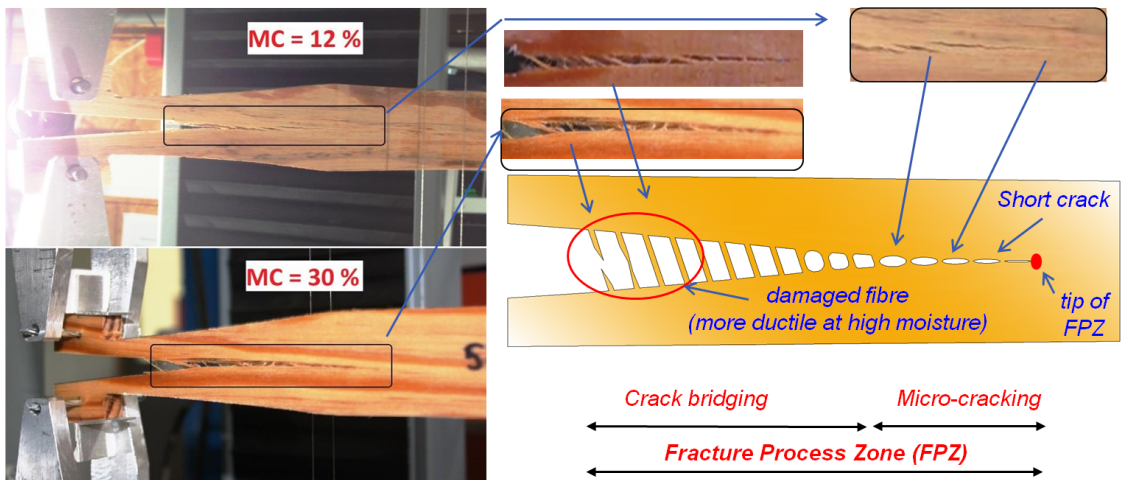
Figure 4.1: Schematic representation of a crack growth mechanism in wood

Using the proposed concept of the crack growth mechanism, we obtain interesting crack growth results from the monotonic experiments (load-displacement curves) at low and high moisture contents.

Under low moisture, load-displacement curves have several local minor peaks as shown in Figure 4.2. These peaks generally occur in the range of $3 - 7\ mm$ of the displacement, and occasionally up to $9\ mm$ or more. Conversely, at high moisture, load-displacement curves do not present any local peak (Fig. 4.2).
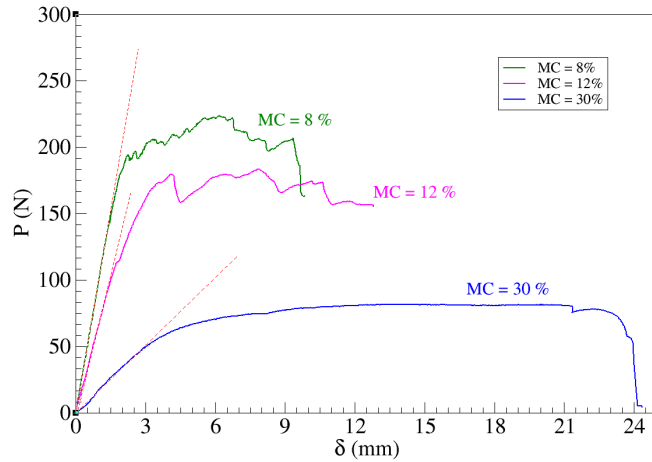
Figure 4.2: Typical load-displacement curves at 3 moisture (8%, 12% and 30%)

The minor peaks under low moisture may be caused by short cracks occurring ahead of the crack tip (observed at naked eye) during the fracture test. These short cracks are connected to the main crack while the locally high stress around the crack tip decreases. Note that, in this study, the term 'main crack' is defined as a crack where fibers are completely damaged (broken or failure) (i.e., stress-free).

As the macroscopic stiffness of specimen depends on the fracture mechanism that occurs at the fracture process zone. Due to the short cracks, the macroscopic stiffness of the specimen (rigidity) decreases and then sometimes leads to a local drop of the load (in case of imposed displacement in the fracture test).

Under the same imposed displacement increment in the fracture test, due to the decreasing of the macroscopic stiffness, the load increment corresponding to this displacement increment can be sightly decreased or increased or even stay constant if the fiber bridging mechanisms in FPZ is significantly important (fibers are slowly damaged). Conversely, if fibers are rapidly damaged and/or short cracks simultaneously occur, the load increment is significantly decreased.

As shown in Figure 4.2, local minor peaks (followed next by a drop of the load) at 8% MC occur more frequently than those at 12% MC. This observation suggests that the micro-cracking mechanism at low moisture is more important than at high moisture; conversely, the fiber bridging mechanism at high moisture is more significant than at low moisture.

In the following paragraphs, we would like to further describe the crack growth phenomenon at different moisture contents in order to better understand the evolution of the FPZ versus the moisture content and also to propose an adapted methodology to study the crack growth phenomenon. Figure 4.3 shows a schematic representation of the development of the fracture process zone at low and high moisture and summarizes the effect of the MC on the cohesive parameters (results developed in the session 4.3).
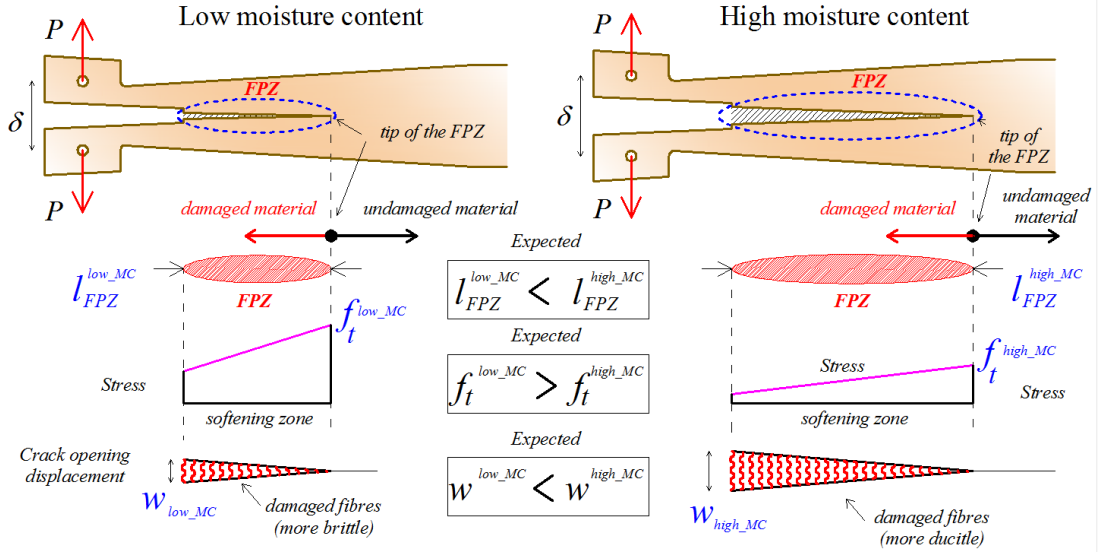
Figure 4.3: Schematic representation of the development of the FPZ at low and high moisture contents

By applying a loading at low and high moisture contents, a softening zone or FPZ develops in both cases (Fig. 4.3). The FPZ is limited by its tip; two different zones in the structure are distinguished: a damaged zone in the FPZ and an undamaged zone outside the FPZ.

Due to loading, the stress field in function of the crack opening in the FPZ (Fig. 4.3) is redistributed following a criterion: the maximal singular stress at the crack tip do not exceed the tensile strength f_t. As shown in Figure 4.3, it is expected that the tensile strength f_t at low moisture content is higher than at high moisture content ($f_t^{low\_MC} > f_t^{high\_MC}$); so, the FPZ tip at high moisture moves faster than at low moisture; also the length of the FPZ for the high moisture is longer than for the low moisture ($l_{FPZ}^{low\_MC} < l_{FPZ}^{high\_MC}$). The same tendency is expected for the crack opening such as $w_{low\_MC} < w_{high\_MC}$. The energy stored in the FPZ (or energy release rate, dissipated energy) depends on the stress and on the crack opening in the FPZ. Consequently, all parameters such as the tensile strength, the crack opening displacement, the length of the FPZ and the dissipated energy in the FPZ also depend on moisture content.

In the next section, the characterization results of the R-curve in function of the moisture content are presented and analyzed. The relative energy release and crack length at the peak load versus moisture content are compared to those at the steady-state (at the plateau regime).

4.2 Moisture effect on the crack growth resistance (R-curve)

A typical evolution of the R-curve (calculated based on the strain energy release rate $G(a)$) at 3 moisture contents is illustrated in Figure 4.4. In this figure, the experimental results undoubtedly exhibit a plateau on resistance curve. From the R-curves plotted in Figure 4.4, the fracture process zone does exist with a certain length, which is in agreement with the previous studies on the fracture properties of quasi-brittle material such as wood [39, 43, 45, 111, 113, 115, 173, 174].
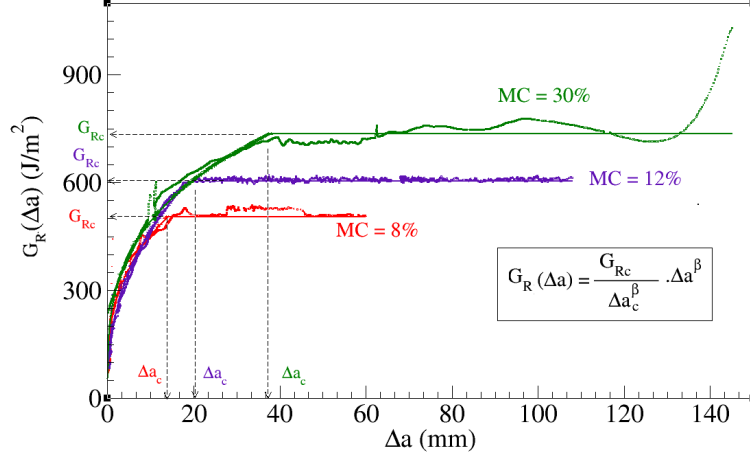
Figure 4.4: Typical R-curves at 3 moisture contents (8%, 12% and 30%). Dash lines represent the experimental R-curve; solid lines are R-curve fitted from the experiments (cf. eq.(2.4))

Table 4.1 summarizes the fracture characteristic parameters obtained at 10 MC. Firstly, maximal load P_{max}, the longitudinal experimental modulus E_L^{exp} and the multiplicative correction factor ψ are reported. The longitudinal experimental modulus E_L^{exp} is obtained from the correction factor ψ and the reference module given in Table 3.1. Secondly, the average results obtained from the fitting of the R-curves are summarized. Thirdly, Table 4.1 gives the release rate G_u and the crack length Δa_u corresponding to the peak load P_{max}.

In this table, the plateau resistance G_{Rc}, the characteristic equivalent crack length Δa_c and the power coefficient β obtained for each moisture content are reported for 255 of the 300 tested specimens. We do not report results from the R-curve for 45 specimens due to some technical problems. For example, due to unstable crack during the fracture test at moisture content lower than 15%, the load-displacement curves for 18 specimens were not obtained. Four other specimens were excluded due to the failure at the interface between the head of the specimen and the metal rod (where the loading is applied) as shown in Figure 4.5. For the test with moisture content higher than 20%, 7 specimens develop a huge local deformation due to the reduced section (Fig. 4.5). Sixteen specimens which do not exhibit a clear plateau regime of the resistance were also set aside.

Table 4.1: Fracture characteristic parameters and R-curve parameters at 10 moisture contents: mean values and standard deviation in brackets

MC (%)	Number of specimens	P_{max} (N)	ψ	E_L^{exp} (MPa)	G_{Rc} (J/m^2)	Δa_c (mm)	β	G_u (J/m^2)	Δa_u (mm)
4.96	28	205	1.116	13273	477	10.0	0.235	450	8.9
(0.35)		(25)	(0.154)	(2278)	(58)	(4.0)	(0.053)	(58)	(3.6)
7.93	20	209	1.128	12570	503	13.1	0.233	490	12.0
(0.38)		(26)	(0.204)	(2882)	(62)	(3.8)	(0.048)	(57)	(3.4)
9.89	31	197	1.098	12631	538	18.6	0.239	499	16.7
(0.42)		(30)	(0.252)	(3461)	(52)	(5.6)	(0.040)	(49)	(5.1)
11.85	30	194	1.106	12167	599	18.7	0.272	573	17.3
(0.72)		(26)	(0.240)	(3192)	(52)	(5.5)	(0.049)	(49)	(5.3)
15.16	24	156	1.005	12907	643	24.5	0.301	631	23.1
(0.53)		(22)	(0.213)	(2708)	(54)	(4.5)	(0.037)	(54)	(4.4)
18.14	19	149	1.136	10725	693	27.5	0.383	651	25.5
(0.63)		(21)	(0.191)	(2307)	(48)	(5.2)	(0.039)	(47)	(4.8)
19.91	28	140	1.016	11772	725	26.9	0.428	695	25.8
(0.58)		(19)	(0.179)	(2094)	(46)	(5.5)	(0.032)	(52)	(5.2)
22.05	17	147	1.121	10198	742	29.4	0.437	703	27.2
(0.64)		(23)	(0.227)	(2094)	(61)	(3.7)	(0.043)	(58)	(3.6)
25.33	25	125	1.085	10053	748	30.2	0.407	732	29.3
(0.66)		(21)	(0.242)	(2575)	(62)	(5.1)	(0.044)	(57)	(5.1)
29.63	33	121	1.114	8865	752	28.1	0.396	722	27.0
(1.20)		(29)	(0.264)	(2539)	(64)	(5.7)	(0.047)	(63)	(5.6)

Figure 4.5: Representation of local deformations in the specimen during a fracture test

We will now further investigate the role of the moisture content on the crack growth resistance by considering its influence on each parameter of the R-curve, i.e, the critical energy release rate G_{Rc} and the characteristic equivalent crack length Δa_c. As discussed in the light of many studies performed in recent years, the fracture behavior of wood is influ-

enced by many factors such as the wood density, the material nature, the configuration, the loading mode, the strain rate, the geometry and the moisture content [12, 45, 112, 115, 159] (see Section 2.2). Moreover, elastic proprieties of wood can be sensitively variable (i.e., the covariance of 10% to 40% for elastic properties of wood [63, 68]). Therefore, the fracture behavior results can be widely variable.

4.2.1 Effect of the moisture content on G_{Rc}

As shown in Figure 4.6, the critical energy release rate G_{Rc} increases with the increasing of the moisture content. This phenomenon can be explained by the fact that more fracture energy is needed for a high moisture content in order to completely delaminate the specimen during the crack growth process due to the fiber bridging effect.
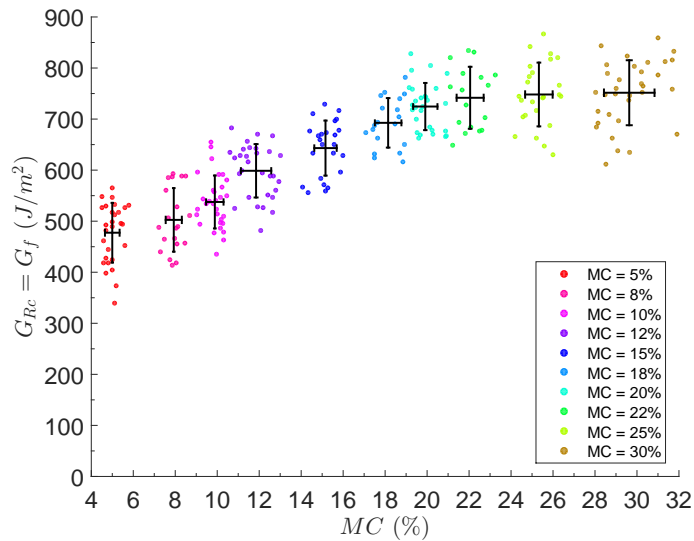

Figure 4.6: Plateau resistance energy G_{Rc} as a function of moisture content. The error bars indicate the standard deviation. Vertical bar represents the standard deviation of G_{Rc}; horizontal bar represents the standard deviation of MC

We observe that the mean value of G_{Rc} varies in range from 477 to 752 J/m^2 for all moisture contents, which is two or three times higher than those obtained by Reiterer et al. [138], Vasic et al. [169, 170], Xavier et al. [173]. In addition, a difference of 1.58 between the smallest and the highest value of G_{Rc} was obtained; the same than the result obtained in [138, 169, 170], but it is different to [173] where a ratio of 3.5 was found. This difference may be due to the geometry and the size of the specimen as well as due to the wood species. For example, in the study of Reiterer et al. [138] and Vasic et al. [169, 170], a WST specimen of spruce and pine wood was used which gave mean fracture energy on the total ligament G_F from 150 - 275 J/m^2 in the range of 7% to 30% of moisture (i.e., 7%, 12%, 18% and 30%) by considering a negligible fracture process zone at the crack tip. In other study Xavier et al. [173] using a DCB specimen of pine, the plateau resistance G_{Rc} varies from 100 - 350J/m^2 in the range of moisture of 0%-13%.

As shown in Table 4.1 and Figure 4.6, two clear responses of G_{Rc} versus moisture can be observed: firstly G_{Rc} considerably increases until the moisture reaches 22% MC (from 477 J/m^2 at 5% MC to 742 J/m^2 at 22% MC) and then remains stable for moisture higher than 22% (around $750 J/m^2$ at 22% to 30% MC). This behavior may be related to the real value of the saturated moisture of the material which may be around 22% - 26%, and not at 30% as assumed.

Furthermore, the coefficient of variation of G_{Rc} also varies from 6% to 13% for all moisture. The minimal and the maximal values correspond to the series tested under 20% and 5-8% MC, respectively.

The standard deviation of the moisture in each series varies from 0.35% to 1.2%. For most of moisture series, the standard deviation of moisture is around of 0.35% for MC < 25%, the maximal standard deviation of 1.2% is found for 30% MC. For most specimens, the moisture perturbation may be linked to technical problems of the conditioning box or to the wood species scattering. In the case 30% MC, an important amount of the free water may be stored in the specimens.

4.2.2   Effect of the moisture content on Δa_c

As shown in Table 4.1 and Figure 4.7, the characteristic equivalent crack length Δa_c at high moisture is longer than the one at low moisture. The mean characteristic equivalent crack length Δa_c is obtained in the range from 8.5 mm to 33.0 mm for all moisture contents. As expressed by Morel et al. [113], the characteristic length of the fracture process zone l^c_{coh} is proportional to the characteristic equivalent crack length Δa_c for most of the geometries of wood specimens ($l^c_{coh} \approx 1.5$ to 2.0 x Δa_c). Hence, the length l^c_{coh} probably appears in the inclined zone of the mTDCB specimen (remember that the maximal length of the inclined zone is 85 mm as shown in 3.1). This fact is confirmed by the chosen geometric shape for the mTDCB specimen, as mentioned in section 3.1.2.

Furthermore, the coefficient of variation of Δa_c also varies from 12% to 40% for all moisture. The minimal and the maximal values correspond to the series tested under 22% and 5% MC, respectively. These perturbations of Δa_c may be caused by the same reasons than for G_{Rc}.

Given the impression of the same evolution and deviation, we are now curious about the relation between G_{Rc} and Δa_c so that next section is dedicated to provide the answer.

4.2.3   Relation between G_{Rc} and Δa_c

In Figure 4.8, the critical energy release rate G_{Rc} is plotted versus the characteristic equivalent crack length for all moisture contents: a strong scattering is observed. We can still observe that the critical energy release rate has a tendency to increase with the characteristic equivalent crack length Δa_c.
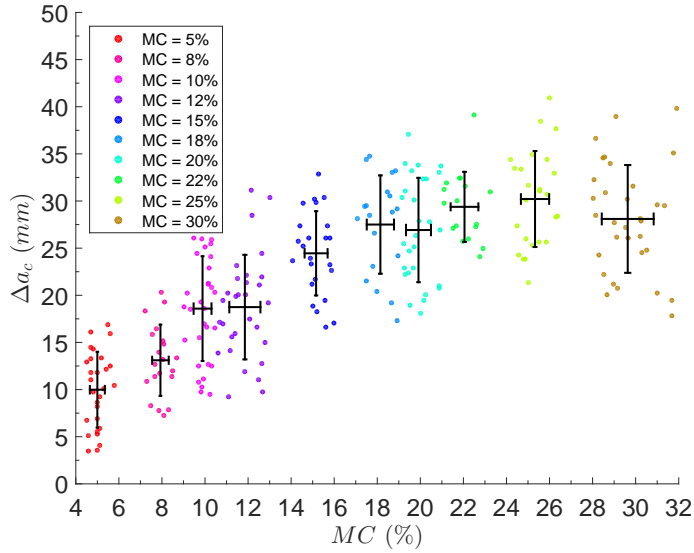
Figure 4.7: Characteristic equivalent crack length Δa_c as a function of moisture content. The error bars indicate the standard deviation. Vertical bar represents the standard deviation of Δa_c; horizontal bar represents the standard deviation of MC
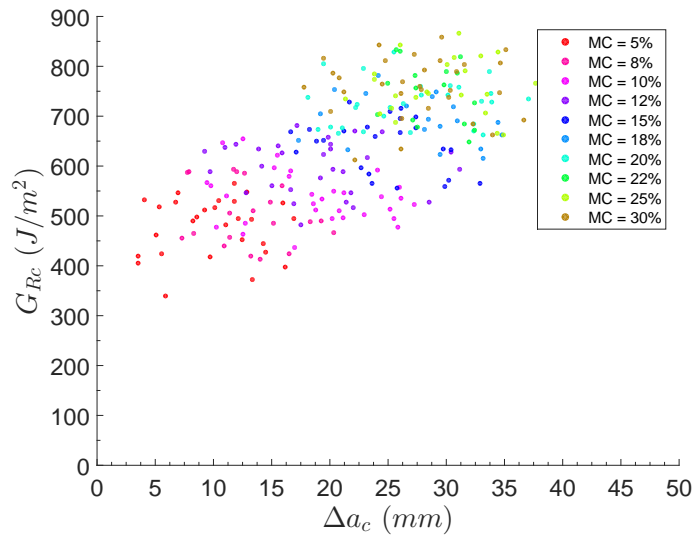

Figure 4.8: Relation between the plateau resistance energy G_{Rc} and the characteristic equivalent crack length Δa_c

For the same critical fracture energy G_{Rc}, the characteristic equivalent crack length Δa_c is longer for quasi-brittle materials compared to brittle materials [12]. On the other hand, the characteristic length of the FPZ in quasi-brittle materials is longer than those in brittle materials (note that the value of Δa_c is approximated zero for brittle material in the framework of LEFM). In this study, G_{Rc} and Δa_c simultaneously increase with the increase of moisture content: dry wood seems to be more 'brittle' in terms of fracture behavior than wet wood. The size of the FPZ in wet wood is undoubtedly larger than that shown dry wood.

Visibly in Figure 4.9a, the maximum load P_{max} has the tendency to decrease with the increase of moisture content due to the reduction of rigidity of the specimen in function of moisture content.
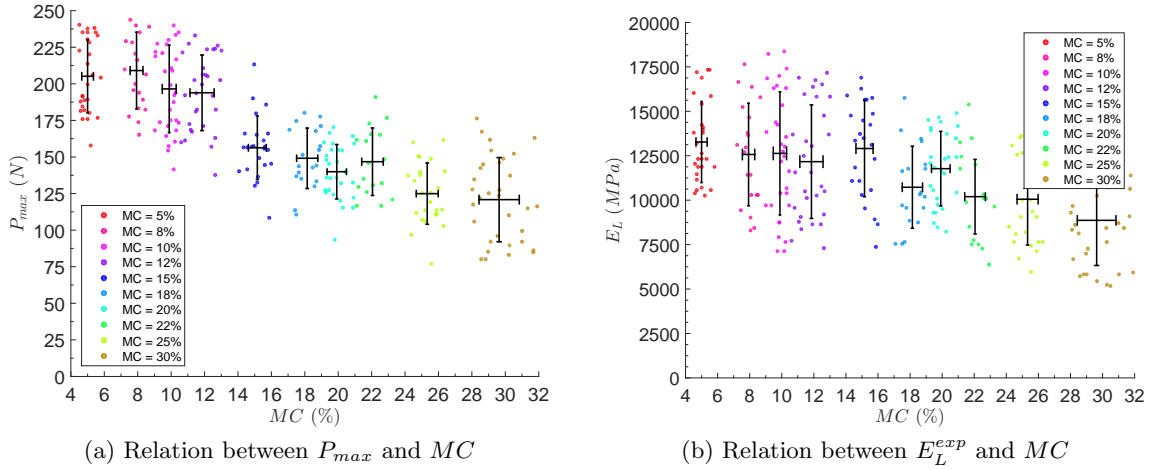

(a) Relation between P_{max} and MC (b) Relation between E_L^{exp} and MC

Figure 4.9: Peak-load P_{max} and Longitudinal modulus E_L^{exp} (experiment) as a function of moisture. The error bars indicate the standard deviation. Vertical bar represents the standard deviation of P_{max} or E_L^{exp}; horizontal bar represents the standard deviation of MC

Figure 4.9b gives the relation between the moisture content and the longitudinal experimental modulus obtained using the correction coefficient ψ on the elastic properties given in Table 3.1. The longitudinal modulus obtained in the fracture test are smaller than those found in the literature. It may be explained by the wood specie as well as the density of the material which is smaller that those used in literature.

4.2.4   Energy release rate G_u and crack length Δa_u at the peak load

Table 4.1 also presents the average energy release rate and the crack length corresponding to the peak load (G_u, Δa_u). The energy release rate G_u and the corresponding crack lengths Δa_u are plotted in Figure 4.10a and Figure 4.10b versus the moisture, respectively. It is observed that the values of G_u and Δa_u increase with the increase of the moisture content in the same way that G_{Rc} and Δa_c.

(a) Relation between G_u and MC

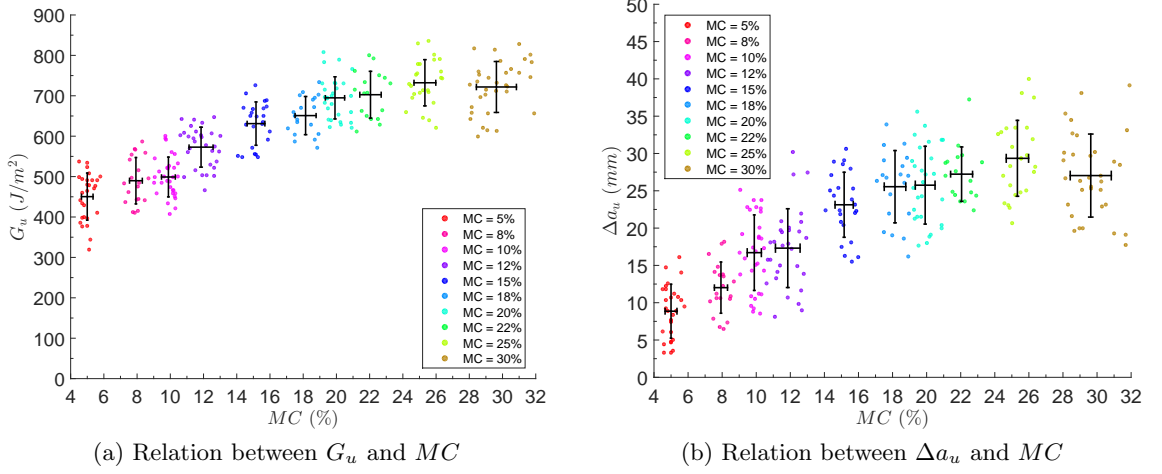(b) Relation between Δa_u and MC

Figure 4.10: G_u and Δa_u evolution versus moisture. The error bars indicate the standard deviation. Vertical bar represents the standard deviation of G_u or Δa_u; horizontal bar represents the standard deviation of MC

As reported in Table 4.1 and shown in Figure 4.11, the energy release rate G_u associated to the peak load is sightly smaller than that at the steady-state G_{Rc} since the peak load is obtained when the fracture energy has not yet reached the plateau resistance G_{Rc}. Identically, the results of the crack length corresponding to the ultimate load Δa_u is also smaller than Δa_c. Nevertheless, the difference of the energy release rate as well as of the crack length between those two states (the steady-state and the state at the peak load) is about 5% and 10%, respectively, which can be considered negligible (Fig. 4.11). These negligible differences were expected thanks to the chosen dimension and geometry of the mTDCB specimen. As shown in Figure 4.11, the ratio of G_u/G_{Rc} and $\Delta a_u/\Delta a_c$ do not present relationship with the moisture content.
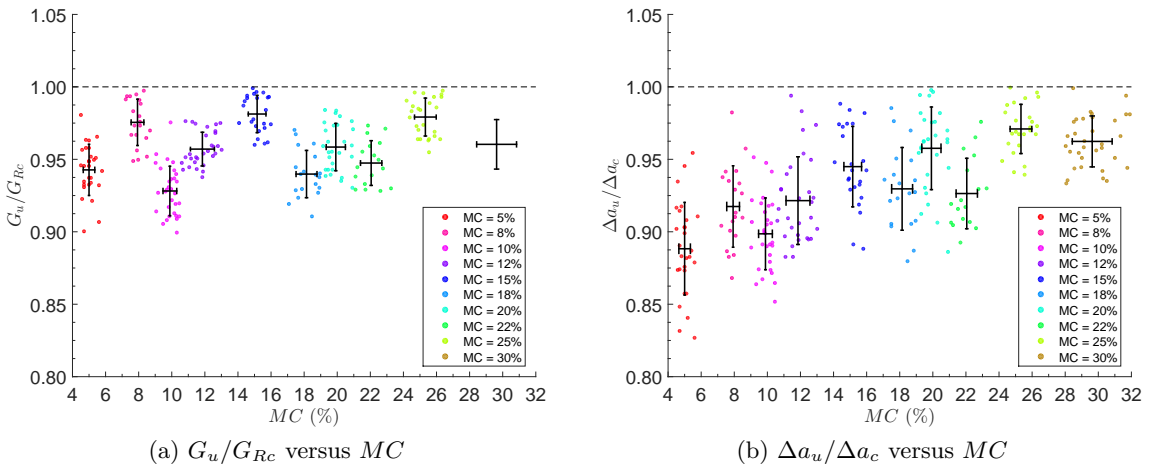

(a) G_u/G_{Rc} versus MC

(b) $\Delta a_u/\Delta a_c$ versus MC

Figure 4.11: Ratio G_u/G_{Rc} and ratio $\Delta a_u/\Delta a_c$ versus moisture content. The error bars indicate the standard deviation. Vertical bar represents the standard deviation of G_u/G_{Rc} or $\Delta a_u/\Delta a_c$; horizontal bar represents the standard deviation of MC

4.3 Effect of the moisture content on the cohesive parameters

Based on the experimental R-curve, parameters of the bi-linear softening law were identified and summarized in Table 4.2 for all moisture contents using the procedure described in Section 3.3.2.3. Firstly, the table gives the mean as well as the standard deviation of the critical cohesive energy G_f, the critical crack opening w_c, the tensile strength f_t and the cohesive energy ratio $G_{f\mu}/G_f$ (defined by the ratio between the cohesive energy corresponding to the part attributed to the micro-cracking zone $G_{f\mu}$ and the critical cohesive energy G_f). Secondly, the characteristic length of the FPZ l^c_{coh} and the characteristic length of the micro-cracking zone l_μ are also presented.

Table 4.2: Cohesive parameters and the characteristic length of the cohesive zone l^c_{coh} and of the micro-crack zone l_μ at 10 MCs: mean values and standard deviation in brackets

MC (%)	Number of specimens	G_f (J/m^2)	w_c (mm)	f_t (MPa)	$G_{f\mu}/G_f$	l^c_{coh} (mm)	l_μ (mm)
4.96	28	477	0.27	6.21	0.630	13.8	6.4
(0.35)		(58)	(0.10)	(0.40)	(0.033)	(4.3)	(1.2)
7.93	20	503	0.38	5.18	0.618	18.1	7.9
(0.38)		(62)	(0.09)	(0.38)	(0.048)	(4.2)	(1.5)
9.89	31	538	0.57	4.40	0.613	25.1	10.1
(0.42)		(52)	(0.14)	(0.32)	(0.034)	(6.5)	(2.0)
11.85	30	599	0.64	3.88	0.587	26.5	11.8
(0.72)		(52)	(0.17)	(0.38)	(0.038)	(6.3)	(2.2)
15.16	24	643	0.90	3.24	0.509	35.0	14.1
(0.53)		(54)	(0.16)	(0.27)	(0.036)	(5.6)	(1.7)
18.14	19	693	1.03	2.68	0.459	41.4	17.9
(0.63)		(48)	(0.19)	(0.32)	(0.052)	(6.1)	(2.6)
19.91	31	725	1.14	2.29	0.397	42.8	18.6
(0.58)		(46)	(0.25)	(0.31)	(0.055)	(7.0)	(3.1)
22.05	17	742	1.25	2.13	0.364	47.0	19.6
(0.64)		(61)	(0.17)	(0.23)	(0.036)	(4.7)	(2.8)
25.33	25	748	1.35	2.13	0.291	48.2	16.7
(0.66)		(62)	(0.24)	(0.32)	(0.050)	(7.2)	(3.1)
29.63	33	752	1.35	2.09	0.287	44.6	15.0
(1.20)		(64)	(0.28)	(0.27)	(0.052)	(7.6)	(3.1)

Moreover, the bi-linear softening parameters at all moisture contents are also graphically presented: the critical crack opening w_c, the tensile strength f_t and the ratio of $G_{f\mu}/G_f$ versus the moisture content are presented in Figures 4.12, 4.13 and 4.14, respectively.

4.3.1 Effect of the moisture content on the critical cohesive energy G_f

As mentioned in section 3.3.2.3, the plateau resistance and the critical cohesive fracture energy are equal ($G_f = G_{Rc}$) [113, 162]. Hence, the moisture effect on the critical cohesive energy G_f was expressed in the previous section (cf. Section 4.2.1)

4.3.2 Effect of the moisture content on the critical crack opening w_c

As shown in Table 4.2 and Figure 4.12 similarly to the critical cohesive energy G_f, the critical crack opening displacement w_c has a tendency to linearly increase with the moisture content until 22% and then remains stable for higher values of MC.

The critical crack opening displacement w_c obtained in this work varies on average from 0.3 to 1.4 mm from dry to wet wood. In previous studies (Dourado et al. [44], Xavier et al. [173]), using a linear softening for DCB specimen of pine, the w_c was found equal to 0.06 mm (at 12% MC). The difference may be related to the used geometry, the size of specimen, the fracture system; especially link to the chosen softening law for the fracture analysis (i.e., linear in [44, 173] and bi-linear function in this thesis). The bi-linear softening law is different from the linear one by taking into account the crack bridging part of wood which is considerably important and leads to the increase of w_c, while the linear function does not work.
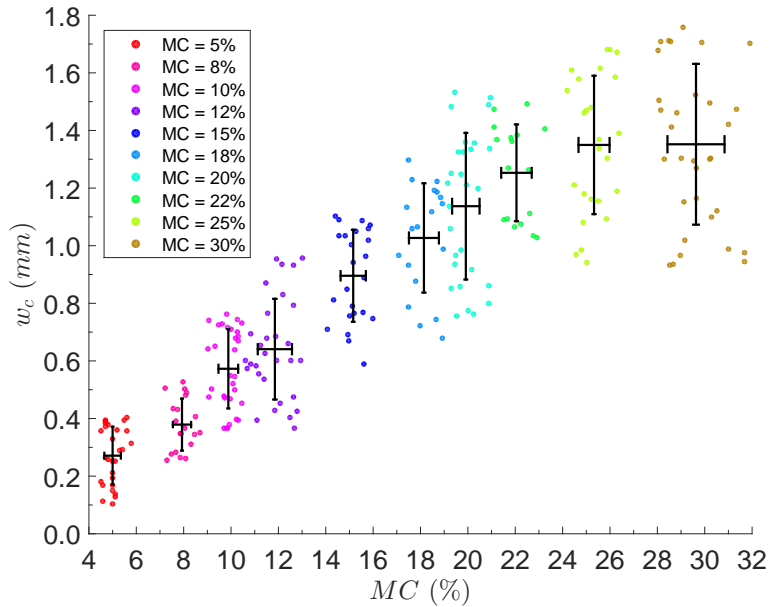

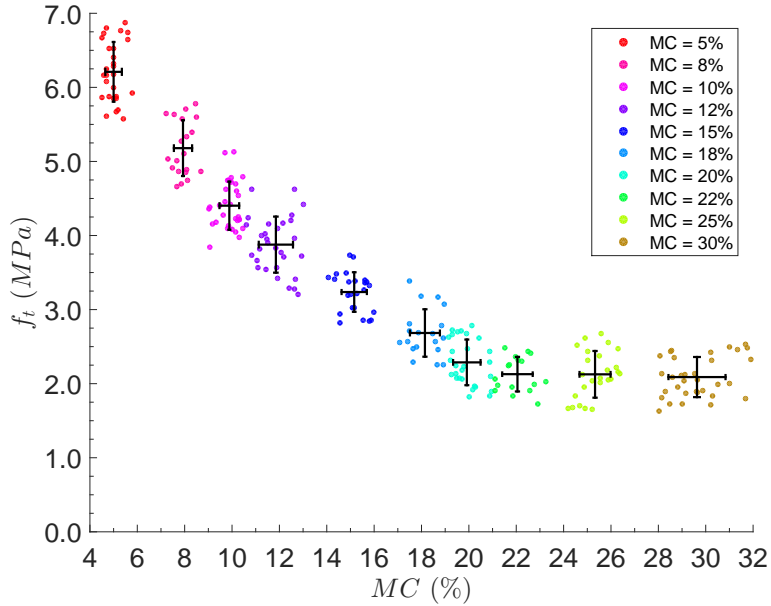Figure 4.12: Critical crack opening w_c versus moisture content. The error bars indicate the standard deviation. Vertical bar represents the standard deviation of w_c; horizontal bar represents the standard deviation of MC

4.3.3 Effect of the moisture content on the tensile strength f_t

As illustrated in Figure 4.13, the tensile strength f_t decreases when the moisture content increases up to 22%, and f_t is stable for higher MC values. This tendency is in agreement with the results reported in the literature: the wood strength is constant above the fiber saturation point. This can be related to the absorption of the water in the micro-structure. The standard deviation of the tensile strength for most of moisture series is around 0.35 MPa while the mean tensile strength f_t is in range of 1.5 to 7.0 MPa as shown in Table 4.2 and Figure 4.13.

Figure 4.13: Tensile strength f_t versus moisture content. The error bars indicate the standard deviation. Vertical bar represents the standard deviation of f_t; horizontal bar represents the standard deviation of MC

Compared to the tensile strength of wood found in the literature [63, 68](e.g., from 11 to 18 MPa for stress parallel to the grain and from 0.3 to 0.7 MPa for stress perpendicular to the grain), the tensile strength obtained in this thesis is found between these two cases (i.e, parallel and perpendicular to the grain). It can be explained by the fact that the material in the FPZ is initially and principally damaged in the tangential direction and then be completely broken in the longitudinal direction. Hence, it can be said that the tensile strength f_t of the cohesive law is obtained from a transitional fracture angle (compared to the loading direction), which is different from the previous studies where the tensile strength of wood is obtained in uni-axial tests.

4.3.4 Effect of the moisture content on the cohesive energy ratio $G_{f\mu}/G_f$

The ratio $G_{f\mu}/G_f$ (defined by the cohesive energy related to the micro-cracking $G_{f\mu}$ on the critical cohesive energy G_f) is graphically presented in Figure 4.14 versus the moisture content: the ratio $G_{f\mu}/G_f$ decreases with the increase of the moisture content.
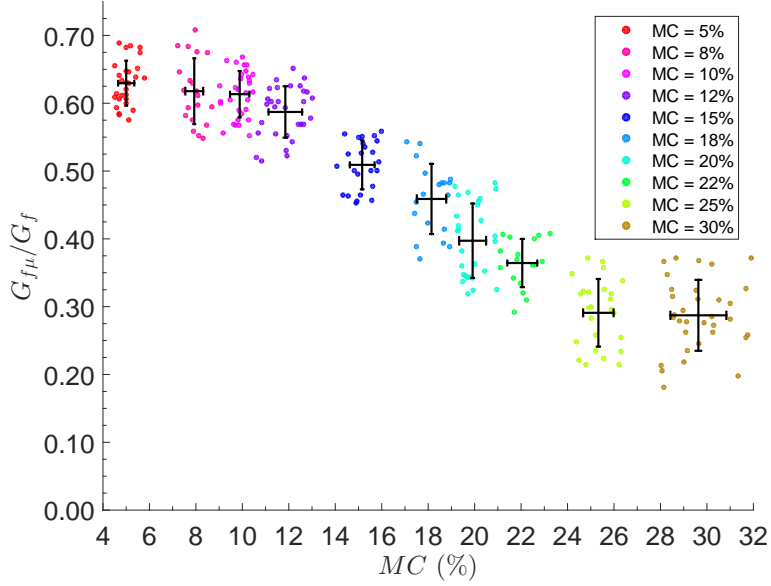

Figure 4.14: Ratio of $G_{f\mu}/G_f$ versus moisture content. The error bars indicate the standard deviation. Vertical bar represents the standard deviation of $G_{f\mu}/G_f$; horizontal bar represents the standard deviation of MC

This results suggest that the micro-cracking energy plays an important role in the cohesive energy at low moisture contents and then the ratio of $G_{f\mu}/G_f$ decreases when moisture content increases. On the other hand, it can be deduced that the mechanism of the crack bridging (fiber bridging) - the most essential phenomenon at high moisture - can be related to the fracture behavior of fibers which are assumed to be more ductile at high moisture contents. As mentioned in Section 4.1, and once again, we could confirm that the cohesive energy ratio $G_{f\mu}/G_f$ corresponding to the micro-cracking mechanism decreases when the moisture increases. This suggestion is in agreement with the schematic representation of crack growth process at low and high moisture contents (Fig. 4.3) as well as the load-displacement curve at three MCs (8%, 12% and 30%) as shown in Fig. 4.2.

4.4 Influence of the moisture content on the lengths l_{coh}^c, l_μ

Figure 4.15 also shows typical stress distributions on the cohesive interface corresponding to the state of the fully developed FPZ for 10 moisture contents. Based on these stress distributions in the cohesive interface, the mean value of l_{coh}^c and l_μ for each series of moisture contents were determined and presented in Table 4.2. The l_{coh}^c and l_μ versus

moisture are also illustrated in Figure 4.16a and Figure 4.16b, respectively.
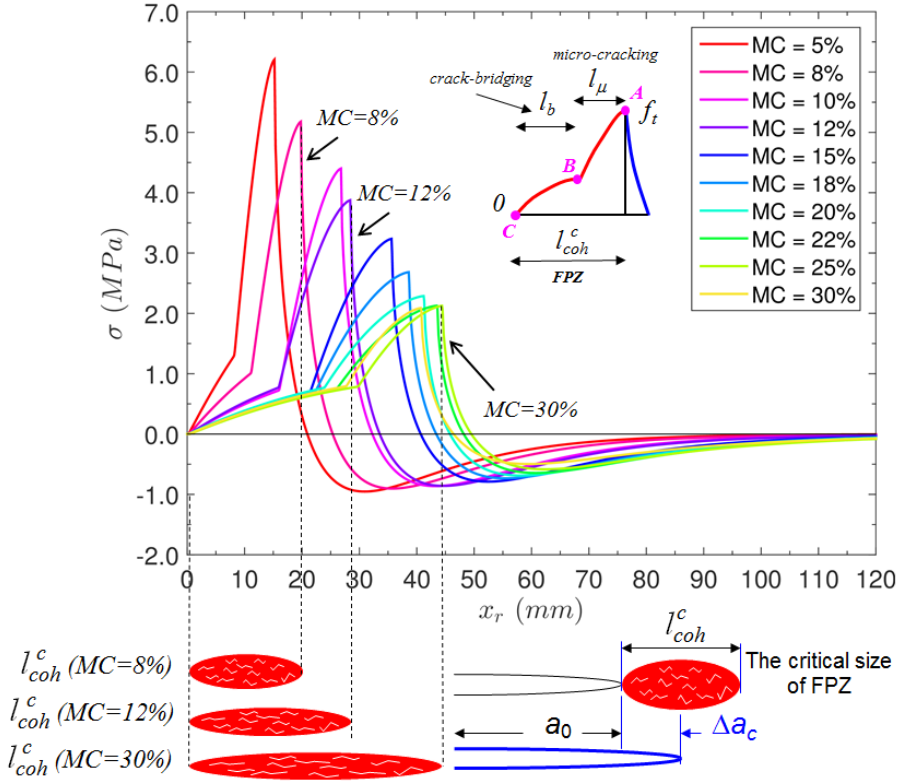

Figure 4.15: Evolution of normal stresses in the cohesive interface for all MCs. x_r denotes the abscissa along the cohesive interface considered from the tip of the stress-free crack
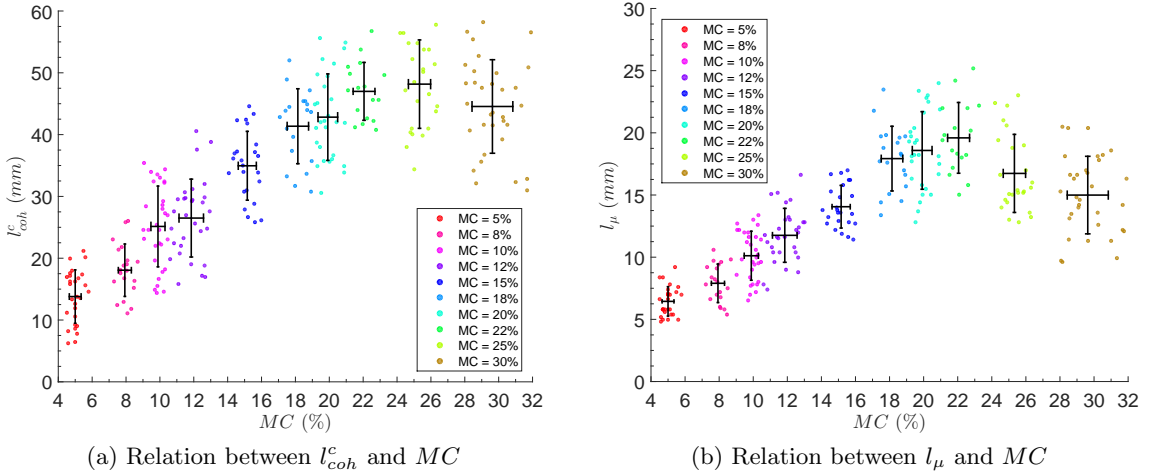

(a) Relation between l_{coh}^c and MC

(b) Relation between l_μ and MC

Figure 4.16: Characteristic cohesive length l_{coh}^c and characteristic micro-crack length l_μ versus moisture content. The error bars indicate the standard deviation. Vertical bar represents the standard deviation of l_{coh}^c or l_μ; horizontal bar represents the standard deviation of MC

As shown in Figure 4.16 and Table 4.2, the characteristic lengths l_{coh}^c and l_μ increase with the increasing of the moisture content, which is expected.

4.5 Correlation between the R-curve, the cohesive parameters and the characteristic lengths of the FPZ

4.5.1 Relation between Δa_c, w_c and l^c_{coh}

Figure 4.17 shows the relation between the characteristic crack length Δa_c and the critical crack opening displacement w_c and also the characteristic length l^c_{coh}. An approximately linear evolution of w_c and of the cohesive length l^c_{coh} versus Δa_c is observed. It is shown that the values of w_c and l^c_{coh} increase with the increasing of Δa_c. From the results plotted in Figure 4.17a, the relation can be approximately given as: $l^c_{coh} \approx 1.63 \cdot \Delta a_c$. This coefficient of 1.63 is comparable with the previous study: for most of geometry, l^c_{coh} $\approx$1.5-2.0 xΔa_c [100, 113].

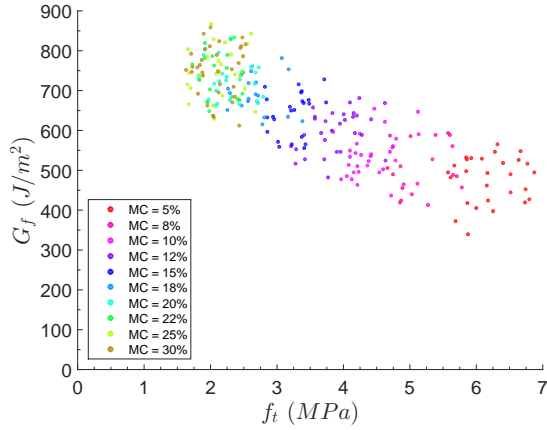(a) Relation between w_c and Δa_c (b) Relation between l^c_{coh} and Δa_c
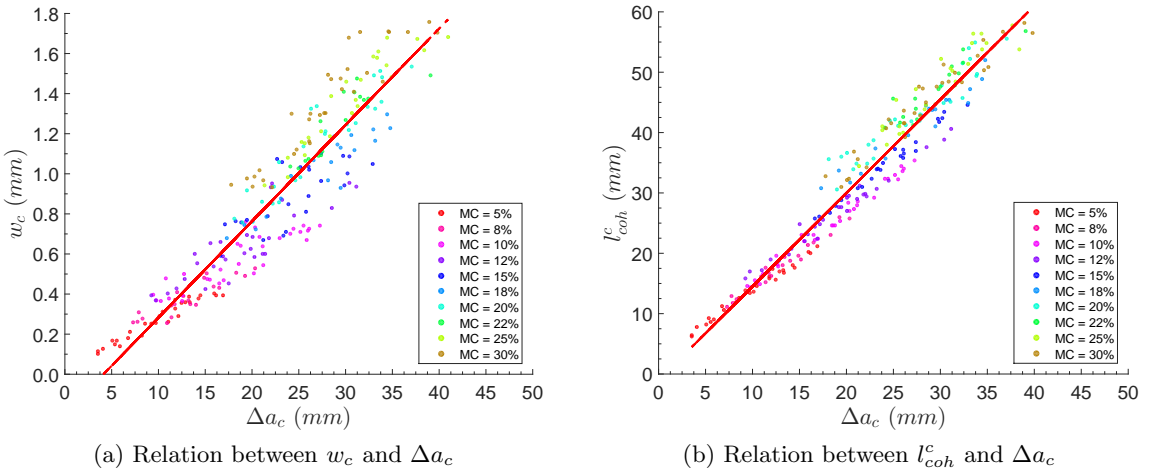
Figure 4.17: Relation between the critical crack opening w_c, the characteristic cohesive length l^c_{coh} and the characteristic crack length Δa_c at whatever moisture
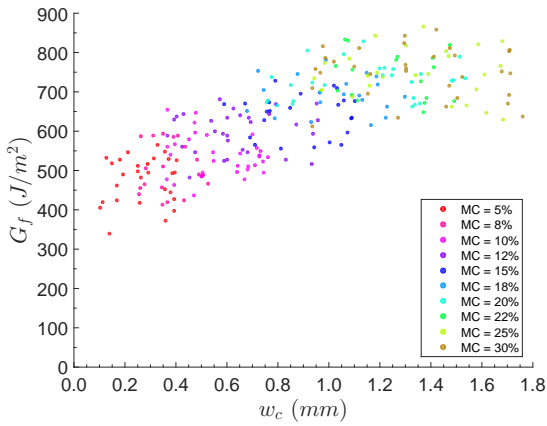
4.5.2 Relation between the cohesive parameters G_f, w_c, f_t and $G_{f\mu}/G_f$

Figure 4.18 shows relations between the cohesive parameters: the critical cohesive energy G_f, the critical crack opening w_c, the tensile strength f_t, and the ratio of cohesive energies $G_{f\mu}/G_f$ with moisture contents. In all cases, a scattered evolution is observed.
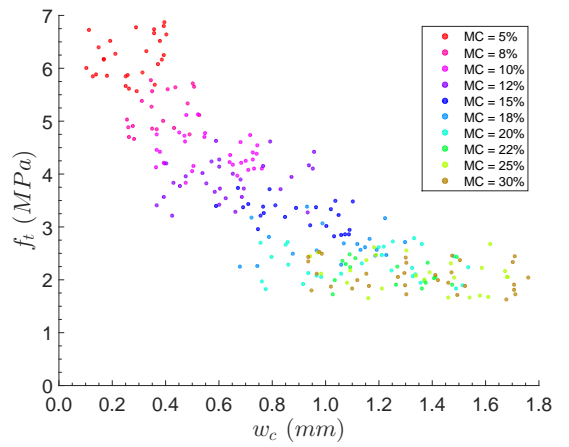
As shown in Figure 4.18a, the critical cohesive energy G_f is nearly inversely proportional to the tensile strength f_t. The critical cohesive energy G_f increases with increasing of w_c (Fig. 4.18b), but decreases when the cohesive energy ratio $G_{f\mu}/G_f$ increases (Fig. 4.18d). In addition, the tensile strength f_t has a inverse tendency with the critical crack opening w_c (Fig. 4.18c), but it increases with the cohesive energy ratio $G_{f\mu}/G_f$ (Fig. 4.18e).
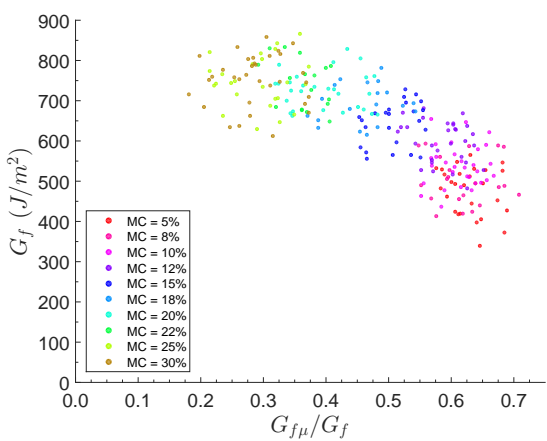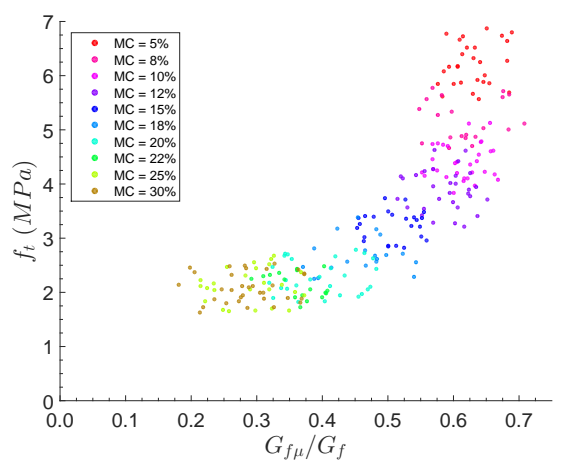
(a) Relation between G_f and f_t

(b) Relation between G_f and w_c

(c) Relation between f_t and w_c

(d) Relation between G_f and $G_{f\mu}/G_f$

(e) Relation between f_t and $G_{f\mu}/G_f$

Figure 4.18: Relations between the cohesive parameters: the critical cohesive energy G_f, the critical crack opening w_c, the tensile strength f_t, and the cohesive energy ratio $G_{f\mu}/G_f$ at whatever moisture

4.5.3 Relation between G_f, f_t and l^c_{coh}, l_μ

Figure 4.19 shows relations between the critical cohesive energy G_f, the tensile strength f_t, the characteristic length l^c_{coh} and the micro-cracking length l_μ.
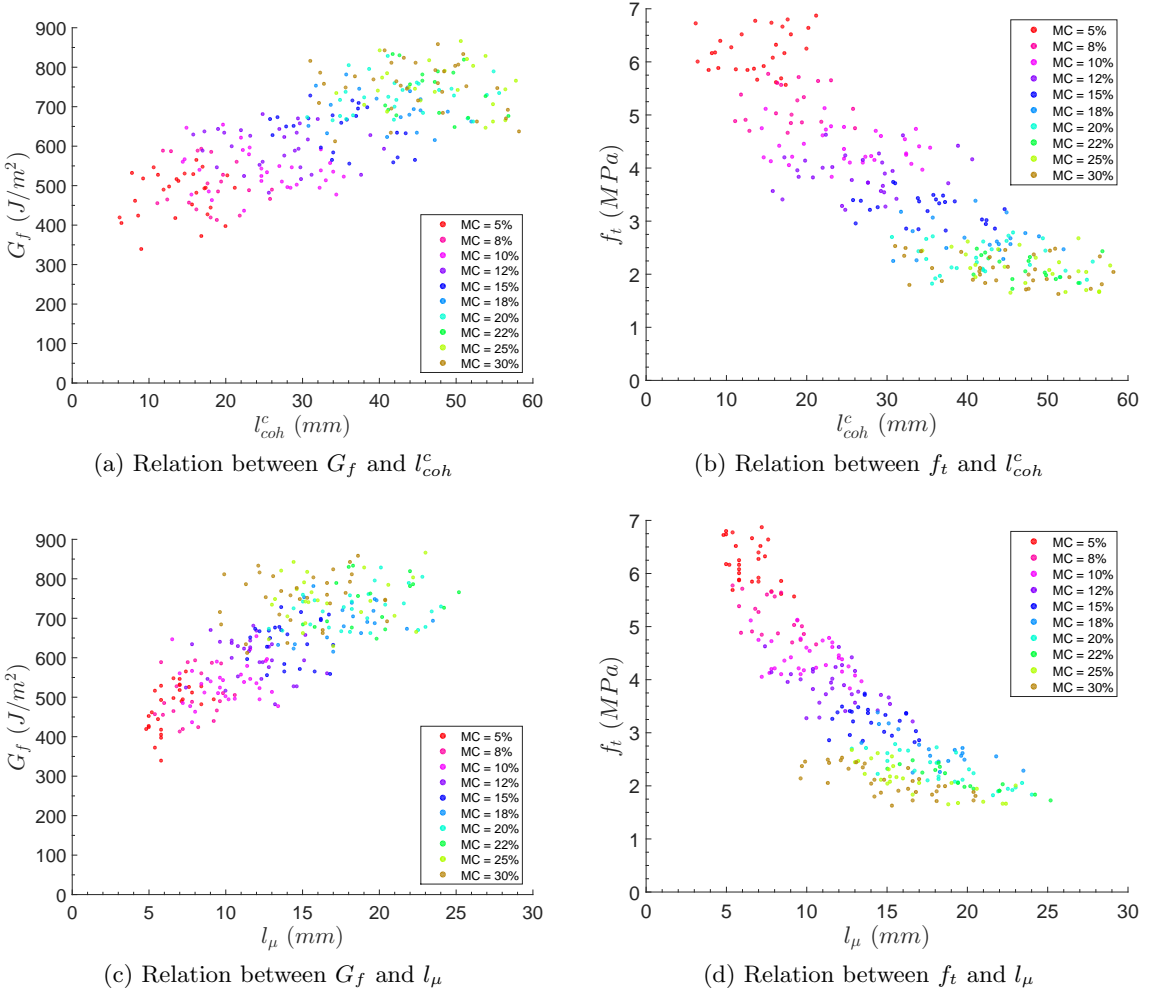

(a) Relation between G_f and l^c_{coh}

(b) Relation between f_t and l^c_{coh}

(c) Relation between G_f and l_μ

(d) Relation between f_t and l_μ

Figure 4.19: Relation between the critical cohesive energy G_f, the tensile strength f_t and the characteristic FPZ length l^c_{coh} as well as the micro-cracking length l_μ at whatever moisture

As shown in Figure 4.19, the critical cohesive energy G_f increases with the increase of l^c_{coh} (Fig. 4.19a) as well as l_μ (Fig. 4.19c). Conversely, the tensile strength f_t decreases with the increase of l^c_{coh} (Fig. 4.19b) as well as l_μ (Fig. 4.19d).

4.5.4 Relation between G_f, f_t and P_{max}, E_L^{exp}

Figure 4.20 shows relations between the critical cohesive energy G_f, the tensile strength f_t, the peak-load P_{max} and the longitudinal experimental modulus E_L^{exp} at whatever moisture.
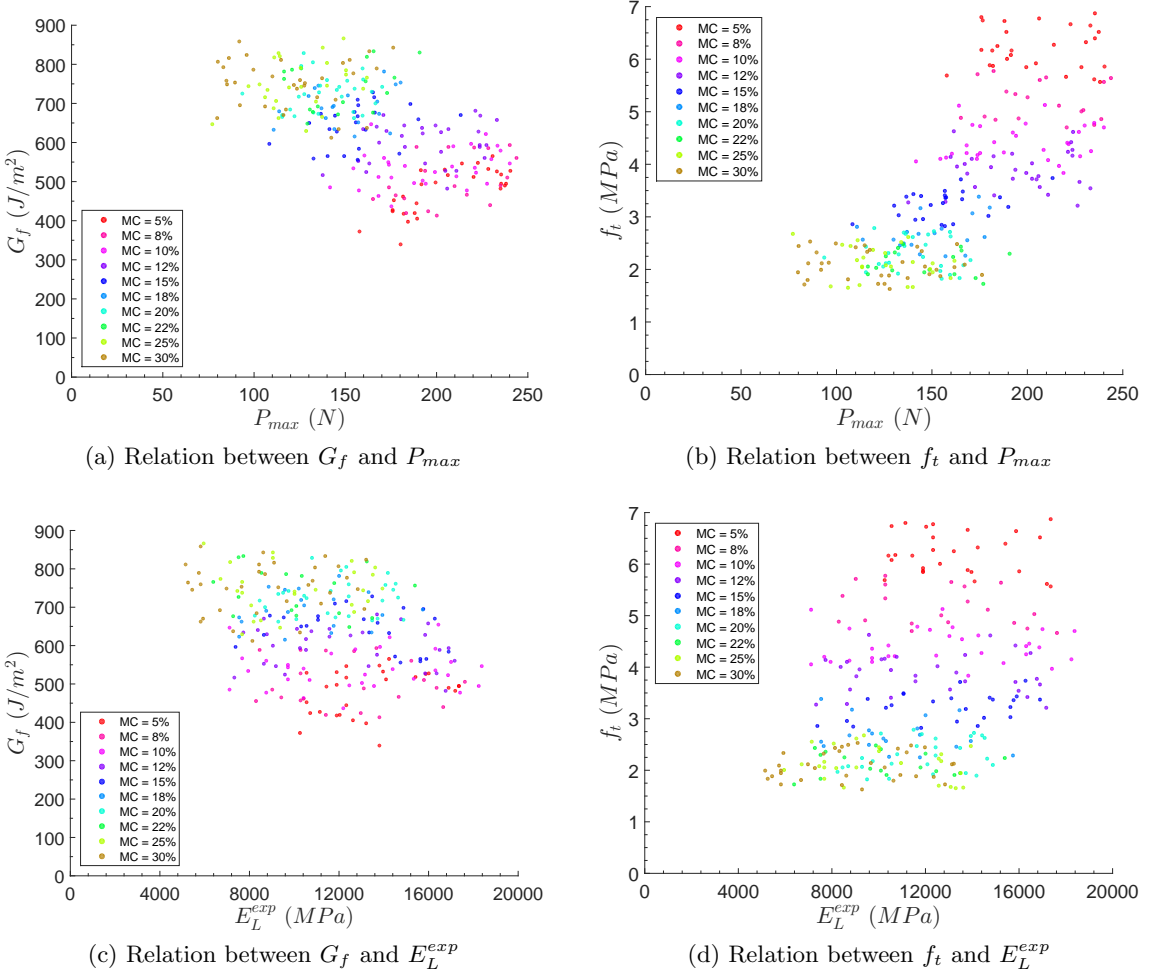

(a) Relation between G_f and P_{max}

(b) Relation between f_t and P_{max}

(c) Relation between G_f and E_L^{exp}

(d) Relation between f_t and E_L^{exp}

Figure 4.20: The critical cohesive energy G_f and the tensile strength f_t evolutions versus the peak-load P_{max} and the longitudinal experimental modulus E_L^{exp}

As shown in Figure 4.20, we do not have a clearly trend for the relations between G_f and P_{max}, f_t and P_{max}, G_f and E_L^{exp}, f_t and E_L^{exp}.

4.5.5 Relation between l_μ/l_{coh}^c and G_f, f_t, $G_{f\mu}/G_f$, l_{coh}^c, E_L^{exp}

Figure 4.21 shows relations between the ratio l_μ/l_{coh}^c with the following parameters: the critical cohesive energy G_f, the tensile strength f_t, the moisture content, the ratio $G_{f\mu}/G_f$, the characteristic length l_{coh}^c of FPZ and E_L^{exp}. It was observed that there is not a correlation between each pair of the above mentioned parameters.
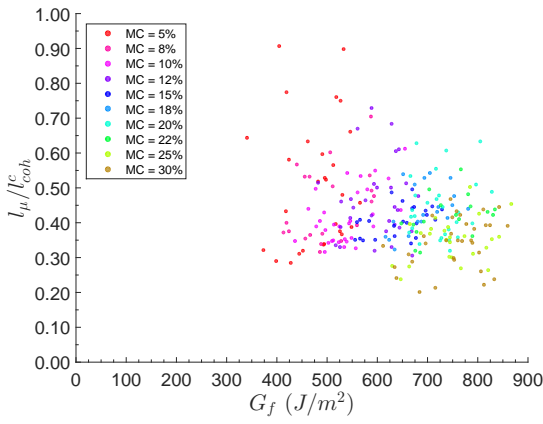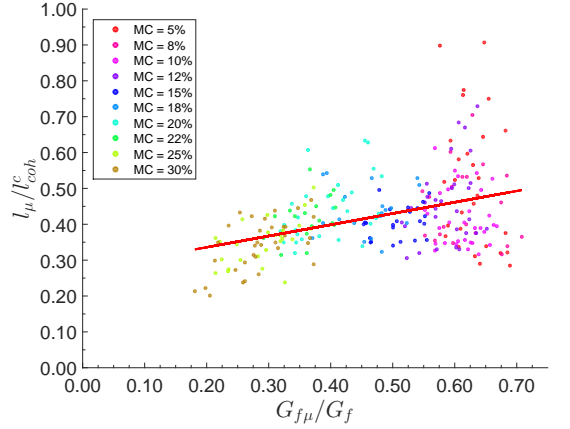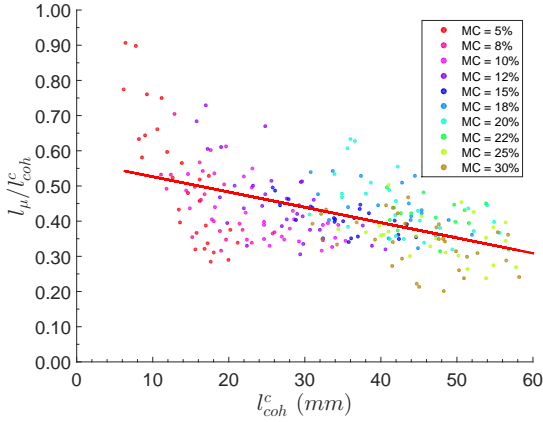
(a) Relation between l_μ/l_{coh}^c and G_f
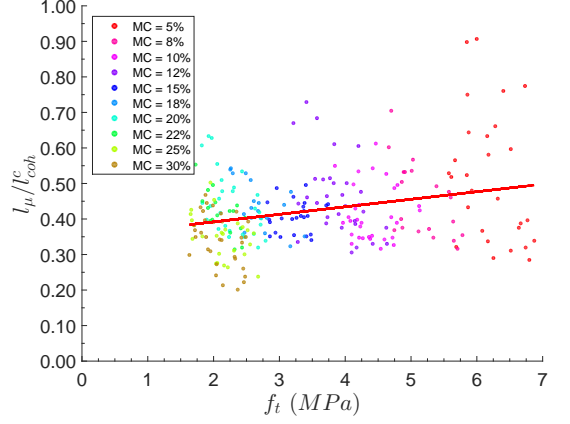
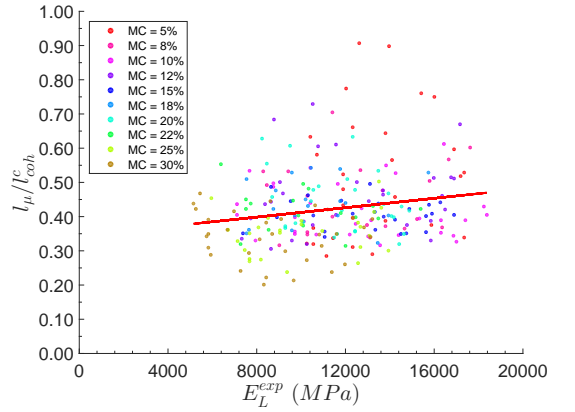(b) Relation between l_μ/l_{coh}^c and f_t
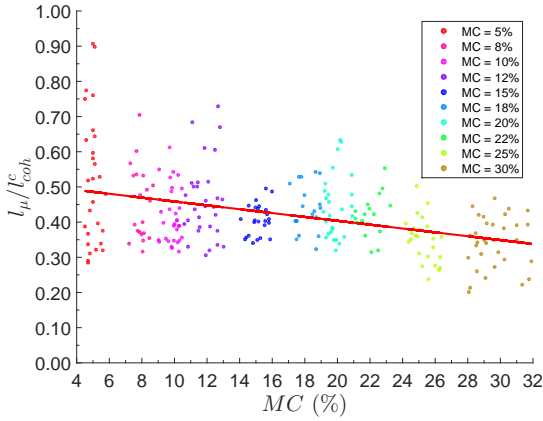
(c) l_μ/l_{coh}^c in function of MC

(d) Relation between l_μ/l_{coh}^c and $G_{f\mu}/G_f$

(e) Relation between l_μ/l_{coh}^c and l_{coh}^c

(f) Relation between l_μ/l_{coh}^c and E_L^{exp}

Figure 4.21: Relation between l_μ/l_{coh}^c and MC, G_f, f_t, $G_{f\mu}/G_f$, l_{coh}^c as well as E_L^{exp}

Under several moisture content, each cohesive law parameter has its own evolution as well as variation. The question is raised whether theses parameters respect a certain general distribution whatever the moisture content. Distribution functions are then proposed which are based on a probabilist approach, the Weibull distribution. The details as well as their application on the current approach are described in the next section.

4.6 Weibull distribution

The Weibull distribution is quite popular in engineering since it has been firstly successfully introduced several decades ago. The Weibull distribution is characterized by 3 parameters: the shape parameter k (dimensionless), the scale parameter W and the location parameter x_0. Two function are necessary: the cumulative distribution function $F(x)$ and the probability density function $f(x)$ of Weibull parameters, respectively defined as:

$$F(x) = 1 - exp\left[-\left(\frac{x - x_0}{W}\right)^k\right], \ x > x_0 \tag{4.1}$$

$$f(x) = \frac{k}{W}\left(\frac{x - x_0}{W}\right)^{k-1} exp\left[-\left(\frac{x - x_0}{W}\right)^k\right], \ x > x_0 \tag{4.2}$$

4.6.1 Weibull distribution for G_f, w_c, f_t and G_m/G_f

The Weibull cumulative distribution functions for the bi-linear softening parameters at all examined moisture contents are plotted in Figure 4.22.

(a) Weibull distribution for G_f

(b) Weibull distribution for w_c

(c) Weibull distribution for f_t

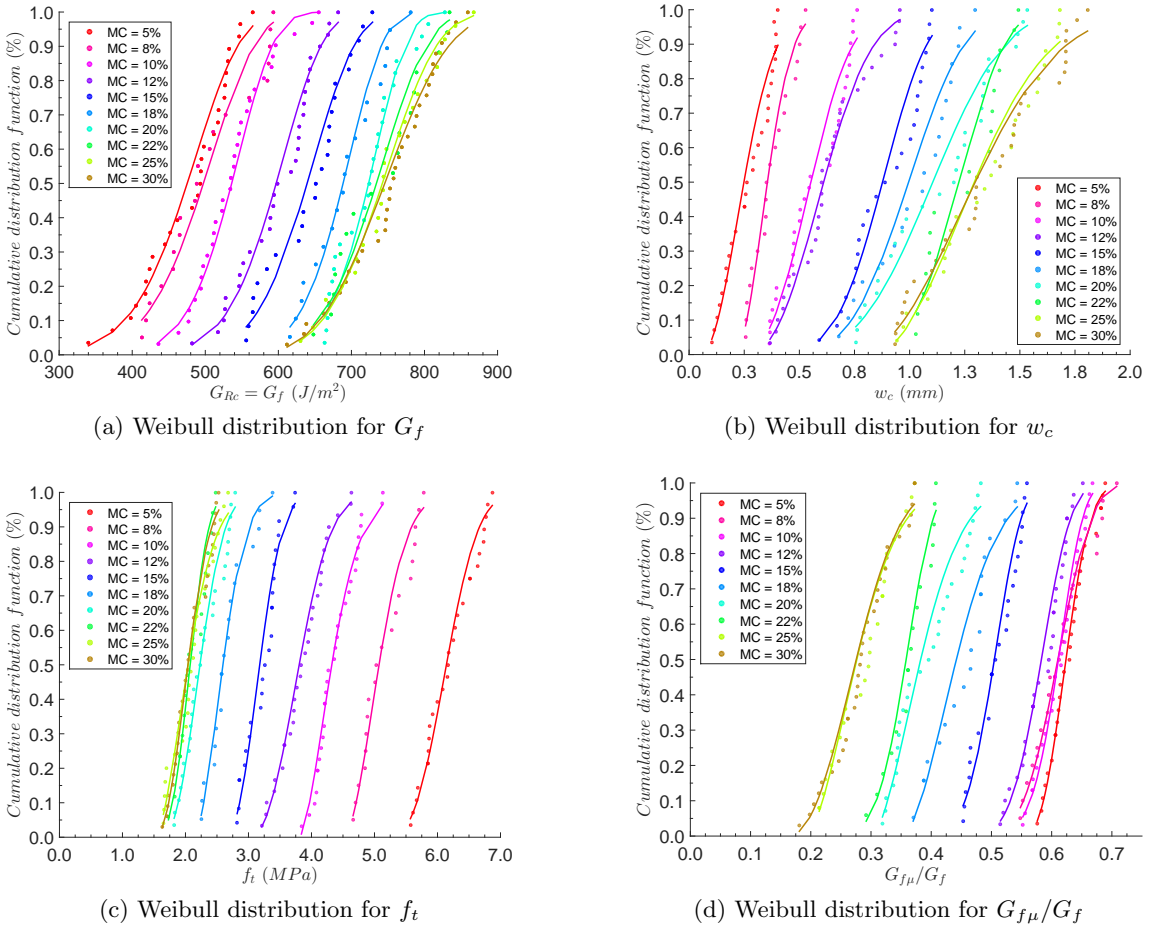(d) Weibull distribution for $G_{f\mu}/G_f$

Figure 4.22: Cumulative distribution function for each cohesive parameter. The points present the experimental data, while the lines present the Weibull distribution

Moreover, Table 4.3 summarizes coefficients (k, W and x_0) of Weibull distribution for each cohesive parameter at 10 moisture contents.

Table 4.3: Fitted coefficients x_0, k and W of Weibull distribution for each cohesive parameter at 10 moisture contents

MC (%)	Number of specimens		G_f (J/m^2)	w_c (mm)	ft (MPa)	$G_{f\mu}/G_f$
		x_0	120	0.05	5.2	0.55
4.96	28	k	6.8039	2.0641	2.7079	2.6619
(0.35)		W	375	0.24	1	0
		x_0	160	0.2	4.5	0.47
7.93	20	k	6.4850	2.0359	1.8642	3.5928
(0.38)		W	357	0	1	0
		x_0	250	0.22	3.8	0.46
9.89	31	k	6.8104	2.6112	1.6736	5.0724
(0.42)		W	302	0.38	0.65	0.16
		x_0	300	0.25	3	0.45
11.85	30	k	6.4412	2.4233	2.3218	3.8515
(0.72)		W	314	0.42	0.94	0.15
		x_0	370	0.32	2.6	0.37
15.16	24	k	5.6627	3.8843	2.3588	4.1943
(0.53)		W	287	0.61	0.68	0.15
		x_0	400	0.37	2.1	0.35
18.14	19	k	7.2472	3.5262	1.9723	1.8219
(0.63)		W	304	0.69	0.60	0.11
		x_0	420	0.38	1.6	0.3
19.91	31	k	7.9225	3.2085	2.3832	1.7180
(0.58)		W	318	0.81	0.73	0.10
		x_0	450	0.65	1.5	0.22
22.05	17	k	5.6132	3.9298	2.8367	4.2497
(0.64)		W	303	0.63	0.65	0.15
		x_0	500	0.82	1.5	0.19
25.33	25	k	4.5280	2.0558	1.7972	1.7609
(0.66)		W	263	1	1	0
		x_0	530	0.75	1.5	0.16
29.63	33	k	3.5347	2.1131	2.2514	2.3029
(1.20)		W	239	1	1	0

4.6.2 Random values of CZM parameters (at 12% MC)

Our objective is to establish a Weibull distribution function at all moisture contents usable and practical in civil engineering and in the laboratory. To do that, a study of random values in Weibull distribution function for each bi-linear softening parameter is analyzed. From the Weibull distribution function at 12%MC, random values of these distributions for each bi-linear softening parameter in CZM (i.e. G_f, w_c, f_t and $G_{f\mu}/G_f$) are used to simulate and to obtain load-displacement curves. Hence, 35 load-displacement curves and resistance curves obtained from random simulations are presented in Figure 4.23 with two extreme experimental results.

(a) Load-displacement curves   (b) Resistance curves
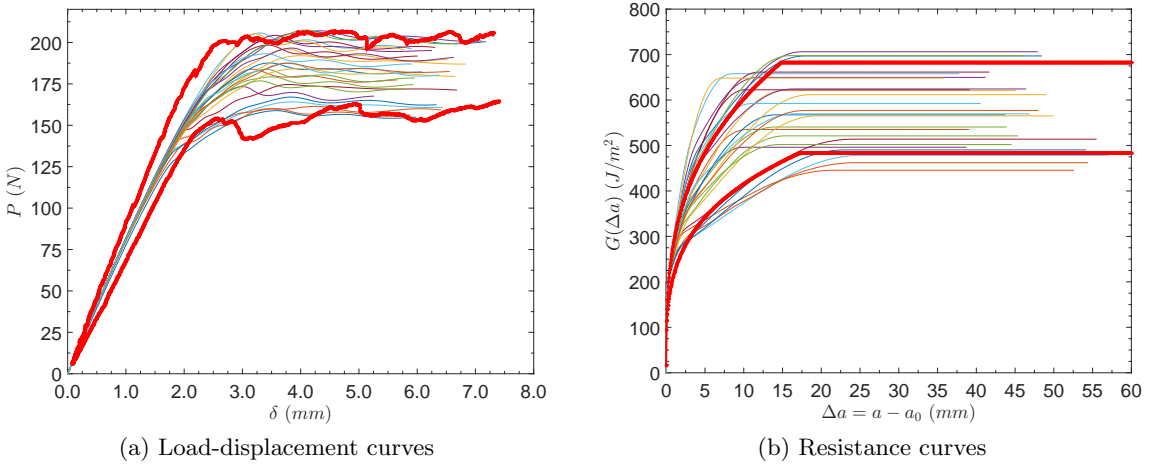
Figure 4.23: Weibull scenarios at 12% MC (red lines: extreme experimental curves)

Extreme curves (red lines) of all the experimental fracture test corresponding to the series of 12% MC, are plotted in Figure 4.23 for 2 cases: the load-displacement case and the resistance case. These two extreme curves have two different initial stiffness (initial slope) due to the differences of mechanical properties (i.e., modulus Young). In the simulation, all initial stiffness of specimen are similar because the same mechanical properties are used in the numerical analysis (Table 3.1). It seems that the random simulations are in agreement with the experiments: the 2 extreme experimental curves well enclose the simulated ones. Same simulations are also performed at other MC and compared to the experimental results.

Therefore, the choice for a Weibull distribution to describe the bi-linear softening parameters at different moisture contents seems appropriate.

4.7   Conclusion

The influence of the moisture content on the fracture behavior (mode I) of Maritime pine is investigated on mTDCB specimen. From fracture tests carried out under a widely range of moisture content, R-curve and cohesive zone model parameters were determined. Based on the equivalent LEFM approach, the equivalent elastic crack length during crack growth is obtained. Consequently, the resistance to crack growth and the cohesive zone parameters for each fracture test are obtained and identified.

The results show that the fracture behavior of wood strongly depends on the moisture content. For the moisture below $22 - 25\%$, the plateau resistance (G_{Rc} or G_f), the critical opening w_c, the characteristic length corresponding to micro-cracking zone as well as the characteristic length of the FPZ increase with moisture content. Moreover, the tensile strength f_t and the ratio $G_{f\mu}/G_f$ decrease with the increasing moisture content. However, for moisture content equivalent or higher than $22 - 25\%$, the influence of moisture on the fracture behavior seems to be negligible.

In order to establish fracture properties of wood able to be used in fracture analysis in civil engineering, the Weibull distribution function for each CZM parameter at several moisture contents was also analyzed in the framework of the probabilistic approach. Hence, random numerical analysis were reasonable similar to the experimental results.

In the next chapter, a method to analyze the crack growth under humidity variation is proposed and studied. The numerical results obtained from this method will be compared to the experimental ones.

Chapter 5

Modeling of crack propagation under RH variations

In order to analyze cracked timber structures under real service conditions, the changes of moisture content in wood during the loading must be considered in the framework of fracture mechanic. On the other hand, the main problem is the coupling between the hydride state and the mechanical state in the material, as well as the coupling between the configuration with and without the crack propagation.

In this thesis, in order to have a better comprehension of the loaded structure behavior under RH variations, the modeling of the cracked structure taking into account the moisture variation is proposed and studied. As shown in Figure 5.1, three principal problems will be investigated thanks to 3D modeling:

- the moisture diffusion in wood,
- the viscoelastic mechano-sorptive behavior in wood substrate,
- the fracture process zone.
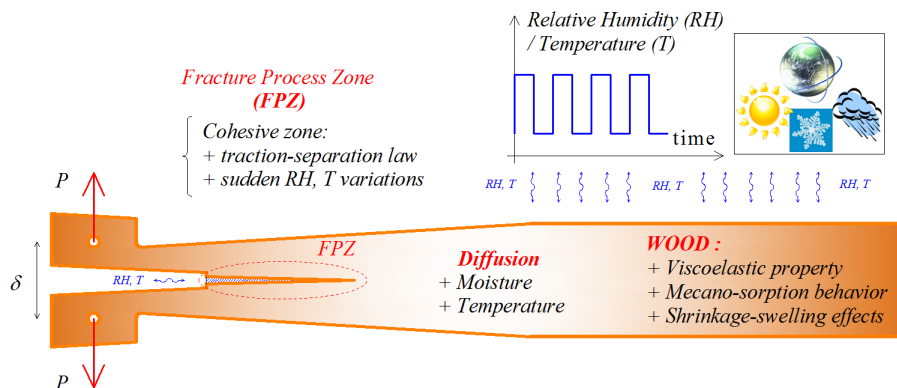
Figure 5.1: Problematic of the crack growth of wood under RH variations

In this thesis, a 3D modeling is proposed and proved to be efficient for 3D coupled engineering problems. This modeling integrates the Fick's law for the moisture diffusion in wood, the 3D orthotropic creep model that takes into account the shrinkage-swelling

effect and the viscoelastic mechano-sorptive creep behavior of wood as well as the effect of rapid RH variations on the Fracture Process Zone.

Generally, a timber structure is loaded with a load P_0 smaller than the maximal load P_{max} (or ultimate load obtained from a quasi-static test), as shown in Figure 5.2. Under this load P_0, an energy release rate $G(a, P_0)$ is obtained at the initial structure configuration. As illustrated in Figure 5.2, the evolution of the energy release rate corresponding to the load P_0 (blue curve) is put into relation with the R-curve (red curve). For the load P_0, we observe two states of the crack growth: firstly, the crack grows and propagates; secondly it becomes stable. These two states correspond to two different parts of the energy release rate curve (before and after the intersection with the R-curve). The crack length a for which the crack is stable under P_0 corresponds to the intersection of the energy release rate curve and the R-curve (Fig. 5.2).
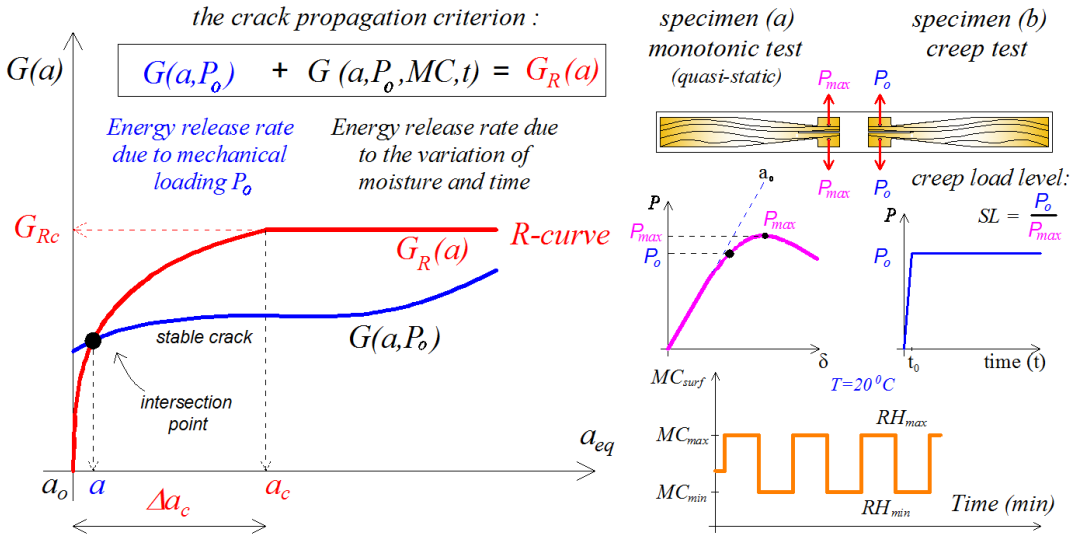
Figure 5.2: Propagation criterion for the structure under variable humidity

In the absence of RH variations, if we consider that the viscoelastic deformation is negligible, the crack will be stable and will not propagate (the blue curve is below the red curve as seen in Figure 5.2). Otherwise, due to viscoelastic properties of wood and/or with humidity variations, the energy release rate will increase or decrease. If the energy release rate increases, then the crack propagates up to the new intersection point with the R-curve: $a_{new} > a$.

Before analyzing the cracked structures under varying relative humidity, we would like to present the basis of the moisture transfer phenomenon in wood, and then an extension of the moisture diffusion phenomenon for cracked structures.

5.1 Moisture diffusion in wood

For a cracked timber structure, the problematic of the diffusion phenomenon in wood can be illustrated in Figure 5.3. The diffusion process depends not only on diffusion properties which are related to mechanical state (i.e., stress and strain) and hydric state but also on the structure configuration. For example, moisture transfer in wood is rapid under high strain in fiber. In the diffusion phenomenon (i.e., thermal-hydric conduction ...), the boundary condition for the exchange surface is changed due to the crack growth process which leads to the modification of structure configuration.
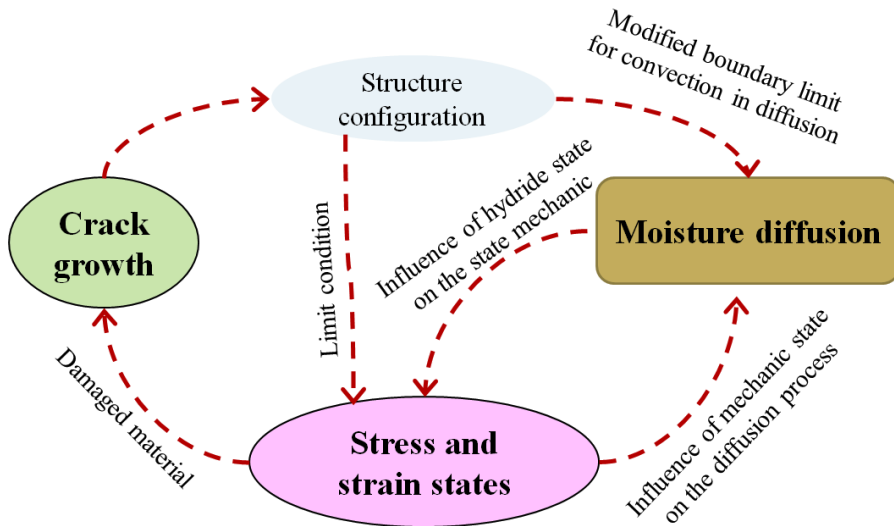
Figure 5.3: Schematic representation of the diffusion problem

5.1.1 3D diffusion model

Before presenting the basis of the 3D diffusion model in wood, a brief resume of some essential definitions for the diffusion problem is made (Fig. 5.4).
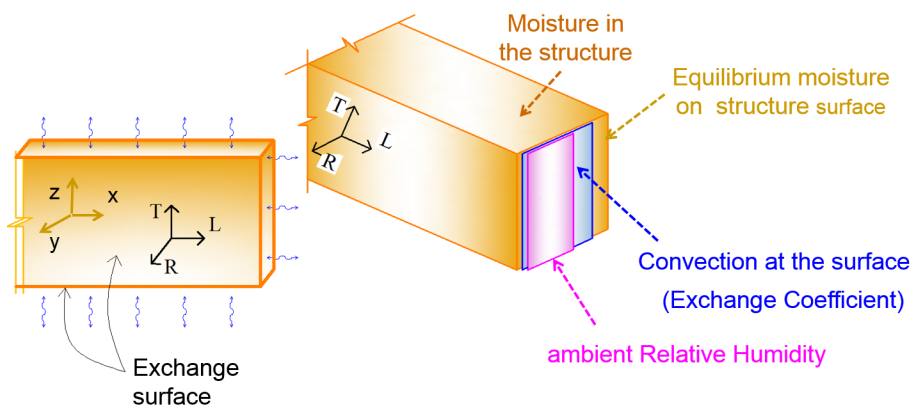
Figure 5.4: Some definitions in the diffusion problem

In the present work, wood is assumed to follow the Fick's law for the moisture transfer [124] and the temperature is considered to be constant. The second Fick's law is written as:

$$\frac{\partial MC}{\partial t} = \nabla.(\mathbb{D}.\nabla MC) \tag{5.1}$$

where $\mathbb{D}$ is the second-order diffusion tensor of the moisture transfer.

According to Perré et al. [124], the hydric convection between the above mass transfer coefficient and surface emission coefficient based on the analogousness of the flux for the different potentials can be expressed as:

$$-\mathbb{D}(MC).\nabla MC.\vec{n} = (MC_{surf} - MC_{eq}).S \tag{5.2}$$

where S is the surface emission coefficient (m/s). MC_{surf} is the moisture content at the wood surface. MC_{eq} is the equilibrium moisture of wood corresponding to the environment humidity [97] obtained from the sorption isotherm of wood (e.g., Maritime pine).

In the literature [1, 74, 101, 102, 107, 108, 153], the moisture diffusion has been isotropically studied. The diagonal terms (values) of the tensor $\mathbb{D}$ are written as $\{D_L, D_T, D_R\}$ (other values equal zero). Note that D_L, D_T, D_R are the diffusion coefficients for the longitudinal, tangential and radial directions, respectively.

As the diffusion coefficients $\{D_L, D_T, D_R\}$ depend also on the mechanical state [107], eq.(5.1) can be rewritten in the general form as:

$$
\begin{aligned}
\frac{\partial MC(x,y,z,\sigma)}{\partial t} =\ & \frac{\partial}{\partial x}\left(D_L(MC,\sigma)\frac{\partial MC}{\partial x}\right) + \frac{\partial}{\partial y}\left(D_T(MC,\sigma)\frac{\partial MC}{\partial y}\right) \\
& + \frac{\partial}{\partial z}\left(D_R(MC,\sigma)\frac{\partial MC}{\partial z}\right)
\end{aligned} \tag{5.3}
$$

However, if we take into account the stress effect, the diffusion problem will become more complicated due to the viscoelastic mechano-sorptive behavior of wood and the elasto-damaged behavior in the FPZ. As a consequence, let us assume, in a first approximation, that the moisture transfer is independent of mechanical variables in this study. Hence, eq.(5.3) can be simply rewritten as:

$$
\begin{aligned}
\frac{\partial MC(x,y,z)}{\partial t} =\ & \frac{\partial}{\partial x}\left(D_L(MC)\frac{\partial MC}{\partial x}\right) + \frac{\partial}{\partial y}\left(D_T(MC)\frac{\partial MC}{\partial y}\right) \\
& + \frac{\partial}{\partial z}\left(D_R(MC)\frac{\partial MC}{\partial z}\right)
\end{aligned} \tag{5.4}
$$

As suggested in Simpson and Liu's work [101, 102, 153], the diffusion coefficients D_L, D_T and D_R of eq.(5.4), are nonlinear and depend on the moisture state. These diffusion coefficients can be expressed as:

$$D_\alpha(MC) = D_0^\alpha.e^{\kappa_0 MC} \qquad \text{with} \qquad \alpha = (L, R, T) \tag{5.5}$$

where D_0^α is the anhydrous transversal moisture diffusion coefficient in the α direction and κ_0 characterizes the non linear properties of the moisture diffusion coefficient.

The identification of all parameters $(D_L, D_T, D_R, \kappa_0, S...)$ will be presented in the next section. Note that, in the literature until now, moisture transfer is commonly analyzed without the crack growth phenomenon in order to remain unchanged the boundary condition for diffusion problem during the whole loading period.

5.1.2 Extension of the diffusion problem to cracked structure

For cracked structure, the diffusion process inside the FPZ is more complex because the moisture exchange surface is increased and sensitive to the RH of the surrounding air due to the crack opening, the damaged fibres. In order to simplify such a problem, the exchange surface or the boundary condition of the diffusion at the FPZ is assumed to be limited by a stress-free crack length a_{sf} as shown in Figure 5.5. The end of the stress-free crack length a_{sf} is defined at the position for which the tensile stress in the cohesive joint (FPZ) becomes different from zero (onset of the cohesive zone). The moisture distribution in wood is obtained by solving eq.(5.4). The moisture distribution inside the FPZ will be presented in section 5.3.1.
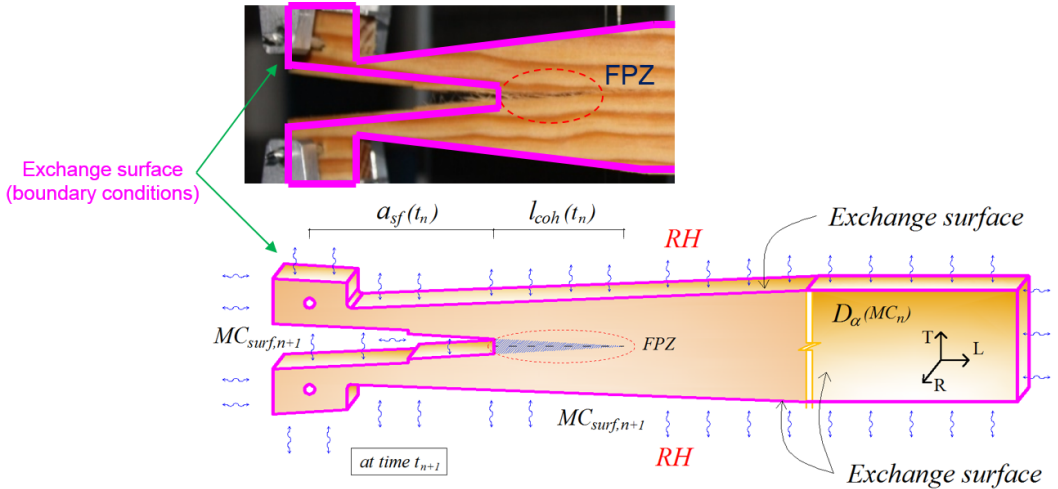
Figure 5.5: Exchange surface (boundary conditions) used in the diffusion analysis

When the crack propagates, as shown in Figure 5.5, the moisture exchange surface of the structure changed and needs a geometric re-meshing and then a projection of the hygro-thermal field before the crack propagation is necessary in the new configuration (with the new crack length a_{sf}).

5.1.3 Identification of the diffusion model parameters

According to Sderstrm and Salin [155], the surface emission coefficient S for wood drying is in range between 1.E-7 and 1.E-6 m/s. This coefficient depend on the wood surface interaction with the surrounding air. In this study, we assume that the surface emission coefficients are similar for the three directions (longitudinal, tangential and radial). The

surface emission coefficient S for Maritime pine is given in Agoua et al.'s work [1] ($S=$ 1.8E-7 m/s).

For the three orthotropic directions, values of diffusion coefficients $\mathbb{D}(MC)$ (eq.(5.5)) are obtained from Agoua and Perré [1] by fitting experimental results. The non linear moisture diffusion coefficient κ_0 for the absorption and the desorption phases is obtained from Herritsich's work on Radiata pine [74] because K_0 is unknown for Maritime pine; Radiata pine and Maritime pine have quite similar characteristics.

Table 5.1: Diffusion coefficients used in this study

Name	Unit	Longitudinal	Tangential	Radial	Ref.
Coefficient D_0	m^2/s	23.2E-10	2.87E-10	4.08E-10	Agoua and Perré [1]
κ_0 Absorption	-	3.7	1.64	1.97	Herritsich [74]
κ_0 Desorption	-	9.2	6.58	5.95	Herritsich [74]

5.1.4 Numerical diffusion analysis in the mTDCB specimen

This section presents the diffusion analysis in the mTDCB specimen without mechanical loading. Four cases corresponding to different stress-free crack lengths a_{sf} (40 mm, 60 mm, 80 mm, 100 mm) were analyzed. Note that the specimen is initially conditioned at 12% MC. The moisture at the specimen surface has been changed per 12 hours cycles (22% - 7%), as shown in Figure 5.6. The mesh size of mTDCB specimen is presented in Figure 5.6.
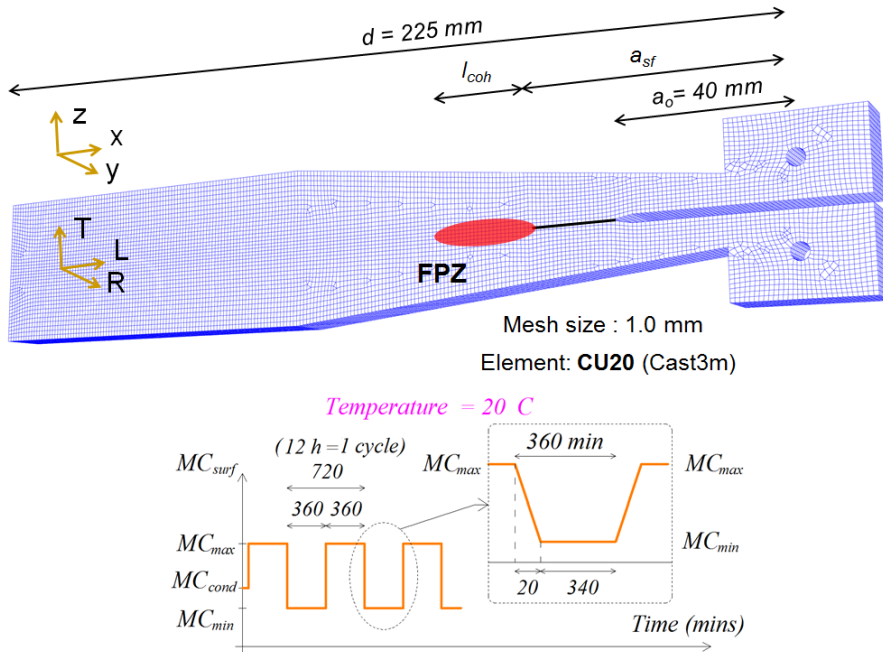
Figure 5.6: Mesh size and the consign of the varying moisture for the diffusion analysis

In order to study the moisture distribution around the tip of the FPZ, the moisture distribution of three plane sections of the specimen were analyzed (Fig. 5.7). These sections were all connected to the FPZ and correspond to the three principal directions of wood. We obtained the moisture distribution along the specimen width (line LA in section 1), along the specimen height (line LB in section 1) and along the center plane of specimen (lines LC and LD in section 2 and 3), as shown in Figure 5.7. In order to observe the moisture distribution inside the cohesive zone (FPZ), lines LC and LD have been extended to include this zone, too. Note that, l_{coh} was taken equal to 20 mm.
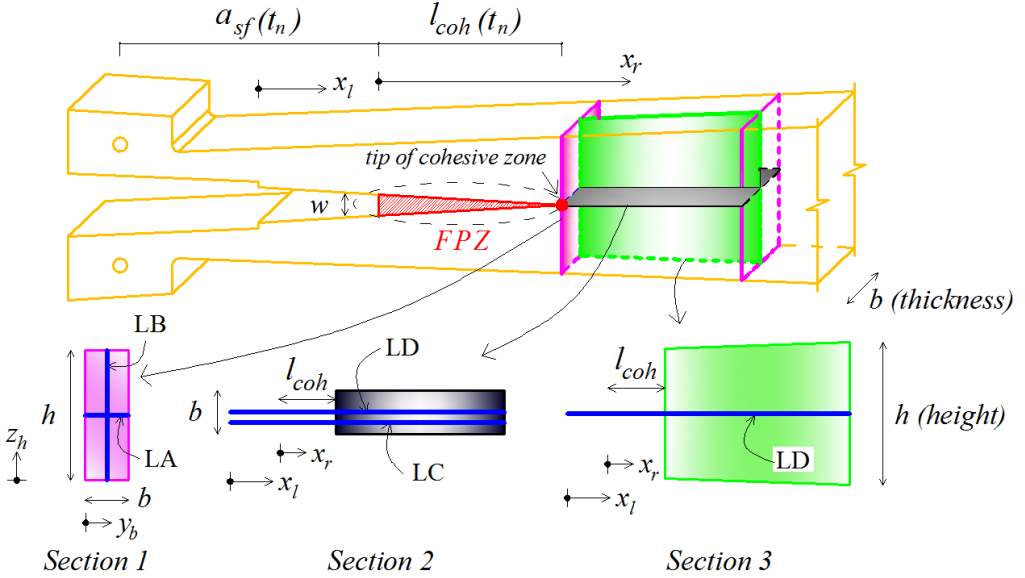
Figure 5.7: Position of three sections used to analyze moisture distributions

Figures 5.8 shows the moisture diffusion fields on the middle section of the mTDCB specimen and on the 3 chosen sections for different a_{sf}. Figure 5.9 shows the average moisture on the specimen and the moisture distribution along 4 lines LA, LB, LC, LD obtained from 4 different a_{sf}.

From the results in Figure 5.9, the average moisture of the specimen (Fig. 5.9a), the moisture distribution along the line LA (Fig. 5.9b) versus the diffusion time for the 4 cases are superimposed; while the moisture distribution along lines LB (Fig. 5.9c), LC (Fig. 5.9d) and LD (Fig. 5.9f) exhibit the same shape but are different due to the fact that different values of a_{sf} have been used.

As shown in Figure 5.9e, the curves (along the line LD) present a tangential shape horizontal asymptotes extreme parts corresponding to the moisture at the crack surface (beginning part) and the moisture at the heart of the specimen (ending part). Moreover, the shape length for moisture distribution between two parts is approximately in range of 20 - 30 mm.

As illustrated in Figure 5.9, it can be deduced that the moisture transfers are more

significant in the longitudinal direction than those in the tangential and the radial directions, which is related to the diffusion coefficients (Table 5.1): the diffusion coefficient in the longitudinal direction is 8 times higher than the one corresponding to the tangential direction.
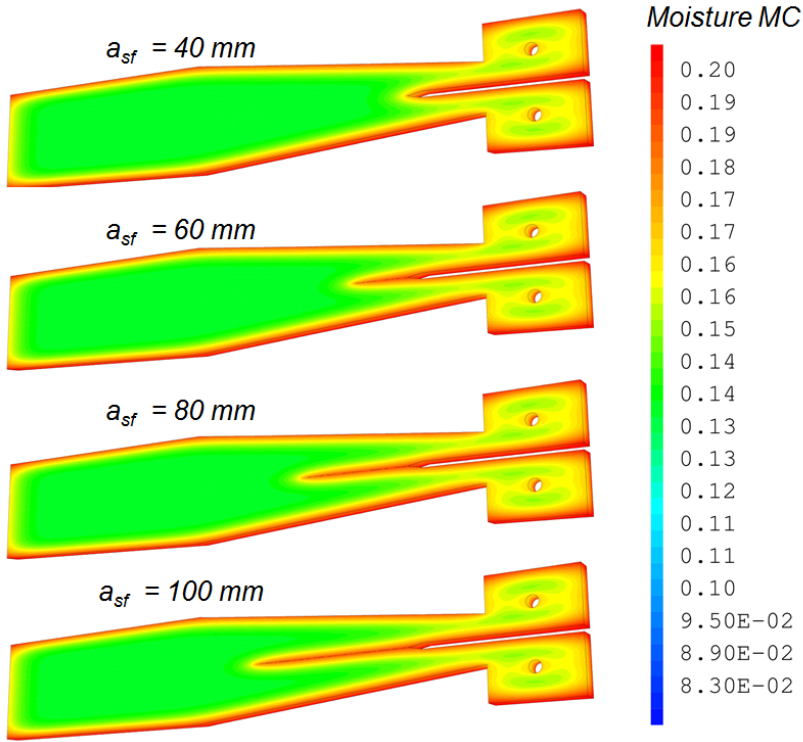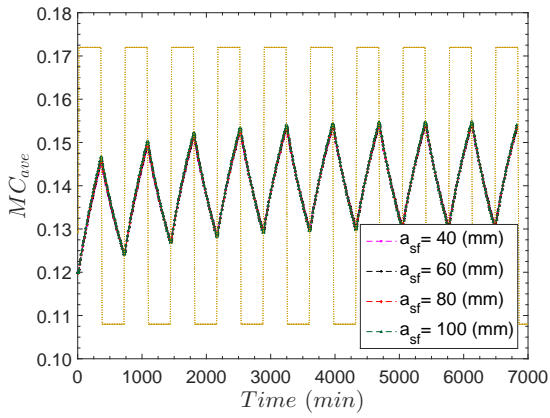

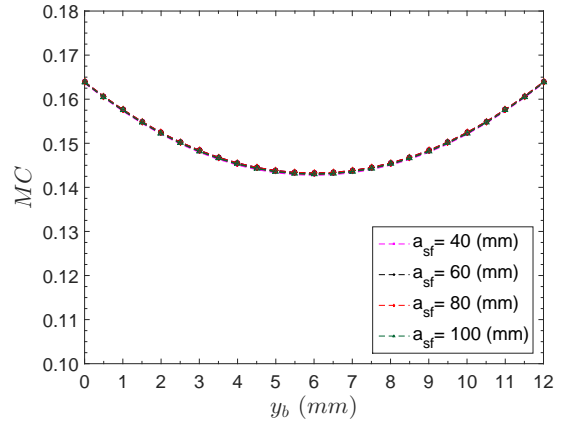(a) the middle section of the specimen
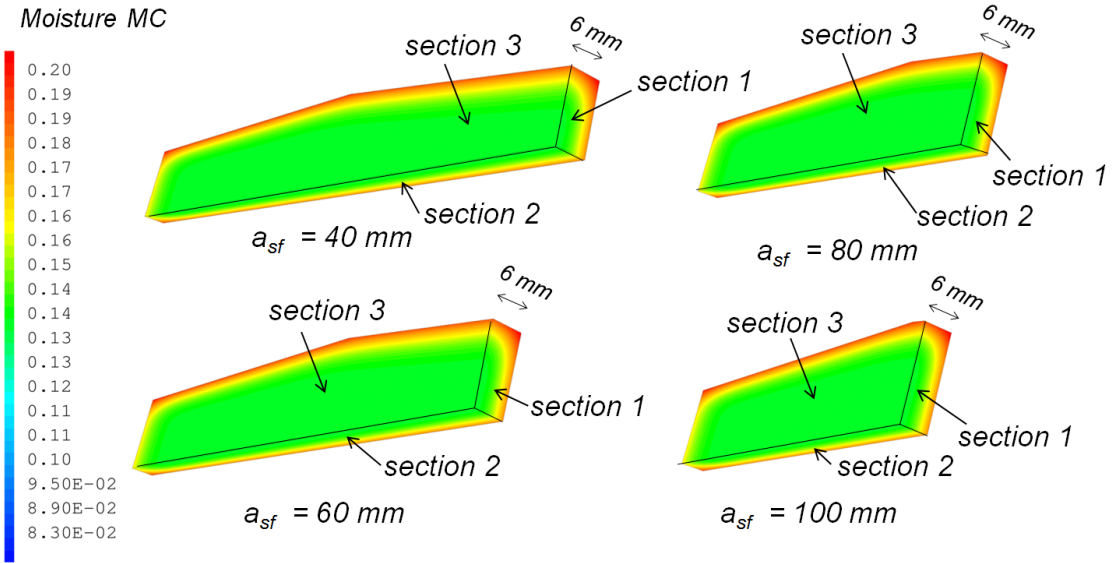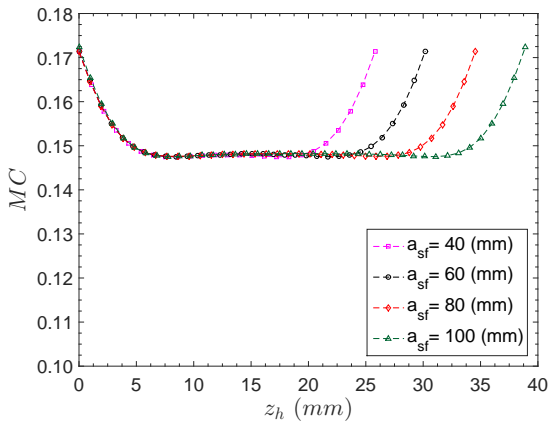

(b) three sections of the specimen

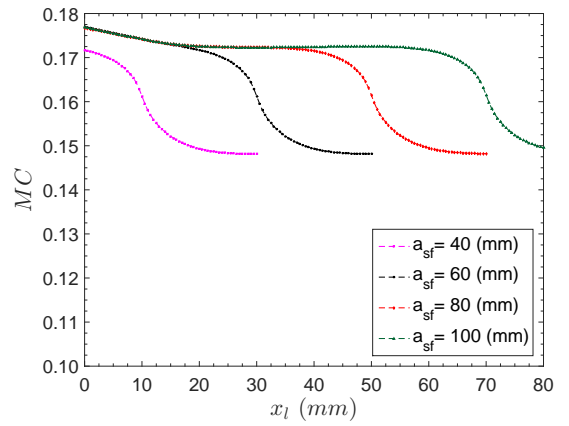Figure 5.8: Moisture field obtained at the diffusion time $t = 6820\ min$
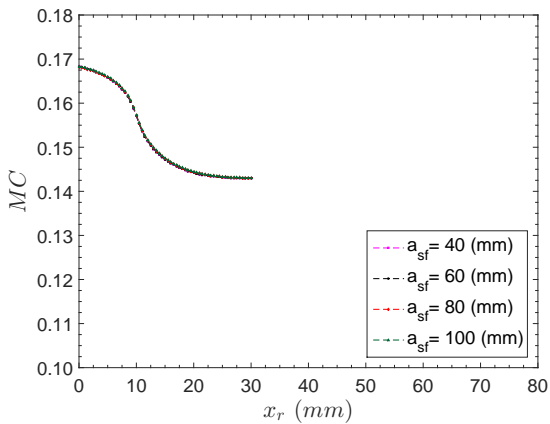
(a) Evolution of average moisture versus time

(b) Moisture distribution along the line LA

(c) Moisture distribution along the line LB

(d) Moisture distribution along the line LC

(e) Identical shape of moisture diffusion along the line LD
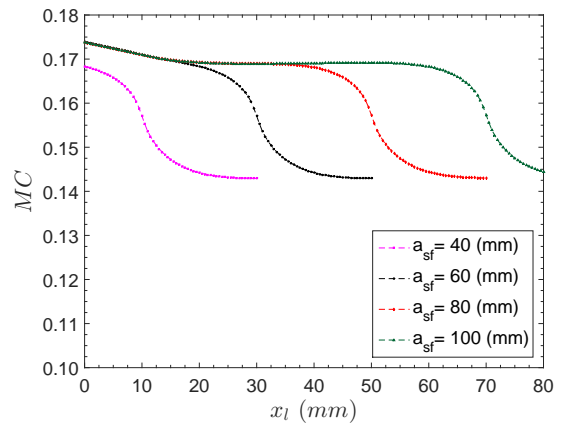
(f) Moisture distribution along the line LD

Figure 5.9: Moisture content distribution for 4 a_{sf} values. Note that, x_r, x_l, y_b and z_h are presented in Figure 5.7

5.2 Viscoelastic properties of wood under RH variations

Under moisture variations, an incremental formulation for a 1D viscoelastic mechano-sorptive behavior has been proposed and validated by Husson, Dubois et al. [49, 80–82]: the wood behavior is unidirectional formulated based on the thermodynamic theory. According to the authors, it is possible and necessary to extend 1D formulation into a 3D viscoelastic mechano-sorptive behavior. An attempt to extend the mechano-sorptive behavior in 3D is proposed in the following.

5.2.1 Development of a 3D viscoelastic mechano-sorptive model in FEA

Before describing the 3D mechano-sorptive behavior, let us recall the 1D formulation basis. This 1D formulation is based on the incremental formulation proposed by Husson, Dubois et al. [49, 80–82] and on the algorithm suggested by Ghazlan et al. [59] in which the moisture effect is considered as an external pseudo-load vector taking into account the past history of the mechanical loading and the moisture content variations. However, such method [49, 59, 80–82] is difficult to be combined with another model to analysis the fracture problem due to the non-linear problem (e.g., the viscoelastic mechano-sorptive model is used for wood substrate; the cohesive zone model is used to represent the FPZ in the cracked wood structure). Therefore, in order to combine two or more models in FEA, an algorithmic tangent operator is used to solve the non-linear problem [134, 156, 178].

As a result, in this thesis, the 3D mechano-sorptive model will be implemented thanks to the algorithmic tangent operator, which is detailed in the followings sections. The establishment of the total tangent operator for the 3D mechano-sorptive behavior is established from the thermodynamic theory.

5.2.1.1 Thermodynamic formulation

Thermodynamics is a powerful theoretical tool for the formulation of general problems characterized by the interdependence of the heat, the moisture and the deformation [49, 80–82]. In this thesis, the temperature is assumed to be constant and the moisture transfer is considered to be independent of mechanical variables as previously mentioned (see Section 5.1).

From a rheological point of view, the material model presented in this work is composed of four deformation mechanisms (Fig. 5.10 and eq.(5.6)) which provide an additive decomposition of the strain into instantaneous elastic response ε^e, shrinkage-swelling effect ε^{MC}, recoverable elastic mechano-sorption response ε^{e_ms} and recoverable viscoelastic mechano-sorption creep ε^{ve_ms}. The recoverable viscoelastic mechano-sorptive creep is described by Kelvin Voigt elements, which are very suitable for the whole thermodynamic formulation of the problem. In this thesis, the irrecoverable viscoelastic mechano-sorptive

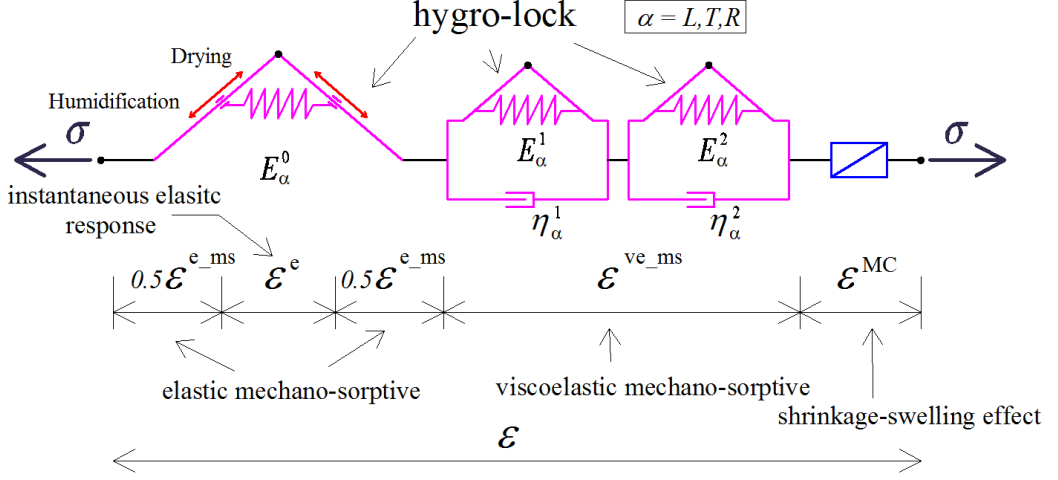creep is not considered due to the lack of experimental results.

Figure 5.10: Schematic representation of deformation mechanisms for the mechano-sorptive behavior

Based on the 4 deformation mechanisms (as shown in Figure 5.10), total strain $\underline{\varepsilon}$ is defined as:

$$\underline{\varepsilon} = \underline{\varepsilon}^e + \underline{\varepsilon}^{MC} + \underline{\varepsilon}^{e\_ms} + \sum_{i=1}^{N} \underline{\varepsilon}_i^{ve\_ms} \tag{5.6}$$

where $\underline{\varepsilon}_i^{ve\_ms}$ is the elemental viscoelastic mechano-sorptive strain in the ith element (N is the number of viscoelastic mechano-sorptive Kelvin Voigt elements. In this study, $N = 2$).

In order to establish the 3D mechano-sorptive behavior, the Helmholtz free energy Ψ is expressed as a function of the temperature T, the moisture content MC, the total strain $\underline{\varepsilon}$, the elemental strain tensors: $\underline{\varepsilon}^e$, $\underline{\varepsilon}^{e\_ms}$ and $\underline{\varepsilon}^{ve\_ms}$. Then the Helmholtz free energy can be expressed as:

$$\Psi(T, MC, \underline{\varepsilon}^e, \underline{\varepsilon}_i^{e\_ms}, \underline{\varepsilon}_i^{ve\_ms}) = \Phi(T, MC) + \Phi^e(\underline{\varepsilon}^e) + \Phi^{e\_ms}(\underline{\varepsilon}_i^{ve\_ms}) + \Phi^{ve\_ms}(\underline{\varepsilon}_i^{ve\_ms}) \tag{5.7}$$

where $\Phi(T, MC)$ is a general expression for the thermal energy and $\Phi^e(\underline{\varepsilon}^e)$ represents the elastic strain energy given by:

$$\Phi^e(\underline{\varepsilon}^e) = \frac{1}{2}\underline{\varepsilon}^e : \mathbb{C}^{e^{-1}} : \underline{\varepsilon}^e \tag{5.8}$$

where $\mathbb{C}^e$ is the elastic compliance tensor.

The terms $\Phi^{e\_ms}(\underline{\varepsilon}^{e\_ms})$ and $\Phi^{ve\_ms}(\underline{\varepsilon}^{ve\_ms})$ correspond to the energy stored in the elastic and viscoelastic parts of the mechanosorptive elements which are written in eqs.(5.9) and (5.10), respectively.

$$\Phi^{e\_ms}(\underline{\varepsilon}^{e\_ms}) = \frac{1}{2}\underline{\varepsilon}^{e\_ms} : \mathbb{C}^{e\_ms^{-1}} : \underline{\varepsilon}^{e\_ms} \tag{5.9}$$

$$\Phi_i^{ve\_ms}(\underline{\varepsilon}_i^{ve\_ms}) = \frac{1}{2}\underline{\varepsilon}_i^{ve\_ms^{-1}} : \mathbb{C}_i^{ve\_ms^{-1}} : \underline{\varepsilon}_i^{ve\_ms} \tag{5.10}$$

where $\mathbb{C}^{e\_ms}$ and $\mathbb{C}^{ve\_ms}$ represent the elemental elastic and viscoelastic mechano-sorptive compliance tensors, respectively.

In the FEA for this thesis, the components of any fourth-order or second-order tensor will follow the base $\vec{e_L} = (1,0,0)$, $\vec{e_T} = (0,0,1)$, $\vec{e_R} = (0,1,0)$ aligned with axes L-T-R, respectively. The relation between the stress and the elastic strain in 3D is given in the general forms as:

$$\underline{\varepsilon}^e = \mathbb{C}^e : \underline{\sigma} \tag{5.11}$$

$$
\begin{pmatrix}
\varepsilon_{LL} \\
\varepsilon_{TT} \\
\varepsilon_{RR} \\
\varepsilon_{LT} \\
\varepsilon_{LR} \\
\varepsilon_{TR}
\end{pmatrix}
=
\begin{bmatrix}
\dfrac{1}{E_L} & \dfrac{-\nu_{TL}}{E_T} & \dfrac{-\nu_{RL}}{E_R} & 0 & 0 & 0 \\
\dfrac{-\nu_{TL}}{E_T} & \dfrac{1}{E_T} & \dfrac{-\nu_{TR}}{E_T} & 0 & 0 & 0 \\
\dfrac{-\nu_{RL}}{E_R} & \dfrac{-\nu_{TR}}{E_T} & \dfrac{1}{E_R} & 0 & 0 & 0 \\
0 & 0 & 0 & \dfrac{1}{G_{LT}} & 0 & 0 \\
0 & 0 & 0 & 0 & \dfrac{1}{G_{LR}} & 0 \\
0 & 0 & 0 & 0 & 0 & \dfrac{1}{G_{TR}}
\end{bmatrix}
:
\begin{pmatrix}
\sigma_{LL} \\
\sigma_{TT} \\
\sigma_{RR} \\
\sigma_{LT} \\
\sigma_{LR} \\
\sigma_{TR}
\end{pmatrix}
\tag{5.12}
$$

5.2.1.2 Elastic or viscoelastic mechano-sorptive compliance

In this thesis, viscoelastic property of wood is described with a generalized Kelvin Voigt model as shown in Figure 5.11. The generalized Kelvin Voigt model is composed of one elastic spring and two hygro-lock Kelvin Voigt branches. The elastic spring represents the elastic instantaneous or the elastic mechano-sorptive behavior of wood. The two Kelvin Voigt branches represent the viscoelastic or the viscoelastic mechano-sorptive behavior.
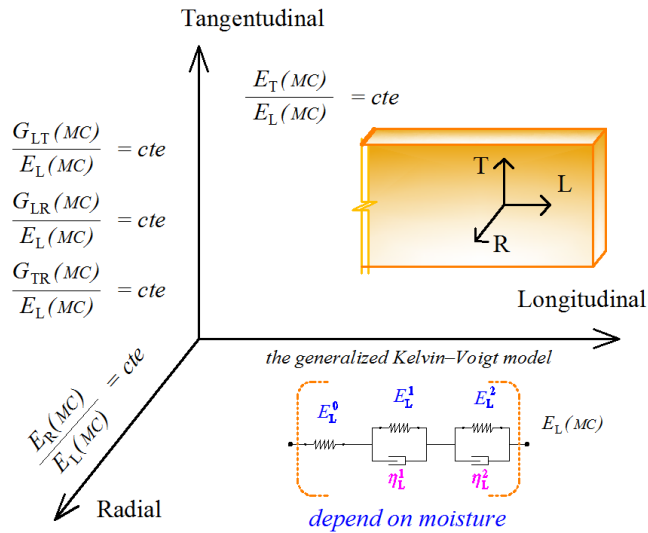
Figure 5.11: Schematic representation of the generalized Kelvin Voigt model

Based on the generalized Kelvin Voigt model, the viscoelastic creep compliance for a direction α (with $\alpha = L, T, R$) can be expressed as (Fig. 5.11):

$$\frac{1}{E_\alpha(MC)} = \frac{1}{E_\alpha^0(MC)} + \frac{1}{E_\alpha^1(MC)}\left[1 - e^{-\frac{t}{\tau_\alpha^1(MC)}}\right] + \frac{1}{E_\alpha^2(MC)}\left[1 - e^{-\frac{t}{\tau_\alpha^2(MC)}}\right] \quad (5.13)$$

where τ_α^i (MC)$= \dfrac{\eta_\alpha^i(MC)}{E_\alpha^i(MC)}$ (with $i = 1$ or 2).

The identification of creep parameters of 3D models for wood is a very difficult task. In spite of the available experimental data on the viscoelastic creep and the mechano-sorptive effect in timber structures, there is still a lack of both experimental work and theoretical background (i.e., the characterization of viscoelastic properties or the Poisson ratios of the orthotropic wood material are depending on the moisture gradients of each orthotropic direction: L-T-R).

Through few experimental tests in literature, viscoelastic creep compliance in the longitudinal direction for 3 different moisture contents for Maritime pine were obtained in Cariou's thesis [23]. In this study, the viscoelastic creep compliance was represented by a simple power law relationship. In order to apply the Kelvin Voigt model, we need to determine the viscoelastic creep compliance coefficients corresponding to Kelvin Voigt model. As a results, these coefficients in function of MC for the longitudinal direction are determined as:

$$\begin{cases} E_L^0(MC) & = 1,35.10^4\left[1 - 0,015(MC - 12)\right] & (MPa) \\ E_L^1(MC) & = 1,09.10^5\left[1 - 0,024(MC - 12)\right] & (MPa) \\ E_L^2(MC) & = 6,01.10^4\left[1 - 0,039(MC - 12)\right] & (MPa) \\ \eta_L^1(MC) & = 6,27.10^6\left[1 + 0,004(MC - 12)\right] & (MPa.h) \\ \eta_L^2(MC) & = 6,92.10^4\left[1 + 0,012(MC - 12)\right] & (MPa.h) \end{cases} \quad (5.14)$$

where MC is expressed in %.

As mentioned in the previous paragraph, we do not know the viscoelastic creep compliance versus moisture for other directions. Based on Guitard [68], we assume that the orthotropic factor for all directions is constant at any time and independent of moisture. Based on this assumption, Young moduli and shear moduli versus moisture such as $E_T(MC)$, $E_R(MC)$, $G_{LT}(MC)$, $G_{LR}(MC)$ and $G_{TR}(MC)$ (Fig. 5.11) are obtained from the following expressions:

$$\begin{cases} \dfrac{E_T^i(MC)}{E_L^i(MC)} & = \dfrac{E_T^0}{E_L^0}(12\%) & = 0.078 \\[2mm] \dfrac{E_R^i(MC)}{E_L^i(MC)} & = \dfrac{E_R}{E_L^0}(12\%) & = 0.123 \\[2mm] \dfrac{G_{LT}^i(MC)}{E_L^i(MC)} & = \dfrac{G_{LT}^0}{E_L^0}(12\%) & = 0.081 \\[2mm] \dfrac{G_{LR}^i(MC)}{E_L^i(MC)} & = \dfrac{G_{LR}^0}{E_L^0}(12\%) & = 0.076 \\[2mm] \dfrac{G_{TR}^i(MC)}{E_L^i(MC)} & = \dfrac{G_{TR}^0}{E_L^0}(12\%) & = 0.006 \end{cases} \tag{5.15}$$

where i denotes the element of the generalized Kelvin Voigt model ($i = 0$, 1 or 2).

5.2.1.3   Strain increment calculation

From a computational point of view, creep problem can be solved by using an incremental formulation in relation with time. Moreover, by taking into account the coupling of moisture and stresses, the incremental formulation for the mechano-sorptive creep is presented in eq.(5.6), the total strain increment $\Delta\varepsilon$ is obtained as:

$$\Delta\underline{\varepsilon} = \Delta\underline{\varepsilon}^e + \Delta\underline{\varepsilon}^{MC} + \Delta\underline{\varepsilon}^{e\_ms} + \sum_{i=1}^{N} \Delta\underline{\varepsilon}_i^{ve\_ms} \tag{5.16}$$

where $\Delta\underline{\varepsilon}^e$ is elastic strain increment, $\Delta\underline{\varepsilon}^{MC}$ is shrinkage-swelling strain increment, $\Delta\underline{\varepsilon}^{e\_ms}$ is recoverable elastic mechano-sorptive strain increment and $\Delta\underline{\varepsilon}^{ve\_ms}$ is recoverable viscoelastic mechano-sorptive strain increment.

5.2.1.3.a   Elastic strain

The main constitutive equation of the model is obtained by differentiating the free energy of eq.(5.16) which respects the total strain tensor:

$$\underline{\sigma} := \frac{\partial\Psi}{\partial\varepsilon} = \mathbb{C}^{e^{-1}} : \underline{\varepsilon}^e \tag{5.17}$$

A linear evolution of the stress is assumed during each time increment so the increment of the elastic strain depending on Δt_n at the current time step t_{n+1} is:

$$\Delta\underline{\varepsilon}_n^e = \mathbb{C}_{n+1}^e : \Delta\underline{\sigma}_n \tag{5.18}$$

In the case of orthotropic materials as wood, the elastic compliance tensor $\mathbb{C}^e_{n+1}(MC)$ is defined as:

$$\mathbb{C}^e_{n+1}(MC) = \begin{bmatrix} \frac{1}{E^0_L(MC)} & \frac{-\nu_{TL}}{E^0_T(MC)} & \frac{-\nu_{RL}}{E^0_R(MC)} & 0 & 0 & 0 \\ \frac{-\nu_{TL}}{E^0_T(MC)} & \frac{1}{E^0_T(MC)} & \frac{-\nu_{TR}}{E^0_T(MC)} & 0 & 0 & 0 \\ \frac{-\nu_{RL}}{E^0_R(MC)} & \frac{-\nu_{TR}}{E^0_T(MC)} & \frac{1}{E^0_R(MC)} & 0 & 0 & 0 \\ 0 & 0 & 0 & \frac{1}{G^0_{LT}(MC)} & 0 & 0 \\ 0 & 0 & 0 & 0 & \frac{1}{G^0_{LR}(MC)} & 0 \\ 0 & 0 & 0 & 0 & 0 & \frac{1}{G^0_{TR}(MC)} \end{bmatrix} \tag{5.19}$$

Note that MC written in eq.(5.19) is the moisture corresponding to MC_{n+1} at the current time step t_{n+1}. Based on eq.(5.15), the elastic compliance tensor $\mathbb{C}^e_{n+1}(MC)$ in eq.(5.19) can be simply expressed in function of $E^0_L(MC)$ as:

$$\mathbb{C}^e_{n+1}(MC) = \frac{1}{E^0_L(MC_{n+1})} \begin{bmatrix} 1 & \frac{-\nu_{TL}}{0.078} & \frac{-\nu_{RL}}{0.123} & 0 & 0 & 0 \\ \frac{-\nu_{TL}}{0.078} & \frac{1}{0.078} & \frac{-\nu_{TR}}{0.078} & 0 & 0 & 0 \\ \frac{-\nu_{RL}}{0.123} & \frac{-\nu_{TR}}{0.078} & \frac{1}{0.123} & 0 & 0 & 0 \\ 0 & 0 & 0 & \frac{1}{0.081} & 0 & 0 \\ 0 & 0 & 0 & 0 & \frac{1}{0.076} & 0 \\ 0 & 0 & 0 & 0 & 0 & \frac{1}{0.006} \end{bmatrix} \tag{5.20}$$

where Poisson's coefficients ($\nu_{TL} = 0.425$, $\nu_{RL} = 0.385$ and $\nu_{TR} = 0.315$) are supposed to be independent of the moisture (Table 3.1).

5.2.1.3.b Shrinkage-swelling strain

Under variable moisture content conditions, wood is subjected to swelling-shrinkage effects. In this work, we assumed a total decoupling between the viscoelastic mechano-sorptive behavior and swelling-shrinkage effects. Based on this consideration, the free shrinkage-swelling strain increment can be expressed as:

$$\Delta \underline{\varepsilon}^{MC}_n = \underline{\underline{\alpha}} . \Delta MC_n \tag{5.21}$$

where $\Delta MC_n = MC_{n+1} - MC_n$. And, $\underline{\underline{\alpha}}$ is second-order shrinkage-swelling tensor (assumed to be independent of moisture content and of stress level) which is rewritten as:

$$\underline{\underline{\alpha}} = \begin{bmatrix} \alpha_L & 0 & 0 & 0 & 0 & 0 \\ 0 & \alpha_T & 0 & 0 & 0 & 0 \\ 0 & 0 & \alpha_R & 0 & 0 & 0 \\ 0 & 0 & 0 & 0 & 0 & 0 \\ 0 & 0 & 0 & 0 & 0 & 0 \\ 0 & 0 & 0 & 0 & 0 & 0 \end{bmatrix} \tag{5.22}$$

The values of the shrinkage-swelling coefficients used in eq.(5.22) are those reported by Guitard [68]: $\alpha_L = 0.005\%/\%$, $\alpha_T = 0.32\%/\%$, $\alpha_R = 0.19\%/\%$.

5.2.1.3.c   Recoverable elastic mechano-sorptive strain

For describing the recoverable elastic mechano-sorptive strain, an equation similar to the simple elastic response is used:

$$\underline{\sigma}^{e\_ms} := -\frac{\partial \Psi}{\partial \varepsilon^{e\_ms}} = \underline{\sigma} - \mathbb{C}^{e\_ms^{-1}} : \underline{\varepsilon}^{e\_ms} \tag{5.23}$$

The solution of eq.(5.23) is obtained from the work of Husson et al. [49, 80–82]:

$$\Delta \underline{\varepsilon}_n^{e\_ms} = \mathbb{C}_{n+1}^{e\_ms} : \Delta \underline{\sigma}_n + \widetilde{\underline{\varepsilon}}_n^{e\_ms} \tag{5.24}$$

where $\mathbb{C}_{n+1}^{e\_ms}$ is elastic mechano-sorptive compliance tensor and $\widetilde{\underline{\varepsilon}}_n^{e\_ms}$ summarizes history effects of the humidity and those of the external mechanical loadings.

Two mechano-sorptive compliance tensors can be determined: one for drying period (hardening case) and the other for wetting period (softening case).

- For the hardening case $(MC_n > MC_{n+1})$:

$$\begin{cases} \mathbb{C}_{n+1}^{e\_ms} = \left[\frac{C_n^0 + C_{n+1}^0}{2} \left(\frac{1}{C_{n+1}^0} \right) - 1 \right] \mathbb{C}_{n+1}^e \\ \widetilde{\underline{\varepsilon}}_n^{e\_ms} = 0 \end{cases} \tag{5.25}$$

- For the softening case $(MC_n < MC_{n+1})$:

$$\begin{cases} \mathbb{C}_{n+1}^{e\_ms} = 0 \\ \widetilde{\underline{\varepsilon}}_n^{e\_ms} = \mathbb{C}_{n+1}^e : (\underline{\sigma}_n - \underline{\sigma}(\bar{t})) - \{ \underline{\varepsilon}_n^{e\_ms} - \underline{\varepsilon}^{e\_ms}(\bar{t}) \} \end{cases} \tag{5.26}$$

In the framework of the hygro-lock approach, during the softening case (Fig. 5.12), $\bar{t}$ is the time in which the compliance (in the compliance history) is equal to the current compliance of this element. The elastic compliance C_n^0 and C_{n+1}^0 (Fig. 5.12 and eq.(5.25)) are defined in eq.(5.27). The values of the stress $\underline{\sigma}(\bar{t})$ and of the strain $\underline{\varepsilon}^{e\_ms}(\bar{t})$ are the stress and the strain corresponding to the time $\bar{t}$, respectively.

$$C_n^0 = \frac{1}{E_L^0(MC_n)} \quad \text{and} \quad C_{n+1}^0 = \frac{1}{E_L^0(MC_{n+1})} \tag{5.27}$$
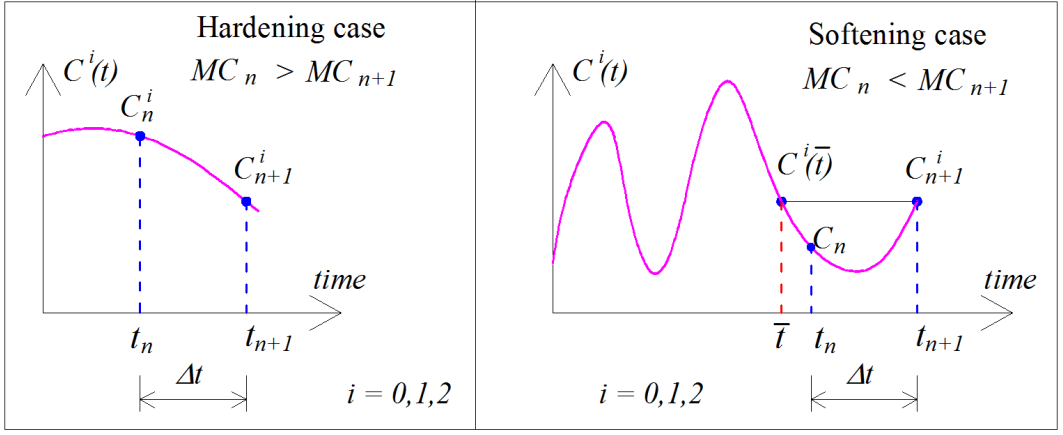
Figure 5.12: Compliance evolution for one direction

5.2.1.3.d Recoverable viscoelastic mechano-sorptive strain

For describing the recoverable viscoelastic mechano-sorption, an equation similar to the simple viscoelastic creep one for the ith branch of the generalized Kelvin Voigt model is given:

$$\underline{\sigma}_i^{ve\_ms} := -\frac{\partial \Psi}{\partial \underline{\varepsilon}_i^{ve\_ms}} = \underline{\sigma} - \mathbb{C}_i^{ve\_ms^{-1}} : \underline{\varepsilon}_i^{ve\_ms} \tag{5.28}$$

The solution of eq.(5.28) is also obtained in the work of Husson et al. [49, 80–82]:

$$\Delta \underline{\varepsilon}_{i,n}^{ve\_ms} = \mathbb{C}_{i,n+1}^{ve\_ms} : \Delta \underline{\sigma}_n + \widetilde{\underline{\varepsilon}}_{i,n}^{ve\_ms} \tag{5.29}$$

where $\mathbb{C}_{i,n+1}^{ve\_ms}$ is viscoelastic mechano-sorptive compliance tensor and $\widetilde{\underline{\varepsilon}}_{i,n}^{ve\_ms}$ summarizes history effects of the humidity and of the external mechanical loadings.

From Kelvin-Voigt model with 2 branches, one can define viscoelastic parameters used in the following of this work (at the moisture MC_n and MC_{n+1}) as:

$$\begin{cases} C_n^i = \dfrac{1}{E_L^i(MC_n)} \text{ and } C_{n+1}^i = \dfrac{1}{E_L^i(MC_{n+1})} \\ \beta_n^i = \dfrac{1}{\eta_L^i(MC_n)} \text{ and } \beta_{n+1}^i = \dfrac{1}{\eta_L^i(MC_{n+1})} \end{cases} \text{ where } i = 1 \text{ or } 2 \tag{5.30}$$

- For the hardening case $(MC_n < MC_{n+1})$:

$$\begin{cases} \mathbb{C}_{i,n+1}^{ve\_ms} = \left[A_{i,n+1}^h \dfrac{1}{C_{n+1}^0} \right] \mathbb{C}_{n+1}^e \\ \widetilde{\underline{\varepsilon}}_{i,n}^{ve\_ms} = \mathbb{C}_{i,n+1}^{ve\_ms} . \sigma_{i,n}^{\eta,ve\_ms} . \dfrac{3.[\beta_n^i + \beta_{n+1}^i]}{[\beta_n^i + 2.\beta_{n+1}^i]} \end{cases} \tag{5.31}$$

where $A_{i,n+1}^h$ as written as:

$$A_{i,n+1}^h = \frac{[C_n^i + C_{n+1}^i].[\beta_n^i + 2.\beta_{n+1}^i].\Delta t_n}{6.[C_n^i + C_{n+1}^i] + 2.[\beta_n^i + 2.\beta_{n+1}^i].\Delta t_n} \tag{5.32}$$

- For the softening case $(MC_n < MC_{n+1})$:

$$\begin{cases}
\mathbb{C}_{i,n+1}^{ve\_ms} = \left[A_{i,n+1}^s \dfrac{1}{C_{n+1}^0} \right] \mathbb{C}_{n+1}^e \\[2mm]
\widetilde{\varepsilon}_{i,n}^{ve\_ms} = \mathbb{C}_{i,n+1}^{ve\_ms} : \left[\dfrac{3.[\beta_n^i + \beta_{n+1}^i]}{[\beta_n^i + 2.\beta_{n+1}^i]} . \underline{\sigma}_{i,n}^{\eta,ve\_ms} + \underline{\sigma}_{i,n}^{k,ve\_ms} - \underline{\sigma}_i^{k,ve\_ms}(\bar{t}) \right] \\[2mm]
\quad - \left\{ \mathbb{F}_{i,n+1}^s \left(\underline{\varepsilon}_{i,n}^{ve\_ms} - \underline{\varepsilon}_i^{ve\_ms}(\bar{t}) \right) \right\}
\end{cases} \tag{5.33}$$

where $A_{i,n+1}^s$ as written as:

$$A_{i,n+1}^s = \frac{C_{n+1}^i.[\beta_n^i + 2.\beta_{n+1}^i].\Delta t_n}{6.C_{n+1}^i + [\beta_n^i + 2.\beta_{n+1}^i].\Delta t_n} \tag{5.34}$$

and $\mathbb{F}_{i,n}^s$ as written as:

$$\mathbb{F}_{i,n+1}^s = \left[\frac{[\beta_n^i + 2.\beta_{n+1}^i].\Delta t_n}{6.C_n^i + [\beta_n^i + 2.\beta_{n+1}^i].\Delta t_n} \right] \tag{5.35}$$

In the framework of the hygro-lock approach, during the softening case (Fig. 5.12), $\bar{t}$ is the time in which the compliance (in the compliance history) is equal to the current compliance of this element. The values of the stress $\underline{\sigma}_i^{k,ve\_ms}(\bar{t})$ and of the strain $\underline{\varepsilon}_i^{ve\_ms}(\bar{t})$ are the stress and the strain corresponding to the time $\bar{t}$, respectively. The mechanical field at all Gaussian points in each element are stored during the calculation.

Based on eqs.(5.17), (5.21), (5.24), (5.29) (which indicate the 4 deformations in the viscoelastic mechano-sorptive model), the total deformation (eq.(5.16)) is then obtained. In order to facilitate the implantation of the total deformation in FEA, a total tangent operator is introduced and presented in the next paragraphs.

5.2.1.4 Computation of total tangent operator

From eqs.(5.17), (5.21), (5.24), (5.29) and eq.(5.16), the total tangent operator $\mathbb{C}^{tan}$ of the whole model is obtained from eqs.(5.36) to eq.(5.39):

$$\Delta\underline{\sigma}_n = \mathbb{C}^{e^{-1}} : \Delta\underline{\varepsilon}_n^e = \mathbb{C}^{e^{-1}} : (\Delta\underline{\varepsilon}_n - \Delta\underline{\varepsilon}_n^{e\_ms} - \sum_{i=1}^{N} \Delta\underline{\varepsilon}_{i,n}^{ve\_ms} - \Delta\underline{\varepsilon}_n^{MC}) \tag{5.36}$$

$$\Delta\underline{\sigma}_n = \mathbb{C}_{n+1}^{e^{-1}} : (\Delta\underline{\varepsilon}_n - (\mathbb{C}_{n+1}^{e\_ms} : \Delta\underline{\sigma}_n + \widetilde{\underline{\varepsilon}}_n^{e\_ms}) - \sum_{i=1}^{N}(\mathbb{C}_{i,n+1}^{ve\_ms} : \Delta\underline{\sigma}_n + \widetilde{\underline{\varepsilon}}_{i,n}^{ve\_ms}) - \Delta\underline{\varepsilon}_n^{MC}) \tag{5.37}$$

$$(\mathbb{C}_{n+1}^e + \mathbb{C}_{n+1}^{e\_ms} + \sum_{i=1}^{N}\mathbb{C}_{i,n+1}^{ve\_ms}) : \Delta\underline{\sigma}_n = (\Delta\underline{\varepsilon}_n - \widetilde{\underline{\varepsilon}}_n^{e\_ms} - \sum_{i=1}^{N}\widetilde{\underline{\varepsilon}}_{i,n}^{ve\_ms} - \Delta\underline{\varepsilon}_n^{MC}) \tag{5.38}$$

$$\Delta\underline{\sigma}_n = \mathbb{C}^{tan^{-1}}(\Delta\underline{\varepsilon}_n - \widetilde{\underline{\varepsilon}}_n^{e\_ms} - \sum_{i=1}^{N}\widetilde{\underline{\varepsilon}}_{i,n}^{ve\_ms} - \Delta\underline{\varepsilon}_n^{MC}) \tag{5.39}$$

where $\mathbb{C}^{tan}$, representing the tangent compliance operator of the whole model, is defined as:

$$\mathbb{C}^{tan} = \mathbb{C}^e_{n+1} + \mathbb{C}^{e\_ms}_{n+1} + \sum_{i=1}^{N} \mathbb{C}^{ve\_ms}_{i,n+1} \tag{5.40}$$

Based on eq.(5.40), when the properties of wood are only elastic, the term $\mathbb{C}^{ve\_ms}_{i,n+1}$ is equal to zero. On the other hand, when the moisture is considered to be constant, the term $\mathbb{C}^{e\_ms}_{n+1}$ is equal to zero; and the term $\mathbb{C}^{ve\_ms}_{i,n+1}$ represent the viscoelastic compliance tensor.

5.2.1.5   Newton-Raphson algorithm for the non-linear FE solution

At time t_{n+1} $(= t_n + \Delta t_n)$, the displacement of the whole structure $\mathbf{u}_n$ (at the end of the time t_n) and the external loading $\mathbf{F}^{ext}_{n+1}$ are known. We would like to determine the stress and the strain at the time t_{n+1}.

Due to the non-linear problem in FEA, at time t_{n+1}, we want to find an equilibrium state between the internal loading $\mathbf{F}^{int}_{n+1}$ and the external loading $\mathbf{F}^{ext}_{n+1}$ on the structure. This internal loading $\mathbf{F}^{int}_{n+1}$ is generated by the stress and the strain in the structure. To do that, a procedure iteration to find the minimum residual force at the time t_{n+1}, which is defined by the difference between the internal and external loading, is required.

Figure 5.13 shows a schematic of the iteration process to find the minimum residual force in which the Newton-Raphson algorithm is used for the Non-Linear Finite Element solution.
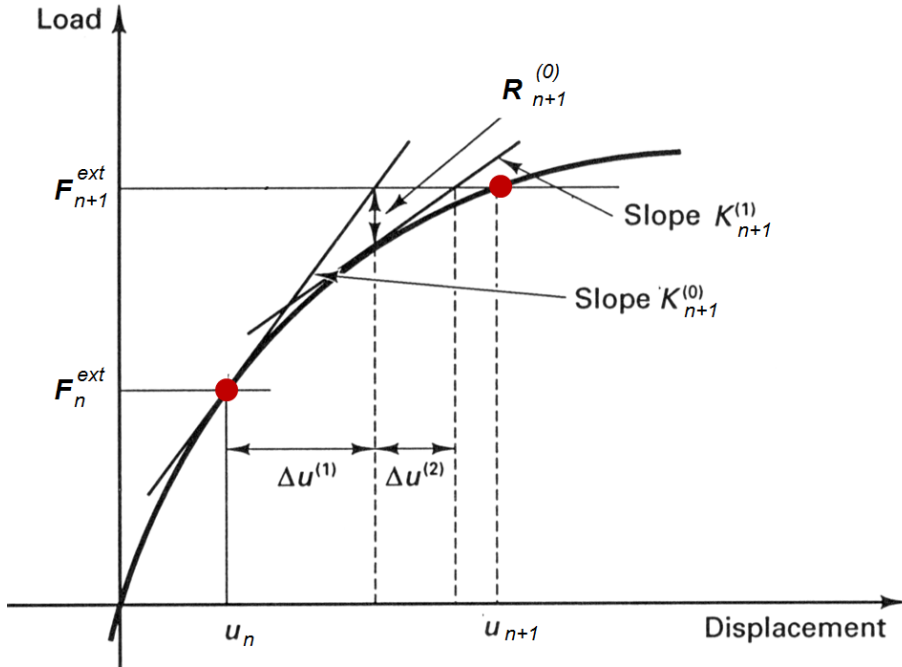
Figure 5.13: Newton-Raphson algorithm for Non-Linear Finite Element solution

At the time t_{n+1}, the residual force $\mathbf{R}(\mathbf{u}_{n+1}^j)$ for the jth iteration is written as:

$$\left|\mathbf{R}(\mathbf{u}_{n+1}^j)\right| = \left|\mathbf{F}_{n+1}^{j,int} - \mathbf{F}_{n+1}^{ext}\right| < TOL \qquad (5.41)$$

where $\mathbf{F}_{n+1}^{int}$ is expressed as:

$$\mathbf{F}_{n+1}^{j,int} = \int_V \mathbb{B}^T : \underline{\sigma}(\mathbf{u}_{n+1}^j)dV \qquad (5.42)$$

in which $\mathbb{B}$ is the strain-displacement transformation matrix. $\mathbf{u}_{n+1}^j$ is the displacement corresponding to the jth iteration at the time t_{n+1}. TOL is a reasonable tolerance.

Moreover, a displacement increment during the iteration is obtained by:

$$\delta\mathbf{u}^{j+1} = \delta\mathbf{u}_{n+1}^{j+1} = \mathbf{u}_{n+1}^{j+1} - \mathbf{u}_{n+1}^j = -\left[\frac{\partial\mathbf{R}(\mathbf{u}_{n+1}^j)}{\partial\mathbf{u}}\right]^{-1}\mathbf{R}(\mathbf{u}_{n+1}^j) \qquad (5.43)$$

With $\mathbf{K}(\mathbf{u}_{n+1}^j) = \left[\dfrac{\partial\mathbf{R}(\mathbf{u}_{n+1}^j)}{\partial\mathbf{u}}\right]^{-1}$, eq.(5.43) can be written as:

$$\mathbf{K}(\mathbf{u}_{n+1}^j)\delta\mathbf{u}_{n+1}^{j+1} = -\mathbf{R}(\mathbf{u}_{n+1}^j) \qquad = -(\mathbf{F}_{n+1}^{j,int} - \mathbf{F}_{n+1}^{ext}) \qquad (5.44)$$

The current displacement increment for the jth iteration is expressed as:

$$\mathbf{u}_{n+1}^j - \mathbf{u}_{n+1} = \Delta\mathbf{u}^j = \sum_{k=1}^j \delta\mathbf{u}^k \qquad (5.45)$$

Therefore, $\mathbf{K}(\mathbf{u}_{n+1}^j)$ is rewritten as:

$$\mathbf{K}(\mathbf{u}_{n+1}^j) = \int_V \mathbb{B}^T \mathbb{C}^{tan^{-1}}\mathbb{B}dV \qquad (5.46)$$

where $\mathbb{C}^{tan}$ is the compliance tangent matrix (the Jacobian of constitutive law) obtained by eq.(5.40).

Let us remember that, for each iteration, by varying incremental displacements, $\mathbf{K}$ and $\mathbf{R}$ are obviously different. For the time increment Δt, the iteration is performed until a convergence criterion is achieved with a reasonable tolerance TOL. The convergence criterion is expressed as:

$$\left|\mathbf{R}(\mathbf{u}_{n+1}^j)\right| < TOL \qquad (5.47)$$

The stress and the strain at the time t_{n+1} are obtained when the eq.(5.47) is satisfied. In this thesis, the iteration procedure, called a Stress Updating Algorithm, is detailed in the following paragraph and implanted in the source Esope of the finite element code Cast3m [26].

5.2.1.6 Implementation of stress updating algorithm into the subroutine of Castem

At the beginning of the current time t_{n+1}, the moisture content MC_{n+1}, the moisture increment ΔMC_{n+1} and the total strain increment $\Delta\underline{\varepsilon}_{n+1}$ have been calculated. The value of the strain increment $\Delta\underline{\varepsilon}_{n+1}$ is preliminarily estimated considering the whole material behavior as elastic (instantaneous elastic response). Moreover, the initial values of the stress, the strain for each elemental deformation mechanism are equal to those provided at the end of the previous time t_n. In particular, the stress and the strain for each elemental deformation mechanism corresponding to all step time are stored in the array form. The algorithm at the current time step t_{n+1} can be schematically listed as the following steps:

1. The elastic compliance tensor $\mathbb{C}^e_{n+1}$ (eq.(5.19)), the elastic and viscoelastic mechanosorptive compliance tensor $\mathbb{C}^{e\_ms}_{n+1}$ (eq.(5.25) or eq.(5.26)), $\mathbb{C}^{ve\_ms}_{i,n+1}$ (eq.(5.31) or eq.(5.33)) and the strain increments $\widetilde{\underline{\varepsilon}}^{e\_ms}_{n}$ (eq.(5.25) or eq.(5.26)) and $\widetilde{\underline{\varepsilon}}^{ve\_ms}_{i,n}$ (eq.(5.31) or eq.(5.33)) are computed.

2. The tangent compliance operator of the whole model $\mathbb{C}^{tan}$ (eq.(5.40)) is then obtained.

3. The new stress increment $\Delta\underline{\sigma}_n$ (eq.(5.39)) and the mechano-sorptive creep strain increments $\Delta\underline{\varepsilon}^{e\_ms}_n$ (eq.(5.24)), $\Delta\underline{\varepsilon}^{ve\_ms}_{i,n}$ (eq.(5.29)) are calculated.

4. The updated values of the total stress, the viscoelastic mechano-sorptive strain are performed as:

$$\Delta\underline{\sigma}_{n+1} = \underline{\sigma}_n + \Delta\underline{\sigma}_n \tag{5.48}$$

$$\underline{\varepsilon}_{n+1} = \underline{\varepsilon}_n + \Delta\underline{\varepsilon}_n \tag{5.49}$$

$$\underline{\varepsilon}^e_{n+1} = \underline{\varepsilon}^e_n + \Delta\underline{\varepsilon}^e_n \tag{5.50}$$

In the ith Kelvin Voigt branch ($i = 1, 2$):

$$\underline{\varepsilon}^{ve\_ms}_{i,n+1} = \underline{\varepsilon}^{ve\_ms}_{i,n} + \Delta\underline{\varepsilon}^{ve\_ms}_{i,n} \tag{5.51}$$

$$\underline{\sigma}^{k,ve\_ms}_{i,n+1} = \underline{\sigma}^{k,ve\_ms}_{i,n} + \Delta\underline{\sigma}^{k,ve\_ms}_{i,n} \tag{5.52}$$

$$\underline{\sigma}^{\eta,ve\_ms}_{i,n+1} = \underline{\sigma}^{\eta,ve\_ms}_{i,n} + \Delta\underline{\sigma}^{\eta,ve\_ms}_{i,n} \tag{5.53}$$

In eq.(5.53), $\Delta\underline{\sigma}^{\eta,ve\_ms}_{i,n}$ is given as:

$$\Delta\underline{\sigma}^{\eta,ve\_ms}_{i,n} = \mathbb{C}^{\eta^{-1}}_{i,n+1} : \Delta\underline{\varepsilon}^{ve\_ms}_{i,n} - \left[\frac{3(\beta^i_n + \beta^i_{n+1})}{\beta^i_n + 2.\beta^i_{n+1}}\right]\underline{\sigma}^{\eta,ve\_ms}_{i,n} \tag{5.54}$$

where:

$$\mathbb{C}^{\eta}_{i,n+1} = \left[\left(\frac{(\beta^i_n + \beta^i_{n+1})\Delta t_n}{6}\right)\left(\frac{1}{C^0_{n+1}}\right)\right]\mathbb{C}^e_{n+1} \tag{5.55}$$

In eq.(5.52), $\Delta\underline{\sigma}_{i,n}^k$ depends on the hardening case or the softening case, and is given as:

- For the hardening case:

$$\Delta\underline{\sigma}_{i,n}^k = \mathbb{C}_{i,n+1}^{h^{-1}} : \Delta\underline{\varepsilon}_{i,n}^{ve\_ms} \tag{5.56}$$

where:

$$\mathbb{C}_{i,n+1}^h = \left[\left(\frac{C_n^i + C_{n+1}^i}{2}\right)\left(\frac{1}{C_{n+1}^0}\right)\right]\mathbb{C}_{n+1}^e \tag{5.57}$$

- For the softening case:

$$\Delta\underline{\sigma}_{i,n}^k = \mathbb{C}_{i,n+1}^{s^{-1}} : \left[\underline{\varepsilon}_{i,n}^{ve\_ms} + \Delta\underline{\varepsilon}_{i,n}^{ve\_ms} - \underline{\varepsilon}_i^{ve\_ms}(\bar{t})\right] + \underline{\sigma}_i^{k,ve\_ms}(\bar{t}) - \underline{\sigma}_{i,n}^{k,ve\_ms} \tag{5.58}$$

where:

$$\mathbb{C}_{i,n+1}^s = \left[\frac{C_{n+1}^i}{C_{n+1}^0}\right]\mathbb{C}_{n+1}^e \text{ with } i = 1,2 \tag{5.59}$$

5. **K**, **R** are determined. The jth iteration is continued until eq.(5.47) is satisfied (i.e., $\left|\mathbf{R}(\mathbf{u}_{n+1}^j)\right| < TOL$).

6. The final values of $\underline{\sigma}_{n+1}$ and $\underline{\varepsilon}_{n+1}$ are stored in the array form and used for a new iteration of the next time step.

5.2.2 Extension of the 3D mechano-sorptive behavior for the crack

As presented in the section 1.4.2, most of mechano-sorptive models are developed for specimens without the crack propagation phenomenon because this one affects the boundary conditions of the specimen.

For the viscoelastic case without moisture variation, some authors studied the crack evolution of wood specimen by using the viscoelastic integral method (e.g., $G\theta_v$ or J_{ve}) based on LEFM (see Section 2.3.3). For a given crack length a, the energy release rate $G_{tot}(a)$ accumulated in function of the time is compared to the crack propagation criterion (such as $G_{tot}(a) = G_R(a)$, R-curve). When the crack propagates, a projection of the mechanical field between the old and the new configuration is performed which leads to a perturbation of the mechanical field due to the mesh differences.

To overcome the perturbation of the mechanical field, we will use in this study the cohesive joint element which is successfully applied to describe the delamination phenomenon of the material based on the joint (node) release following a traction-separation law. Within the framework of CZM, the cohesive zone represents the FPZ of the structure. Moreover, CZM does not require to re-mesh the specimen when the crack propagates. During the crack propagation process, the response from the viscoelastic mechano-sorptive behavior of the wood substrate interact with the cohesive zone.

Using the cohesive zone model associated with the mechano-sorptive model (for wood substrate), the balance equation of the internal and external loading at the time t_{n+1}, based on the eq.(5.41), can be rewritten as:

$$\mathbf{R}(\mathbf{u}_{n+1}) = \left| \left(\underbrace{\int_V \mathbb{B}^T \underline{\sigma}(\mathbf{u}_{n+1})dV}_{\text{wood substrate}} + \underbrace{\int_S \mathbb{B}^{joint^T} \underline{\sigma}^{joint}(\mathbf{u}_{n+1})dS}_{\text{FPZ}} \right) - \underbrace{\mathbf{F}^{ext}_{n+1}}_{\text{external}} \right| < TOL \quad (5.60)$$

where $\mathbb{B}$ is the strain-displacement transformation matrix of standard elements (used for wood substrate), $\mathbb{B}_{joint}$ is the strain-displacement transformation matrix of the joint. T denotes a transpose action in matrix.

In eq.(5.60), we would like to emphasize that the complex coupling interaction between the response of the wood substrate and the cohesive zone under varying moisture can only be solved by the numerical analysis.

5.2.3 Application of the moisture-dependent cohesive law

When the crack propagates, the traction-separation law (TSL) of the new damaged zone is directly function of the moisture at the tip of the FPZ MC_{FPZ}. Note that one assumes here that the fracture properties (i.e., the cohesive parameters), do not depend on the sudden RH variations on the FPZ but only depend on the average moisture of an imposed volume located ahead of the FPZ (MC_{FPZ}). The fracture properties and their corresponding cohesive parameters (reported in Section 4.3 and Table 4.2) have been estimated from fracture tests performed at a given moisture content and not under RH variations.

Figure 5.14 presents a schematic representation of the cohesive law in relation with the average moisture of the imposed volume ahead of the crack tip during the crack propagation.

In this study, the imposed volume for determining the MC_{FPZ} is considered as a volume with a height of 1 mm (i.e., 0.5mm from the cohesive interface, considered as the size of an element in the wood substrate), a length of $0.4 - 0.5$ mm (corresponding to the infinitesimal crack extent used in the eq.LEFM) and a width responding to the thickness of the specimen, i.e., 12 mm. The studied volume is then 0.5 mm x 1 mm x 12 mm (Fig. 5.14). Note that, the evolution of MC_{FPZ} versus time depends not only on the diffusion process inside the structure but also on the crack growth kinetics.

The cohesive parameters of the TSL at a certain moisture content will be estimated on the basis of an interpolation of two experimental TSL values corresponding to two nearest moisture content (upper and lower MC). For example, cohesive law parameters at the moisture 16% (i.e., $MC_{FPZ} = 16\%$) will be determined using those corresponding to 15% MC and 18% MC, which are reported in Table 4.2.
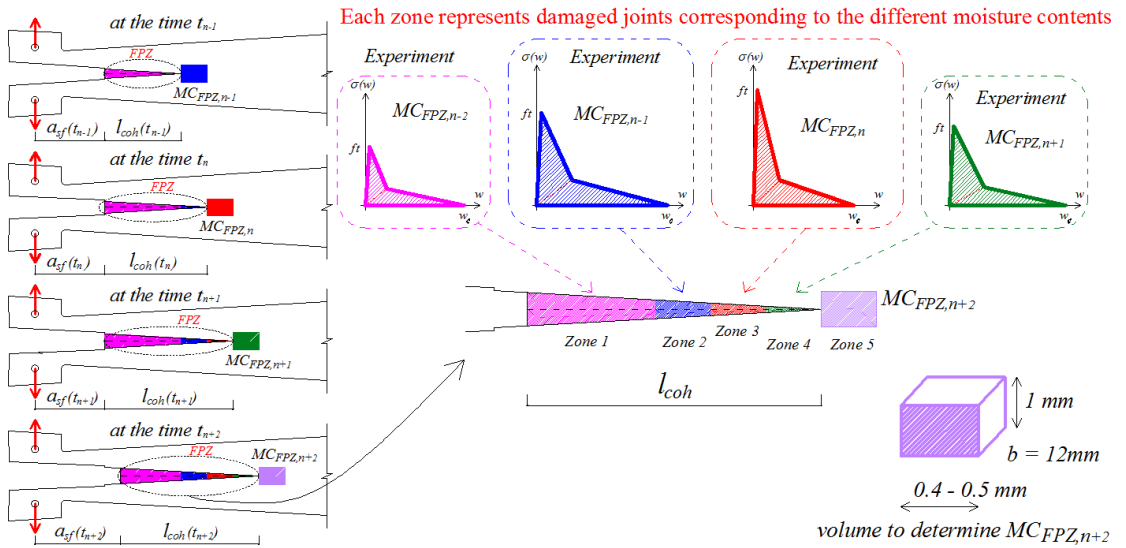
Figure 5.14: Schematic representation of the application of the cohesive law during the crack propagation for varying $MC_{FPZ,i}$

As illustrated in Figure 5.15, the fracture process zone is naturally a zone in which the moisture exchange surface is increased due to the crack bridging phenomenon more exactly fiber bridging for wood. As a consequence, it is expected that the mechanical equilibrium of the FPZ is strongly affected by sudden RH variations which can lead to possible crack propagation or inversely to stabilization of the main crack. This phenomenon is taken into account in the following through a modification of the CZM [129]. Indeed, the alone moisture diffusion process in the specimen (mechano-sorptive behavior of the wood substrate) cannot explain the observed instability of the crack propagation when RH evolves suddenly (in experimental tests).
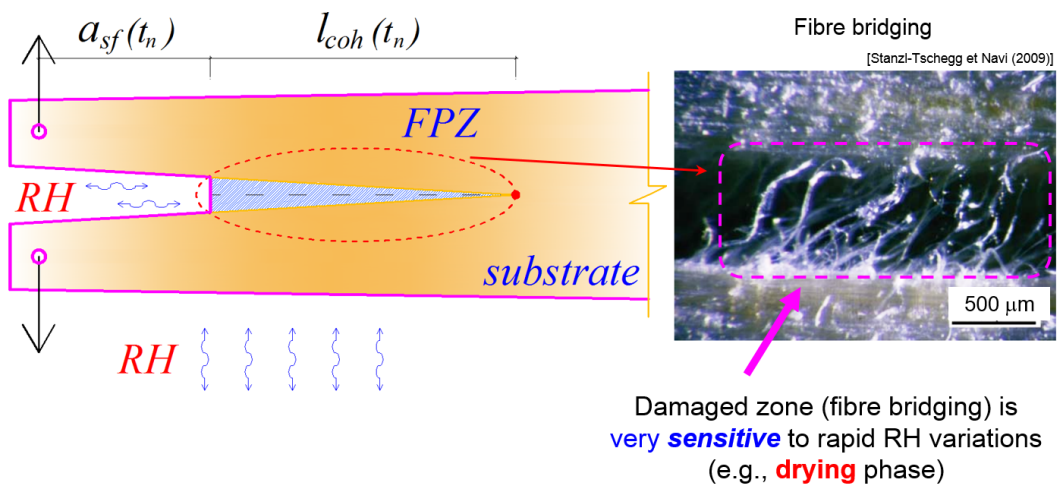
Figure 5.15: The fracture process zone affected by the rapid RH variations

5.3 Integration of the moisture effect on the fracture process zone

As previously mentioned, the crack bridging phenomenon taking place on the FPZ increases the exchange surface and leads the mechanical equilibrium of FPZ to be dependent of the sudden RH variations. Such a phenomenon is expected to be the source of instability of the main crack even if the external loading remained unchanged.

In this section, one proposes a method taking into account the varying moisture effect on the FPZ by introducing an additional *climatic* loading (additional stress field) along the cohesive zone. This additional stress field depends on the moisture in the joint and on the sudden RH variation but also on the stress and on the crack opening state.

5.3.1 Moisture distribution at the FPZ

As previously mentioned, the alone moisture diffusion process in the specimen cannot explain the observed instability of the crack propagation when RH evolves suddenly. In order to describe such a phenomenon, one assumes here that the moisture content of each cohesive link (characterized by the cohesive stress-opening law of both corresponding nodes of the cohesive interface) is immediately dependent of RH variations. Nevertheless, this immediate dependency of the FPZ moisture content should be also function of the crack opening of the FPZ (Fig. 5.16).
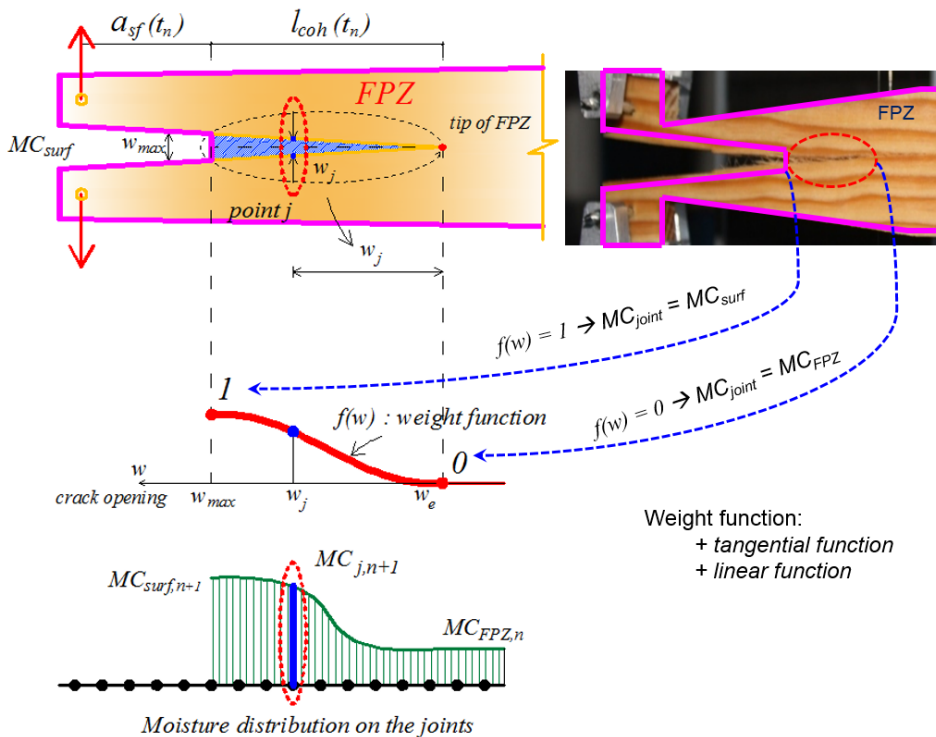
Figure 5.16: Moisture distribution on the Fracture Process Zone

Indeed, if an immediate variation of the moisture is expected where the opening of the FPZ is large, the moisture variation is expected to be nil or very low when the opening of the FPZ tends toward zeros (Fig. 5.16). Note that the small opening of the FPZ are furthermore associated to the micro-cracking phenomenon and not to the crack bridging one (intuitively, the micro-cracking is not expected to be immediately dependent of the RH variation). Thus, the moisture distribution along the cohesive zone is assumed to be weighted by a function $f(w)$ as shown in Figure 5.16, the moisture along the cohesive joint evolves as:

$$MC_{joint}(w) = MC_{FPZ,n} + f(w)(MC_{surf,n+1} - MC_{FPZ,n}) \qquad (5.61)$$

where $MC_{surf,n+1}$ is the moisture at the wood surface at the time t_{n+1}, $MC_{FPZ,n}$ is the moisture at the tip of the FPZ at the end of the time t_n.

The weight function $f(w)$ is given in eq.(5.62). The weight function is chosen by a linear or a tangential shape..

$$f(w) = \begin{cases} 0 & \text{if } w < w_e \\ [0,1] & \text{if } w_e < w < min(w_{max}, w_c) \\ 1 & \text{if } \begin{cases} w = w_{max}(< w_c) \text{ in case FPZ not fully developed} \\ w \geq w_c \text{ in case FPZ fully developed} \end{cases} \end{cases} \qquad (5.62)$$

In eq.(5.62), w_c is the critical crack opening displacement when the FPZ is fully developed. w_e is the crack opening displacement corresponding to the tensile strength f_t (in this thesis, $w_e \approx 5.10E^{-4} \ mm$). Thus, the position assumed by the crack opening displacement w_e was considered as the FPZ tip. At the crack opening displacement $w < w_e$, the material is not yet damaged.

As seen in Figure 5.16 and eq.(5.61), the moisture distribution on the cohesive zone depends not only on the crack opening w (through the weight function $f(w)$) but also on the both moisture at the wood surface $MC_{surf,n+1}$ and at the tip of the fracture process zone $MC_{FPZ,n}$.

Now we propose to analysis the effect of rapid varying moisture on the FPZ. For a given crack opening of the cohesive zone, the corresponding damaged stiffness driving the stress-opening relationship of both corresponding points is expected to be influenced by this variation. In the next paragraph, we introduce the influence of rapid varying moisture on the FPZ by considering this influence as an external climatic loading.

5.3.2 Incremental formulation of the external climatic loading on the FPZ

At the beginning of a current computation time t_{n+1}, the moisture content field of the specimen is calculated by the diffusion process in the previous step MC_n and the moisture

distribution on the cohesive zone $MC_{joint,n}(w)$ is then obtained.

Figure 5.17 summarizes a procedure for integrating the effect of the rapid varying moisture on the FPZ (represented by the cohesive zone).
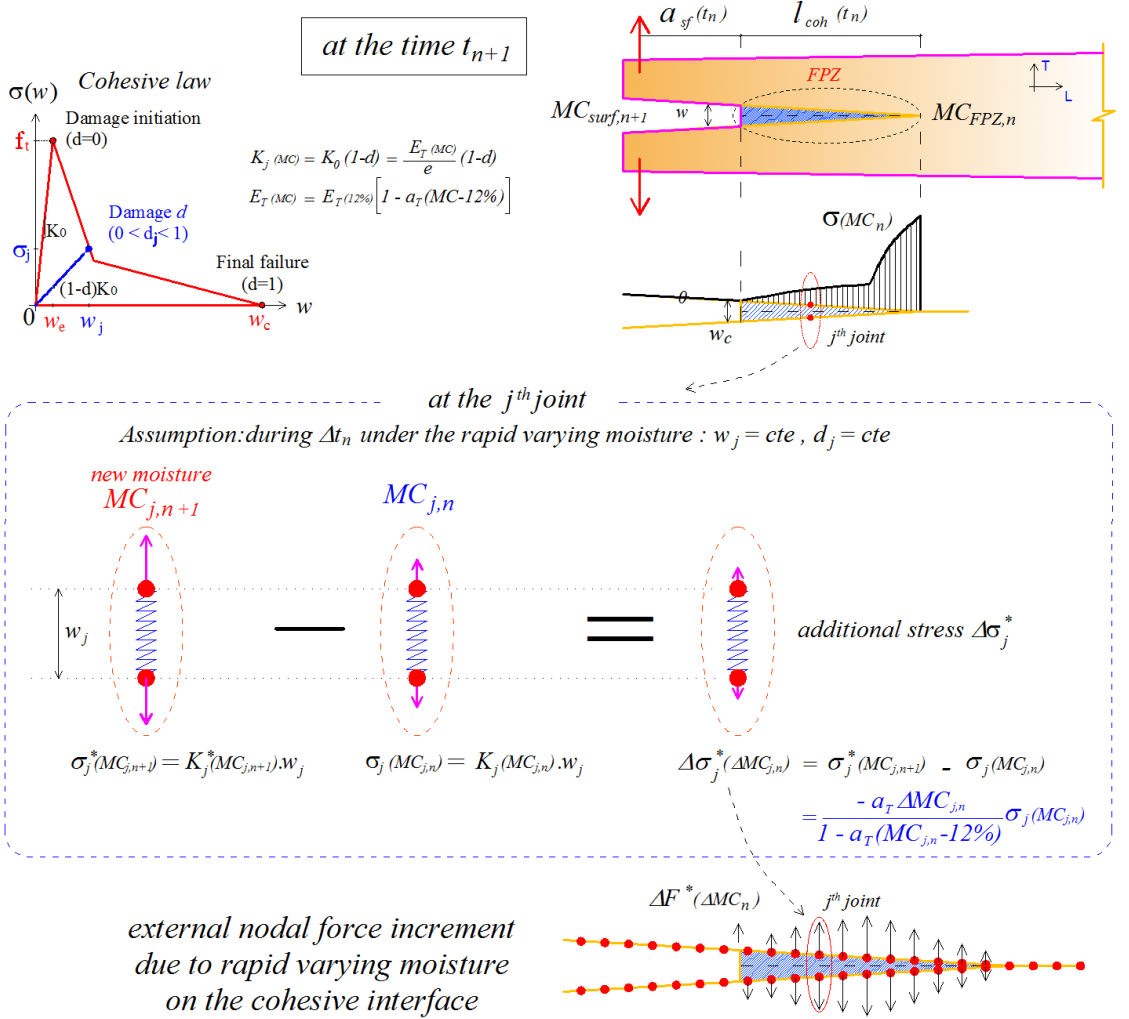
Figure 5.17: Schematic representation of integration of the rapid varying moisture effect on the FPZ

In order to introduce the additional incremental climatic stress field along the cohesive zone during $\Delta t_n = (t_{n+1} - t_n)$, due to the rapid variation of the moisture, the opening field w along the cohesive zone is considered constant; the damage d of each joint element is assumed to be independent of the moisture variation. Then, the varying moisture only influences the elastic stiffness of the joint element (damaged fiber).

In the cohesive element, the normal stress σ is a function of the initial elastic stiffness K_o, the damage state d and the crack opening w at the joint element. This relation can be expressed as $\sigma = K_o(1-d)w$. Thus, the stress at the jth joint element of cohesive zone corresponding to the moisture content $MC_{j,n}$ can be written as eq.(5.63).

$$\sigma_j(MC_{j,n}) = K_j(MC_{j,n})w_j \qquad (5.63)$$

133

while the stress corresponding to the new moisture $MC_{j,n+1}$ should be:

$$\sigma_j^*(MC_{j,n+1}) = K_j(MC_{j,n+1})w_j \tag{5.64}$$

where K_j is the joint stiffness at the the jth joint element corresponding to the damaged state d_j.

Moreover, the joint stiffness K_j can be expressed as a function of the moisture content by the following expression:

$$K_j(MC_j) = K_0(MC_j)(1 - d_j) = \frac{E_T(MC_j)}{e}(1 - d_j) \text{ if } w_e \leq w_j \leq w_c \tag{5.65}$$

where e is the thickness of the cohesive joint and w_j is the crack opening displacement of the cohesive joint element and E_T corresponds to the tangential moduli (crack opening in the tangential direction).

Due to the rapid moisture variation from $MC_{j,n}$ to $MC_{j,n+1}$ at the jth joint element, the perturbation $\Delta\sigma_{j,n}^*$ of the stress corresponding to this variation can be obtained as (d_j and w_j are constants):

$$\begin{aligned} \Delta\sigma_{j,n}^* &= \sigma_j^*(MC_{j,n+1}) - \sigma_j(MC_{j,n}) & (5.66) \\ &= \left[\frac{\sigma_j^*(MC_{j,n+1})}{\sigma_j(MC_{j,n})} - 1\right]\sigma_j(MC_{j,n}) & (5.67) \\ &= \left[\frac{E_T(MC_{j,n+1})}{E_T(MC_{j,n})} - 1\right]\sigma_j(MC_{j,n}) & (5.68) \end{aligned}$$

where the relation of the tangential moduli E_T versus the moisture is $E_T(MC) = E_T(12\%)[1 - a_T(MC - 12\%)]$ (with $a_T = 0.03\%/\%$). Thus, the pertubation $\Delta\sigma_{j,n}^*$ of the cohesive stress defined in eq.(5.68) can be rewritten as:

$$\Delta\sigma_{j,n}^* = \left[\frac{-a_T(MC_{j,n+1} - MC_{j,n})}{1 - a_T(MC_{j,n} - 12\%)}\right]\sigma_j(MC_{j,n}) = A_{j,n}\sigma_j(MC_{j,n}) \tag{5.69}$$

where $A_{j,n}$ is a function of the moisture content $MC_{j,n}$ and the moisture increment $\Delta MC_{j,n} = MC_{j,n+1} - MC_{j,n}$:

$$A_{j,n} = \frac{-a_T\Delta MC_{j,n}}{1 - a_T(MC_{j,n} - 12\%)} \tag{5.70}$$

Based on eq.(5.70), for an humidification phase at the joint ($\Delta MC_{j,n} > 0$), the value of $A_{j,n}$ is negative ($A_{j,n} < 0$), and hence the additional stress has the tendency to induce the crack closure. Conversely, for a drying phase at the joint ($\Delta MC_{j,n} < 0$), the value of $A_{j,n}$ is positive ($A_{j,n} > 0$), and the additional stress has the tendency to lead to additional crack opening.

In the same way, the perturbation stress due to moisture variation at all joint elements along the cohesive zone $\Delta\sigma_{FPZ,n}$ is obtained as the following expression:

$$\Delta\sigma_{FPZ,n} = \mathbb{A}\sigma_{joint}(MC_n) \tag{5.71}$$

where $\sigma_{joint}(MC_n)$ is the stress field corresponding to the time t_n of the cohesive zone and $\mathbb{A}$ is the perturbation stress coefficient of the cohesive zone.

The perturbation stress $\Delta\sigma_n^{FPZ}$ due to rapid varying moisture is considered as an external climatic loading applied along the cohesive zone. On this basis, one can express the vector of the additional external climatic loading increment $\Delta\mathbf{F}_n^{FPZ}$ on the cohesive zone at the time t_{n+1} as:

$$\Delta\mathbf{F}_{FPZ,n} = \int_S \mathbb{B}_{joint}^T \Delta\sigma_{FPZ,n} dS = \int_S \mathbb{B}_{joint}^T \mathbb{A}\sigma_{joint}(MC_n) dS \tag{5.72}$$

where $\mathbb{B}_{joint}$ is the strain-displacement transformation matrix of joint and T denotes a transpose action in matrix.

5.3.3 The coupled effect of the viscoelastic mechano-sorptive behavior of wood substrate and the rapid varying moisture on the FPZ

As shown in eq.(5.72), the additional climatic loading increment $\Delta\mathbf{F}_{FPZ,n}$ at the time t_{n+1}, depends on both the coupling hygro-mechanical state and on the moisture variation on the FPZ. Note that the additional increment $\Delta\mathbf{F}_n^{FPZ}$ must be accumulated at all time steps in the history of the specimen until the time t_{n+1}. Therefore, the total external climatic loading until the time t_{n+1} is written as:

$$\mathbf{F}_{n+1}^{MC\_FPZ} = \sum_{k=1}^n \Delta\mathbf{F}_{FPZ,k} \tag{5.73}$$

Consequently, the balance equation of the internal and the total external loading (i.e., mechanical and climatic loading as illustrated in Figure 5.18) at the time t_{n+1}, based on the eq.(5.41) mentioned in Section 5.2.1, can be rewritten as:

$$\mathbf{R}(\mathbf{u}_{n+1}) = \left| \mathbf{F}_{n+1}^{int} - \underbrace{(\mathbf{F}_{n+1}^{ext} + \mathbf{F}_{n+1}^{MC\_FPZ})}_{\mathbf{F}_{n+1}^{ext\_total}} \right| < TOL \tag{5.74}$$

where $\mathbf{F}_{n+1}^{ext}$ is the external mechanical loading, $\mathbf{F}_{n+1}^{MC\_FPZ}$ is the climatic loading acting on FPZ, $\mathbf{F}_{n+1}^{int}$ is the internal loading based on the constitutive behavior at t_{n+1}.

Using the mechanical responses of the wood substrate (mechano-sorptive model) and of the fracture process zone (cohesive zone model), eq.(5.74) can be rewritten as:

$$\mathbf{R}(\mathbf{u}_{n+1}) = \left| \left(\underbrace{\int_V \mathbb{B}^T \sigma(\mathbf{u}_{n+1}) dV}_{\text{wood substrate}} + \underbrace{\int_S \mathbb{B}^{joint^T} \sigma^{joint}(\mathbf{u}_{n+1}) dS}_{\text{FPZ}} \right) - \left(\underbrace{\mathbf{F}_{n+1}^{ext}}_{\text{external}} + \underbrace{\mathbf{F}_{n+1}^{MC\_FPZ}}_{\text{climatic}} \right) \right| < TOL \tag{5.75}$$
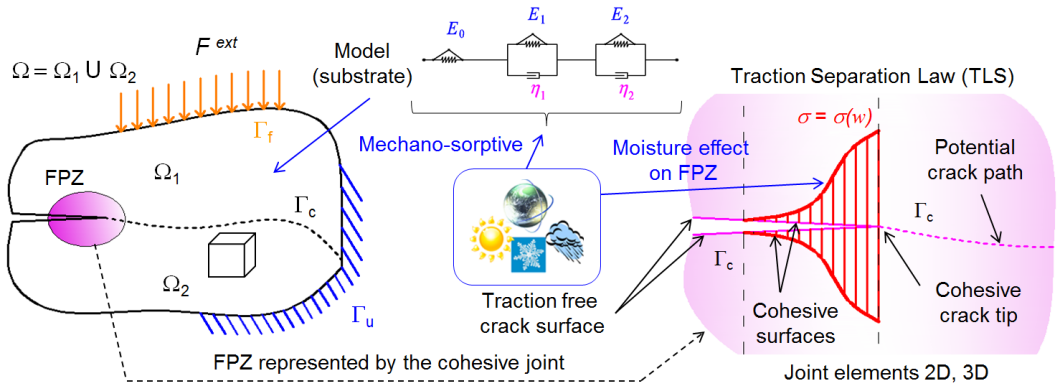
Figure 5.18: Schematic representation of the energy balance thermodynamics

Compared to eq.(5.60), the eq.(5.75) has added the influence of the rapid varying moisture effect on the FPZ on the crack growth process through the climatic loading component $\mathbf{F}_{n+1}^{MC\_FPZ}$. This equation takes into account simultaneously the effect of the varying moisture and of the time due to the viscoelastic property in wood, as well as the effect of the crack propagation on the mechanical response of the structure.

5.4 Explicit algorithm for crack growth under RH variations

These models have been implemented in source code Esope of the finite element code Cast3m. Figure 5.19 shows an explicit algorithm, which is a two-parallel algorithm, for the crack growth under relative humidity variation [127].

In this algorithm, two main points are considered, firstly the diffusion coefficient is assumed to be independent of the mechanical state and secondly the computation manipulation must not take too much time. This is the reason why we would like to propose a two-parallel algorithm in which two computation procedures for the diffusion process and for mechanical problems are proceed in parallel.

As shown in Figure 5.19 at any time step t_n, we already have all internal variables, the thermal-hygro field and the mechanical field of all previous steps. In this algorithm, the meshing technique for both procedures is the same while carefully choosing the number of elements and the element positions in order to minimize the perturbation of the projection of the thermal-hygro field in the mechanical problem. The cohesive joint element is used for the mechanical problem. Note that the proposed algorithm can be directly applied to evaluate the stresses induced by the variation of both temperature and moisture.
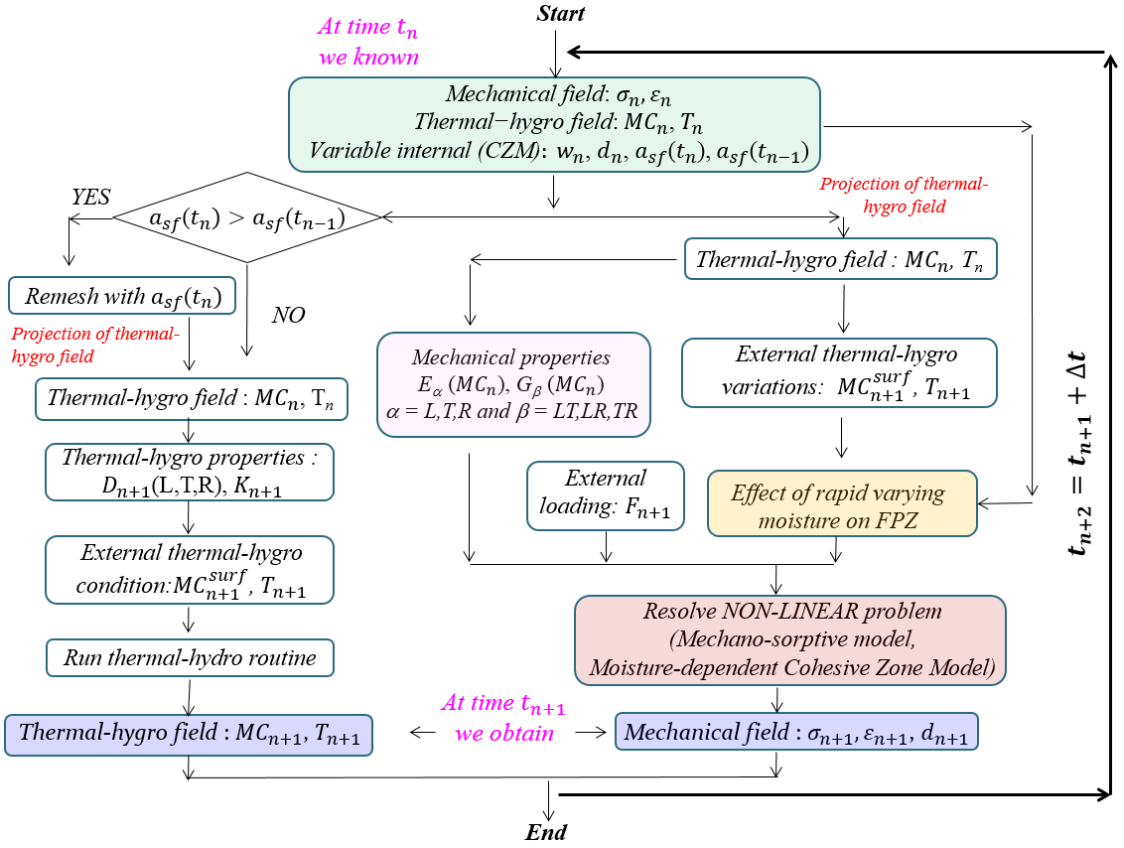
Figure 5.19: Explicit algorithm for the crack growth under RH variations

5.5 Conclusion

This Chapter has presented a FE numerical model to describe the effect of varying RH on the mechanical behavior of cracked wood structures.

This model developed in the source code Esope of Cast3m takes into account: (i) the coupling between the hydric state and the mechanical loading on the crack growth in the structure, (ii) the 3D viscoelastic mechano-sorptive behavior of wood; and (iii) the effect of the sudden RH variation on the FPZ.

The next chapter compares crack propagation in wood specimen with or without moisture variation in order to clarify the influence of varying moisture effect, shrinkage-swelling effect, mechano-sorptive behavior or viscoelastic properties of wood. The numerical results obtained from our proposed method is confronted with the experimental results.

Chapter 6

Numerical simulations

In this chapter, we propose to analyze not only the individual effects of each moisture-dependent phenomenon (i.e., the mechano-sorptive behavior associated to shrinkage-swelling effect, the rapid varying moisture on the FPZ) but also the coupled effects of the different phenomena on the crack growth.

6.1 Numerical simulations

In the first time, one proposes an analysis of each moisture-dependent phenomenon (i.e., moisture transfer in wood, mechano-sorptive effect, shrinkage-swelling effect, effect of the rapid varying moisture on FPZ). The results are obtained using the FEA.
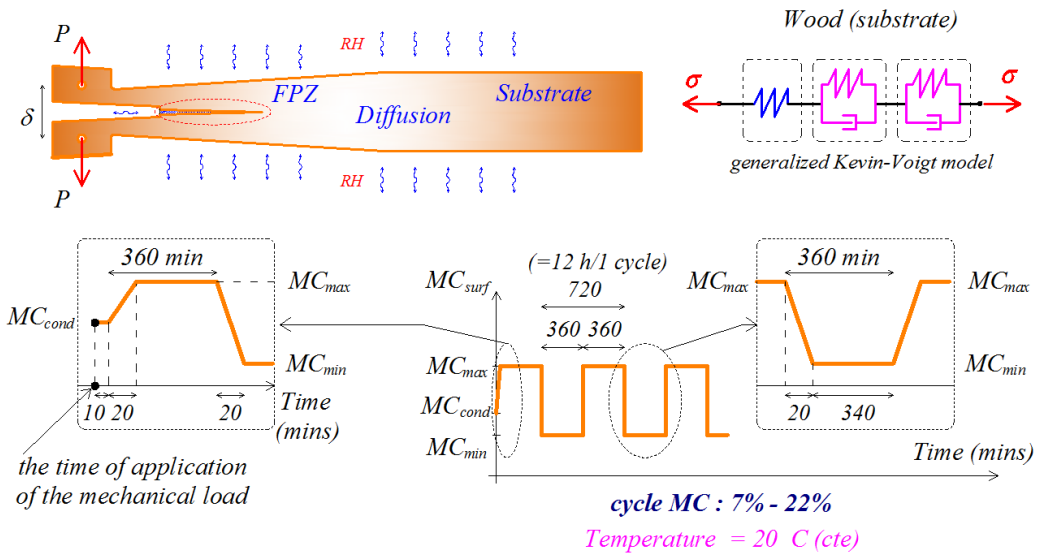
Figure 6.1: Phenomena acting on the crack growth in wood structure

FE simulations are performed in 3D from mTDCB submitted to cyclic surface moisture (7% - 22%) corresponding to relative humidity cycles of 45% - 90% as presented in Figure 6.1. The specimen is considered to be initially conditioned at the moisture 12% ($MC_{cond} = 12\%$). The humidity is only changed after 10 minutes, which corresponds to

the loading time. Two different moisture cycles are considered corresponding to a first humidification phase (scenario H) and a first drying phase (scenario D), respectively, as illustrated in Figure 6.2. The parameters for the 3D diffusion model in wood are presented in section 5.1.3. In the numerical results, MC_{FPZ} is the average moisture at the FPZ tip; $MC_{average}$ is the average moisture in the specimen.
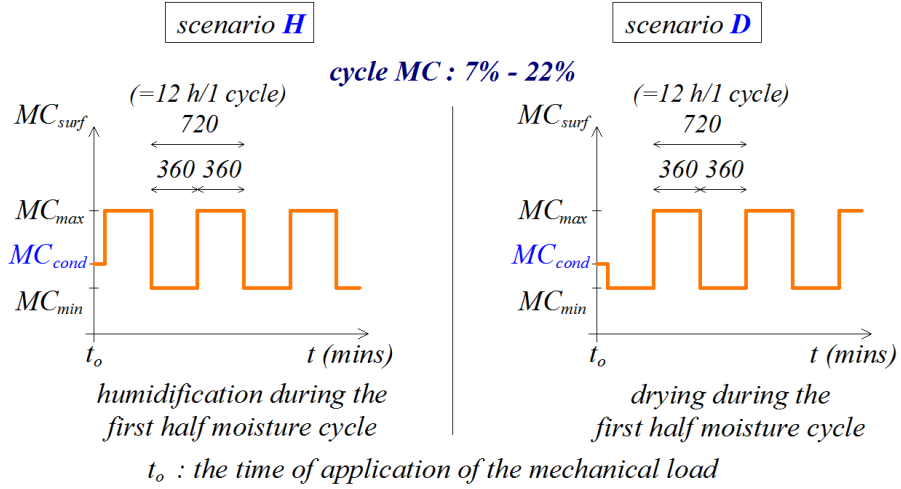
Figure 6.2: Two different moisture cycles corresponding to a first humidification phase or a first drying phase

For the wood substrate, the generalized Kelvin Voigt model with two branches is employed for the viscoelastic case (Fig. 6.1). The parameters of viscoelastic properties are presented in Sections 5.2. The first spring of the generalized Kelvin Voigt model describes the elastic behavior (Fig. 6.1). Note that in case of the varying moisture in wood, the relation between mechanical properties and the moisture are given in eqs.(5.14) and (5.15) in Section 5.2.1.2.

The fracture of wood is described from cohesive zone model considering the bi-linear softening. The relation between the cohesive law and the moisture is described in Table 4.2 and Section 4.3. Note that, the cohesive zone parameters at a given moisture are estimated from a linear interpolation of those previously identified and given in Table 4.2.

Figure 6.3 illustrates the mTDCB specimen with the 3D meshing and the cohesive joint. The imposed force is around $170 - 175$ N, corresponding to 85% of the maximal load (at the moisture 12%).
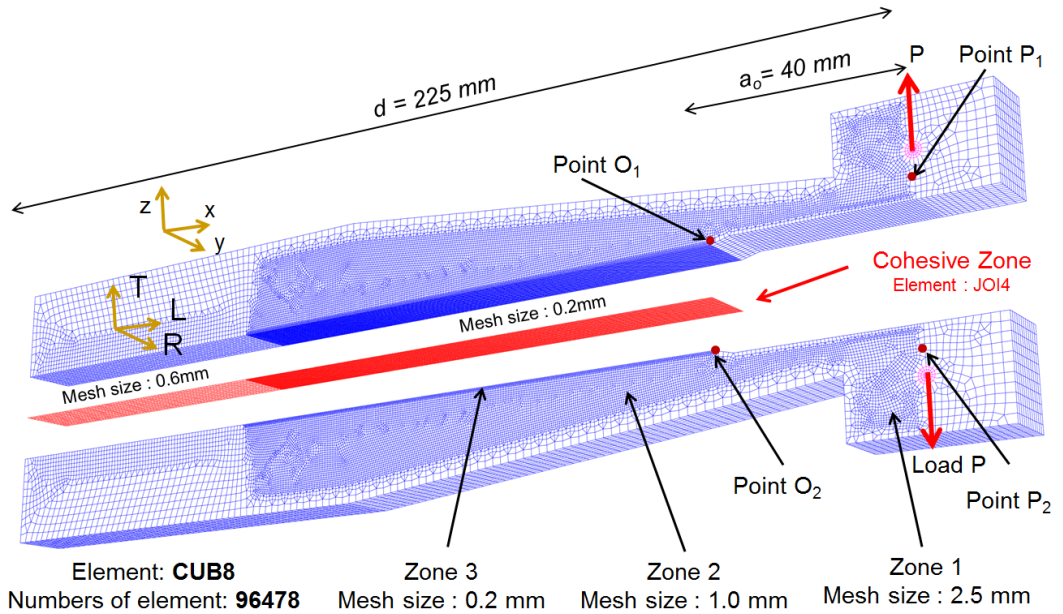
Figure 6.3: 3D mesh and cohesive joint of the mTDCB specimen

In the numerical results, δ is the displacement of the loading point (relative distance between the point P_1 and the point P_2), w is the crack opening displacement (relative distance between the point O_1 and the point O_2), as shown in Figure 6.3. During crack propagation, we would like to focus on two important parameters such as l_{coh} (the length of the FPZ) and a_{sf} (the stress-free crack length).

In order to achieve our objective (the individual effect and the coupled effect on the crack growth), twelve different simulation cases are proposed and detailed in Table 6.1.

Table 6.1: Twelve different cases in the crack growth under the moisture variation. Five notations are used in which: V denotes the viscoelastic property in wood substrate, T denotes the moisture transfer, HL denotes the hygro-lock model in wood substrate (mechano-sorptive), S denotes the shrinkage-swelling effect, mCZ denotes the rapid varying moisture effect on FPZ. The value of 1 and 0 beside each letter corresponds to 'Yes' or 'No' situation, respectively

Analysis case	Wood substrate				Cohesive zone taken account of rapid vaying moisture effect
	Mechanical properties	Moisture transfert	Hygro-Lock (Mechano-sorptive)	Shrinkage-swelling effect	
Notation	V	T	HL	S	mCZ
Case 1 V0T0HL0S0mCZ0	Elastic				
Case 2 V0T0HL0S0mCZ1	Elastic				Yes
Case 3 V0T1HL1S0mCZ0	Elastic	Yes	Yes		
Case 4 V0T1HL1S0mCZ1	Elastic	Yes	Yes		Yes
Case 5 V0T1HL1S1mCZ0	Elastic	Yes	Yes	Yes	
Case 6 V0T1HL1S1mCZ1	Elastic	Yes	Yes	Yes	Yes
Case 7 V1T0HL0S0mCZ0	Viscoelastic				
Case 8 V1T0HL0S0mCZ1	Viscoelastic				Yes
Case 9 V1T1HL1S0mCZ0	Viscoelastic	Yes	Yes		
Case 10 V1T1HL1S0mCZ1	Viscoelastic	Yes	Yes		Yes
Case 11 V1T1HL1S1mCZ0	Viscoelastic	Yes	Yes	Yes	
Case 12 V1T1HL1S1mCZ1	Viscoelastic	Yes	Yes	Yes	Yes

The evolution of the average moisture $MC_{average}$ in the specimen, of the average moisture MC_{FPZ} at the tip of the FPZ tip as well as the displacement δ, the length l_{coh} and the stress-free (main) crack length a_{sf} for the 12 cases are detailed in Appendix A.

From the numerical results obtained from 12 cases (Appendix A), the crack growth can be significantly influenced by two impacts such as the varying moisture content and the viscoelastic process. Consequently, by considering wood substrate as viscoelastic, we

classifies some cases into two groups in order to better visualize these effects on the crack growth.

1. **Individual effects:**

    - Case 7 (V1T0HL0S0mCZ0): viscoelastic property of wood without the varying humidity (reference case)
    - Case 8 (V1T0HL0S0mCZ1): effect of the rapid varying moisture on the FPZ
    - Case 9 (V1T1HL1S0mCZ0): effect of the mechano-sorptive behavior
    - Case 11 (V1T1HL1S1mCZ0): effect of the mechano-sorptive behavior associated to the shrinkage-swelling

2. **Coupled effects:**

    - Case 7 (V1T0HL0S0mCZ0): viscoelastic property of wood without the varying humidity (reference case)
    - Case 8 (V1T0HL0S0mCZ1): effect of the rapid varying moisture on the FPZ
    - Case 11 (V1T1HL1S1mCZ0): effect of the mechano-sorptive behavior associated to the shrinkage-swelling
    - Case 12 (V1T1HL1S1mCZ1): coupled effect of the rapid varying moisture on the FPZ and the mechano-sorptive behavior associated to the shrinkage-swelling

In two groups, the default simulation (case 7: V1T0HL0S0mCZ0) corresponds to viscoelastic property in wood substrate (i.e., without moisture transfer, shrinkage-swelling effect and hygro-lock) and the CZM (i.e., without effect of the sudden moisture variation).

For each group, the crack growth are studied in two scenarios (Fig. 6.2):

- humidification during the first half moisture cycle (**scenario H**)
- drying during the first half moisture cycle (**scenario D**)

6.1.1 Individual effects

Let us start the analysis with the case 7 (V1T0HL0S0mCZ0) which corresponds to the fracture behavior expected from the alone effect of the viscoelastic in the wood substrate. The case 7 is here compared to case 1 (V0T0HL0S0mCZ0) which characterizes the expected fracture behavior in the absence of the time-dependent phenomenon linked to the viscoelastic character of the wood substrate. Note that, in both cases (i.e., case 1 and case 7), the moisture transfer is not taken into account in the simulations.

6.1.1.1 Time-dependent crack growth in a quasi-brittle material

As mentioned in Section 2.3.1, the time-dependent crack growth phenomenon can be described from the evolution of the energy release rate with time due to an additional

elastic energy related to the viscoelastic strain in the whole specimen. One can assume that this additional energy is a part of the total elastic energy induced by the viscoelastic deformation. The main difficulty in numerical analysis involving the crack growth versus time is the coupling between the viscoelastic strain configuration and the evolution of the boundary condition of the considered specimen due to the crack propagation.

6.1.1.1.a   Equivalent LEFM for viscoelastic fracture mechanics

As mentioned in Section 2.1.2, within the framework of equivalent LEFM, an equivalent elastic crack length a_{eq} is defined as the crack length of a structure considered as linear elastic everywhere which gives the same compliance as the one of the actual cracked structure with its FPZ [12, 39, 111, 115, 177].

Figure 6.4 shows a schematic representation of the elastic compliance in the quasi-static and the viscoelastic cases. From the quasi-static (elastic) load-displacement curve plotted in Figure 6.4a, the secant compliance corresponding to a given point of the load-displacement curve is defined as the slope of the straight line passing through the considered point and the origin. In the elastic case, the secant compliance corresponds to the elastic one as previously shown. In the viscoelastic case, the secant compliance does not coincide with the elastic compliance due to an addition of viscoelastic deformations in the wood substrate.
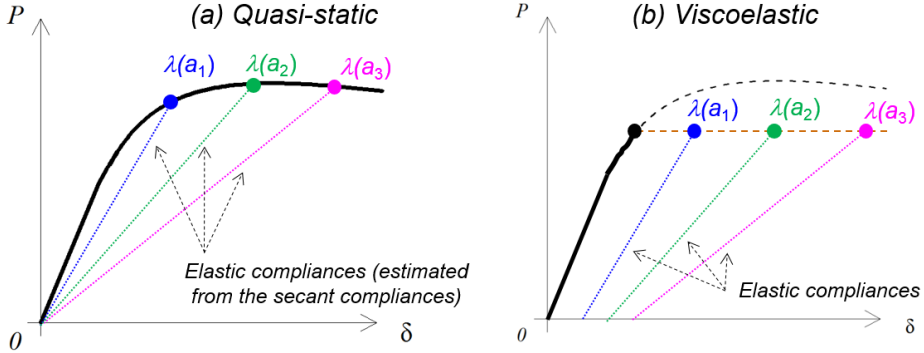
Figure 6.4: Schematic representation of the elastic compliance in the quasi-static and the viscoelastic cases

Consequently, we suggest to use the equivalent LEFM crack length in the viscoelastic analysis. Note that, the elastic compliance of the specimen is only influenced by the main crack length and the FPZ size. For the same main crack length and the size of the FPZ, the elastic compliance of the structure in the viscoelastic case is expected to be the same in the quasi-static case (Fig. 6.4).

In order to enrich the understanding of crack propagation phenomenon in viscoelastic media, we would like to introduce the estimation of the strain energy release rate based on a semi-analytic approach.

6.1.1.1.b   Semi-analytic approach

Let us consider two consecutive points M_1 (δ_1, P_1) and M_2 (δ_2, P_2) of the load-displacement curve in quasi-static case (Fig. 6.5a). For viscoelastic case, M_2 (δ_{vis}, P_1) is presented in (Fig. 6.5b). Note that $\delta_{vis} = \Delta\delta_v + \delta_2$. Within the framework of eq.LEFM: $\delta_2 = \lambda(a_2)P_1$ and $\delta_1 = \lambda(a_1)P_1$. Figure 6.5 shows the sketch of an eq.LEFM crack of two advances due to viscoelastic strain during a time interval $\Delta t = (t_2 - t_1)$.
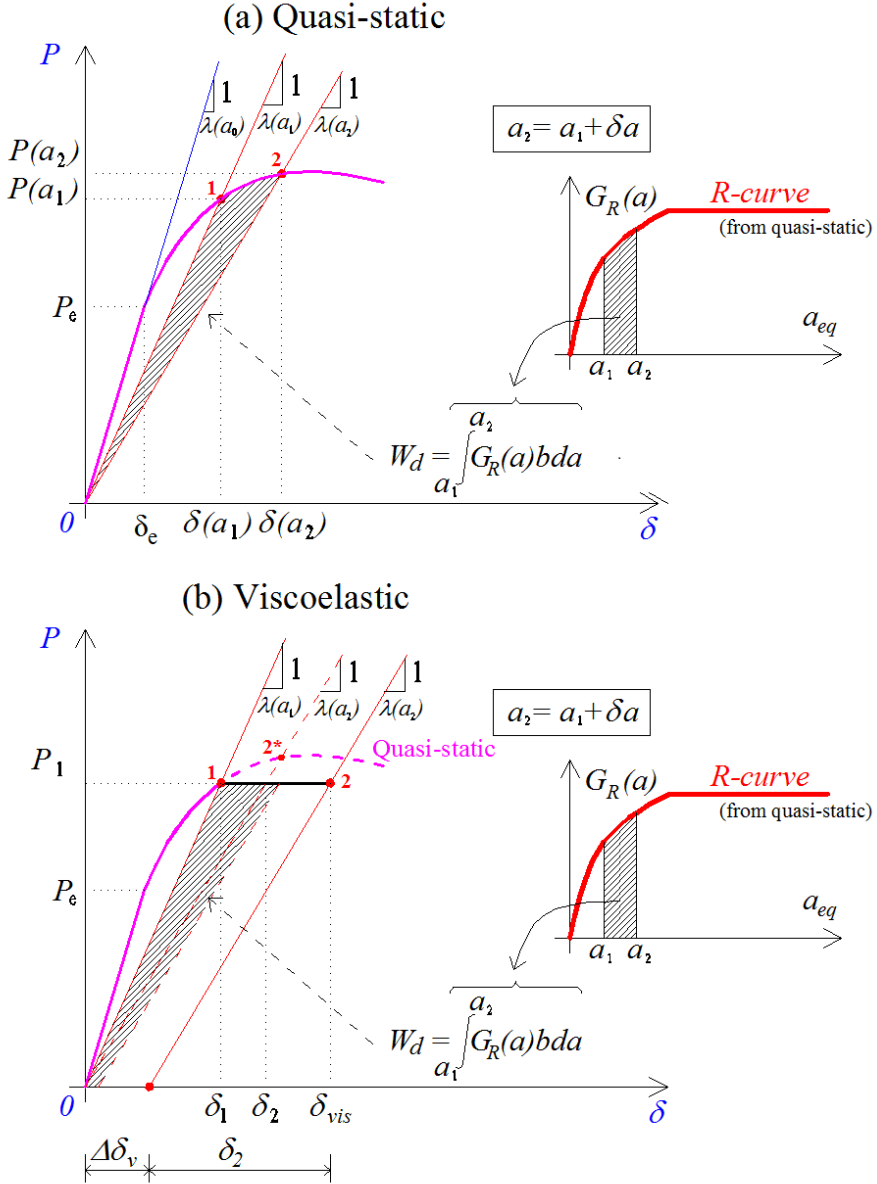
Figure 6.5: Schematic representation of the energy release rate in the quasi-brittle (a) and the viscoelastic case (b)

Any increase of the elastic energy in the system leads to an increase of the cohesive length and then a crack growth of the eq.LEFM crack. In Figure 6.6, the elastic energy U_{ve} due to the viscoelastic strain during Δt is the sum of the elastic energy $W_{ve\_available}$ and

the elastic energy stored in wood substrate W_{ve_locked}. The energy $W_{ve\_available}$ is available to mobilize for the elastic energy dissipation W_{ve_Wd} (i.e., $W_{ve\_available} = W_{ve\_Wd} = W_d$). While the energy W_{ve_locked} is controlled by the viscous damper and locked when the sudden unloading takes place. But this energy is recoverable, as a function of time.
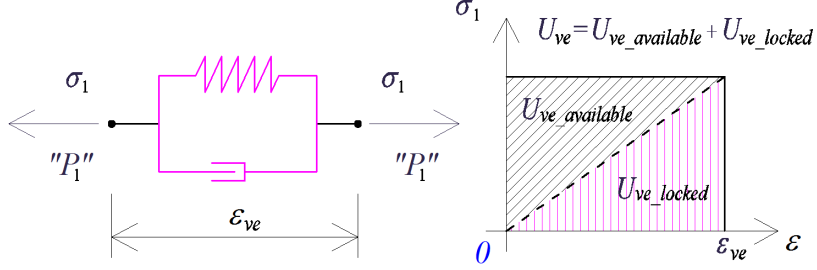
Figure 6.6: Schematic representation of the elastic energy due to viscoelastic strain

With an assumption that the stress σ_1 (for a Kelvin Voigt branch) is constant during the time increment $\Delta t = (t_2 - t_1)$ and the crack extend $\delta a = (a_2 - a_1)$, the elastic energy U_{ve} due to the viscoelastic strain (Fig. 6.6) can be expressed as:

$$U_{ve} = \int \sigma_1 \varepsilon_{ve} dV = W_{ve\_W_d} + W_{ve\_locked} \tag{6.1}$$

where the elastic energy $W_{ve\_available}$ is given as:

$$W_{ve\_available} = W_{ve\_locked} \tag{6.2}$$

From eq.(6.2), eq.(6.1) can be reduced to:

$$U_{ve} = 2W_{ve\_available} = 2W_{ve\_Wd} = 2W_d \tag{6.3}$$

In the load-displacement curve for the viscoelastic case (Fig. 6.5b), the elastic strain energy δE, released during a crack growth extension $\delta a = a_2 - a_1$, can be expressed as:

$$\delta E = \delta W - \delta U \tag{6.4}$$

where δW represents the external work of the applied load and δU corresponds to the complementary energy due to the applied load P as given in eqs.(6.5) and (6.6), respectively.

$$\delta W = W_2 - W_1 = P_1(\delta_{vis} - \delta_1) \tag{6.5}$$

$$\delta U = U_2 - U_1 = \frac{1}{2}P_1\delta_2 - \frac{1}{2}P_1\delta_1 + (U_{2_{ve}} - U_{1_{ve}}) \tag{6.6}$$

where $U_{1_{ve}} = 0$.

From eqs.(6.5) and (6.6), eq.(6.4) can be rewritten as:

$$\delta E = \delta W - \delta U = P_1(\Delta\delta_v + \delta_2 - \delta_1) - \frac{1}{2}P_1(\delta_2 - \delta_1) - U_{2_{ve}} \tag{6.7}$$

But $\delta E = W_d$ and $U_{2_{ve}} = U_{ve}$; hence $U_{2_{ve}} = 2W_d$. Based on this, eq.(6.7) can be rewritten as:

$$3W_d = \frac{1}{2}P_1\delta_2 - \frac{1}{2}P_1\delta_1 + P_1\Delta\delta_v \tag{6.8}$$

Thus, the displacement $\Delta\delta_v$ can be obtained as:

$$\Delta\delta_v = \frac{1}{P_1}\left[3W_d - \frac{1}{2}P_1(\delta_2 - \delta_1)\right] = \frac{1}{P_1}\left[3W_d - \frac{1}{2}P_1^2(\lambda(a_2) - \lambda(a_1))\right] \tag{6.9}$$

In eq.(6.9), the displacement $\Delta\delta_v$ can be estimated according to the semi-analytic approach by using a compliance function $\lambda(a)$ and an energy dissipation W_d. Based on the R-curve (obtained in the quasi-static test), the elastic energy dissipation W_d is given:

$$W_d = \int_{a_1}^{a_2} G_R(a)da \tag{6.10}$$

Let us consider now the first simulation of the quasi-static load-displacement response of the mTDCB specimen under 12% MC obtained from the CZM and its corresponding R-curve estimated from eq.LEFM approach plotted in Figure 6.5a. The crack propagation criterion is given as R-curve $G_R(a)$ with $G_{Rc} = 598 \ J/m^2$, $\beta = 0.27$ and $\Delta a_c = 18.7 \ mm$. The bi-linear cohesive joint parameters used are: $G_f = 598 \ J/m^2$, $w_c = 0.6 \ mm$, $f_t = 3.85 \ MPa$, $G_{f\mu}/G_f = 0.58$ [128].

On this basis, let us consider a second CZM simulation (with the same cohesive zone parameters) in which the mTDCB specimen is loaded in a quasi-static way up to $P_n = (175 \ N)$, corresponding to 85% of the quasi-static ultimate load, then the load P_n is remained constant as a function of the time (Fig. 6.5b). Figure 6.7 shows a comparison of the displacement $\Delta\delta_v$ in the viscoelastic case.
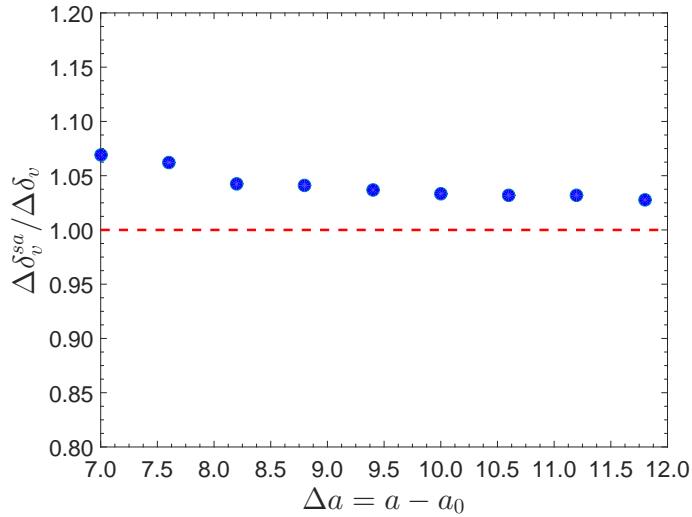
Figure 6.7: Comparison of the displacement $\Delta\delta_v$ in the viscoelastic case

In Figure 6.7, the displacement $\Delta\delta_v$ is obtained from the CZM, while the displacement $\Delta\delta_v^{sa}$ is obtained from eq.(6.9) in the semi-analytic approach. Intuitively, the difference of

$\Delta\delta_v$ at some crack length a in two cases remain lower than 6% (Fig. 6.7). This difference has tendency to decrease and stabilizes (3%) with the increasing of the equivalent crack length a. This dispersion can be induced by the fitting procedure in the numerical function of the R-curve (exponent function) and of the compliance function (polynomial function) (see Section 3.3.1). Nevertheless, with these error values (smaller than 6%), the semi-analytic approach, proposed in the previous paragraph, seems acceptable for the analysis of the time-dependent crack growth in the quasi-brittle material.

6.1.1.1.c   Comparison of integral J_{ve} and CZM methods

A comparison between the results obtained from CZM and J-integral method is also performed. The CZM is used in the framework of NLFM while the J-integral method, using the equivalent crack length obtained from the eq.LEFM, is performed in the framework of the LEFM approach. For the J-integral method, the energy release rate $G(a,t)$ is estimated by the invariant viscoelastic integral J_{ve} method (detailed in the Section 2.3.3). The extended crack length selected is 0.4 mm. The propagation of crack occurs when $G(a,t) = G_R(a)$. Figure 6.8 shows the evolution of the displacement, of the energy release rate and of the equivalent crack length obtained from these two methods.

One can be observed in Figure 6.8 that the displacement increases and this increasing is associated to the viscoelasticity as well as the crack growth. The result obtained from the CZM and the integral J_{ve} method are close to each other. This agreement may be explained by the fact that in the integral J_{ve} method, the energy release rate is correlated with the total viscoelastic energy. Moreover, the displacement evolution obtained with CZM case is smooth, while the remaining case exhibits local perturbations. By modeling with a predefined equivalent crack length (cases using the integral J_{ve} method), the jump occurs when the crack propagates.

In summary, the time-dependent crack growth behavior of quasi-brittle material has been presented. Based on the equivalent LEFM, the equivalent crack length for the fracture behavior having the FPZ is determined from the concept of the elastic compliance for two analysis cases: the quasi-static and the viscoelastic. The elastic compliance depends on the size and the position of the FPZ (elastic compliance = secant compliance). The time-dependent crack growth is driven by:

- the increase of the elastic energy due to the addition of viscoelastic strain in the specimen.
- the resistance curve which is the same as the one estimated from a quasi-static test.

Finally, in a first global approximation, the time-dependent crack growth can be simulated with a reasonable accuracy on the basis of the semi-analytical method used for quasi-static test (based on the R-curve).

(a) Load-displacement curve

(b) Evolution of the displacement

(c) Crack growth resistance curve

(d) Evolution of the equivalent crack length
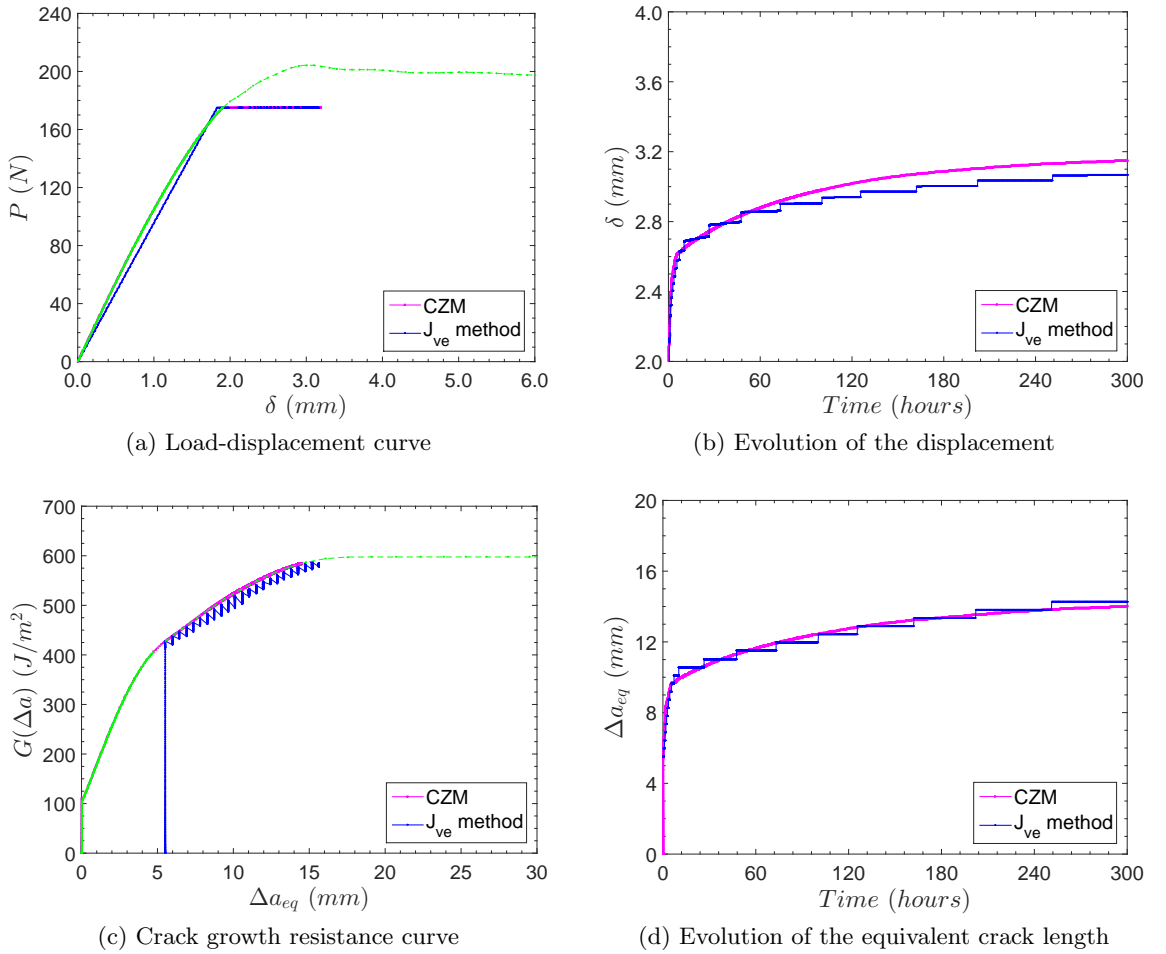
Figure 6.8: Comparison of the displacement, the energy release rate, and the crack length obtained using CZM and the integral J_{ve} method. The green curves plotted in the graph (a) and (c) represent the results obtained under a quasi-static loading

6.1.1.2 Effects of the moisture-dependent phenomena

Considering wood substrate as viscoelastic, the crack growth is influenced by the varying moisture and/or the viscoelastic process. The impact of moisture can also be distinguished under the viscoelastic mechano-sorptive effect (with or without shrinkage-swelling) in the wood substrate and under the rapid moisture variation on the FPZ.

As previously mentioned, four cases (such as case 7, 8, 9 and 11) are selected in order to visualize the individual effects on the crack growth:

- Case 7 (V1T0HL0S0mCZ0): viscoelastic property of wood without the varying humidity (reference case)
- Case 8 (V1T0HL0S0mCZ1): effect of the rapid varying moisture on the FPZ
- Case 9 (V1T1HL1S0mCZ0): effect of the mechano-sorptive behavior
- Case 11 (V1T1HL1S1mCZ0): effect of the mechano-sorptive behavior associated to the shrinkage-swelling

Figures 6.9 and 6.10 show the numerical results obtained for the two scenarios (H and D).

(a) Legend definition

(b) Evolution of the displacement δ

(c) Evolution of the average moisture $MC_{average}$

(d) Evolution of the length l_{coh} of the FPZ

(e) Evolution of the moisture MC_{FPZ}

(f) Evolution of the a_{sf}
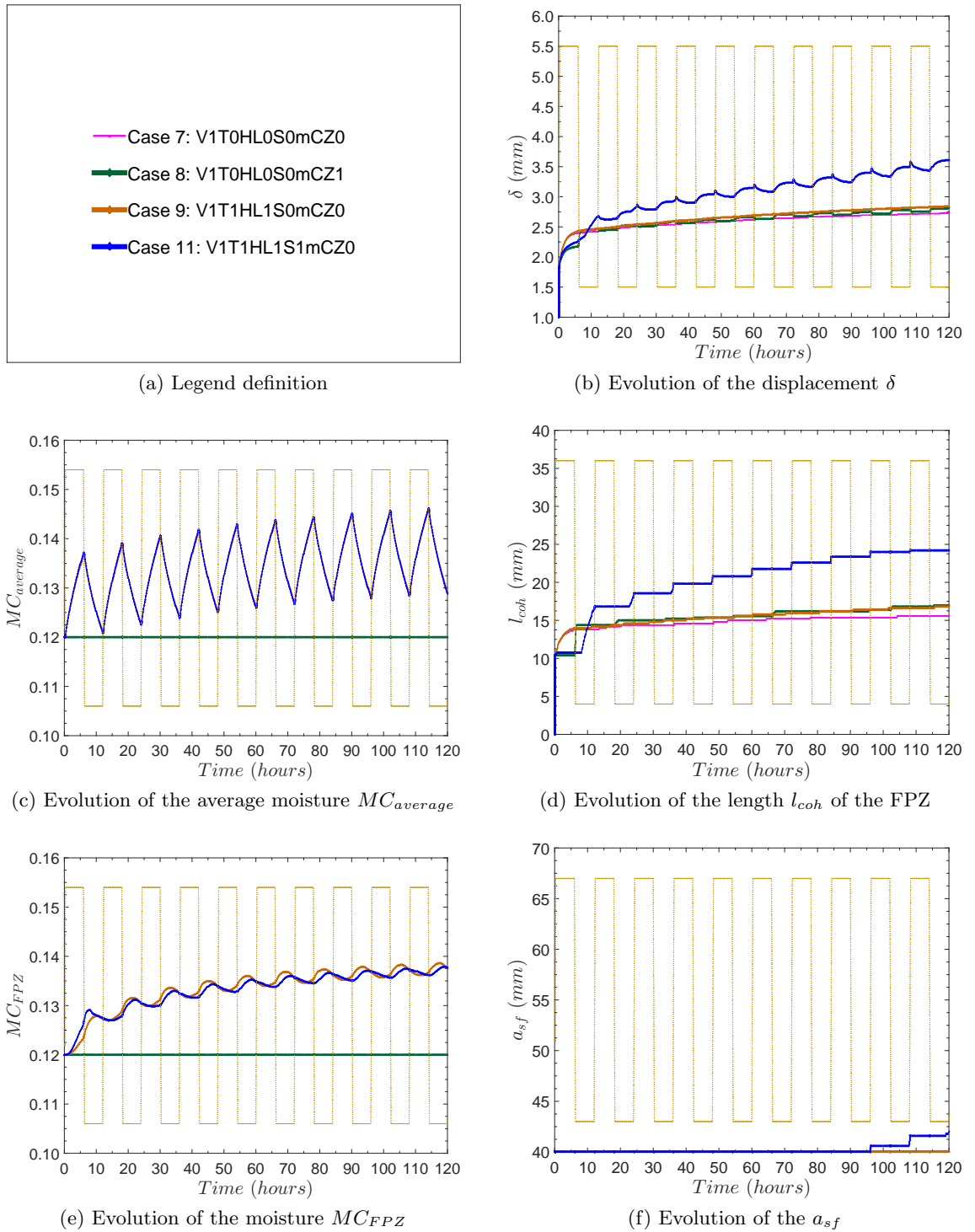
Figure 6.9: Individual effects on the crack growth: scenario H
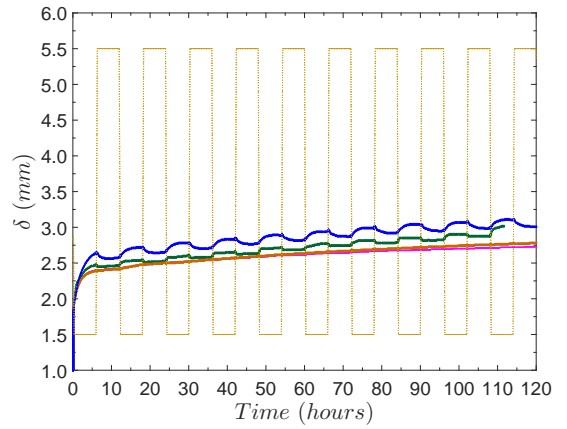
(a) Legend definition

(b) Evolution of the displacement δ
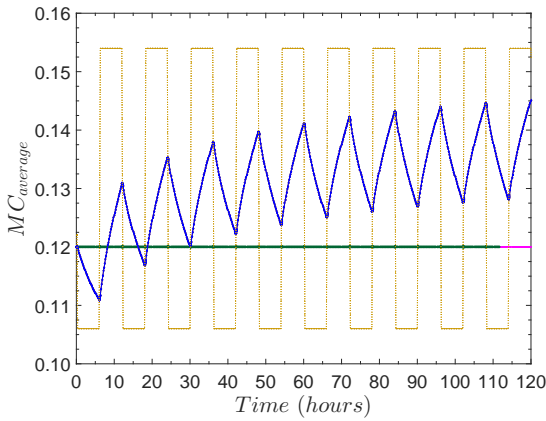
(c) Evolution of the average moisture $MC_{average}$
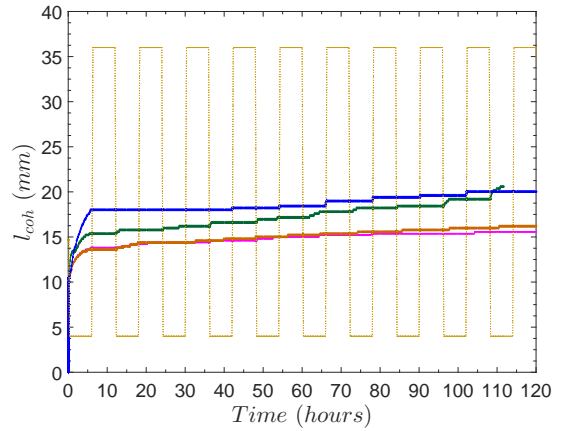
(d) Evolution of the length l_{coh} of the FPZ
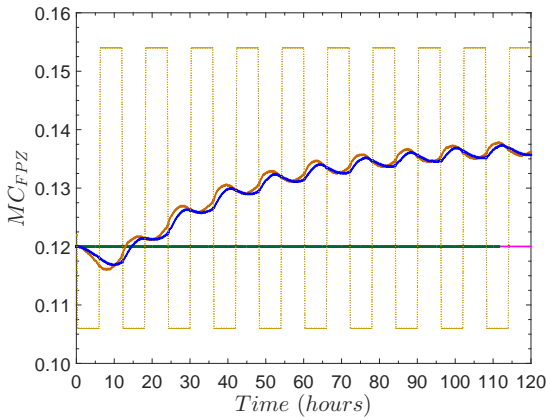
(e) Evolution of the moisture MC_{FPZ}
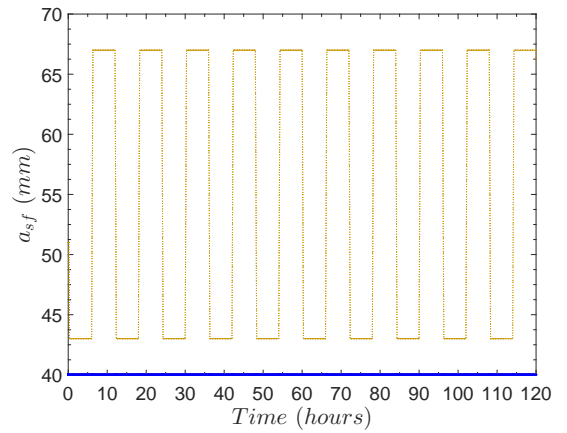
(f) Evolution of the a_{sf}

Figure 6.10: Individual effects on the crack growth: scenario D

From Figures 6.9 and 6.10, we observe that:

- The main crack length a_{sf} (Fig. 6.9f, Fig. 6.10f) is equal to the initial crack length $a_0 = 40\ mm$ because FPZ is not fully developed.

- If we only consider the effect of mechano-sorption behavior associated to the shrinkage-swelling on the crack growth (Case 11: V1T1HL1S1mCZ0), at $t = 12\ hours$ (the first moisture cycle), the length l_{coh} of the FPZ is greater in scenario D than in scenario H (Fig. 6.9d and Fig. 6.10d). After this time, in scenario D, the crack may not propagate because the length l_{coh} of FPZ is quasi-stable and the a_{sf} is equal to the initial crack length (a_0) (Fig. 6.9f and Fig. 6.10f); while in scenario H, the length l_{coh} increases continuously with the crack propagation.

- If we only consider the effect of the rapid varying moisture on the FPZ (case 8: V1T0HL0S0mCZ1), in scenario D, the FPZ length l_{coh} is slightly greater than that in scenario H (Fig. 6.9d and Fig. 6.10d).

- As shown in Figures 6.9d and 6.10d, for both scenarios, the length l_{coh} under the effect of mechano-sorption behavior associated to the shrinkage-swelling (case 11: V1T1HL1S1mCZ0) is higher than under the effect of the rapid varying moisture of the FPZ (case 8: V1T0HL0S0mCZ1).

- However, the amplitude of the displacement δ (Fig. 6.9b and Fig. 6.10b) in the four cases is different: while the displacements obtained in Case 7 (V1T0HL0S0mCZ0), Case 8 (V1T0HL0S0mCZ1) and Case 9 (V1T1HL1S0mCZ0) are similar; those of Case 11 (V1T1HL1S1mCZ0) are far from other cases.

- Based on all above remarks, the effect of the mechano-sorptive behavior associated to the shrinkage-swelling is stronger than the effect of the rapid varying moisture on the FPZ or of the mechano-sorptive behavior on the crack growth. It can be explained that:

  - In the case of the varying moisture on the FPZ (case 8: V1T0HL0S0mCZ1), the moisture effect is only local in the FPZ and then the impact in the crack growth is not significant.

  - In the case of the mechano-sorptive behavior (case 9: V1T1HL1S0mCZ0), the moisture content has a limited effect on whole wood substrate. The period of the moisture cycle (12h) is short, and only 2-3 mm in deep of the wood from the specimen surface is influenced by MC variation.

  - In case 11 (V1T1HL1S1mCZ0), the mechano-sorptive behavior associated to the shrinkage-swelling has a more important influence on the crack propagation

than in the other cases (i.e., case 7, 8 and 9) in the first moisture cycle (scenario D); consequently, in the following cycles, the crack growth and the mechanical state of the specimen are more influenced.

By comparison to the reference case 7 (viscoelastic substrate), each individual phenomenon induces a slight increase of the displacement, which is essentially of the cohesive zone (increase of the eq.LEFM crack length). The mechano-sorptive behavior associated to shrinkage-swelling exhibits the more important influence, followed by the rapid varying moisture on the FPZ and finally the mechano-sorptive behavior leads to a displacement response which is quasi analogous to the one of the reference case (case 7).

6.1.2 Coupled effects

Considering the wood substrate as viscoelastic, the crack growth is influenced by the coupling between the varying moisture and the viscoelastic process. The impact of moisture can also be distinguished under the viscoelastic mechano-sorption in the substrate and under the rapid moisture variation in the FPZ.

As previously mentioned, four cases (such as case 7, 8, 11 and 12) are selected in order to visualize the coupled effects on the crack growth:

- Case 7 (V1T0HL0S0mCZ0): viscoelastic property of wood without the varying humidity (reference case)
- Case 8 (V1T0HL0S0mCZ1): effect of the varying moisture of the FPZ
- Case 11 (V1T1HL1S1mCZ0): effect of the mechano-sorptive behavior associated to the shrinkage-swelling
- Case 12 (V1T1HL1S1mCZ1): coupled effect of the rapid varying moisture on the FPZ and the mechano-sorptive behavior associated to the shrinkage-swelling

Figures 6.11 and 6.12 show the analysis results corresponding to the two moisture cycle scenarios for the 4 cases.

(a) Legend definition
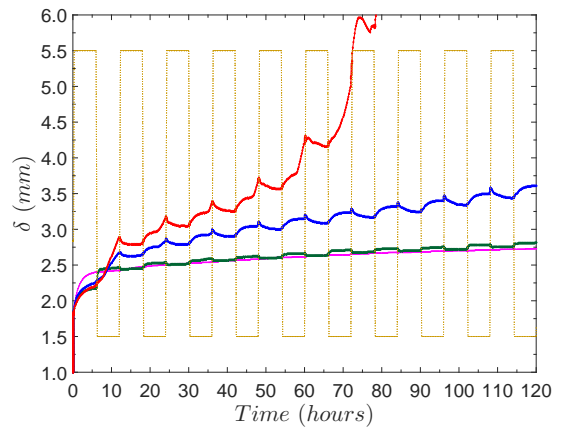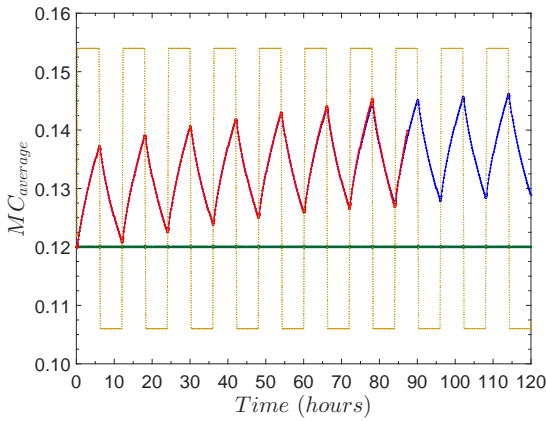
(b) Evolution of the displacement δ

(c) Evolution of the average moisture $MC_{average}$
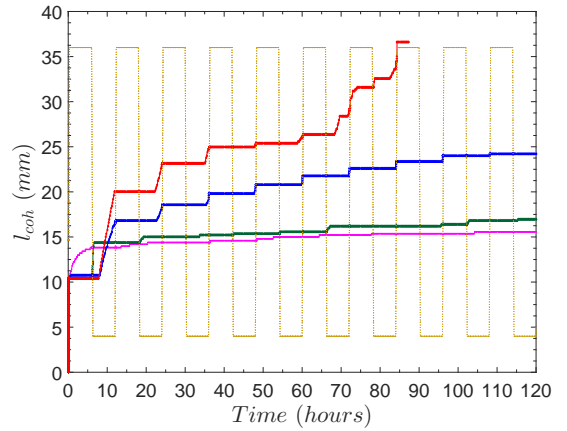
(d) Evolution of the length l_{coh} of the FPZ
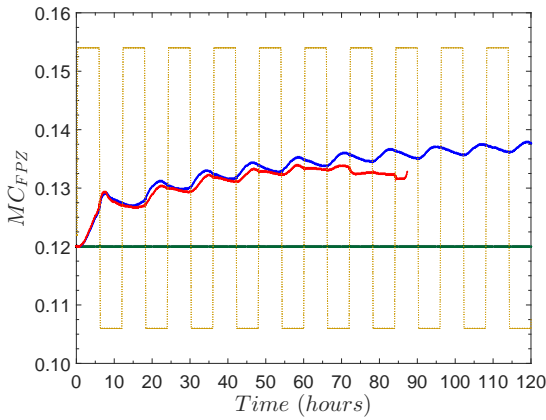
(e) Evolution of the moisture MC_{FPZ}
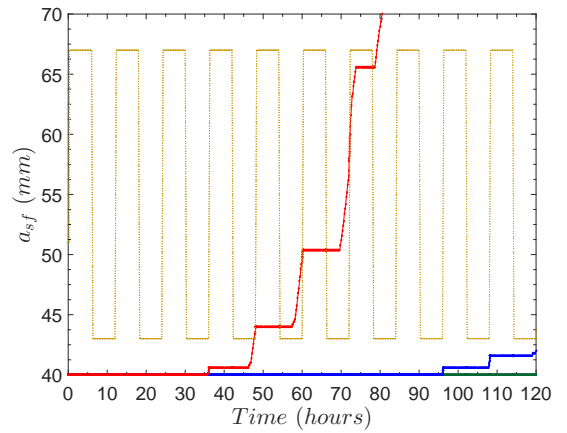
(f) Evolution of the a_{sf}

Figure 6.11: Coupled effect on the crack growth: scenario H
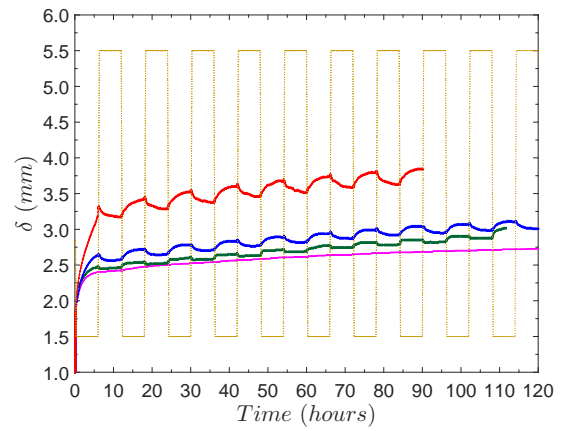
(a) Legend definition

(b) Evolution of the displacement δ
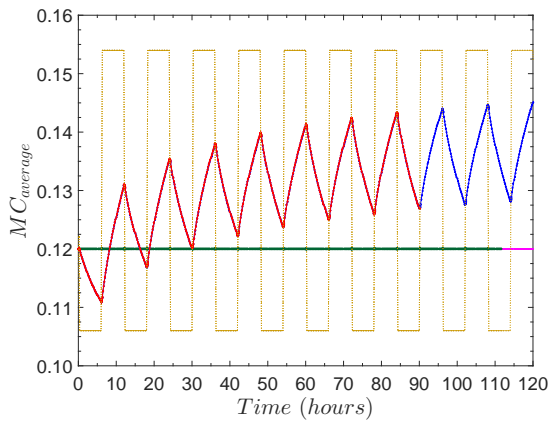
(c) Evolution of the average moisture $MC_{average}$
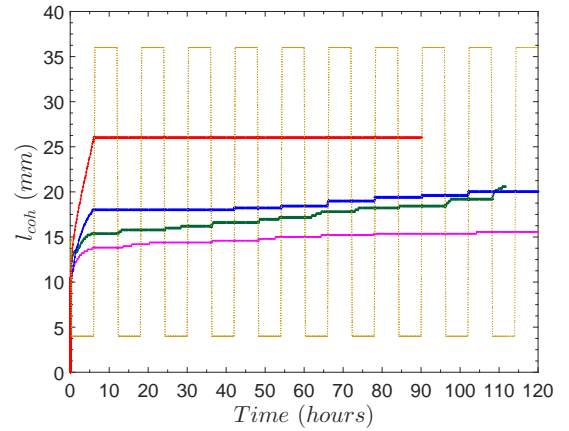
(d) Evolution of the length l_{coh} of the FPZ
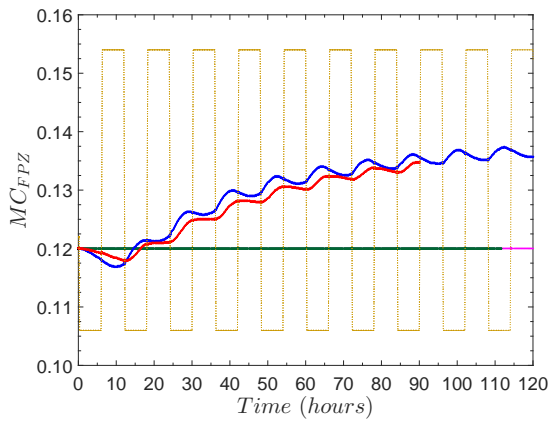
(e) Evolution of the moisture MC_{FPZ}
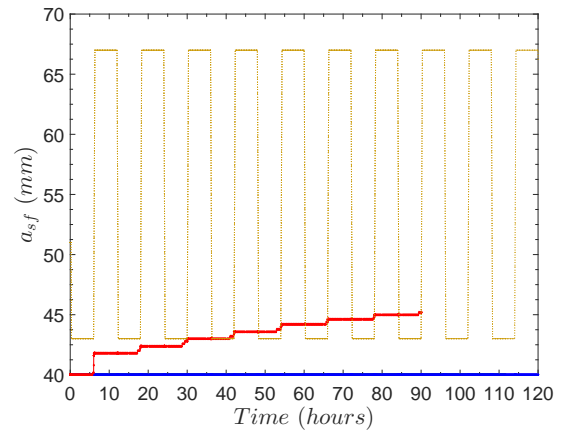
(f) Evolution of the a_{sf}

Figure 6.12: Coupled effect on the crack growth: scenario D

From the results illustrated in Figure 6.11 and Figure 6.12, some points are suggested to be noted and discussed as:

- For a moisture cycle, the crack propagation seems only to occur during the drying phase (Fig. 6.11d, Fig. 6.12d, Fig. 6.11f and Fig. 6.12f). The crack propagation velocity depends on the coupling between the mechanical state and the varying moisture.

- In Figures 6.11d and 6.12d, the length l_{coh} suddenly jumps in the first moisture cycle due to the hydric shock as well as the viscoelastic strain.

- In case of coupled effect between the rapid varying moisture on the FPZ and the viscoelastic mechano-sorptive behavior associated to the shrinkage-swelling on the crack growth (case 12: V1T1HL1S1mCZ1), at $t = 12$ $hours$ (the first moisture cycle), in scenario D, length l_{coh} is higher than that in scenario H (Fig. 6.11d and Fig. 6.12d). After this time, the length l_{coh} in scenario D is constant (i.e., 26 mm in Figure 6.12d), but the main crack length a_{sf} increases. In this scenario, the FPZ is fully developed; so, the a_{sf} increases when the crack propagates. In scenario H, the length l_{coh} and a_{sf} continuously increase. Note that, in this scenario, the length l_{coh} is greater to 26 mm (compared to those obtained in scenario D) because, during the crack growth, the fiber is damaged at different moisture contents (MC_{FPZ}) leading to the applied different moisture-dependent cohesive law.

- For both scenarios, the displacement δ (Fig. 6.11b and Fig. 6.12b), the length l_{coh} (Fig. 6.11d and Fig. 6.12d) and the main crack length a_{sf} (Fig. 6.11f and Fig. 6.12f) under the coupled effect (case 12: V1T1HL1S1mCZ1) is greater than those obtained from the individual effect such as the rapid varying moisture of the FPZ (case 8) or the mechano-sorptive behavior associated to the shrinkage-swelling (case 11).

In summary, the numerical simulation of the cracked structure under RH variations exhibits a strong coupling effect of the viscoelastic mechano-sorptive behavior (associated to shrinkage-swelling effect) and of the rapid varying moisture on the FPZ (Fig. 6.11b and Fig. 6.12b). This coupling induces the failure of the specimen as shown in Figure 6.13 (magnification of the Fig. 6.11b) due to the increase of the stress-free crack length a_{sf} (Fig. 6.11f) and of the cohesive length l_{coh} (Fig. 6.11d). Thus, this coupling plays a major role on the crack growth and cannot be simply considered as the superposition of both phenomena. In this way, such a complex coupling can only be described through a numerical simulation as the one proposed in this study.

The prediction of the numerical model (case 11 and case 12) will be used to confront with the results obtained in the experiment.
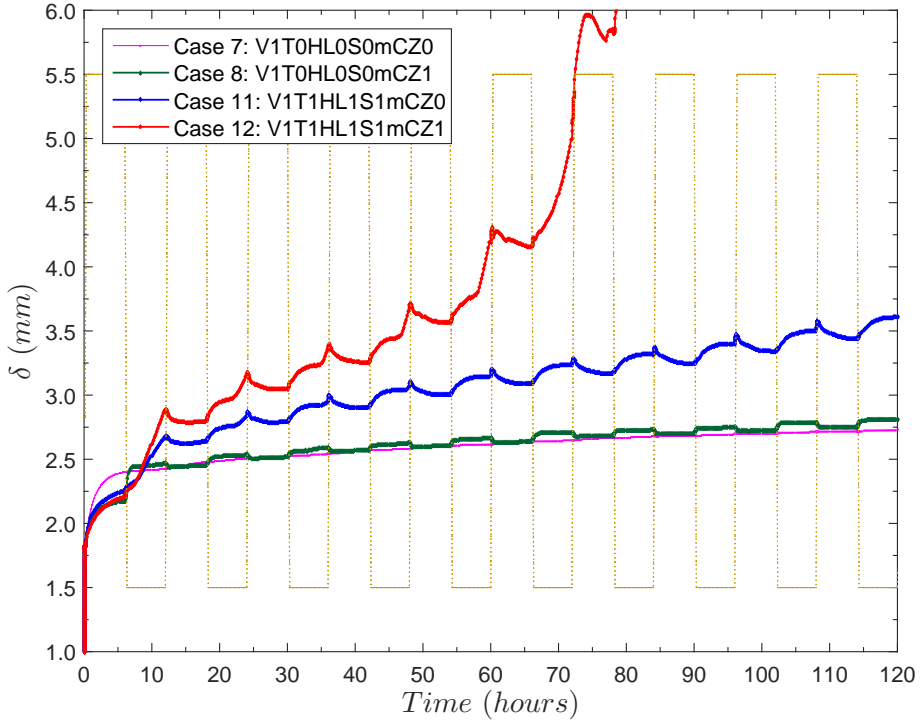
Figure 6.13: Displacement evolution: scenario H

6.2   Comparison with experimental results

In order to compare our proposed method (presented in chapter 5), we have carried out creep tests of mTDCB specimens submitted to varying humidity (scenario H) in which 36 specimens were tested. However, due to technical problems and unstable crack growth for some specimens, only 23 results can be compared with the numerical simulations (case 11 and case 12). Three different test conditions were studied as:

- conditioned moisture 12% with the stress level $SL = 85\%$
- different conditioned moisture $(5\%, 8\%, 18\%, 22\%$ MC) with $SL = 85\%$
- conditioned moisture 12% with different stress levels $(SL = 55\%, 75\%, 80\%$ and $90\%)$

6.2.1   Conditioned moisture 12% with the stress level $SL = 85\%$

Figure 6.14 illustrates the evolution of the displacement δ obtained from simulations and experiments.
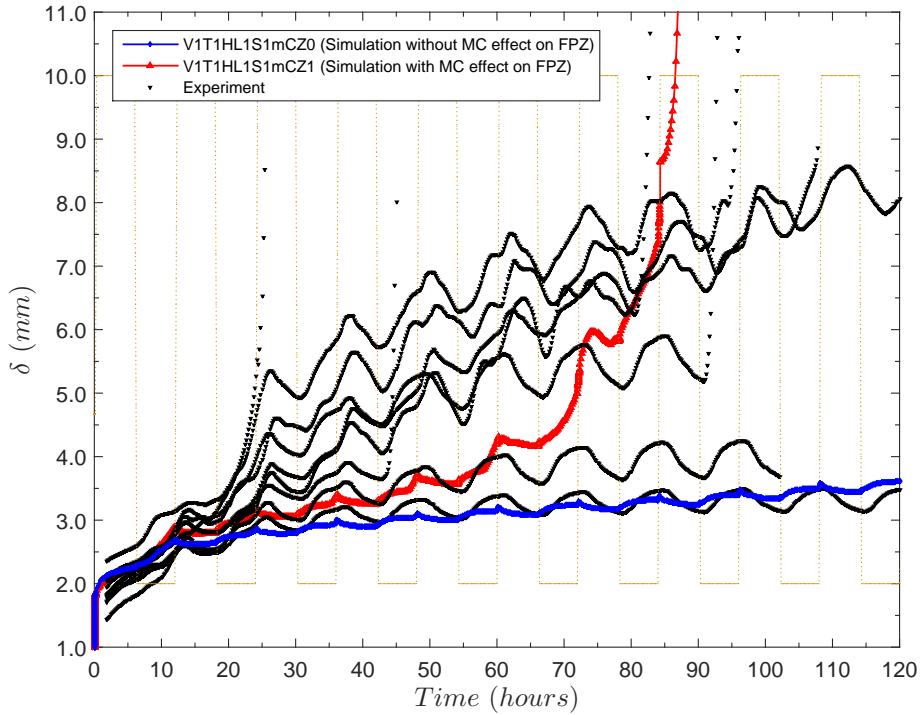
Figure 6.14: Comparison of the displacement obtained from the simulation and the experiment at the conditioned moisture 12% with $SL = 85\%$

In Figure 6.14, a total of 9 experimental curves are presented. The displacement in the experimental test have tendency to increase versus time due to the viscoelastic properties of wood or to the varying moisture. Moreover, the displacement always evolves with the moisture variation in a moisture cycle (a decrease of the displacement during an humidification phase, and an increase conversely during a drying phase).

However, a large scattering of the failure time can be observed from experimental results. Indeed, if the crack appears unstable after 110 hours for most specimens, three of them exhibit an instability after 80 and 100 hours and two specimens failed after 25 hours and 45 hours.

The experimental results appear in agreement with the numerical result obtained on the basis of the complete model (case 12); while the model without the varying moisture effect on FPZ (case 10) only describes the lower experimental response.

Some argumentation are proposed in order to explain the difference between the experimental and simulation results. The simulated displacement in Figure 6.14 can not be well described due not to only an interpolation of creep compliance in function of the moisture but also to the assumption of the viscoelastic properties for three directions during the simulation. Moreover, the difference may also be related to the diffusion properties which are selected from the literature. Nevertheless, the results could confirm the important role of the coupled effect on the crack growth.

Moreover, as shown in Figure 6.14, the failure of the specimens occurs during a drying phase. This phenomenon is in agreement with the previous studies [18, 27–31, 85].

Note that, we cannot deduce the crack propagation from the displacement of the loading points (P_1P_2, Fig. 6.3) because it resulted from the coupling between the crack growth (configuration) and the viscoelastic strain in wood; furthermore, this displacement varies depending on the moisture phase (humidification or drying). A typical evolution of the crack opening displacement versus time during the creep test is presented in Figure 6.15.
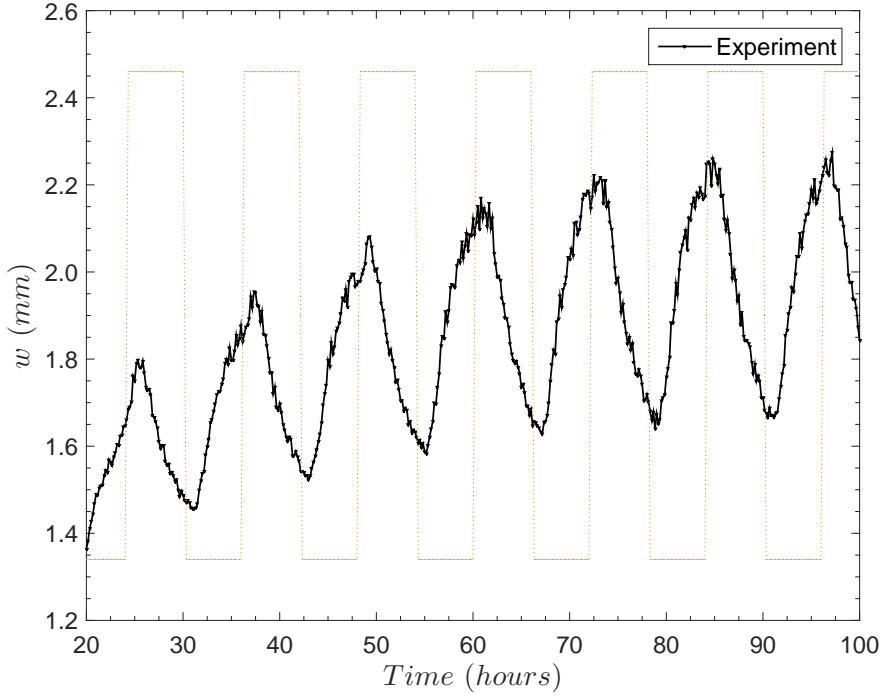
Figure 6.15: The crack opening displacement obtained experimentally at the conditioned moisture 12% and under a stress level $SL = 85\%$

Without the crack propagation, we assume that the effect of the viscoelastic strain in the wood substrate on the crack opening displacement (at the FPZ) is negligible. Based on this, the crack growth process is directly represented by the evolution of the crack opening displacement O_1O_2. The viscoelastic strain or the varying moisture forces the crack to propagate and hence the crack opening increases.

As shown in Figure 6.15, each peak corresponds to a crack length. The peak of the crack opening displacement corresponding to each moisture cycle increases versus time (from 20 hours to 85 hours) and becomes stable (from 85 to 100 hours). It can be concluded that the crack propagation occurs between 20 *hours* and 85 *hours* due to the coupling effect between the viscoelastic strain and the varying moisture.

As seen in Figure 6.15, during moisture cycles, the crack opening has the tendency to re-close during the humidification phase; and conversely, the crack opening has tendency

to open in the drying phase.

In addition, the variation of the mechanical properties of wood substrate is also studied in order to analyze the effect of the scattering of mechanical properties on the crack growth. Figure 6.16 shows the results obtained for 5 cases with the different multiplicative correction factors $\psi = 0.8, 0.9, 1.0, 1.1$ and 1.2 (see Section 3.3.1.3 and Table 4.1). Note that, the correction factor ψ decreases when the Young modulus increases.

Figure 6.16 shows that:

- The evolution of the average moisture $MC_{average}$ are superimposed for all five cases (Fig. 6.16c).

- The evolution of moisture content MC_{FPZ} at the FPZ tip is different due to the crack propagation (Fig. 6.16e).

- Under the same mechanical loading, the evolution of the displacement δ (Fig. 6.16b), the length l_{coh} (Fig. 6.16d) and the crack length a_{sf} (Fig. 6.16f) are significantly important in case of the higher value of ψ due to the small value of the mechanical properties leading to an increase of displacement and hence the crack propagation.

- In case $\psi \geq 1.$, the speed of the crack propagation is high during the drying phase (Fig. 6.16b), the time to rupture are about 12 $hours$, 24 $hours$ and 80 $hours$ corresponding to $\psi = 1.2, 1.1$, and 1.0, respectively. In case $\psi < 1.0$, after $t = 20$ $hours$, the crack growth is stable (Fig. 6.16d). The displacement δ oscillates versus the the moisture cycles (Fig. 6.16b).

- The time to rupture of the specimen decreases with ψ (Fig. 6.16b). The great influence of ψ on the crack propagation can explain the large scattering of the experimental results plotted in Figure 6.14.
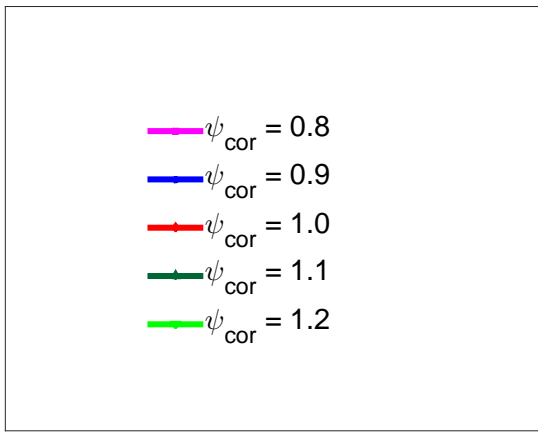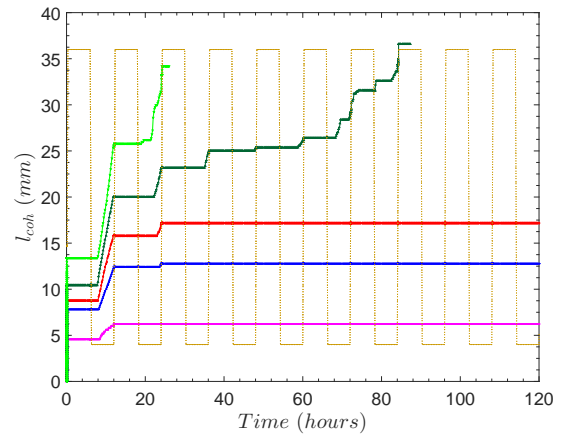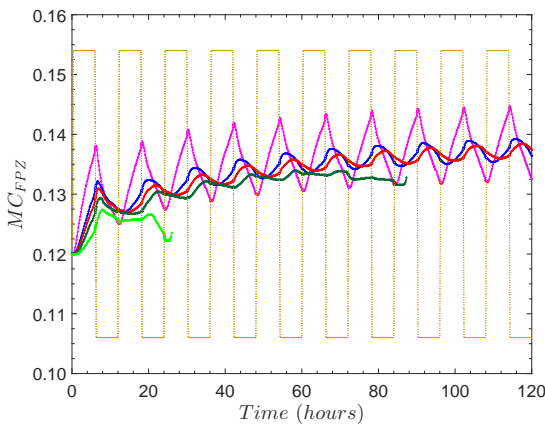
(a) Legend definition
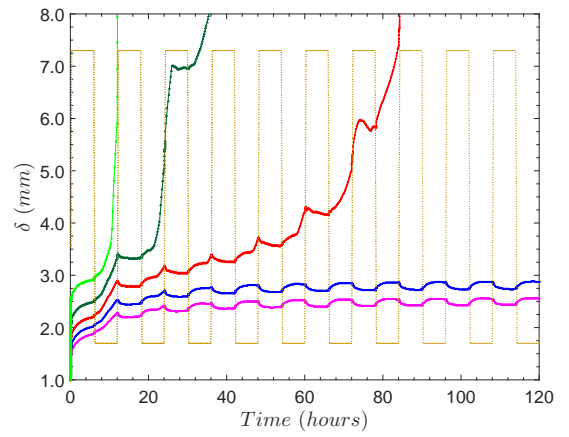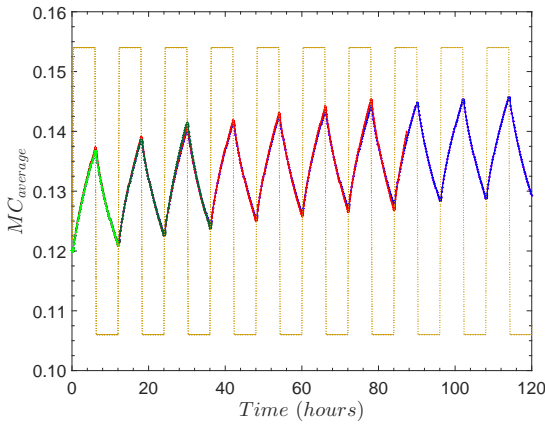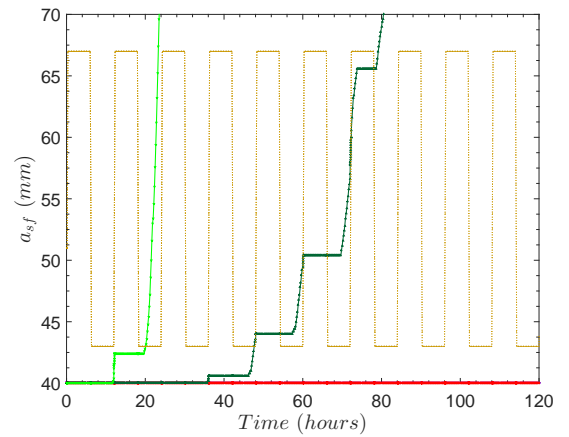
(b) Evolution of the displacement δ

(c) Evolution of the average moisture $MC_{average}$
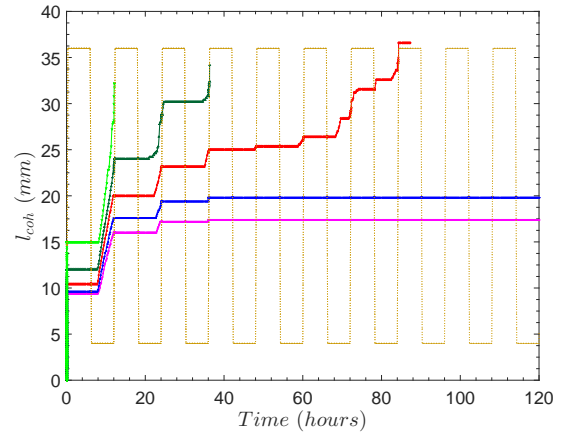
(d) Evolution of the length l_{coh} of the FPZ
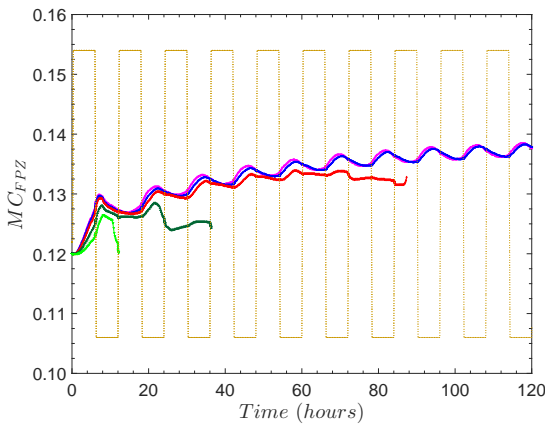
(e) Evolution of the moisture MC_{FPZ}
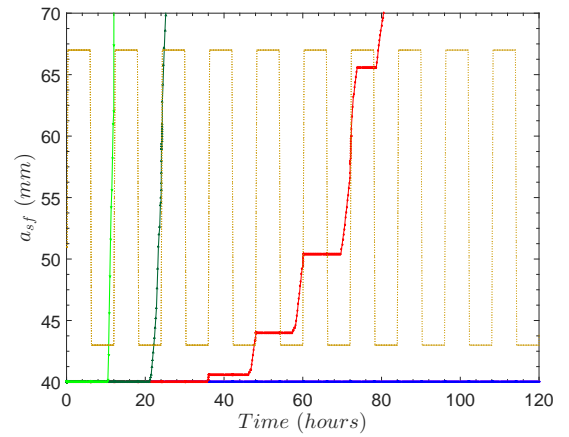
(f) Evolution of the a_{sf}

Figure 6.16: Influence of different correction factors ψ (for case 12: V1T1HL1S1mCZ1 in numerical simulations)

6.2.2 Different conditioned moistures $5\%, 8\%, 18\%, 22\%$ $(SL = 85\%)$

Figure 6.17 illustrates the evolution of the displacement δ obtained from simulations and experiments at different conditioned moisture contents.

(a) at the conditioned moisture of 5%

(b) at the conditioned moisture of 8%

(c) at the conditioned moisture of 18%

(d) at the conditioned moisture of 22%
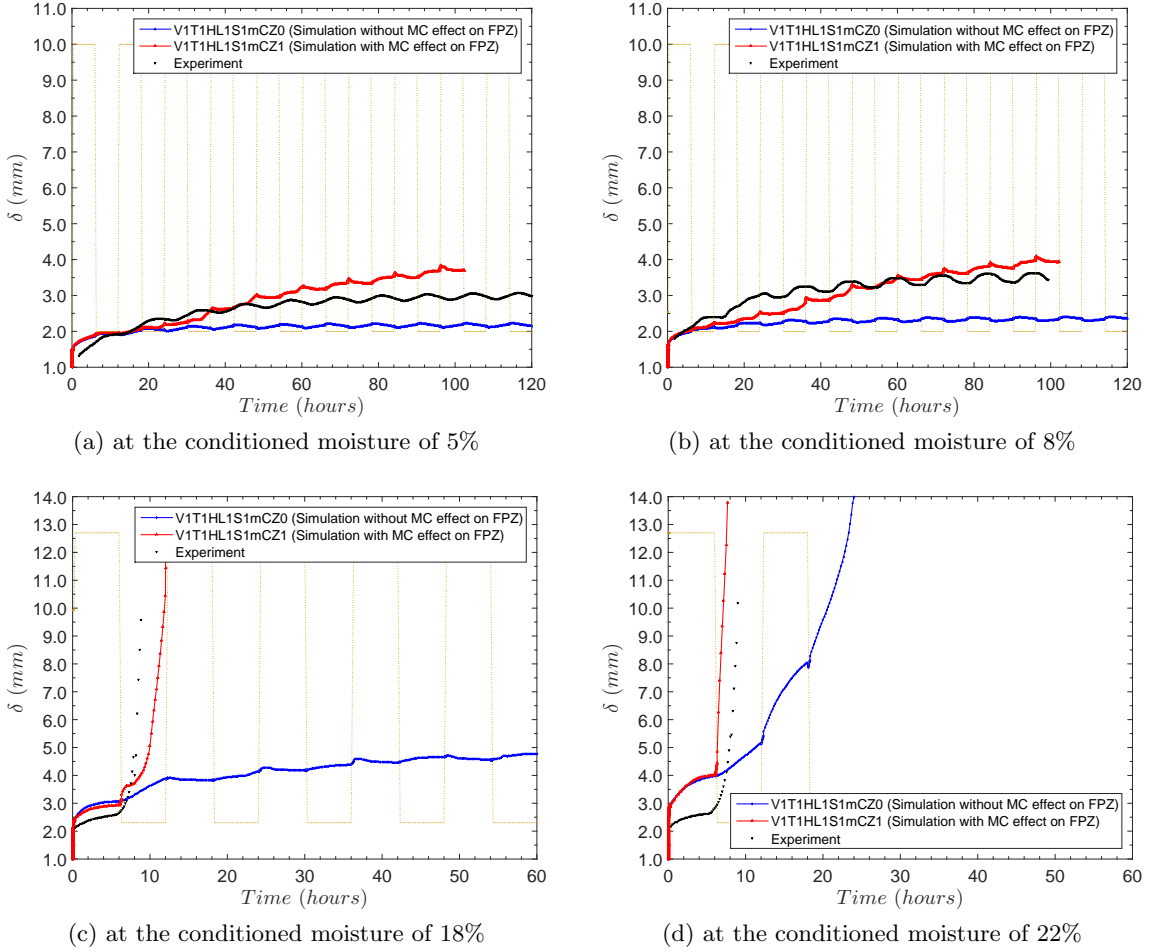
Figure 6.17: Comparison of the displacement obtained from the simulation and the experiments at different conditioned moisture $5\%, 8\%, 18\%, 22\%$ with $SL = 85\%$

In Figure 6.17, the numerical results are comparable to the experimental results. As shown in Figures 6.17c and 6.17d, at the conditioned moisture 18% and 22%, the time to rupture is similar (10 *hours*). Moreover, the crack propagation speed increases during the drying phase. The difference of crack growth process may be related to the mechanical properties which depend on the conditioned moisture. Under the same loading, the crack growth is less influenced (increases slowly) at lower conditioned moisture contents than at high conditioned moisture contents. Moreover, the FPZ length of specimen conditioned at high moisture is longer than that at lower one; consequently, the varying moisture effect on the crack growth is more important for high conditioned moisture.

On the other hand, it can be clearly observed from Fig. 6.17 that the complete model (case 12, i.e., hygro-lock effect associated with the shrinkage-swelling and rapid varying

moisture on the FPZ) is in fair agreement with the experimental results than those obtained from the model describing only the hygro-lock effect associated with the shrinkage-swelling (case 11). Even if the model based on hygro-lock leads to a failure at conditioned moisture of 22% (Fig.6.17d), the coupling between the hygro-lock effect associated with the shrinkage-swelling and the rapid varying moisture on the FPZ (which are implemented in the complete model) seems to play a major role in the crack growth and leads to an early failure in agreement with the experimental one.

In order to observe the evolution of $MC_{average}$, MC_{FPZ}, l_{coh} and a_{sf} under different conditioned moisture contents, we extend our study by varying the conditioned moistures MC_{cond}. Figure 6.18 shows the results obtained for 5 cases: $MC_{cond} = 5\%, 8\%, 12\%, 18\%$ and 22%.

As seen in Figure 6.18, we observe that:

- The evolution of the average moisture $MC_{average}$ is greatly influenced by MC_{cond}. (Fig. 6.18c). Nevertheless, after $t = 100\ h$, $MC_{average}$ becomes stable and appears to be similar for three cases 5%, 8% and 12% MC_{cond}.

- The evolution of moisture MC_{FPZ} at the FPZ tip is similar to the average moisture one $MC_{average}$ one (Fig. 6.18e).

- The evolution of the displacement δ (Fig. 6.18b), the length l_{coh} (Fig. 6.18d) and the crack length a_{sf} (Fig. 6.18f) increase rapidly during the first cycle in case of higher conditioned moistures. As mentioned in the previous paragraph, the crack grows more easily in wet than in dry wood (under the same loading).

- Moreover, in Figure 6.18e, at $t < 12\ hours$, the moisture MC_{FPZ} ($MC_{cond} \geq 18\%$) is higher than the moisture surface (18%) which leads to drying in the FPZ and thus causes more rapid crack propagation.

- In case of higher MC_{cond}, the crack propagation speed is high during the drying phase (Fig. 6.18b), the time to rupture of the specimens is about 6 $hours$ and 9 $hours$ for 22% and 18% MC_{cond}, respectively. However, the crack growth in case of lower MC_{cond} is only unstable after 80 $hours$ or more (Fig. 6.18d and Fig. 6.18f).
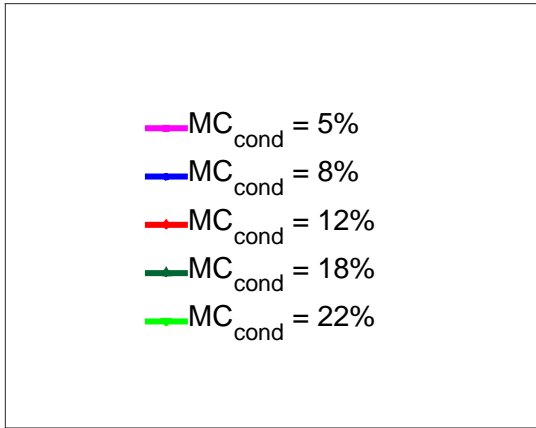
(a) Legend definition
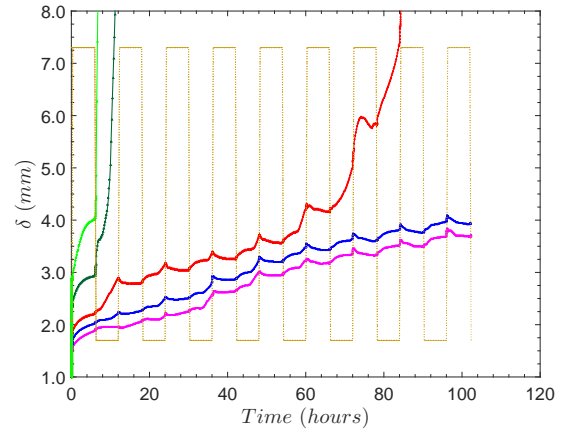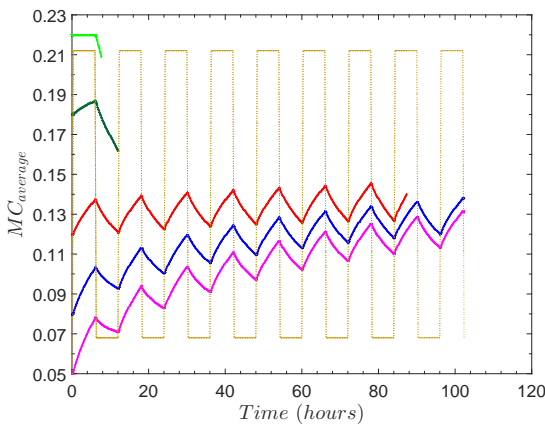
(b) Evolution of the displacement δ

(c) Evolution of the average moisture $MC_{average}$
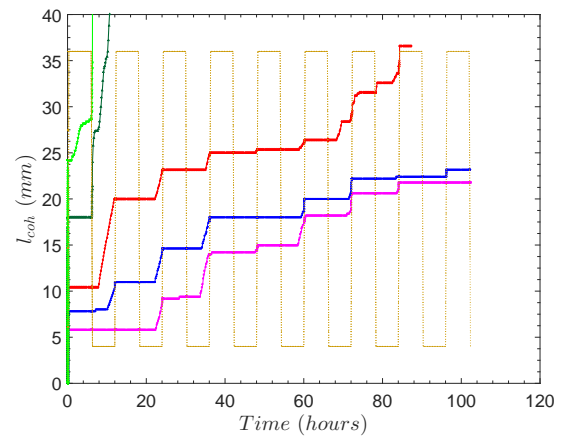
(d) Evolution of the length l_{coh} of the FPZ
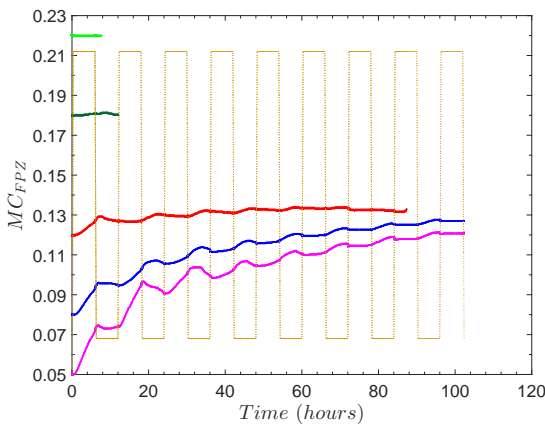
(e) Evolution of the moisture MC_{FPZ}
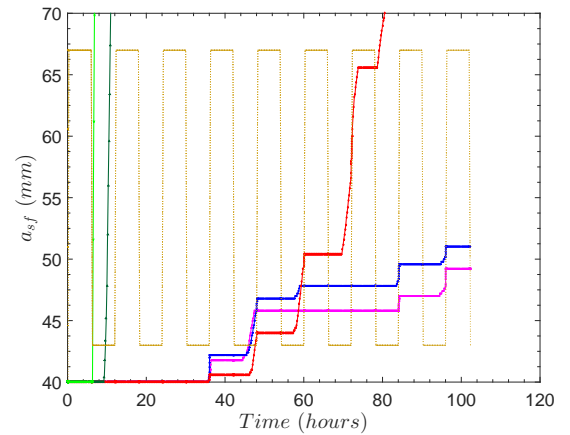
(f) Evolution of the a_{sf}

Figure 6.18: Influence of different conditioned moistures (for case 12: V1T1HL1S1mCZ1 in numerical simulations)

6.2.3 Conditioned moisture 12% with several stress levels

Figure 6.19 illustrates the evolution of the displacement δ obtained from simulations and experiments under different stress levels.

(a) at the stress level $SL = 55\%$

(b) at the stress level $SL = 75\%$

(c) at the stress level $SL = 80\%$

(d) at the stress level $SL = 90\%$
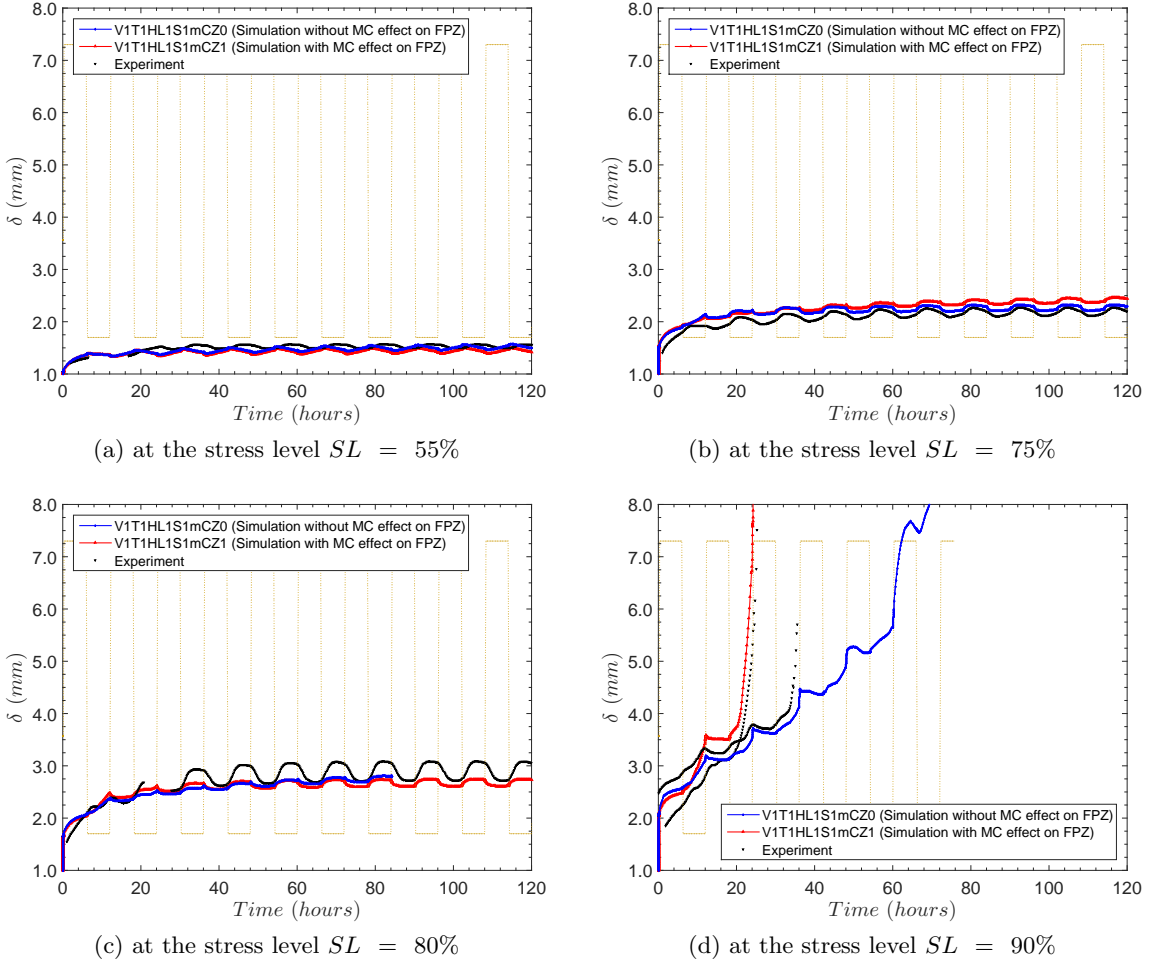
Figure 6.19: Comparison of the displacement obtained from the simulation and the experiments at the conditioned moisture 12% under different stress levels

As shown in Figure 6.19d, at the stress level $SL = 90\%$, the time to rupture of two specimens is obtained about 24 *hours* and 40 *hours*. Moreover, the crack propagation speed increases during the drying phase. In Fig. 6.19, different crack growth processes are related to different stress levels SL.

In Fig. 6.19, the numerical results are comparable to the experimental ones. The numerical simulations are in better agreement with the experimental results using the coupled effect of the hygro-lock and the rapid varying moisture on the FPZ (case 12). As previously mentioned, the complete model leads to a more accurate simulation of the time to failure compared to the model based on the alone hygro-lock phenomenon. As similar to two previous paragraphs in Sections (section 6.2.1 and section 6.2.2), the coupled effect presents an important role on the crack growth (Fig. 6.19).

Figure 6.20 shows the details of the crack growth process obtained from the complete model for different stress levels ($SL = 55\%, 75\%, 80\%, 85\%$ and 90%).
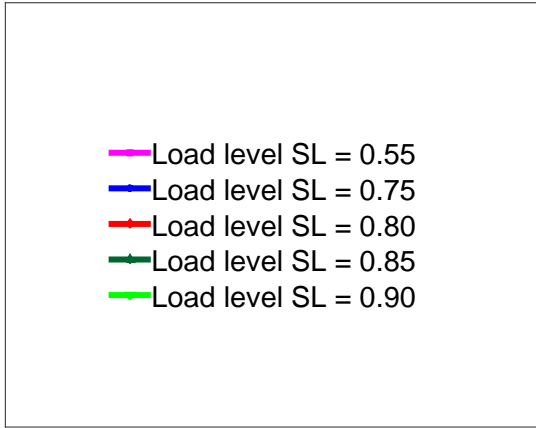
(a) Legend definition
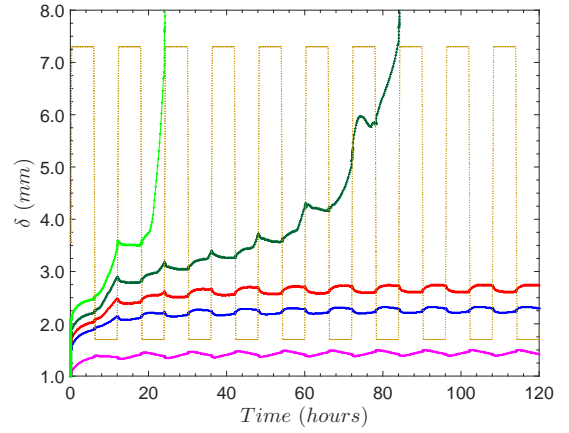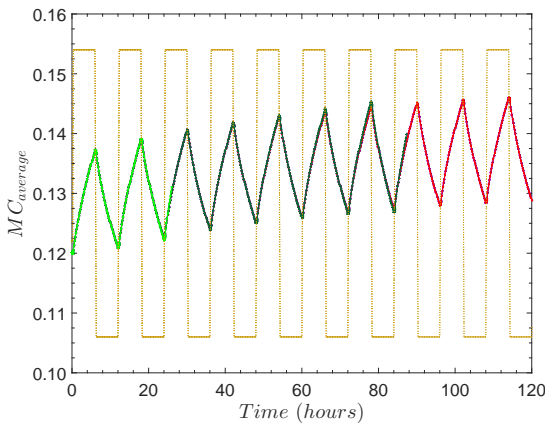
(b) Evolution of the displacement δ

(c) Evolution of the average moisture $MC_{average}$

(d) Evolution of the length l_{coh} of the FPZ

(e) Evolution of the moisture MC_{FPZ}

(f) Evolution of the a_{sf}

Figure 6.20: Effect of different stress levels (for case 12: V1T1HL1S1mCZ1 in numerical simulations)

From Figure 6.20, we can deduce that:

- The evolutions of the average moisture $MC_{average}$ are superimposed (Fig. 6.20c).

- The evolution of MC_{FPZ} at the FPZ tip is different due to the crack propagation (Fig. 6.20e).

- The evolutions of the displacement δ (Fig. 6.20b), the length l_{coh} (Fig. 6.20d) and of l_{coh} (Fig. 6.20f) are significant under higher stress level.

- For the high stress level, the time to rupture is about 24 *hours* and 86 *hours* under $SL = 90\%$ and 85%, respectively (Fig. 6.16b). For other stress level ($SL = 55\%$, 75% and 80%) the displacement δ oscillates with the moisture cycles (Fig. 6.16b). At these slow levels, the crack growth is stable, the length l_{coh} and the main crack length a_{sf} are constant as illustrated in Figure 6.20d.

- As shown in Figure 6.20d, during the drying phase in the first moisture cycle (from 6 *hours* to 12 *hours*), whatever the SL, the length l_{coh} jumps due to the crack propagation. However, the variation of the length l_{coh} is different and depends on the stress level. The higher the stress level, the more the crack propagates.

6.3   Conclusion

In this chapter dedicated to the analysis of the numerical simulations obtained from the model proposed in chapter 5, the effect of each component of the model has been firstly observed. The individual effects difficult to isolate, from an experimental point of view, seem to be in agreement with those expected intuitively. On this basis, the coupled effects are analyzed and the results exhibits a strong coupling between the hygro-lock phenomenon (i.e, effect of the mechano-sorptive behavior associated to the shrinkage-swelling) and the rapid varying moisture on the FPZ. This coupling leads mainly to an increase of the crack growth kinetics and hence to early failures.

The results obtained from the complete model (case 12: the hygro-lock effect associated to the shrinkage-swelling and the rapid varying moisture on the FPZ) and the initial model (case 11: the the hygro-lock effect associated to the shrinkage-swelling) are then compared to the experimental ones performed from mTDCB specimens for various conditioned moistures and different stress levels.

Despite a large scattering of the experimental results, the numerical simulations seem to capture the outline of the experimental responses and especially the sudden change of crack growth leading to early failures.

The comparison with the numerical results obtained on the basis of the alone hygro-lock phenomenon emphasize the necessity to consider the instantaneous varying moisture effect on the cohesive zone. The coupling seems to be the key of relevant description of the experimental responses but such a complex coupling, which is not a simple superposition problem, can be described only through a numerical approach as the one proposed in this thesis.

Nevertheless, the present numerical model requires other validation procedures and especially a comparison to experimental results of crack growths obtained from more complex RH variations where the magnitudes of the drying phase are different from those of the humidification ones.

Conclusions and Perspectives

Nowadays, the Maritime pine is more used for civil structures because of its abundant resources in the Aquitaine region. In the context of the climate change, the continuous changes of environmental climatic conditions create wet and dry states in the material which reduces the strength and leads to crack propagation in timber structures. Under variations of the external environmental conditions, the cracked timber structures are more affected than under constant conditions due to the influence of varying wood moisture on the crack growth.

In this thesis, a method is proposed in order to analyze the crack growth of timber structures under environmental conditions in which moisture effect is integrated into the Fracture Process Zone (FPZ), and leads to express the coupling between the Thermo-Hydro-Mechanical behavior of wood and the crack growth process. A number of simulations obtained from this method allows us to better understand the mechanisms influencing the crack growth caused by drying and humidification phases in the structure. Moreover, due to variations of the external environment, various phenomena related to the crack growth process can be possibly isolated while such phenomena are difficult to obverse from experimental tests.

Based on thermodynamic principles, the viscoelastic properties depending on moisture are introduced in the 3D viscoelastic mechano-sorptive model. The 3D mechano-sorptive model is based on the 1D incremental formulation proposed and validated by Husson and Dubois [49]. Moreover, an incremental formulation introducing the effect of rapid varying moisture on the FPZ was also proposed and analyzed. An increment formulation coupling of the mechano-sorptive behavior, the effect of rapid varying moisture on the FPZ was then implemented in a finite element code in order to analyze the crack growth of timber structures under environmental conditions.

The moisture diffusion process in wood depends on the stress level, on the internal moisture and on the temperature in material in which the coupled thermal-hydro-mechanical process is interacted to each other. In this thesis, the moisture diffusion process was analyzed under constant temperature. In addition, the diffusion coefficient was supposed to

be independent of the stress level.

In the 3D viscoelastic mechano-sorptive model, the generalized Kelvin Voigt with two branches was used. Based on the assumption that the orthotropic factors are independent of moisture, the creep compliance functions related to the tangential and radial directions of wood were considered to be linearly proportional to the creep compliance function related to the longitudinal direction.

The mode I fracture properties of wood were determined experimentally through resistance curves obtained from ten different moisture contents ranging from 5% to 30%. On this basis, the cohesive laws (bi-linear softening) corresponding to these 10 moistures were estimated allowing to describe the fracture process for any moisture (linear interpolation from the known cohesive parameters).

The results of the numerical model showed that in addition to the effect of the viscoelastic on the crack propagation (due to the increase of the elastic energy stored in the structure), the varying moisture might also be at the source of an increase of the crack growth kinetics. The effect of viscoelastic mechano-sorptive behavior on the crack growth appears more important than the effect of rapid varying moisture on the FPZ during the first humidification phase; conversely during the first drying phase. Nevertheless, the coupling of both effects has more influence than each of the individual effect on the crack growth.

During the drying phase, the crack has tendency to propagate. The propagation rate depends on the hydric shock: humidification phase makes the crack propagate slowly or not propagate, whereas drying phase accelerates this rate. These results are confronted with creep tests performed in the climatic room on the Maritime pine specimens.

Even if the present model requires other validations from experimental results in order to check the relevance of the simulation in the case of complex RH variations, the model offers the possibly to estimate the time to rupture for various cracked or uncracked structures submitted to environmental conditions (in so far as potential crack paths is known: location of the cohesive interface). That is one advantage of this method since it is sufficient to give a reference to define an ultimate state for failure of structures.

Implanted into a 3D finite element code (in the source code), this method can be applied for complex structures where the mechanical state of the structure strongly depends on one or more interactions (e.g., the interaction between components of the structure such as connections, assembly, glued-in rods, etc...).

However, some points need to be more investigated in future works in order to improve the relevance of the model proposed in the present thesis.

Firstly, due to the interaction between the wood properties such as the diffusion coefficients, the mechanical properties and the heterogeneity..., a sensitive study of each parameter on the crack growth is necessary. Moreover, the sensibility of these parameters on the time to rupture could be investigated using probabilistic and statistical approaches.

Secondly, to obtain more accurate simulations, a better knowledge of the material behavior is required. Not only the characterization of the viscoelastic properties in function of moisture but also the estimation of the diffusion coefficients as a function of the loading is necessary. A characterization strategy for the experimental test is needed to characterize mechanical properties for each phenomenon in drying and wetting states. However, the great question of this work is how to isolate each effect. Note that, the irreversible mechano-sorptive phenomenon is also not considered in this thesis.

Thirdly, the mechanical and fracture parameters used in the model (e.g., diffusion, fracture properties...) are all obtained from experimental tests performed on small specimen sizes. The use of the model for actual structure dimensions should require to consider a scale effect on all or part of the different phenomena considered in the model.

Fourthly, the evolution of the crack growth under humidity variations is here only considered in mode I in order to simplify the problem, while the structures are frequently submitted to mixed mode of rupture due to the position of loading and the direction of crack. On the basis of the same approach than the one considered for mode I, it is possible to extend this approach to take into account the influence of the rapid varying moisture on the cohesive zone in mixed mode loading.

Fifthly, the crack growth under varying moisture can be more or less influenced by considering the viscous property of the damaged material in the FPZ. However, the characterization of the viscous property in this zone by experimental tests is quasi-impossible to perform due to the coupling between the crack growth and the creep deformation. Nevertheless, it is quite easy to consider viscous properties of the cohesive zone in the numerical model. Moreover, the crack growth of the structure can also be influenced by thermal shocks on the FPZ.

Sixthly, during the structure lifetime, external environment cycles (e.g., night and day, season cycles) considered as a climatic loading, lead to fatigue damage of the material. Although the maximum stress may be much less than the material strength, the structure could be damaged due to fatigue. If fatigue is coupled with the effect of moisture variations on the crack growth, the time to rupture may be reduced. Further studies on damage under fatigue are then encouraged.

Finally, also note that in timber structures, it seems to appear that the locally high stress is at the crack tip or at the connective assembly zone, the viscoelastic properties are non-linear viscoelastic at this zone. It will be necessary to reconsider our model by taking into account this non-linear behavior of wood, especially in the mechano-sorptive model.

A practical application of the proposed method on constructions was one objective of this thesis. However, this task is quite complicated due to the enormous computational effort as well as the validation of adequate formulation. Nevertheless, it gives us the opportunity to better understand the material behavior as well as to predict the lifetime of structures, which encourage further study on this subject.

Appendix

Appendix A

Twelve analysis cases of crack growth in a viscoelastic media under varying moisture effect

Based on the three principal parts (the diffusion problem in wood, the wood substrate and the FPZ), we propose twelve different cases of the simulation which are detailed as shown in Figure A.1.

Analysis case	Wood substrate				Cohesive zone taken account of rapid vaying moisture effect
	Mechanical properties	Moisture transfert	Hygro-Lock (Mechano-sorptive)	Shrinkage -swelling effect	
Notation	V	T	HL	S	mCZ
Case 1 V0T0HL0S0mCZ0	Elastic				
Case 2 V0T0HL0S0mCZ1	Elastic				Yes
Case 3 V0T1HL1S0mCZ0	Elastic	Yes	Yes		
Case 4 V0T1HL1S0mCZ1	Elastic	Yes	Yes		Yes
Case 5 V0T1HL1S1mCZ0	Elastic	Yes	Yes	Yes	
Case 6 V0T1HL1S1mCZ1	Elastic	Yes	Yes	Yes	Yes
Case 7 V1T0HL0S0mCZ0	Viscoelastic				
Case 8 V1T0HL0S0mCZ1	Viscoelastic				Yes
Case 9 V1T1HL1S0mCZ0	Viscoelastic	Yes	Yes		
Case 10 V1T1HL1S0mCZ1	Viscoelastic	Yes	Yes		Yes
Case 11 V1T1HL1S1mCZ0	Viscoelastic	Yes	Yes	Yes	
Case 12 V1T1HL1S1mCZ1	Viscoelastic	Yes	Yes	Yes	Yes

Figure A.1: Twelve different cases in the crack growth under the moisture variation

Sections (from Section A.1 to Section A.12) show the evolution of the average moisture $MC_{average}$ of the specimen, the average moisture MC_{FPZ} at the tip of FPZ as well as the displacement δ for twelve cases. Based on these results, we briefly observe that:

- The average moisture $MC_{average}$ of specimen, the moisture MC_{FPZ} at the tip of FPZ and the displacement δ evolve versus time.

- The initial conditioned moisture of the specimen is 12%. Under the cyclic moisture $(7\% - 22\%)$, the specimen will reach the mean moisture of 14-14.5% after 120 hours. Before reaching the mean moisture, $MC_{average}$ and MC_{FPZ} have the tendency to increase versus time and then become stable after 120 hours.

- For most of viscoelastic analysis cases (with or without moisture transfer in wood), the displacement δ increases versus time. It may be related to the viscoelastic properties of wood.

- For a moisture cycle, it appears that the displacement δ increases during the drying phase and decreases during the humidification phase.

- The length l_{coh} of the fracture process zone evolves not only with time but also with the varying moisture. We assume that the varying time or moisture make crack further propagate.

A.1 Case 1 (V0T0HL0S0mCZ0): elastic property of wood
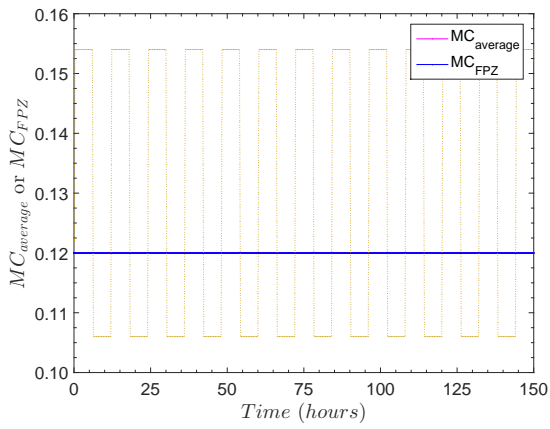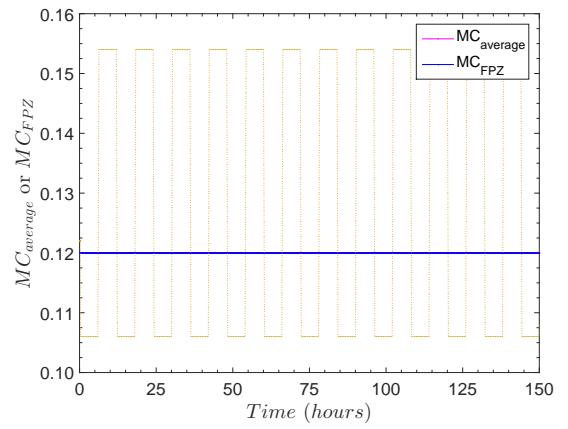
(a) scenario H
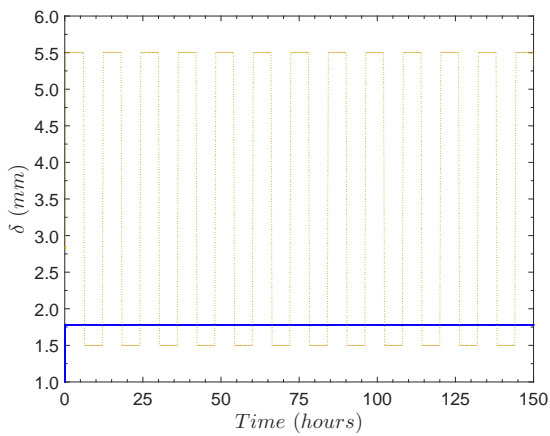
(b) scenario D
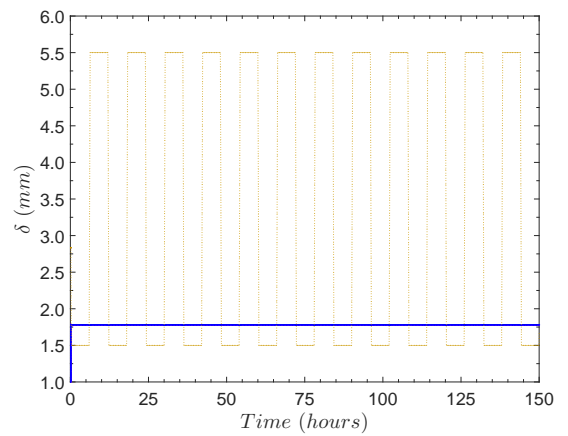
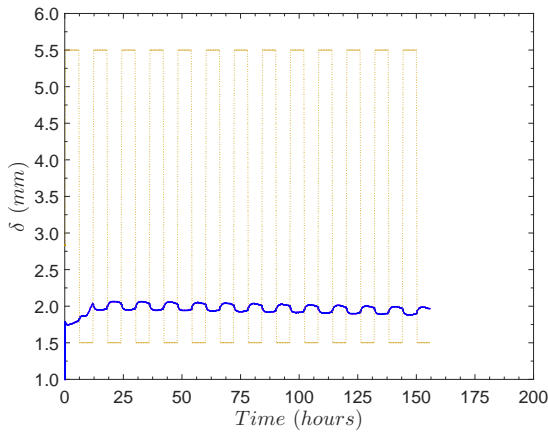(c) scenario H
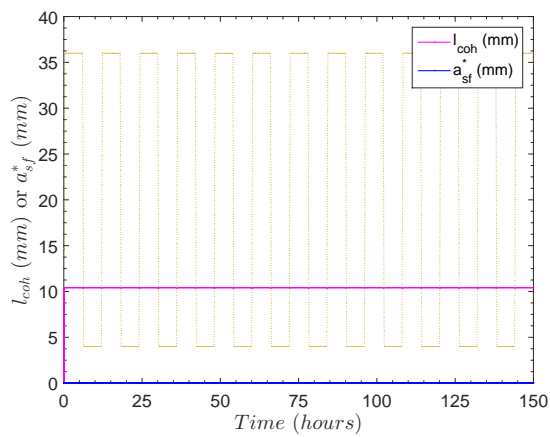
(d) scenario D
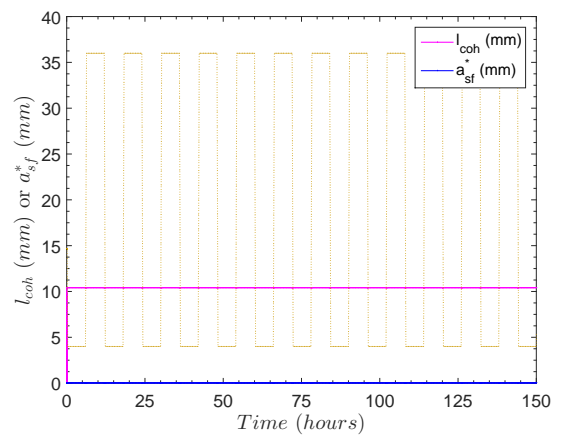
(e) scenario H

(f) scenario D

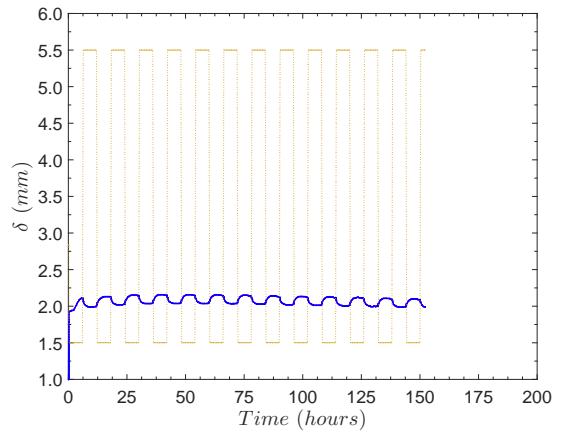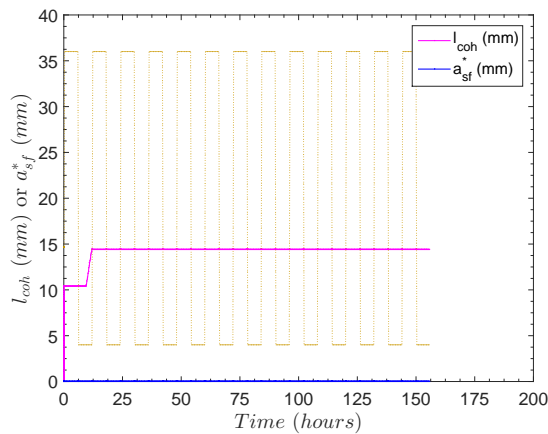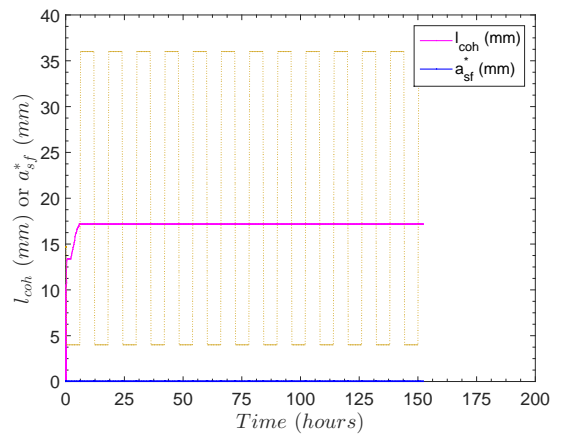## A.2 Case 2 (V0T0HL0S0mCZ1): elastic property of wood with the moisture effect on FPZ
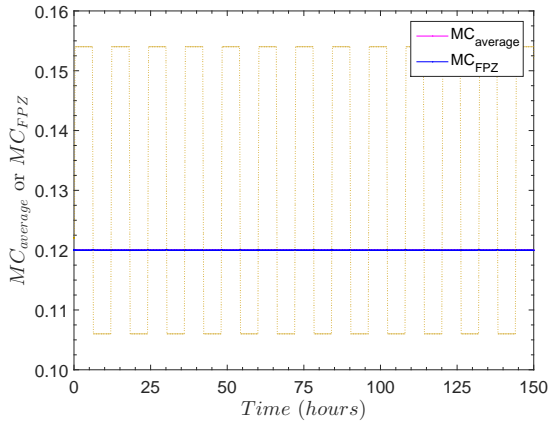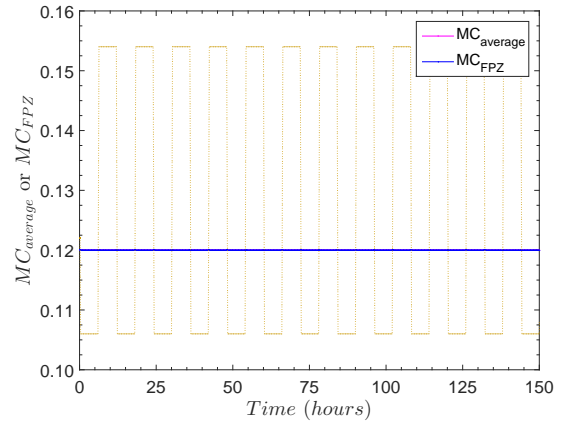
(a) scenario H
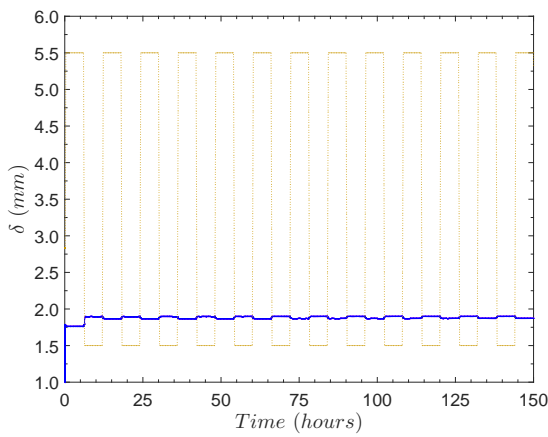
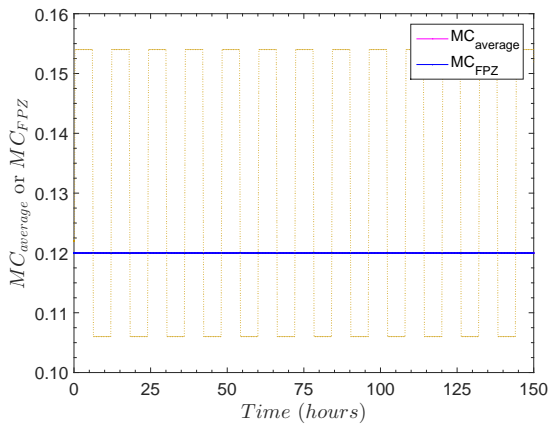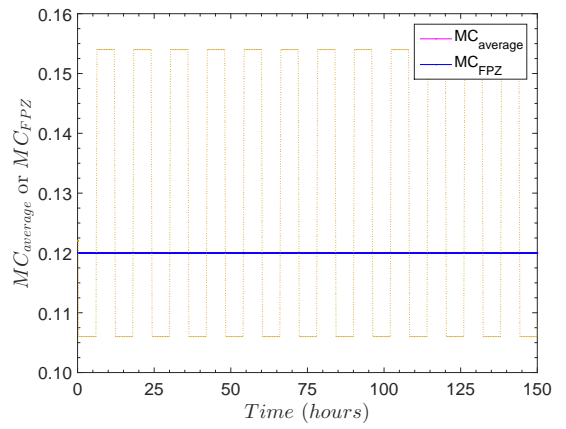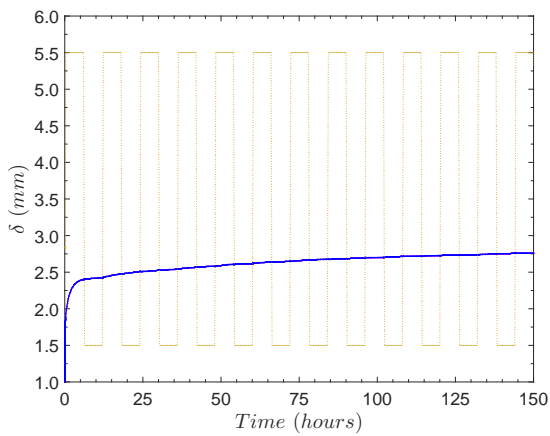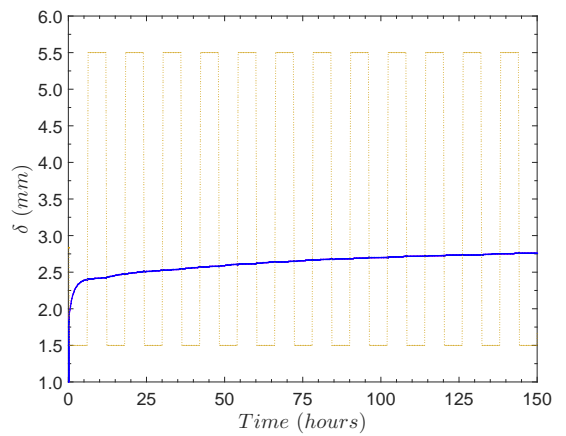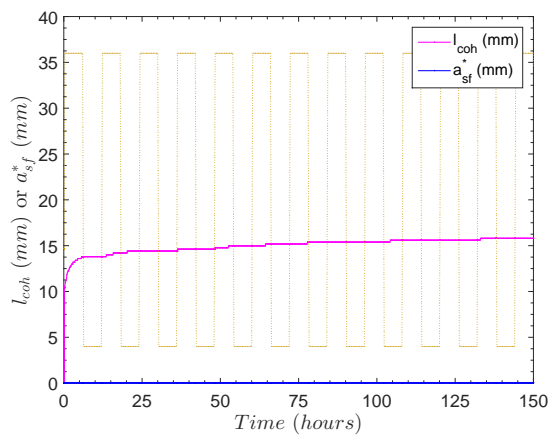(b) scenario D
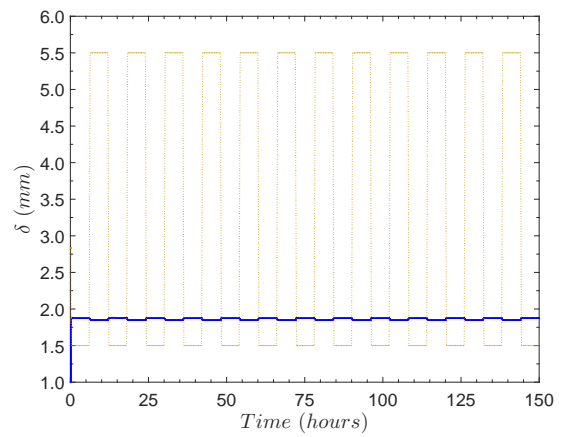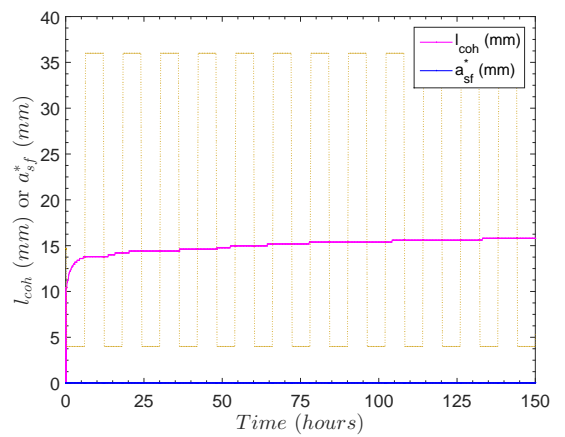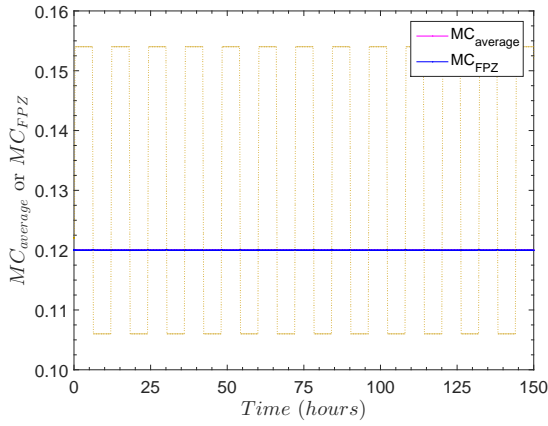
(c) scenario H
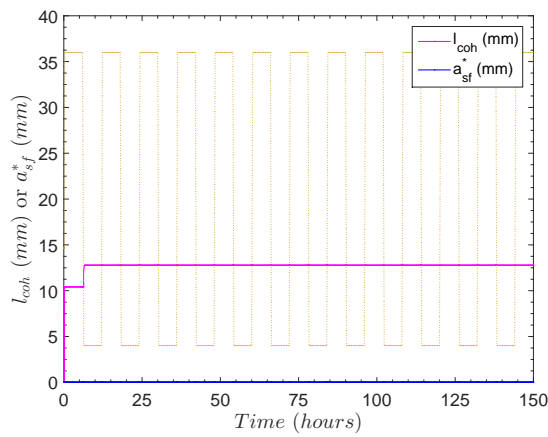
(d) scenario D
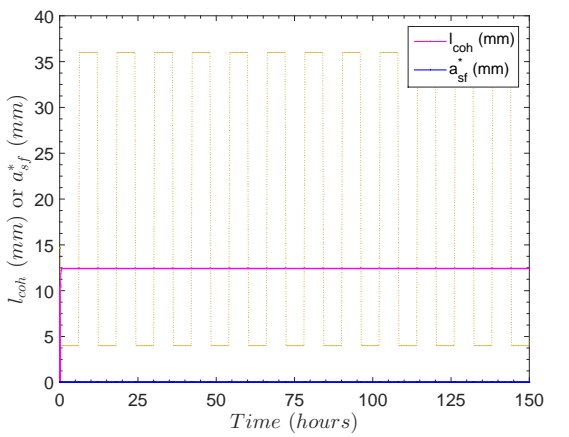
(e) scenario H

(f) scenario D

A.3 Case 3 (V0T1HL1S0mCZ0): elastic mechano-sorptive behavior of wood
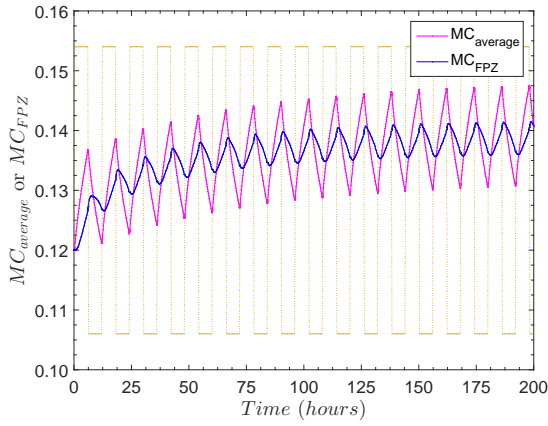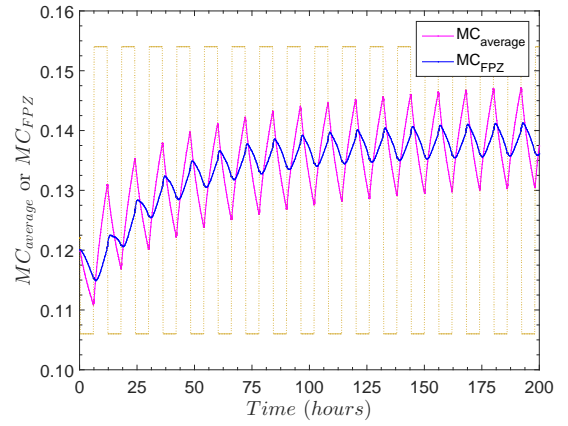
(a) scenario H
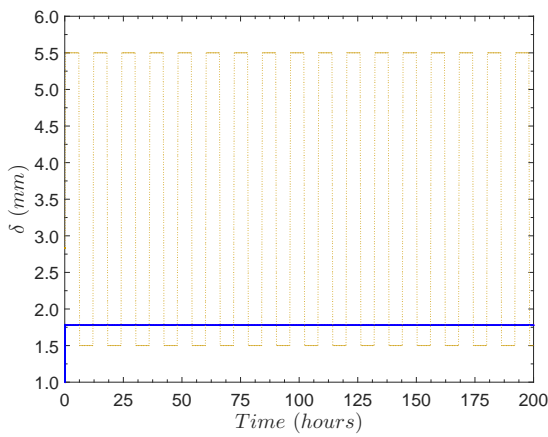
(b) scenario D
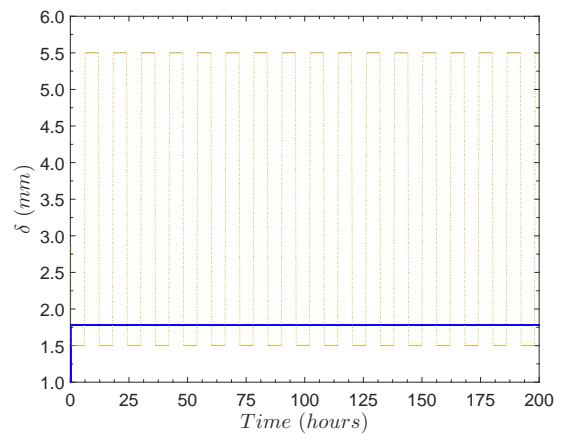
(c) scenario H
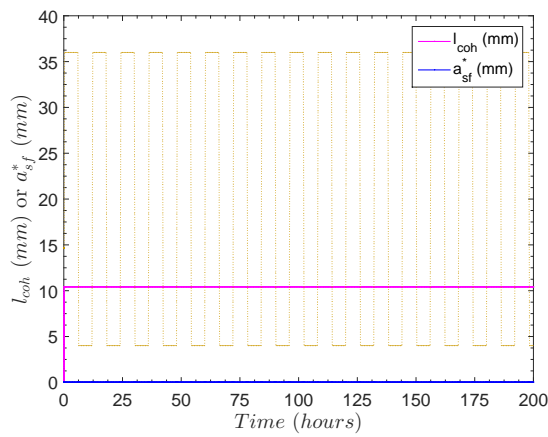
(d) scenario D
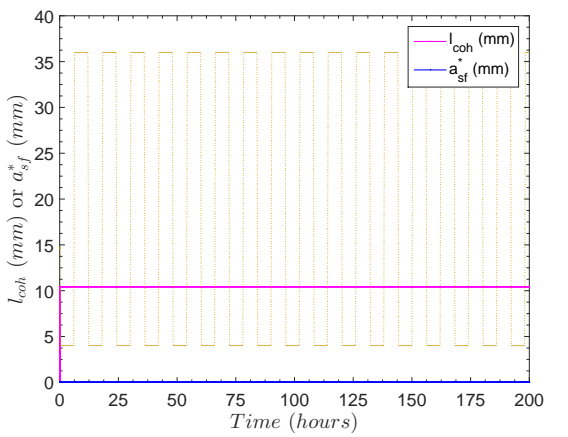
(e) scenario H

(f) scenario D

A.4 Case 4 (V0T1HL1S0mCZ1): elastic mechano-sorptive behavior of wood with the moisture effect on FPZ
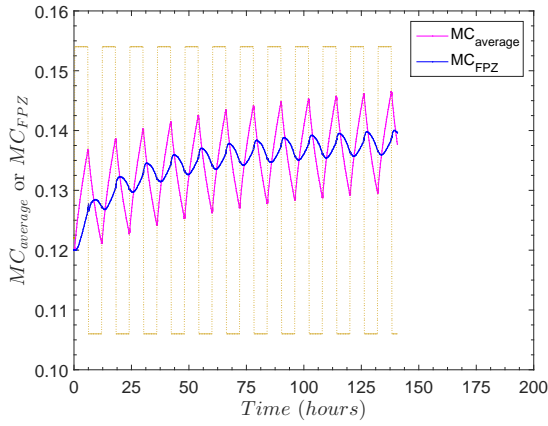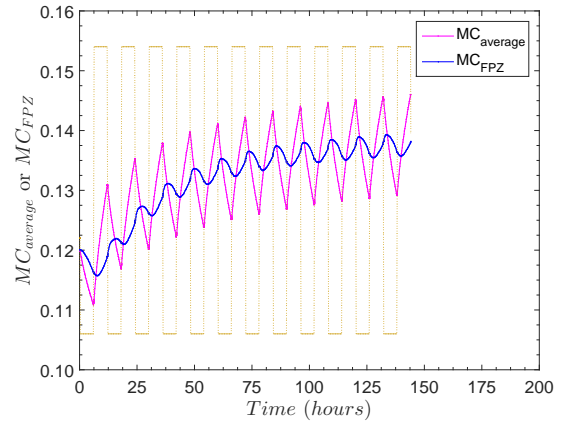
(a) scenario H
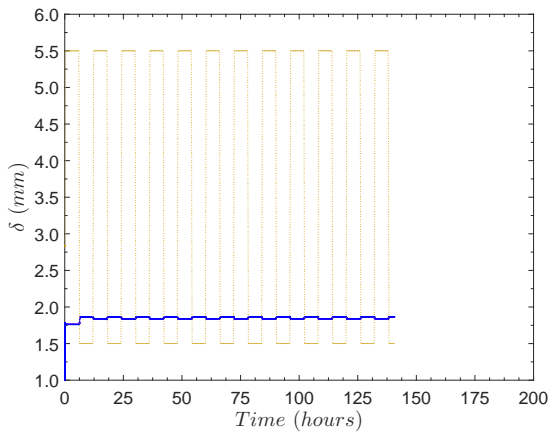
(b) scenario D
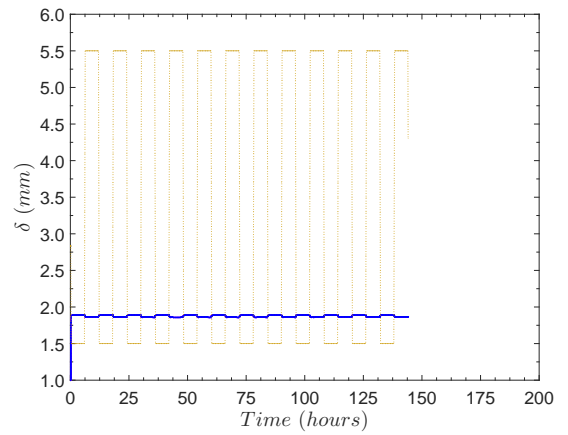
(c) scenario H
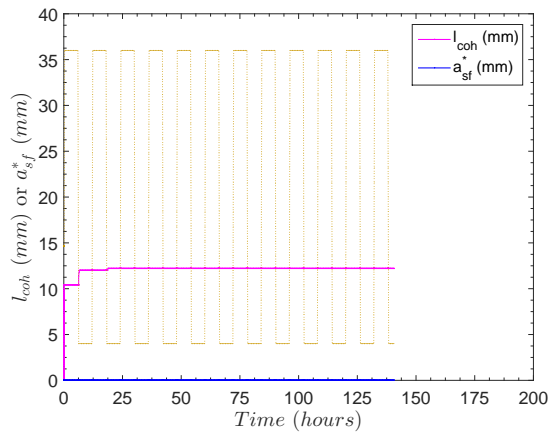
(d) scenario D
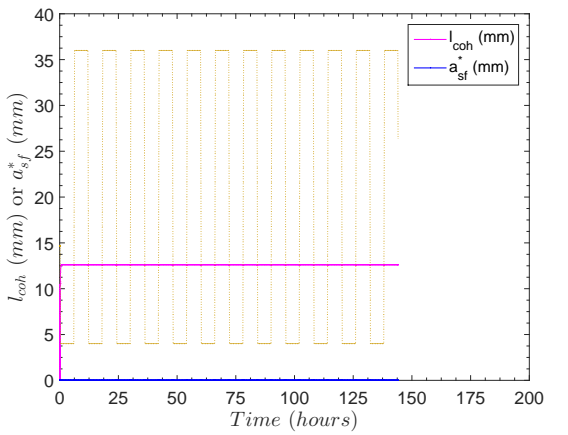
(e) scenario H

(f) scenario D

A.5   Case 5 (V0T1HL1S1mCZ0): elastic mechano-sorptive behavior of wood associated to the shrinkage-swelling effect
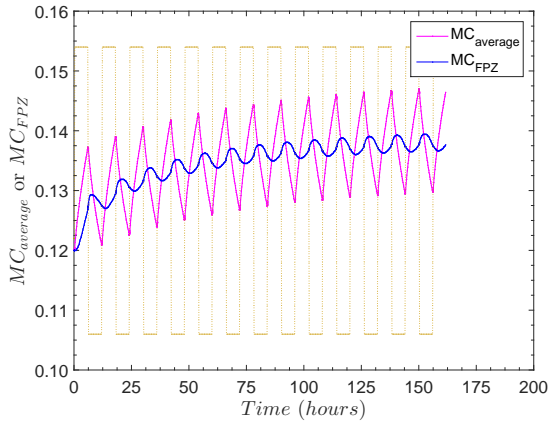
(a) scenario H
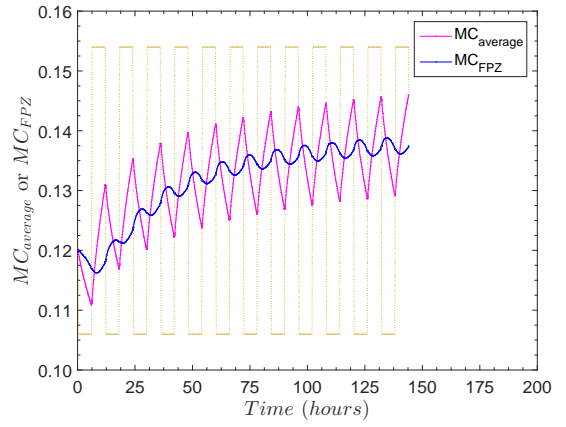
(b) scenario D
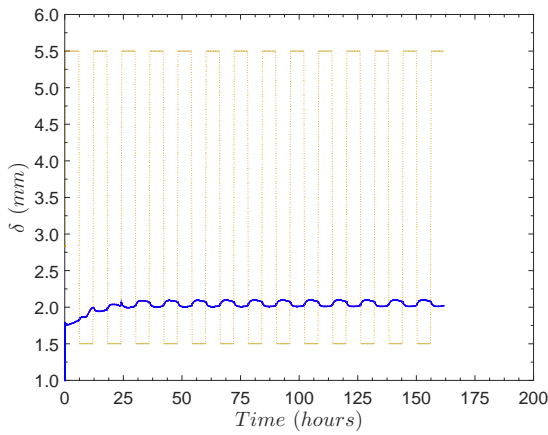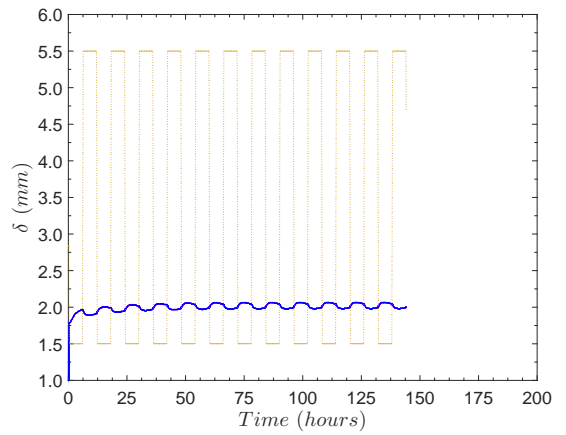
(c) scenario H
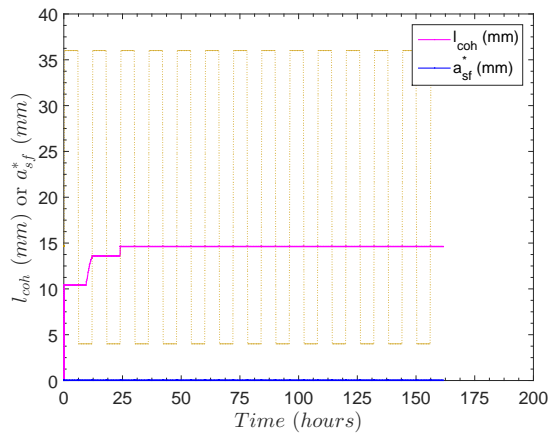
(d) scenario D
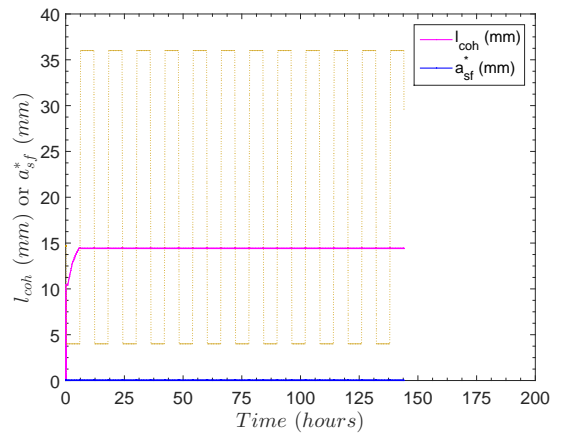
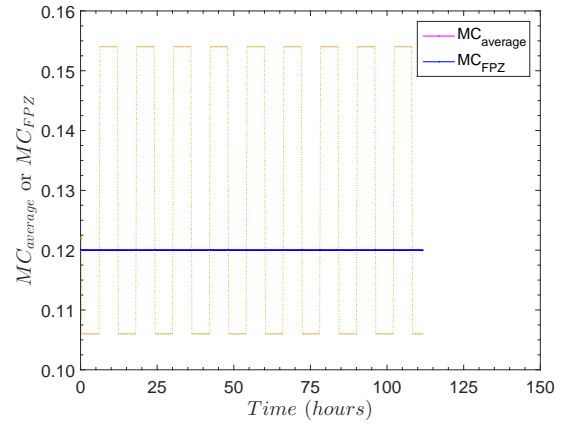(e) scenario H

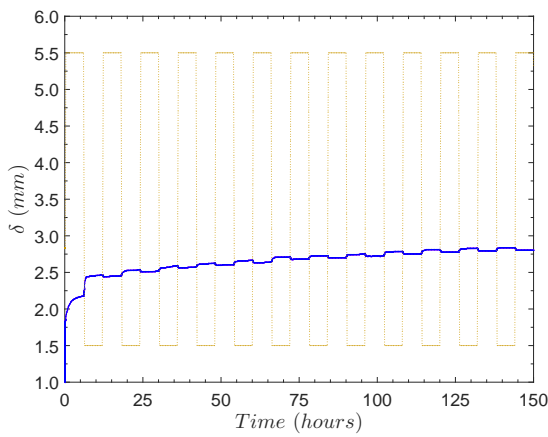(f) scenario D

A.6 Case 6 (V0T1HL1S1mCZ1): elastic mechano-sorptive behavior of wood associated to the shrinkage-swelling effect with the moisture effect on FPZ
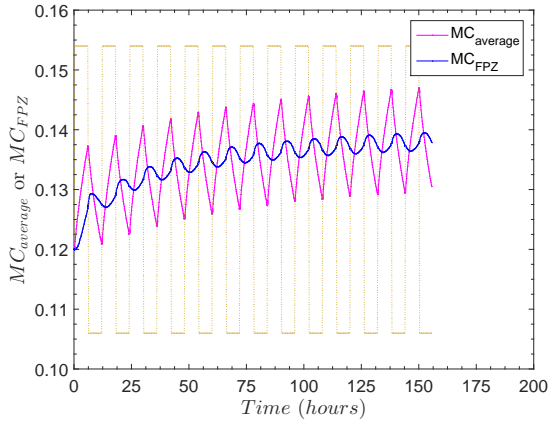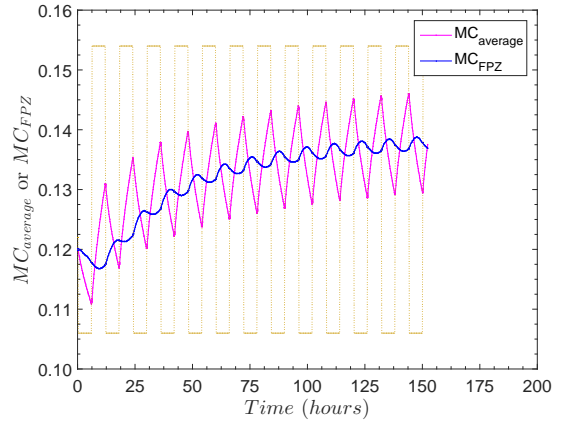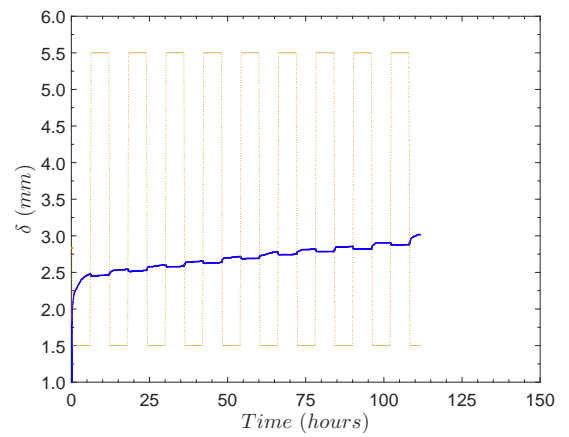

(a) scenario H

(b) scenario D

(c) scenario H

(d) scenario D

(e) scenario H

(f) scenario D

A.7 Case 7 (V1T0HL0S0mCZ0): viscoelastic property of wood

(a) scenario H

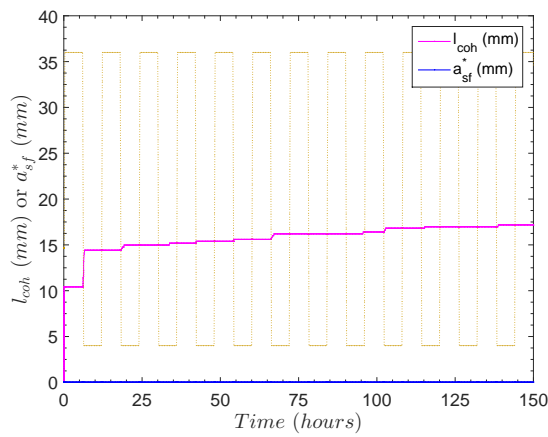(b) scenario D

(c) scenario H

(d) scenario D

(e) scenario H

(f) scenario D

A.8 Case 8 (V1T0HL0S0mCZ1): viscoelastic property of wood with the moisture effect on FPZ
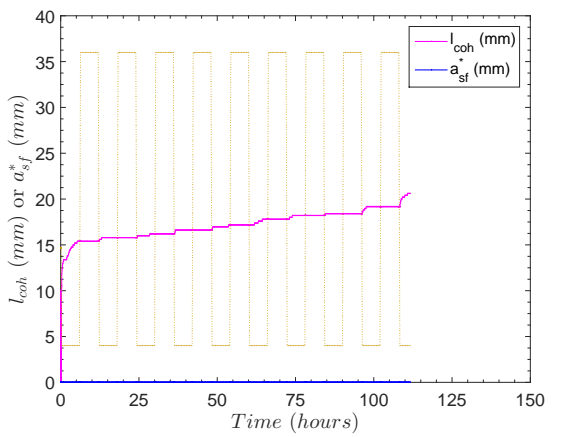

(a) scenario H

(b) scenario D

(c) scenario H

(d) scenario D

(e) scenario H

(f) scenario D

A.9 Case 9 (V1T1HL1S0mCZ0): viscoelastic mechano-sorptive behavior of wood

(a) scenario H

(b) scenario D

(c) scenario H

(d) scenario D

(e) scenario H

(f) scenario D

A.10 Case 10 (V1T1HL1S0mCZ1): viscoelastic mechano-sorptive behavior of wood with the moisture effect on FPZ

(a) scenario H
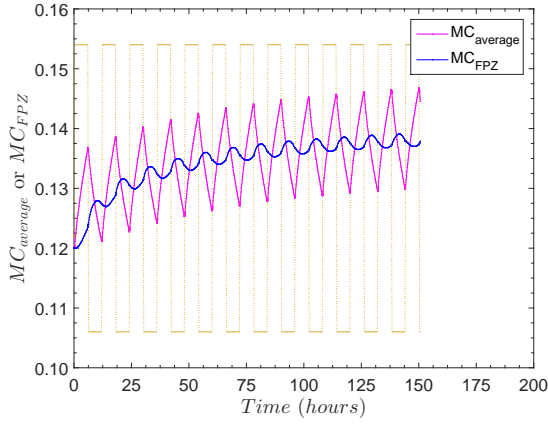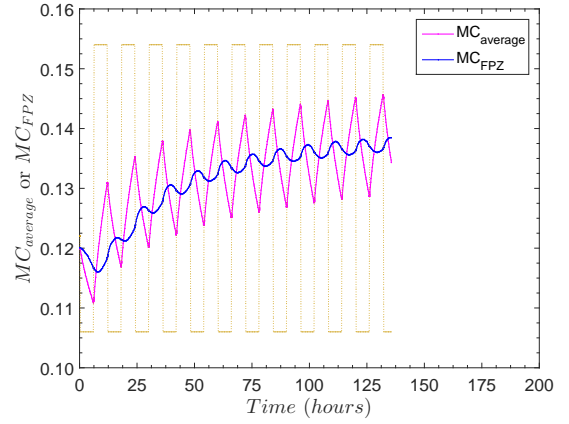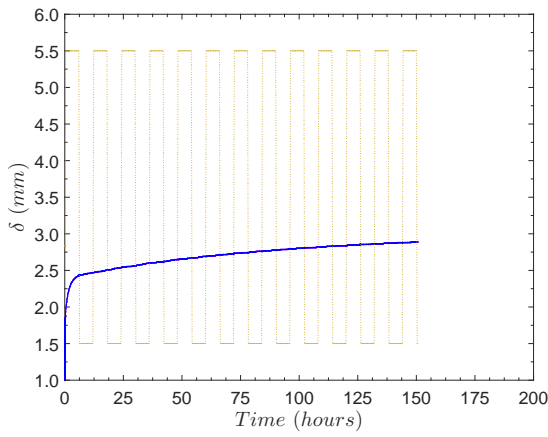
(b) scenario D

(c) scenario H

(d) scenario D

(e) scenario H

(f) scenario D

(a) scenario H

(b) scenario D

(c) scenario H

(d) scenario D

(e) scenario H

(f) scenario D

A.12 Case 12 (V1T1HL1S1mCZ1): viscoelastic mechano-sorptive behavior of wood associated to the shrinkage-swelling effect with the moisture effect on FPZ
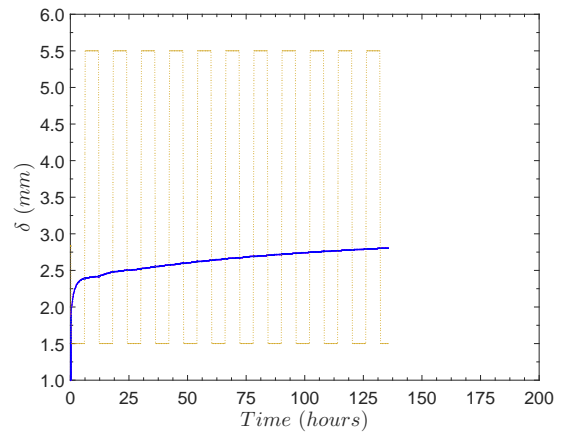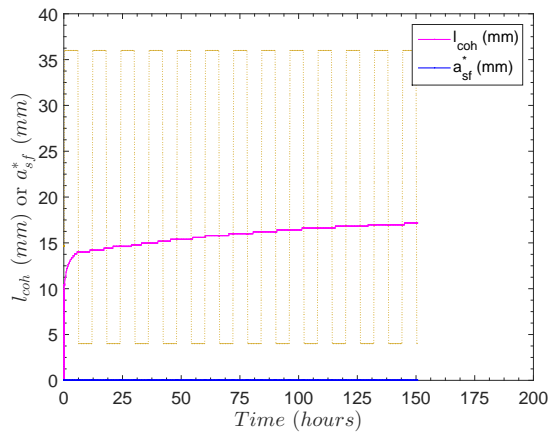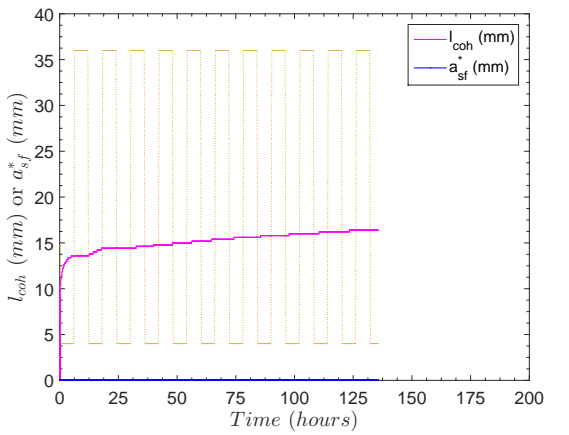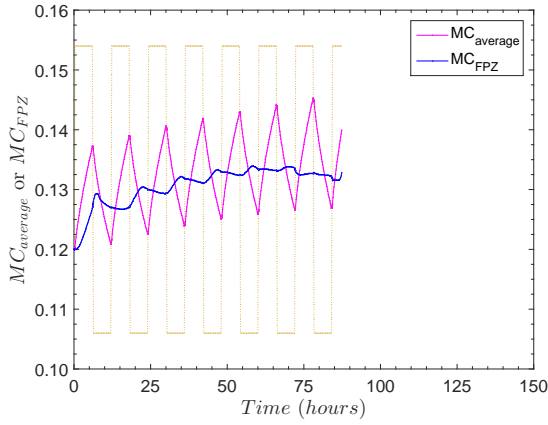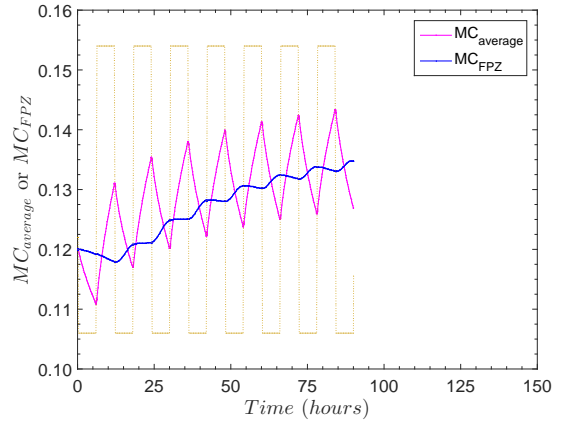

(a) scenario H
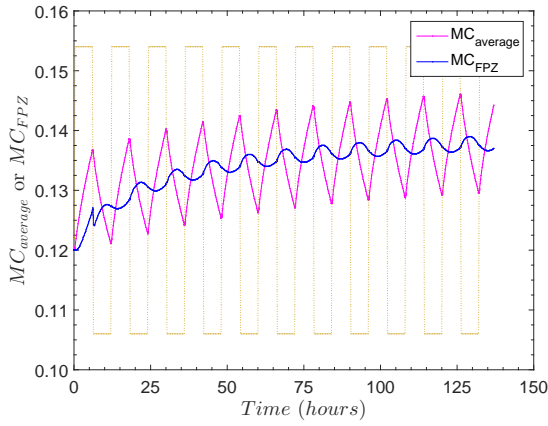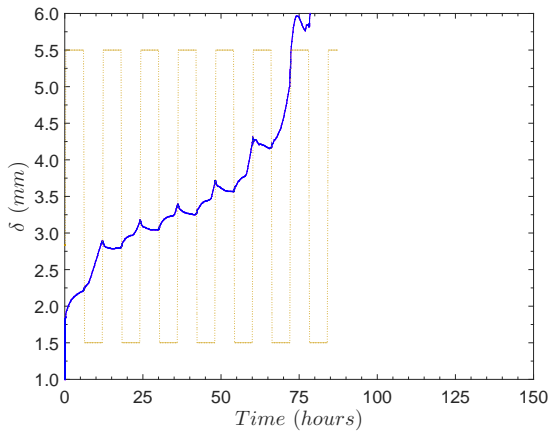

(b) scenario D
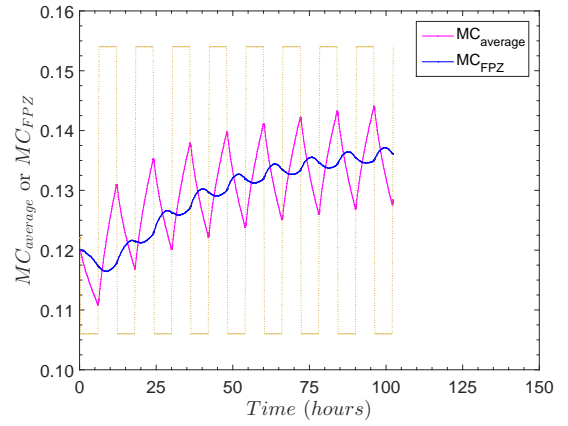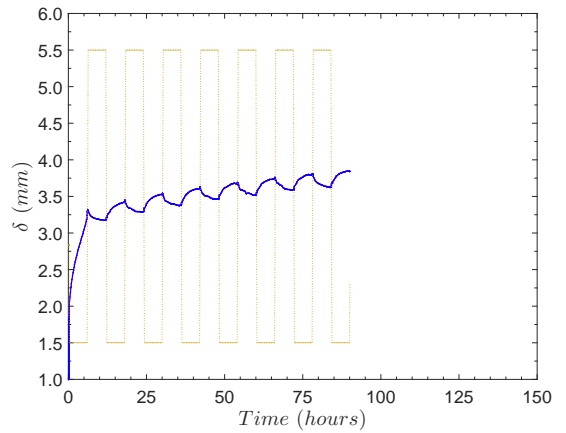

(c) scenario H
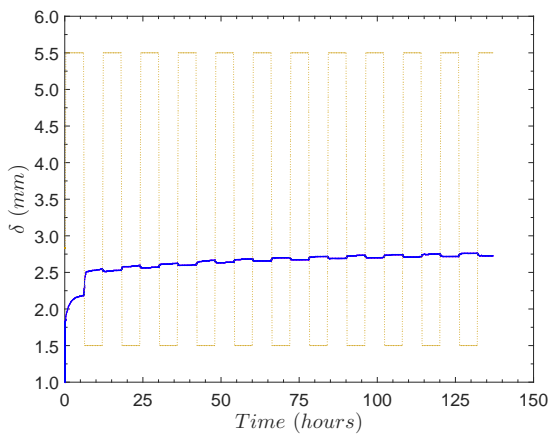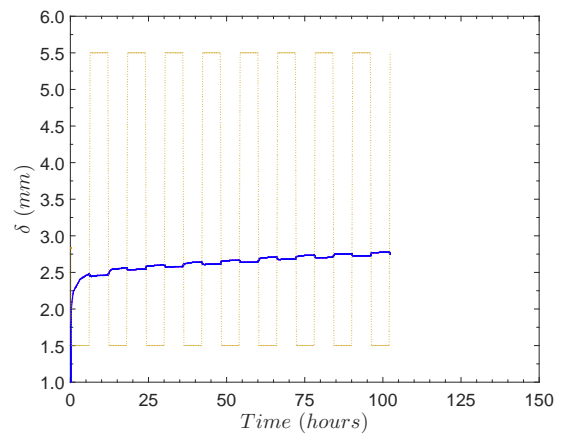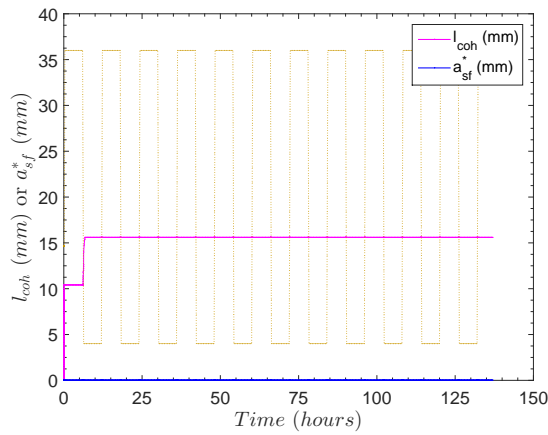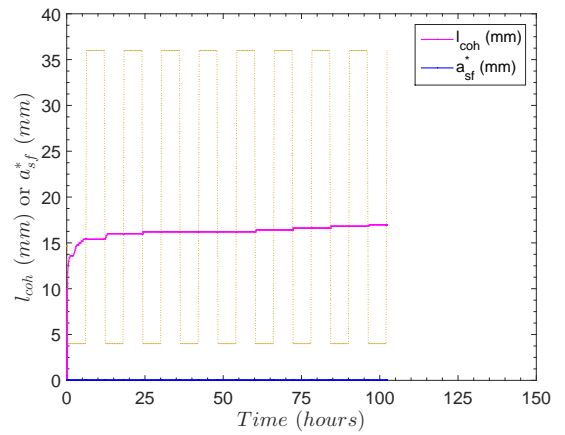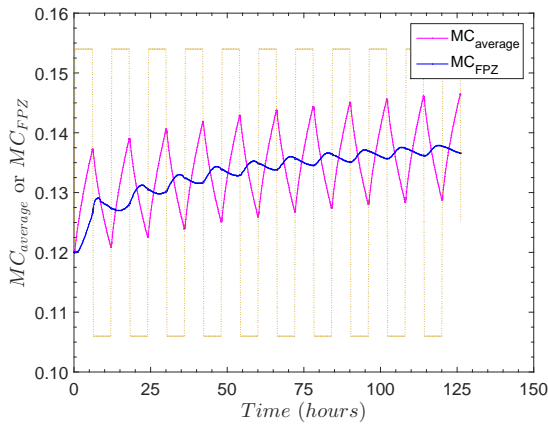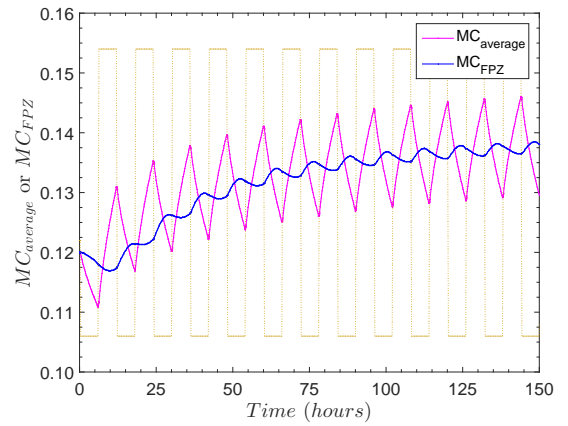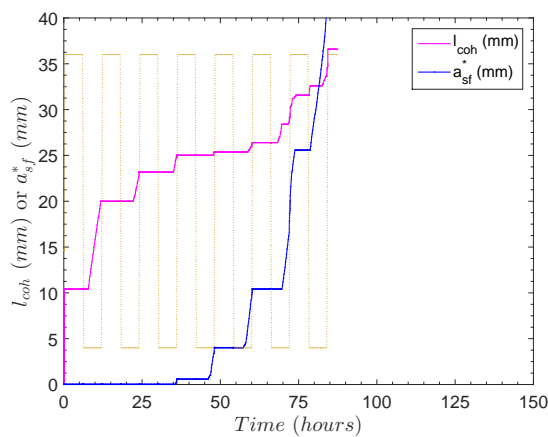

(d) scenario D
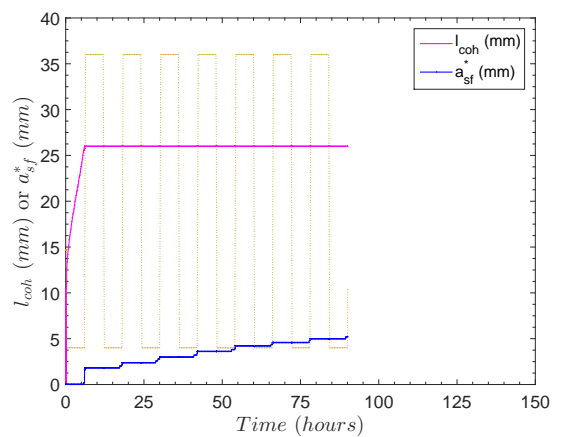
(e) scenario H

(f) scenario D

Bibliography

[1] AGOUA, E., ZOHOUN, S., AND PERRÉ, P. A double climatic chamber used to measure the diffustion coefficient of water in wood unsteady-state conditions: determination of the best fitting method by numerical simulation. *Int. J. Heat Mass Transf. 44* (2001), 3731–3744.

[2] ALFANO, M., FURGIUELE, F., LEONARDI, A., MALETTA, C., AND PAULINO, G. H. Mode I fracture of adhesive joints using tailored cohesive zone models. *Int. J. Fract. 157* (2009), 193–204.

[3] ARMSTRONG, L., AND CHRISTENSEN, G. Influence of Moisture Changes on Deformation of Wood Under Stress. *Nature 191*, 4791 (1961), 869–870.

[4] ARMSTRONG, L., AND GROSSMAN, P. The behaviour of particle board and hardboard beams during moisture cycling. *Wood Sci. Technol. 6*, 2 (1972), 128–137.

[5] ARMSTRONG, L., AND KINGSTON, R. Effect on moisture changes on creep in wood. *Nature 187* (1960), 1048–1049.

[6] ARMSTRONG, L., AND KINGSTON, R. The effect of moisture content changes on the deformation of wood under stress. *Austr. J. Appl. Sci* (1962).

[7] ASHBY, M., EASTERLING, K., HARRYSSON, R., AND MAITI, S. The Fracture and Toughness of Woods. *Proc. R. Soc. A Math. Phys. Eng. Sci. 398*, 1815 (1985), 261–280.

[8] BARENBLATT, G. The Mathematical Theory of Equilibrium Cracks in Brittle Fracture. *Adv. Appl. Mech. 7* (1962), 55–129.

[9] BAZANT, Z. P. Constitutive equation of wood at variable humidity and temperature. *Wood Sci. Technol. 19*, 2 (1985), 159–177.

[10] BAZANT, Z. P. Concrete fracture models : testing and practice. *Eng. Fract. Mech. 69* (2002), 165–205.

[11] BAZANT, Z. P. Quasibrittle fracture scaling and size effect. *Mater. Struct. 37*, October (2004), 547–568.

[12] BAZANT, Z. P., AND PLANAS, J. *Fracture and size effect in concrete and other quasibrittle materials.* CRC Press, 1998.

[13] BEER, G. An isoparametric joint/interface element for finite element analysis. *Int. J. Numer. Methods Eng. 21* (1985), 585–600.

[14] BLACKBURN, W. S. Path independent integrals to predict onset of crack instability in an elastic plastic material. *Int. J. Fract. Mech. 8*, 3 (1972), 343–346.

[15] BLUMER, S. *Moisture induced stresses and deformations in parquet floors - An Experimental and Numerical Study.* PhD thesis, Lund university, 2009.

[16] BORG, R., NILSSON, L., AND SIMONSSON, K. Modeling of delamination using a discretized cohesive zone and damage formulation. *Compos. Sci. Technol. 62*, 10-11 (aug 2002), 1299–1314.

[17] BOSTROM, L. The stress-displacement relation of wood perpendicular to the grain. *Wood Sci. Technol. 28* (1994), 319–327.

[18] BOYANCE, P. *Modelisation de la rupture differee d'un materiau orthotrope viscoelastique en environnement naturel application a un composite a base de bois: le LVL.* PhD thesis, University of Bordeaux I, 1999.

[19] BRADLEY, W., CANTWELL, W., AND KAUSCH, H. Viscoelastic Creep Crack Growth : A Review of Fracture Mechanical Analyses. *Mech. Time-Dependent Mater. 1* (1998), 241–268.

[20] BRINCKER, R. *Crack Tip Parameters for Growing Cracks in Linear Viscoelastic Materials.* Dept. of Building Technology and Structural Engineering, Aalborg University, 1990.

[21] BURDEKIN, F., AND STONE, D. The crack opening displacement approach to fracture mechanics in yielding. *J. Strain Anal. Eng. Des. 1* (1966), 145–55.

[22] CAMACHO, G., AND ORTIZ, M. Computational modelling of impact damage in brittle materials. *Int. J. Solids Struct. 33*, 2 (1996), 2899–2938.

[23] CARIOU, J.-L. *Caracterisation d'un materiau viscoelatisque anisotrope: le bois.* PhD thesis, Universite de Bordeaux 1, 1987.

[24] CARPINTERI, A. Post-peak and post-bifurcation analysis of cohesive crack propagation. *Eng. Fract. Mech. 32*, 2 (1989), 265–278.

[25] CARPINTERI, A., AND SIH, G. Damage accumulation and crack growth in bilinear materials with softening: Application of strain energy density theory. *Theor. Appl. Fract. Mech. 1*, 2 (jun 1984), 145–159.

[26] CASTEM. http://www-cast3m.cea.fr/.

[27] CHAPLAIN, M., DETHAN, T., AND CASTERA, P. Effects of climatic conditions changes on crack growth. In *World Conf. Timber Eng.* (2006).

[28] CHAPLAIN, M., AND VALENTIN, G. Modelisation of delayed failure of wood beams. *ICF XI - 11th Int. Conf. Fract.* (2005).

[29] CHAPLAIN, M., AND VALENTIN, G. Fracture mechanics models applied to delayed failure of LVL beams. *Holz als Roh- und Werkst. 65*, 1 (oct 2006), 7–16.

[30] CHAPLAIN, M., AND VALENTIN, G. Modelling relative humidity effect on load duration of timber beams. In *World Conf. Timber Eng.* (2008).

[31] CHAPLAIN, M., AND VALENTIN, G. Effects of relative humidity conditions on crack propagation in timber: experiments and modelling. In *World Conf. Timber Eng.* (2010), pp. 1–8.

[32] CHASSAGNE, P. *Contribution à la prédiction des conséquences mécaniques des phénomènes thermo- hydriques couplés : Application au bois .* PhD thesis, Institut National des Sciences Appliquées de Lyon, 2006.

[33] CHASSAGNE, P., SAÏD, E. B., JULLIEN, J.-F., AND GALIMARD, P. Three Dimensional Creep Model for Wood Under Variable Humidity-Numerical Analyses at Different Material Scales. *Mech. Time-Dependent Mater. 9*, 4 (apr 2006), 1–21.

[34] CHAZAL, C., AND DUBOIS, F. A New Incremental Formulation in the Time Domain for Crack Initiation in an Orthotropic Linearly Viscoelastic Solid. *Mech. Time-Dependent Mater. 5* (2001), 229–253.

[35] CHOWDHURY, S. R., AND NARASIMHAN, R. A cohesive finite element formulation for modelling fracture and delamination in solids. *Sadhana 25* (2000), 561–587.

[36] CONRAD, M. P., SMITH, G. D., AND FERNLUND, G. Fracture of solid wood : a review of structure and properties at different length scales. *Wood Fiber Sci. 35*, 4 (2003), 570–584.

[37] COUREAU, J.-L., MOREL, S., AND DOURADO, N. Cohesive zone model and quasibrittle failure of wood: A new light on the adapted specimen geometries for fracture tests. *Eng. Fract. Mech. 109* (sep 2013), 328–340.

[38] DE BORST, R., REMMERS, J. J., AND NEEDLEMAN, A. Computational Aspects of Cohesive Zone Models. *Adv. Fract. Mech. Life Saf. Assessments* (2004), 1–18.

[39] DE MOURA, M., MORAIS, J., AND DOURADO, N. A new data reduction scheme for mode I wood fracture characterization using the double cantilever beam test. *Eng. Fract. Mech. 75*, 13 (sep 2008), 3852–3865.

[40] DE MOURA, M., OLIVEIRA, J., DE MORAIS, A. B., AND XAVIER, J. Mixed-mode I/II wood fracture characterization using the mixed-mode bending test. *Eng. Fract. Mech. 77*, 1 (jan 2010), 144–152.

[41] DE MOURA, M., OLIVEIRA, J., MORAIS, J., AND DOURADO, N. Mixed-mode (I+II) fracture characterization of wood bonded joints. *Constr. Build. Mater. 25*, 4 (apr 2011), 1956–1962.

[42] DILLARD, D. A., WANG, J. Z., AND PARVATAREDDY, H. A Simple Constant Strain Energy Release Rate Loading Method for Double Cantilever Beam Specimens. *J. Adhes. 41*, 1-4 (1993), 35–50.

[43] DOURADO, N. *R-Curve behaviour and size effect of a quasibrittle material: Wood*. PhD thesis, Universite de Bordeaux I, 2008.

[44] DOURADO, N., DE MOURA, M., MORAIS, J., AND SILVA, M. Estimate of resistance-curve in wood through the double cantilever beam test. *Holzforschung 64*, 1 (2010), 119–126.

[45] DOURADO, N., MOREL, S., DE MOURA, M., VALENTIN, G., AND MORAIS, J. Comparison of fracture properties of two wood species through cohesive crack simulations. *Compos. Part A Appl. Sci. Manuf. 39*, 2 (feb 2008), 415–427.

[46] DUBOIS, F. *Modelisation du comportement mecanique des milieux viscoelastiques fisssures: Application au materiau bois*. PhD thesis, Universite de Limoges, 1997.

[47] DUBOIS, F., CHAZAL, C., AND PETIT, C. A Finite Element Analysis of Creep-Crack Growth in Viscoelastic Media. *Mech. Time-Dependent Mater. 2* (1999), 269–286.

[48] DUBOIS, F., CHAZAL, C., AND PETIT, C. Viscoelastic crack growth process in wood timbers : An approach by the finite element method for mode I fracture. *Int. J. Fract. 113*, 1 (2002), 367–388.

[49] DUBOIS, F., HUSSON, J.-M., SAUVAT, N., AND MANFOUMBI BOUSSOUGOU, N. Modeling of the viscoelastic mechano-sorptive behavior in wood. *Mech. Time-Dependent Mater. 16*, 4 (may 2012), 439–460.

[50] DUBOIS, F., AND PETIT, C. Modelling of the crack growth initiation in viscoelastic media by the Gθv-integral. *Eng. Fract. Mech. 72*, 18 (dec 2005), 2821–2836.

[51] Dugdale, D. Yielding of steel sheets containing slits. *J. Mech. Phys. Solids 8* (1960), 100–104.

[52] Elices, M., Guinea, G., Gómez, F., and Planas, J. The cohesive zone model: advantages, limitations and challenges. *Eng. Fract. Mech. 69*, 2 (jan 2002), 137–163.

[53] Findley, W. N., Lai, J. S., and Onaran, K. *Creep and Relaxation of Nonlinear Viscoelastic Materials.* North-Holland Publishing Company, 1976.

[54] Fortino, S., Mirianon, F., and Toratti, T. A 3D moisture-stress FEM analysis for time dependent problems in timber structures. *Mech. Time-Dependent Mater. 13*, 4 (nov 2009), 333–356.

[55] Foulk, J., Allen, D. H., and Helms, K. Formulation of a three-dimensional cohesive zone model for application to a finite element algorithm. *Comput. Methods Appl. Mech. Eng. 183* (2000), 51–66.

[56] Fridley, K. J., and Tang, R. Thermal effects on load-duration behaviour of lumber. Part I. Effect of constant temperature. *Wood Fiber Sci. 21*, 4 (1989), 420–431.

[57] Fruhmann, K., Reiterer, A., Tschegg, E. K., and Stanzl-Tschegg, S. E. Fracture characteristics of wood under mode I, mode II and mode III loading. *Philos. Mag. A 82*, 17-18 (2002), 3289–3298.

[58] Genevaux, J., and Guitard, D. Anisotropie du comportement différé: essai de fluage à température croissante dun bois de peuplier. In *Colloq. Sci. Eur. du Group. Sci. rhéologique du bois* (1988).

[59] Ghazlan, G., Caperaa, S., and Petit, C. An incremental formulation for the linear analysis of the thin viscoelastic structures using generalized variables. *Int. J. Numer. Methods Eng. 38* (1995), 3315–3333.

[60] Gibson, E. J. Creep of Wood: Role of Water and Effect of a Changing Moisture Content. *Nature 206*, 4980 (1965), 213–215.

[61] Gibson, L. J., and Michael F. Ashby. *Cellular solids: Structure and properties.* Pergamon Press, New York, NY., 1999.

[62] Graham, G. The correspondence principle of linear viscoelasticity theory for mixed boundary value problems involving time dependent boundary regions. *Q. Appl. Math.* (1968).

[63] GREEN, D. W., WINANDY, J. E., AND KRETSCHMANN, D. E. Wood handbook - Wood as an engineering material. Chapter 4: Mechanical Properties of Wood. In *Wood.* Madison, WI: U.S. Department of Agriculture, Forest Service, Forest Products Laboratory, 1999.

[64] GRIFFITH, A. The Phenomena of Rupture and Flow in Solids. *Phys. Charater 221* (1921), 163–198.

[65] GRIL, J. *Une modélisation du comportement hygro-rhéologique du bois à partir de sa microstructure.* PhD thesis, Université de Paris 6, France, 1988.

[66] GROSSMAN, P. Requirements for a model that exhibits mechano-sorptive behaviour. *Wood Sci. Technol. 10*, 3 (1976), 163–168.

[67] GUINEA, G. Modelling the fracture of concrete: the cohesive crack. *Mater. Struct. 28* (1995), 187–194.

[68] GUITARD, D. *Mecanique materiau bois et composites.* CEPAD, 1987.

[69] GUO, X., AND LI, H. Determination of quasibrittle fracture law for cohesive crack models. *Cem. Concr. Res. 29*, June 1998 (1999), 1055–1059.

[70] HANHIJARVI, A. Advances in the knowledge of the influence of moisture changes on the long-term mechanical performance of timber structures. *Mater. Struct. 33*, February (2000), 43–49.

[71] HANHIJARVI, A., AND MACKENZIE-HELNWEIN, P. Computational Analysis of Quality Reduction during Drying of Lumber due to Irrecoverable Deformation. I: Orthotropic Viscoelastic-Mechanosorptive-Plastic Material Model for the Transverse Plane of Wood. *ASCE 129*, September (2003), 996–1005.

[72] HANHIJARVI, A., MACKENZIE-HELNWEIN, P., AND RANTA-MAUNUS, A. Two-Dimensional Material Model for Structural Analysis of Drying Wood As Viscoelastic-Mechanosorptive-Plastic Material. In *COST Action E 15* (2001), pp. 1–10.

[73] HEARMON, R., AND PATON, J. Moisture content changes and creep in wood. *For. Prod. J. 14* (1964), 357–359.

[74] HERRITSCH, A. *Investigations on wood stability and related properties of radiata pine.* PhD thesis, University of Canterbury, 2007.

[75] HILLERBORG, A., MODÉER, M., AND PETERSSON, P.-E. Analysis of crack formation and crack growth in concrete by means of fracture mechanics and finite elements. *Cem. Concr. Compos. 6* (1976), 773–782.

[76] HOFFMEYER, P., AND DAVIDSON, R. Mechano-sorptive creep mechanism of wood in compression and bending. *Wood Sci. Technol. 23* (1989), 215–227.

[77] HUNT, D. G. The mechano-sorptive creep susceptibility of two softwoods and its relation to some other materials properties. *J. Mater. Sci. 21*, 6 (1986), 2088–2096.

[78] HUNT, D. G. Linearity and non-linearity in mechano-sorptive creep of softwood in compression and bending. *Wood Sci. Technol. 23*, 4 (1989), 323–333.

[79] HUNT, D. G., AND SHELTON, C. F. Longitudinal moisture-shrinkage coefficients of softwood at the mechano-sorptive creep limit. *Wood Sci. Technol. 22*, 3 (1988), 199–210.

[80] HUSSON, J.-M. *Loi de comportement viscoelastique avec effet memoire application a la mecanosorption dans le bois.* PhD thesis, Université de Limoges, 2009.

[81] HUSSON, J.-M., DUBOIS, F., AND SAUVAT, N. Elastic response in wood under moisture content variations: analytic development. *Mech. Time-Dependent Mater. 14*, 2 (nov 2010), 203–217.

[82] HUSSON, J.-M., DUBOIS, F., AND SAUVAT, N. A finite element model for shape memory behavior. *Mech. Time-Dependent Mater. 15*, 3 (mar 2011), 213–237.

[83] INGLIS, C. Stresses in a plate due to the presnce of cracks and sharp corners. *Trans. Inst. Nav. Archit. 55* (1913), 219–241.

[84] IRWIN, G. Analysis of Stresses and Strains Near the End of a Crack Traversing a Plate. *J. Appl. Mech. 24* (1957), 361–364.

[85] JOURDAIN, C. *Effet de durée de charge sur poutres entaillées, Influence de lenvironnement climatique, Application à un composite à base de bois : le LVL.* PhD thesis, University of Bordeaux I, 1996.

[86] KELLEY, S. S., RIALS, T. G., AND GLASSER, W. G. Relaxation behaviour of the amorphous behaviour the amorphous components of wood. *J. Mater. Sci. 22* (1987), 617–624.

[87] KING, M., SUTHERLAND, I., AND LE, N. L. Fracture toughness of wet and dry Pinus radiata. *Holz als Roh- und Werkst. 57*, 4 (aug 1999), 235–240.

[88] KISHIMOTO, K., AOKI, S., AND SAKATA, M. On the path independent integral-J. *Eng. Fract. Mech. 13*, 3 (1980), 841–850.

[89] KNAUSS, W. Delayed Failure Materials - The Griffith Problem for Linearly Viscoelastic. *Int. J. Fract. Mech. 6*, 1 (1970), 7–20.

[90] KNAUSS, W., AND DIETMANN, H. Crack propagation under variable load histories in linearly viscoelastic solids. *Int. J. Eng. Sci. 8* (1970), 643–656.

[91] KNAUSS, W., AND MUELLER, H. Crack propagation in a linearly viscoelastic strip. *J. Appl. Mech. 38* (1971), 483–488.

[92] KOLLMANN, F., AND COTE, W. A. *Principles of wood science and technology I - Solid wood.* Springer Berlin Heidelberg, 1968.

[93] KRETSCHMANN, D. E., AND GREEN, D. W. Modeling moisture content-mechanical property relationships for clear southern pine. *Wood Fiber Sci.* (1995), 320–337.

[94] KRETSCHMANN, D. E., AND GREEN, D. W. Moisture Content Specific Gravity Relationships for Clear Southern Pine. In *World Conf. Timber Eng.* (1996), vol. 2, pp. 1–8.

[95] KUMAR, S., AND BARAI, S. V. *Concrete Fracture Models and Applications.* Springer-Verlag Berlin Heidelberg, 2011.

[96] LARTIGAU, J., COUREAU, J.-L., MOREL, S., GALIMARD, P., AND MAURIN, E. Mixed mode fracture of glued-in rods in timber structures. *Int. J. Fract. 192*, 1 (2015), 71–86.

[97] LASSERRE, B. *Modelisation thermo-hygro-mecanique du comportement differe de poutres de structure en bois.* PhD thesis, Université de Bordeaux 1, 2000.

[98] LEICESTER, R. A rheological model for Mechano-sorptive deflections of beams. *Wood Sci. Technol. 5* (1971), 211–220.

[99] LEICESTER, R. Fracture strength of wood. In *First Aust. Conf. Eng. Mater.* (1974), pp. 729–742.

[100] LESPINE, C. *Influence de la géométrie des structures sur les propriétés de rupture dans les matériaux quasi-fragiles.* PhD thesis, Université de Bordeaux 1, 2007.

[101] LIU, J., SIMPSON, W. T., AND VERRILL, S. An Inverse Moisture Diffusion Algorithm for the Determination of Diffusion Coefficient. *Dry. Technol. 19*, 8 (aug 2001), 1555–1568.

[102] LIU, J. Y., AND SIMPSON, W. T. Inverse determination of diffusion coefficient for moisture diffusion in wood. In *33RD ASME Natl. Heat Transf. Conf. Heat Mass Transf. Porous Media* (1999).

[103] MACKENZIE-HELNWEIN, P., HANHIJARVI, A., AND EBERHARDSTEINER, J. Long-term behavior of wood under multiaxial states of stress and simulation of structural details. In *World Conf. Timber Eng.* (2000).

[104] MARTENSSON, A. Tensile behaviour of hardboard under combined mechanical and moisture loading. *Wood Sci. Technol. 22*, 2 (1988), 129–142.

[105] MARTENSSON, A. Mechano-sorptive effects in wooden material. *Wood Sci. Technol. 28*, 6 (1994), 437–449.

[106] MEITH, W. A., AND HILL, M. R. Domain-independent values of the J-integral for cracks in three-dimensional residual stress bearing bodies. *Eng. Fract. Mech. 69*, 12 (2002), 1301–1314.

[107] MERAKEB, S. *Modelisation des structures en bois en environnement variable.* PhD thesis, Universite de Limoges, 2006.

[108] MERAKEB, S., DUBOIS, F., AND PETIT, C. Modeling of the sorption hysteresis for wood. *Wood Sci. Technol. 43*, 7-8 (apr 2009), 575–589.

[109] MERAKEB, S., DUBOIS, F., AND PETIT, C. Modélisation des hystérésis de sorption dans les matériaux hygroscopiques. *Comptes Rendus Mécanique 337*, 1 (jan 2009), 34–39.

[110] MOHAGER, S., AND TORATTI, T. Long term bending creep of wood in cyclic relative humidity. *Wood Sci. Technol. 27*, 1 (1992), 49–59.

[111] MOREL, S. R-curve and size effect in quasibrittle fractures: Case of notched structures. *Int. J. Solids Struct. 44*, 13 (jun 2007), 4272–4290.

[112] MOREL, S., BOUCHAUD, E., SCHMITTBUHL, J., AND VALENTIN, G. R-curve behavior and roughness development of fracture surfaces. *Int. J. Fract. 114* (2002), 307–325.

[113] MOREL, S., COUREAU, J.-L., PLANAS, J., AND DOURADO, N. Bilinear softening parameters and equivalent LEFM R-curve in quasibrittle failure. *Int. J. Solids Struct. 47*, 6 (mar 2010), 837–850.

[114] MOREL, S., AND DOURADO, N. Size effect in quasibrittle failure: Analytical model and numerical simulations using cohesive zone model. *Int. J. Solids Struct. 48*, 10 (may 2011), 1403–1412.

[115] MOREL, S., DOURADO, N., VALENTIN, G., AND MORAIS, J. Wood: a quasibrittle material R-curve behavior and peak load evaluation. *Int. J. Fract. 131*, 4 (feb 2005), 385–400.

[116] MOREL, S., MOUROT, G., AND SCHMITTBUHL, J. Influence of the specimen geometry on R-curve behavior and roughening of fracture surfaces. *Int. J. Fract. 121* (2003), 23–42.

[117] MORLIER, P. Creep in timber structures, 1994.

[118] MOUTOU PITTI, R., DUBOIS, F., AND PETIT, C. Generalization of T and A integrals to time-dependent materials: analytical formulations. *Int. J. Fract. 161*, 2 (feb 2010), 187–198.

[119] MUKUDAI, J., AND YATA, S. Further modeling and simulation of viscoelastic behavior (bending deflection) of wood under moisture change. *Wood Sci. Technol. 21* (1987), 49–63.

[120] NAKADA, O. Theory of non-linear responses, 1960.

[121] NAVI, P., AND SANDBERG, D. *Thermo-Hydro-Mechanical Wood Processing.* CRC Press, 2012.

[122] NGUYEN, S.-L., SAIFOUNI, O., DESTREBECQ, J.-F., AND MOUTOU PITTI, R. An incremental model for wood behaviour including hydro-lock effect. *COST-FP0904* (2014), 2–3.

[123] NIELSEN, L. F. Wood as a cracked viscoelastic material. Part 1. Theory and applications.pdf. In *Int. Work. Durat. load Lumber wood Prod.* (1985), pp. 1–13.

[124] PERRÉ, P., AND DEGIOVANNI, A. Simulation par volumes finis des transferts couplés en milieux poreux anisotropes: séchage du bois à basse et à haute température. *Int. J. Heat Mass Transf. 33*, 11 (1990), 2463–2478.

[125] PETERSSON, P.-E. Crack growth and develop ment of fracture zones in plain concrete and similar materials. Tech. rep., Lund Institute of Technology, 1981.

[126] PETTERSON, R. W., AND BODIG, J. Prediction of fracture toughness of conifers. *Wood Fiber Sci. 15* (1982), 302–316.

[127] PHAN, N. A. Integration of rapid variation of moisture content in a cohesive zone model: simulation of crack propagation in wood under the humidity variation. In *Club Util. Cast3M* (2014).

[128] PHAN, N. A., CHAPLAIN, M., AND MOREL, S. Wood moisture content influence on R-curve and on parameters of cohesive zone model. In *20th Eur. Conf. Fract.* (2014), vol. 00, pp. 1–6.

[129] PHAN, N. A., MOREL, S., AND CHAPLAIN, M. On the development of a cohesive model for crack propagation in wood under relative humidity variations. In *Int. Conf. Comput. Model. Fract. Fail. Mater. Struct.* (2015).

[130] Phan, N. A., Morel, S., and Chaplain, M. Mixed-mode fracture in a quasi-brittle material : R-curve and fracture criterion Application to wood. *Eng. Fract. Mech.* (2016).

[131] Pittet, V. *Etude expérimentale des couplages mécanosorptifs dans le bois soumis à des variations hygrométriques controlees sous chargements de longue duree.* PhD thesis, Ecole Polytechnique Fédérale de Lausanne, 1996.

[132] Planas, J., Elices, M., Guinea, G., Gómez, F., Cendón, D. A., and Arbilla, I. Generalizations and specializations of cohesive crack models. *Eng. Fract. Mech. 70*, 14 (sep 2003), 1759–1776.

[133] Prokopski, G. Influence of moisture content on fracture toughness of wood. *Int. J. Fract. 79* (1996), 73–77.

[134] Rahulkumar, P., Jagota, a., Bennison, S., and Saigal, S. Cohesive element modeling of viscoelastic fracture: application to peel testing of polymers. *Int. J. Solids Struct. 37*, 13 (mar 2000), 1873–1897.

[135] Randriambololona, H. *Modelisation du comportement differe du bois en envi-ronement variable.* PhD thesis, Université de Limoges, 2003.

[136] Ranta-Maunus, A. The Viscoelasticity of Wood at Varying Moisture Content. *Wood Sci. Technol. 9* (1975), 189–205.

[137] Reiterer, A. The influence of temperature on the mode I fracture behavior of wood. *J. Mater. Sci.* (2001), 1905–1907.

[138] Reiterer, A., and Stanzl-Tschegg, S. E. The influence of moisture content on the mode I fracture behaviour of sprucewood. *J. Mater. Sci. 37* (2002), 4487–4491.

[139] Reiterer, A., Stanzl-Tschegg, S. E., and Tschegg, E. K. Mode I fracture and acoustic emission of softwood and hardwood. *Wood Sci. Technol. 34*, 6509 (2000), 417–530.

[140] Riahi, H., Moutou Pitti, R., Dubois, F., and Fournely, E. On Numerical Evaluation of Mixed Mode Crack Propagation Coupling Mechanical and Thermal Loads in Wood Material. In *Conf. Proc. Soc. Exp. Mech. Ser.* (2014).

[141] Riahi, H., Moutou Pitti, R., Dubois, F., Fournely, E., and Chateauneuf, A. Numerical fracture analysis coupling thermo-hygro mechanical and viscoelastic behaviour. In *9th Int. Conf. Mech. Time Depend. Mater.* (2014), pp. 1–4.

[142] Rice, J. R. A Path Independent Integral and the Approximate Analysis of Strain Concentration by Notches and Cracks. *J. Appl. Mech. 35* (1968), 379–386.

[143] ROESLER, J. R., PAULINO, G. H., PARK, K., AND GAEDICKE, C. Concrete fracture prediction using bilinear softening. *Cem. Concr. Compos. 29*, 4 (apr 2007), 300–312.

[144] SALIN, J. G. Numerical prediction of checking during timber drying and a new mechano-sorptive creep model. *Holz als Roh- und Werkst. 50*, 5 (1992), 195–200.

[145] SANCHO, J. M., PLANAS, J., AND CENDÓN, D. A. An embedded cohesive crack model for finite element analysis of concrete fracture. *Eng. Fract. Mech. 74* (2007), 75–86.

[146] SCHAPERY, R. A. A theory of crack initiation and growth in viscoelastic media I. Theorical development. *Int. J. Fract. 11*, 1 (1975), 141–159.

[147] SCHAPERY, R. A. A theory of crack initiation and growth in viscoelastic media II. Approximate methods of analysis. *Int. J. Fract. 11*, 3 (1975), 369–388.

[148] SCHAPERY, R. A. Correspondence principles and a generalized J integral for large deformation and fracture analysis of viscoelastic media. *Int. J. Fract. 25*, 3 (1984), 195–223.

[149] SCHNIEWIND, A. P. Creep-rupture life of Douglas-fir under cyclic environmental conditions. *Wood Sci. Technol. 1*, 4 (1967), 278–288.

[150] SCHNIEWIND, A. P., AND CENTENO, J. C. Fracture toughness and duration of load factor I. Six principal systems of crack propagation and the duration factor for cracks propagating parallel to grain. *Wood Fiber Sci. 5* (1973).

[151] SIAU, J. F. *Transport Processes in Wood.* Springer Berlin Heidelberg, 1984.

[152] SIH, G., PARIS, P., AND IRWIN, G. On cracks in rectilinearly anisotropic bodies. *Int. J. Fract. Mech. 1*, 3 (sep 1965).

[153] SIMPSON, W. T., AND LIU, J. Y. Dependence of the water vapor diffusion coefficient of aspen (Populus spec.) on moisture content. *Wood Sci. Technol. 26*, 1 (1991), 9–21.

[154] SINGH, R., AND RAMAKRISHNAN, C. Fracture behavior of creeping materials under biaxial loading by finite element method. *Eng. Fract. Mech. 51*, 4 (1995), 637–648.

[155] SODERSTROM, O., AND SALIN, J. G. On Determination of Surface Emission Factors in Wood Drying. *Holzforschung 47*, 5 (1993), 391–397.

[156] SONG, S. H., PAULINO, G. H., AND BUTTLAR, W. G. A bilinear cohesive zone model tailored for fracture of asphalt concrete considering viscoelastic bulk material. *Eng. Fract. Mech. 73*, 18 (2006), 2829–2848.

[157] STAMM, A. *Wood and cellulose science.* The Ronald Press Company, 1964.

[158] STANZL-TSCHEGG, S. E. Microstructure and fracture mechanical response of wood. *Int. J. Fract. 139*, 3-4 (jun 2006), 495–508.

[159] STANZL-TSCHEGG, S. E., AND NAVI, P. Fracture behaviour of wood and its composites. A review. *Holzforschung 63*, 2 (2009), 150–156.

[160] STANZL-TSCHEGG, S. E., AND NAVI, P. Micromechanics of creep and relaxation of wood. A review. *Holzforschung 63*, mode I (2009), 139–149.

[161] STANZL-TSCHEGG, S. E., TAN, D.-M., AND TSCHEGG, E. K. New splitting method for wood fracture characterization. *Wood Sci. Technol. 29*, 1 (jan 1995), 31–50.

[162] SUO, Z., BAO, G., AND FAN, B. Delamination R-curve phenomena due to damage. *J. Mech. Phys. Solids 40*, I (1992), 1–16.

[163] TAN, D.-M., STANZL-TSCHEGG, S. E., AND TSCHEGG, E. K. Models of wood fracture in Mode I and Mode II. *Holz als Roh- und Werkst. 53* (1995), 159–164.

[164] TORATTI, T. Mechano-sorptive creep rupture. *Raken. Mek.* (1992), 3–11.

[165] TVERGAARD, V., AND HUTCHINSON, J. W. The relation between crack growth resistance and fracture process parameters in elastic-plastic solids. *J. Mech. Phys. Solids 40*, 6 (aug 1992), 1377–1397.

[166] TVERGAARD, V., AND HUTCHINSON, J. W. Effect of Strain Dependent Cohesive Zone Model on Predictions of Interface Crack Growth, 1996.

[167] VAN DER PUT, T. *Deformation and damage processes in Wood.* Delft University Press, 1989.

[168] VASIC, S., CECCOTTI, A., SMITH, I., AND SANDAK, J. Deformation rates effects in softwoods: Crack dynamics with lattice fracture modelling. *Eng. Fract. Mech. 76*, 9 (jun 2009), 1231–1246.

[169] VASIC, S., AND STANZL-TSCHEGG, S. E. Fracture mechanisms and properties of green wood subjected to opening mode I. In *COST Action E35. Rosenheim Work.* (2005).

[170] VASIC, S., AND STANZL-TSCHEGG, S. E. Experimental and numerical investigation of wood fracture mechanisms at different humidity levels. *Holzforschung 61*, 4 (jan 2007), 367–374.

[171] WALTER, R., AND OLESEN, J. F. Cohesive mixed mode fracture modelling and experiments. *Eng. Fract. Mech. 75*, 18 (dec 2008), 5163–5176.

[172] WILLIAMS, J. End corrections for orthotropic DCB specimens. *Compos. Sci. Technol. 35*, 4 (jan 1989), 367–376.

[173] XAVIER, J., MONTEIRO, P., MORAIS, J., DOURADO, N., AND DE MOURA, M. Moisture content effect on the fracture characterisation of Pinus pinaster under mode I. *J. Mater. Sci. 49*, 21 (jul 2014), 7371–7381.

[174] XAVIER, J., OLIVEIRA, M., MONTEIRO, P., MORAIS, J., AND DE MOURA, M. Direct Evaluation of Cohesive Law in Mode I of Pinus pinaster by Digital Image Correlation. *Exp. Mech.* (feb 2014), 829–840.

[175] YANIV, G., AND DANIEL, I. M. Height-tapered double cantilever beam specimen for study of rate effects on fracture toughness of composites. *ASTM Spec. Tech. Publ.* (1988), 241–258.

[176] YOSHIHARA, H. Initiation and propagation fracture toughness of solid wood under the mixed Mode I/II condition examined by mixed-mode bending test. *Eng. Fract. Mech. 104* (may 2013), 1–15.

[177] YOSHIHARA, H., AND KAWAMURA, T. Mode I fracture toughness estimation of wood by DCB test. *Compos. Part A Appl. Sci. Manuf. 37*, 11 (nov 2006), 2105–2113.

[178] ZAGARI, G., AND FORTINO, S. FEM simulation of crack growth in glulam by using a 3D orthotropic viscoelastic model and cohesive elements. In *EUROMECH Solid Mech. Conf.* (2009), pp. 7–11.